Amit Mahajan

Ferroelétricos – CNTs compostos em relação à fabricação de dispositivos funcionais avançados

Ferroelectric – CNTs structures fabrication for advanced functional nano devices

Amit Mahajan

Ferroelétricos – CNTs compostos em relação à fabricação de dispositivos funcionais avançados

Ferroelectric – CNTs structures fabrication for advanced functional nano devices

Dissertação apresentada à Universidade de Aveiro para cumprimento dos requisitos necessários à obtenção do grau de Doutor em Ciência e Engenharia dos Materiais, realizada sob a orientação científica da Professora Dra. Paula Maria Vilarinho, Professora Associada do Departamento de Engenharia de Materiais e Cerâmica da Universidade de Aveiro, Portugal.

A dissertation presented to the University of Aveiro to obtain the Doctor degree in Materials Science and Engineering, under the scientific guidance of Professor Dr. Paula Maria Vilarinho, Associate Professor in the Department of Materials and Ceramic Engineering at University of Aveiro, Portugal.

This thesis work is dedicated to God, My love, Parents and Teachers.

The Board of Examiners

Presidente

Doutor António Manuel Melo do Sousa Pereira
Professor Catedrático da Universidade de Aveiro

Vogais

Doutor Luís António Ferreira Dias Carlos
Professor Catedrático da Universidade de Aveiro

Doutora Isabel Maria das Mercês Ferreira
Professora Auxiliar da Universidade Nova de Lisboa

Doutora Paula Maria Lousada Silveirinha Vilarinho
Professora Associada da Universidade de Aveiro

Doutor José Ramiro Afonso Ferandes
Professor Auxiliar da Universidade de Trás-os-Montes e Alto Douro

Doutora Clara Isabel Barbosa Rodrigues Pereira
Investigadora Auxiliar do REQUIMTE da Universidade do Porto

Acknowledgements

| **Palavras-Chave** | Materiais Ferroelétricos (FE), Métodos Químicos de Solução (CSD), Nanotubos de Carbono Multiparede(MWCNTs), Microeletrónica, Microscópio Eletrónico, Microscopia de Força Atómica e Piezo |

| **Sumário** | Este trabalho é sobre a combinação de óxidos ferroelétricos funcionais com nanotubos de carbono (CNTs) para aplicações na microeletrónica, como por exemplo em potenciais memórias ferroelétricas não voláteis (Non Volatile Ferroelectric Random Access Memories (NV-FeRAM)) de estrutura tridimensional (3D). |

A eletrónica miniaturizada é nos dias de hoje omnipresente.

A necessidade de reduzir o tamanho dos componentes eletrónicos tem sido estimulada por necessidades de maior desempenho em dispositivos de menores dimensões e a custos cada vez mais baixos. Mas esta tendência de miniaturização da eletrónica desafia consideravelmente os processos de fabrico, os materiais a serem utilizados nas montagens das placas e a fiabilidade, entre outros aspetos. Dispositivos semicondutores e tecnologia de circuitos integrados, juntamente com a embalagem eletrónica associada, constituem a espinha dorsal dos sistemas eletrónicos miniaturizados de alto desempenho. No entanto, à medida que o tamanho diminui e a funcionalização aumenta, a redução das dimensões destes dipositivos é cada vez mais difícil; é bem conhecido que abaixo de um tamanho limite o desempenho do dispositivo deteriora-se. Assim, a miniaturização da eletrónica à base de silício tem limitações.

É precisamente neste contexto que desde 2011 o Road Map for Semiconductor Industry (ITRS) sugere tecnologias alternativas às atualmente em uso, designadas por Mais de Moore (More than Moore); sendo uma delas com base em carbono (CNTs e grafeno) [1].

Os CNTs com o seu desempenho único e tridimensionalidade à escala nanométrica, foram considerados como elementos muito promissores para a eletrónica miniaturizada [2]. Nanotubos de carbono possuem uma geometria tubular e um conjunto único de propriedades, incluindo o transporte balístico de eletrões e uma capacidade enorme de transportar a corrente elétrica, o que os tornou de grande interesse para o futuro da microeletrónica [2]. Na verdade, os CNTs podem ter um papel fundamental na miniaturização das memórias ferroelétricas não voláteis (NV-FeRAM). A mudança de uma construção tradicional bidimensional (2D) (ou seja, a duas dimensões, como são os filmes finos) para uma construção tridimensional 3D, com base num arranjo tridimensional de estruturas unidimensionais (1D), como são as estruturas nanotubulares, resultará num desempenho melhorado com deteção de sinal elétrico optimizada, devido à grande contribuição do elétrodo inferior. Uma maneira de conseguir esta configuração 3D é usando nanotubos de carbono.

Os materiais ferroelétricos (FE) são polarizados espontaneamente e possuem constantes dielétricas altas e as suas propriedades piroelétricas, piezoelétricas e eletroópticas tornam-nos materiais funcionais importantes na eletrónica, sendo uma das suas aplicações chave em memórias eletrónicas.

No entanto, combinar os nanotubos de carbono com óxidos FE funcionais é um desafio. Começa logo com a compatibilidade entre os materiais e o seu processamento, já que as temperaturas de cristalização do FE e as temperaturas de oxidação dos CNTs se sobrepõem. Neste caso, o processamento a baixa temperatura dos óxidos FE é absolutamente fundamental.

Dentro deste contexto, neste trabalho foi realizado um estudo sistemático sobre a fabricação e caracterização estruturas combinadas de CNTs – FE, usando métodos de baixa temperatura e de baixo custo. Os FE em estudo foram compostos de titanato zirconato de chumbo ($Pb_{1-x}Zr_xTiO_3$, PZT), titanato de bário ($BaTiO_3$, BT) e ferrite de bismuto ($BiFeO_3$, BFO). Os diversos aspectos relacionados com a síntese e fabricação, como efeito sobre a estabilidade térmica dos nanotubos de carbono multiparede (multiwall CNTs, MWCNTs), formação da fase FE na presença de MWCNTs e interfaces entre CNTs / FE foram abordados neste trabalho. A resposta ferroelétrica medida localmente através de microscopia de ponta de prova piezoelétrica (Piezoresponse Force Microscopy (PFM)), evidenciou claramente que, mesmo para baixas temperaturas de processamento óxidos FE sobre CNTs mantém a sua natureza ferroelétrica.

O trabalho começou pela identificação do comportamento de decomposição térmica em diferentes condições dos nanotubos utilizados neste trabalho. Verificou-se que os MWCNTs purificados são estáveis até 420 ºC no ar, já que não ocorre perda de peso sob condições não isotérmicas, mas foram observadas, por espectroscopia Raman e microscopia eletrónica de transmissão (TEM), alterações na morfologia dos tubos para condições isotérmicas a 400 ºC. Em atmosfera rica em oxigénio os MWCNTs começam a oxidar-se a 200 ºC. No entanto, em atmosfera rica em árgon e sob uma taxa de aquecimento elevada os MWCNTs permanecem estáveis até 1300 ºC com uma sublimação mínima. A energia de ativação para a decomposição destes MWCNTs em ar foi calculada situar-se entre 80 e 108 kJ / mol.

Estes resultados são relevantes para a fabricação de estruturas MWCNTs - FE. De facto, demonstramos que o PZT pode ser depositado por sol-gel a baixas temperaturas sobre MWCNTs. E, particularmente interessante foi provar que a presença de MWCNTs diminui a temperatura e tempo para a formação de PZT, em cerca de ~ 100 ºC comensuráveis com uma diminuição na energia de ativação de 68 ± 15 kJ / mol a 27 ± 2 kJ / mol. Como consequência, foi obtido PZT monofásico a 575 ºC para as estruturas MWCNTs – PZT, enquanto que para PZT (na ausência de MWCNTs) a presença da fase de pirocloro era ainda notória a 650 ºC e onde a fase de PZT foi formada por nucleação homogénea. A natureza piezoelétrica das estruturas de MWCNTs - PZT sintetizadas a 500 ºC por 1 h foi provada por PFM.

Na continuação deste trabalho foi desenvolvida uma metodologia de baixo custo para revestimento de MWCNTs usando uma combinação entre o processamento sol – gel e o processamento hidrotermal. Neste caso o FE usado como prova de conceito foi o BT. BT é uma perovesquita sem chumbo bem conhecida e utilizada em muitas aplicações microeletrónicas. No entanto, a síntese por reação no estado sólido é normalmente realizada entre 1100 - 1300 ºC o que coloca seriamente em risco a combinação com MWCNTs. Neste âmbito, também se ilustrou claramente a ineficácia da síntese hidrotérmica convencional, devido à formação de carbonatos, nomeadamente $BaCO_3$. As estruturas MWCNTs - BT aqui preparadas são ferroelétricas e exibem resposta electromecânica (15 pm / V). Considera-se que estes resultados têm impacto elevado, uma vez que esta estratégia também pode ser estendida a outros compostos de materiais com elevadas temperaturas de cristalização. Além disso, foi também verificado no decurso deste trabalho que a cobertura de MWCNTs com FE pode ser optimizada, neste caso com funcionalização não covalente dos tubos, ou seja, por exemplo com *sodium dodecyl sulfate* (SDS).

Ainda no decurso deste trabalho, os MWCNTs foram utilizados como modelos / andaimes (*templates*) para crescer, neste caso, *nanorods* de multiferroicos de BFO. Mostrou-se que o uso de solventes nítricos promove danos severos nas paredes dos MWCNTs, o que resulta na oxidação prematura dos tubos durante o tratamento de recozimento. Observou-se também que a utilização de solventes nítricos resulta no enchimento parcial dos MWCNTs com BFO, devido à baixa tensão superficial (<119 mN / m) da solução de nitrato. A abertura dos topos dos tubos e o enchimento dos tubos ocorre simultaneamente durante a etapa de refluxo. Verificou-se ainda que os MWCNTs tem um papel crítico na fabricação de BFO monofásico; isto é, a oxidação de nanotubos de carbono durante o processo de recozimento faz com que a atmosfera deficiente em oxigénio, que é gerada como consequência, restrinja a formação das fases secundárias de Bi_2O_3 e se possa obter BFO monofásico. A morfologia das nano estruturas de BFO obtidas indica que os MWCNTs podem atuar como molde ou andaime (*template*) para crescer estruturas 1D de BFO. Medidas magnéticas nestas nano estruturas revelam uma curva de histerese ferromagnética pouco desenvolvida com um campo coercivo de 956 Oe a 5 K.

Também se explorou o possível uso de CNTs alinhados verticalmente (VA-MWCNTs) como elétrodos de base para dispositivos de microeletrónica, por exemplo, para aplicações de memória. Como prova de conceito foram depositados *in-situ* filmes de BFO na superfície dos VA-MWCNTs por pulverização catódica por rádio frequência (rf sputtering). Para uma temperatura de deposição de 400 ºC e tempo de deposição de até 2 h, filmes de BFO cobriram os VA-MWCNTs e não ocorreram danos tanto no filme como nos MWCNTs. Apesar do comportamento macroscópico destes filmes de BFO sobre VA-MWCNTs apresentar perdas dieléctricas, a natureza ferroeléctrica, estrutura de domínios e sua inversão foi confirmada por PFM. Uma histerese ferromagnética pouco desenvolvida com um campo coercivo 700 Oe, caracterizam o comportamento magnético destas estruturas.

O nosso trabalho sistemático é um passo significativo para o desenvolvimento de células de memória 3D; foi assim claramente demonstrado que os nanotubos de carbono podem ser combinados com óxidos FE, para serem por exemplo usados na próxima geração 3D de memórias ferroelétricas não voláteis, não excluindo, no entanto, outras potenciais aplicações na eletrónica.

Abstract   This work is about the combination of functional ferroelectric oxides with Multiwall Carbon Nanotubes for microelectronic applications, as for example potential 3 Dimensional (3D) Non Volatile Ferroelectric Random Access Memories (NV-FeRAM).

Miniaturized electronics are ubiquitous now.

The drive to downsize electronics has been spurred by needs of more performance into smaller packages at lower costs. But the trend of electronics miniaturization challenges board assembly materials, processes, and reliability. Semiconductor device and integrated circuit technology, coupled with its associated electronic packaging, forms the backbone of high-performance miniaturized electronic systems. However, as size decreases and functionalization increases in the modern electronics further size reduction is getting difficult; below a size limit the signal reliability and device performance deteriorate. Hence miniaturization of silicon-based electronics has limitations.

On this background the Road Map for Semiconductor Industry (ITRS) suggests since 2011 alternative technologies, designated as *More than Moore*; being one of them based on carbon (carbon nanotubes (CNTs) and graphene) [1].

CNTs with their unique performance and three dimensionality at the nano-scale have been regarded as promising elements for miniaturized electronics [2]. CNTs are tubular in geometry and possess a unique set of properties, including ballistic electron transportation and a huge current caring capacity, which make them of great interest for future microelectronics [2]. Indeed CNTs might have a key role in the miniaturization of Non Volatile Ferroelectric Random Access Memories (NV-FeRAM). Moving from a traditional two dimensional (2D) design (as is the case of thin films) to a 3D structure (based on a tridimensional arrangement of unidimensional structures) will result in the high reliability and sensing of the signals due to the large contribution from the bottom electrode. One way to achieve this 3D design is by using CNTs.

Ferroelectrics (FE) are spontaneously polarized and can have high dielectric constants and interesting pyroelectric, piezoelectric, and electrooptic properties, being a key application of FE electronic memories.

However, combining CNTs with FE functional oxides is challenging. It starts with materials compatibility, since crystallization temperature of FE and oxidation temperature of CNTs may overlap. In this case low temperature processing of FE is fundamental.

Within this context in this work a systematic study on the fabrication of CNTs - FE structures using low cost low temperature methods was carried out. The FE under study are comprised of lead zirconate titanate ($Pb_{1-x}Zr_xTiO_3$, PZT), barium titanate ($BaTiO_3$, BT) and bismuth ferrite ($BiFeO_3$, BFO). The various aspects related to the fabrication, such as effect on thermal stability of MWCNTs, FE phase formation in presence of MWCNTs and interfaces between the CNTs/FE are addressed in this work.

The ferroelectric response locally measured by Piezoresponse Force Microscopy (PFM) clearly evidenced that even at low processing temperatures FE on CNTs retain its ferroelectric nature.

The work started by verifying the thermal decomposition behavior under different conditions of the multiwall CNTs (MWCNTs) used in this work. It was verified that purified MWCNTs are stable up to 420 ºC in air, as no weight loss occurs under non isothermal conditions, but morphology changes were observed for isothermal conditions at 400 ºC by Raman spectroscopy and Transmission Electron Microscopy (TEM). In oxygen-rich atmosphere MWCNTs started to oxidized at 200 ºC. However in argon-rich one and under a high heating rate MWCNTs remain stable up to 1300 ºC with a minimum sublimation. The activation energy for the decomposition of MWCNTs in air was calculated to lie between 80 and 108 kJ/mol.

These results are relevant for the fabrication of MWCNTs – FE structures. Indeed we demonstrate that PZT can be deposited by sol gel at low temperatures on MWCNTs. And particularly interesting we prove that MWCNTs decrease the temperature and time for formation of PZT by ~100 ºC commensurate with a decrease in activation energy from 68±15 kJ/mol to 27±2 kJ/mol. As a consequence, monophasic PZT was obtained at 575 ºC for MWCNTs - PZT whereas for pure PZT traces of pyrochlore were still present at 650 ºC, where PZT phase formed due to homogeneous nucleation. The piezoelectric nature of MWCNTs - PZT synthesised at 500 ºC for 1 h was proved by PFM.

In the continuation of this work we developed a low cost methodology of coating MWCNTs using a hybrid sol-gel / hydrothermal method. In this case the FE used as a proof of concept was BT. BT is a well-known lead free perovskite used in many microelectronic applications. However, synthesis by solid state reaction is typically performed around 1100 to 1300 ºC what jeopardizes the combination with MWCNTs. We also illustrate the ineffectiveness of conventional hydrothermal synthesis in this process due the formation of carbonates, namely $BaCO_3$. The grown MWCNTs - BT structures are ferroelectric and exhibit an electromechanical response (15 pm/V). These results have broad implications since this strategy can also be extended to other compounds of materials with high crystallization temperatures. In addition the coverage of MWCNTs with FE can be optimized, in this case with non covalent functionalization of the tubes, namely with sodium dodecyl sulfate (SDS).

MWCNTs were used as templates to grow, in this case single phase multiferroic BFO nanorods. This work shows that the use of nitric solvent results in severe damages of the MWCNTs layers that results in the early oxidation of the tubes during the annealing treatment. It was also observed that the use of nitric solvent results in the partial filling of MWCNTs with BFO due to the low surface tension (<119 mN/m) of the nitric solution. The opening of the caps and filling of the tubes occurs simultaneously during the refluxing step. Furthermore we verified that MWCNTs have a critical role in the fabrication of monophasic BFO; i.e. the oxidation of CNTs during the annealing process causes an oxygen deficient atmosphere that restrains the formation of Bi_2O_3 and monophasic BFO can be obtained. The morphology of the obtained BFO nano structures indicates that MWCNTs act as template to grow 1D structure of BFO. Magnetic measurements on these BFO nanostructures revealed a week ferromagnetic hysteresis loop with a coercive field of 956 Oe at 5 K.

We also exploited the possible use of vertically-aligned multiwall carbon nanotubes (VA-MWCNTs) as bottom electrodes for microelectronics, for example for memory applications. As a proof of concept $BiFeO_3$ (BFO) films were in-situ deposited on the surface of VA-MWCNTs by RF (Radio Frequency) magnetron sputtering. For in situ deposition temperature of 400 ºC and deposition time up to 2 h, BFO films cover the VA-MWCNTs and no damage occurs either in the film or MWCNTs. In spite of the macroscopic lossy polarization behaviour, the ferroelectric nature, domain structure and switching of these conformal BFO films was verified by PFM. A week ferromagnetic ordering loop was proved for BFO films on VA-MWCNTs having a coercive field of 700 Oe.

Our systematic work is a significant step forward in the development of 3D memory cells; it clearly demonstrates that CNTs can be combined with FE oxides and can be used, for example, as the next 3D generation of FERAMs, not excluding however other different applications in microelectronics.

References:
1. "http://www.itrs.net/Links/2011ITRS/2011Chapters/2011MEMS.pdf".
2. Robertson, J., "Growth of nanotubes for electronics". Materials Today, 2007. 10(1-2): p. 36-43.

Contents

Ferroelectric – Carbon Nanotubes (CNTs) structures fabrication for advanced functional nano devices

List of figures

List of tables

List of symbols

$\varepsilon_{ij}, \varepsilon$	Dielectric Permittivity
ε_r	Relative Dielectric Permittivity
ε_o	Dielectric Permittivity of the Vacuum (8.85 x 10-12 F/m)
ε''	Imaginary Part of the Permittivity
ε'	Real Part of the Permittivity
λ	Wavelength
θ_{hkl}	Bragg Angle
γ	Interfacial Tensions
ω	Frequency
$\vec{C}_h$	Chiral Vector
C	Curie Weiss Constant
c	Speed of Light in Vacuum
D	Dielectric Displacement
d, d_{33}	Piezoelectric Coefficient
d_{ij}	Piezoelectric Tensor
d_{hkl}	Spacing between Atomic Planes
E_{flux}	Electric Displacement
E	Electric Field
E_d	Depolarizing Field
E_C	Coercive Field
hkl	Miller Indexes
P	Polarization
Pr	Remanent Polarization
P_S	Spontaneous Polarization
Q_{jmk}	Electrostatic Coefficient
R	Gas Constant
r_x	Ionic Radius (where x = O, A and B)
S	Strain
$\tan\delta$	Dielectric Loss
T	Stress

T_C	Curie Temperature
t	Goldschmidt Tolerance Factor
V	Voltage
V_{ac}	ac Voltage
V_{dc}	dc Voltage
$\bar{v}$	Wave Number
W_{dw}	Domain Wall Energy
W_e	Elastic Energy
X	Deflection
ΔZ	Change in Thickness
Z	Thickness of the Sample

List of abbreviations

AFM	Atomic Force Microscope
ac	Alternating Current
BFO	Bismuth Ferrite
BT	Barium Titanate
BE	Bottom Electrode
BCNT	Bamboo Carbon Nanotubes
C	Cubic Structure
CMOS	Complementary Metal Oxide Semiconductor
CNT	Carbon Nanotubes
dc	Direct Current
DTA	Differential Thermal Analysis
DWCNTs	Double Carbon Nanotubes
EDS	Energy Dispersive X-Ray Spectroscopy
FE	Ferroelectric
FeCaps	Ferroelectric Capacitors
FET	Field Effect Transistor
FM	Ferromagnetic
FeRAMs	Ferroelectric Random Access Memories
FTIR	Fourier Transformed Infra-Red
HRTEM	High Resolution Transmission Electron Microscope
IC	Integrated Circuit
ME	Magnetoelectrics
MWCNTs	Multi Wall Carbon Nanotubes
MLCC	Multilayer Ceramic Capacitor
NV-FeRAMs	Non-Volatile Ferroelectric Random Access Memories
NTs	Nanotubes
O	Orthorhombic Structure
P-E	Polarization-Electric Field
PFM	Piezoelectric Force Microscope
PZT	Lead Zirconate Titanate
R	Rhombohedral Structure

SDS	Sodium Dodecyl Sulfate
S-E	Strain-Electric Field
SEM	Scanning Electron Microscope
SPM	Scanning Probe Microscope
SWCNTs	Single Wall Carbon Nanotubes
T	Tetragonal Structure
TE	Top Electrode
TEM	Transmission Electron Microscope
TG	Thermogravimetric Analysis
VAMWCNTs	Vertical Aligned Multi Wall Carbon Nanotube
XRD	X-Ray Diffraction
0D	Zero Dimensional
1D	One Dimensional
2D	Two Dimensional
3D	Three Dimension

Chapter 1

1   *Scientific motivation and rationale*

1.1 Problem statement

The field of electronics is growing exponentially from the last decade and so. This progress is well seen from the miniaturization of devices, devices with multi-functionality and high data transfer rate (4G technology expected to move to 5G by 2025).

In today's world, we all are connected with each other by wireless technology using smart phones and smart devices. All the devices are connected by internet network. The day is not far when we live in ultra-digitally responsive world, where more things are exponentially connected to the internet than people. Thomson Reuters predict by 2025 that this digital connectivity will encompass and join vast geographies [1]. The rising of digitization demands new set of systems, circuits architectures and materials, which can further support the reduction of the size of the devices, increasing the energy storage capacity with high charging rate and memories with high data storage capacity. Thanks to the recent progress in the improvement of semiconductors, development of graphene and carbon nanotubes (CNTs) these predictions will be soon a reality.

Within the electronics industry, one of the major trends in these last few years has been the ability to exponentially decrease the minimum feature size used to fabricate integrated circuits in accordance with Moore's Law [2]. But this miniaturization trend challenges board assembly materials, processes, and reliability. Nevertheless the miniaturization of silicon-based electronics has limits. On this background the Road Map for Semiconductor Industry (ITRS) suggests since 2011 alternative technologies, designated as *More than Moore*; being one of them based on the use of carbon (carbon nanotubes (CNTs) and graphene) [3]. The ITRS has specifically suggested that carbon nano structures, and carbon-based nano composites in particular, are part of the driving force behind this transformation, and are poised to take centre stage in high-energy density and power-density applications for microelectronics. Carbon nano composites can be used as supercapacitive electrodes, either in two-or-three-dimensional structures, with high surface area.

One of the areas of microelectronics where further miniaturization is getting difficult is the area related with Non-Volatile Ferroelectric Random Access Memory (NV-FeRAM).

FeRAM is the memory storage device similar to a dynamic random access memory (DRAM), in which instead of a dielectric it uses of ferroelectric (FE) material, typically as lead zirconium titanate ($PbZr_{1-x}Ti_xO_3$, PZT). FRAM stores information using the polarization of a ferroelectric material placed between two electrodes. At present the memory cells are in the form of planar or stack cells as illustrated in Figure 1-1 (a), where the FE layer is embedded between the top and bottom electrodes and the thickness of the FE layer is from 90 to 150 nm. Further reduction of the FE thickness results in the lowering of the signals below 100 fC (this is the comfort zone for FeRAM cell according to 1T -1C design) and results in a poor signal reliability, cross talk between the memory cells and high leakage current [4].

The possible solution for this problem is to radically alter the configuration and substitute this classical two dimension (2D) memory cell structure by a completely new one, based on a three dimension (3D) structure cell design (Figure 1-1 (b)), taking advantage of one dimension (1D) nanostructures. The 3D memory cells structure provides large areas for bottom and top electrodes resulting in enhancement of capacitance and signal strength. Moreover, it was predicted theoretically that 1D structures increase the storage capacity up to 10,000-fold [5, 6]. Not only in memory cells, the 3D FE structures in form of nanotrenchs, nano rods, nano bars and nanotubes have a vast set of applications, such as energy harvesters, microfluidic systems, electrocaloric coolers for computers, phased-array radar, high-power microwave devices, among others [7]. Very recently Intel Corporation has develop a 3D transistor part of the 13 quad core processors having 20 % better performance with 20 % less power consumption than predecessor [8].

One possible way to get 3D FE cells is to use carbon nanotubes (CNTs) as bottom electrode or template to fabricate FE nanostructures, due to its tubular shape, high conductivity, ballistic electron transport and a huge current - carrying capacity, which make them of great interest [11]. For memories applications CNTs can act as a bottom electrode, on which FE is deposited as shown in Figure 1-2 (a) or interconnects as in transistors and as the channel material in 3 D Field Effect Transistor (FET) (Figure 1-2 (b)) [11].
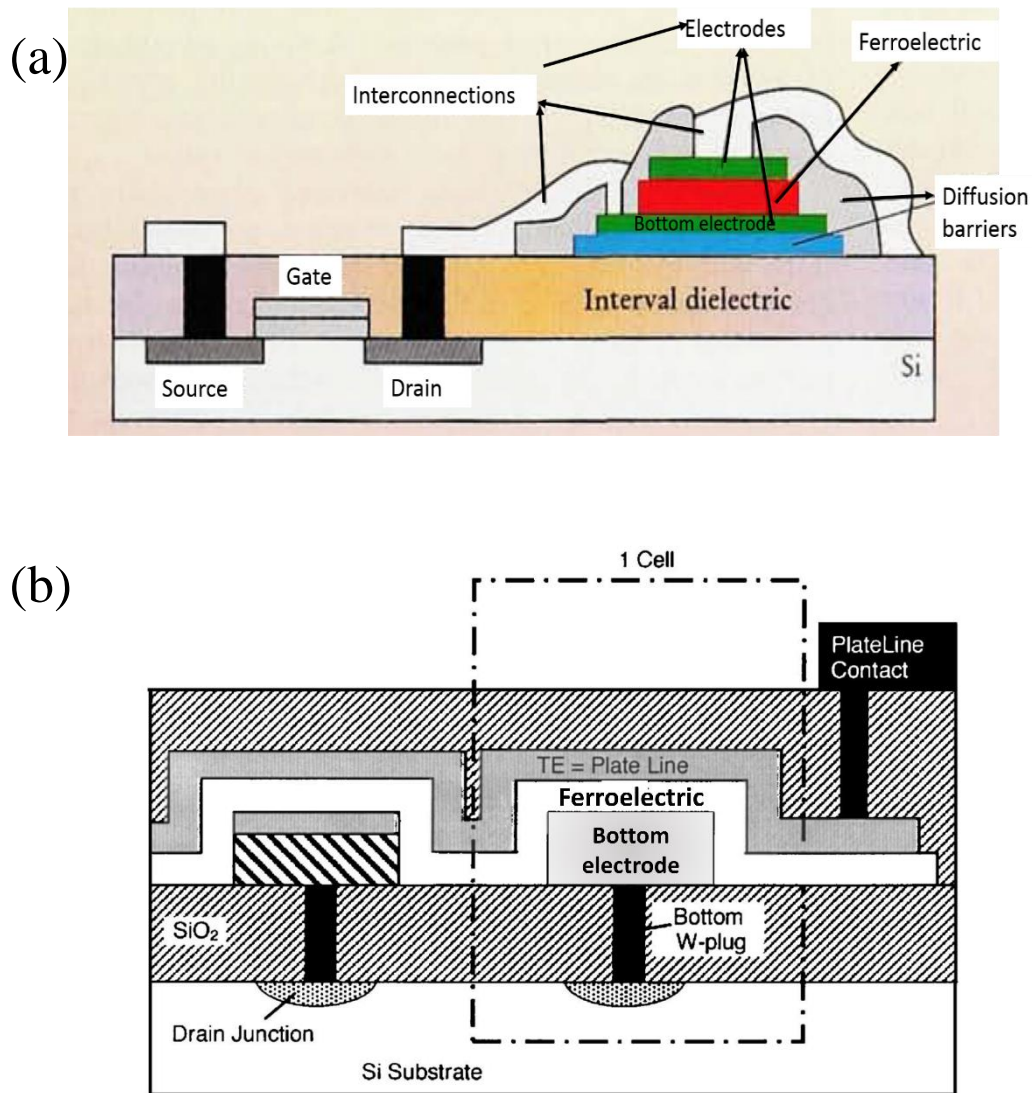
Figure 1-1 (a) Memory cell for FeRAM with one transistor and one capacitor (1T1C) architect planar structure, where bottom electrode is in shape of 2D structure (film) [9] and (b) Schematic illustrates 3D FeRAM cell where bottom electrode is in shape of tube, inset on top left shows the possible schematic of the 3D FeRAM [10].

However these new configurations for FE applications raised many questions that need to be answered before any prototype demonstration and fabrication: Will CNTs work as bottom electrode? How can CNTs be integrated with FE materials, when oxidation temperature and phase formation temperature of FE is so close? How will the

interfaces between FE and CNTs affect the electrical performance. These are some of the many questions to be answered in these new structural designs.
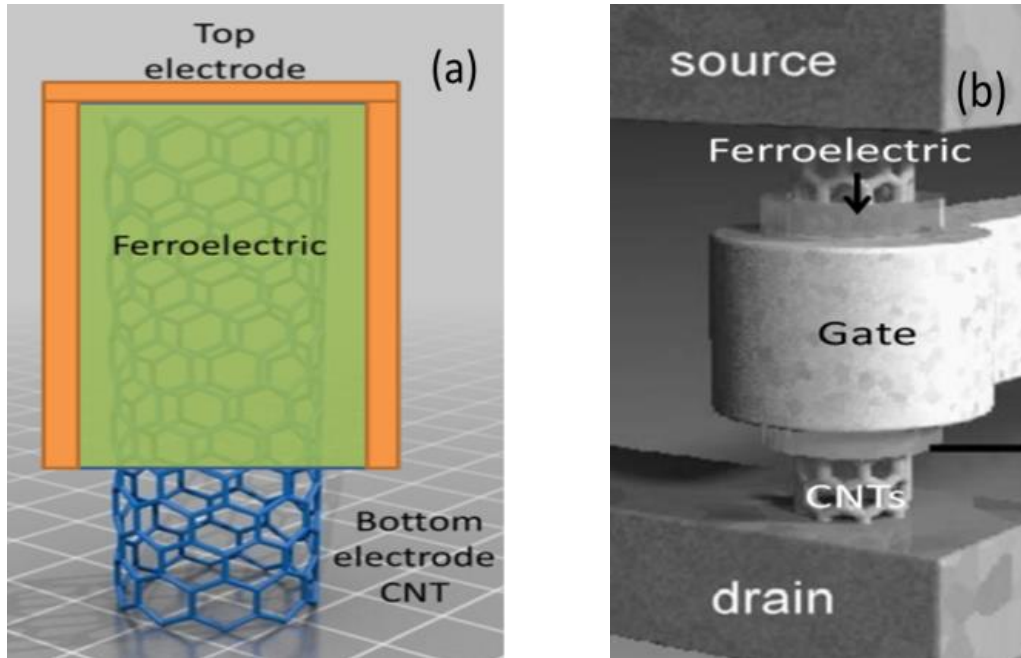
Figure 1-2 Schematic illustration of the possible use of CNTs as a bottom electrode (1 D structure) (a) and for 3D memory cell design covered with FE (b) use of CNTs as a channel in FET transistor (adapted from [12]).

The combination of CNTs with FE can be an elegant approach to reduce capacitor size in integrated FeRAM circuits as well. Pursuing this idea, Kawasaki *et al.* [13] (year 2007) combined successfully for the first time FE thin films and MWCNTs. The authors demonstrated the possibility of conformably coating Multi Wall CNTs (MWCNTs) with high-dielectric oxide as a first step toward ultrahigh integration density of three-dimensional FeRAM. However, this is a very preliminary work and the authors reported several problems associated with carbon lattice damage, siphoning of the substrate material and the stoichiometry of PZT that need to be addressed. Till today there are only a few reports on the combination of FE with CNTs [13-31]. And most of the literature lacks in systematic studies on the phase formation of FE in presence of CNTs, interface studies and measurement of FE properties. The detail summary on the state of the art on CNTs-FE nano structures is given in Chapter 2. Anyhow these works are important being

considered as landmarks, since they demonstrated the feasibility of the fabrication of CNTs-FE nano structures. These previous also highlight the need for more systematic works on the fabrication of these CNTs-FE nanostructures and somehow supporting the R&D performed in the present work. At the same time the development of lead free FE and lead free multiferroic 3D nanostructures is pertinent and highly desirable, as well.

Therefore the main aim of the present work is fabrication and characterization of CNTs-FE structures to: i) identify optimised fabrication strategies, as compatibility of both materials is an issue, ii) accumulate new knowledge on CNTs–FE interface phenomena as the structure properties are largely determined by them, iii) exploit different structures as embryonic forms of high density hard-wired FRAM capacitor arrays and iv) measure the ferroelectric response of the CNTs-FE.

The novelty and originality of these studies include:

-synthesis of functional nanostructures of 1D nano lead based, lead free ferroic structures with CNTs, in which CNTs will be used as the template or bottom conductor to fabricate 1D ferroelectric nanostructures;

-to exploit low cost hydrothermal / chemical methods to grow FE on CNTs;

-to study systematically interfaces/surface modification between CNTs and FE to optimize their growth;

-to measure local electrical properties of MWCNTs-FE structures using piezo force microscope (PFM);

Materials for FeRAM are selected based on the properties, which are considered to be the most important in the operation of memory devices and based on processing requests as well [10] and these are:

-the remanent polarization (Pr), that need to be as high as possible, so that sensing margin between the two states is well defined;

-the coercive field (E_c) should be small so that device can operate at low voltage;

-the fatigue is other aspect to be considered; it is defined as the steady loss of remanent polarization of the material and should be minimal;

-the retention state over time, this need to be about ten year's retention at 85 ºC;

-the crystallization temperature needs to be as low as possible so that FE can be easily integrated on a chip.

Because commercially in use, $PbZr_{0.52}Ti_{0.48}O_3$ (PZT) and $BaTiO_3$ (BT) are the first choice as a material for our studies. Both PZT and BT depict excellent polarization/electric field response. And they have been used as material for sensors, FeRAMs, capacitors and in electro optic devices. In 2006 Fujitsu announced bismuth ferrite ($BiFeO_3$, BFO) as the FE for FeRAM [32]. In addition because BFO, is one of the true single phase multiferroic materials having high polarization (~45 $\mu C/cm^2$), besides being a lead free material make it an obvious choice for our studies, as well. Therefore, the materials under study in this work are: lead free BT and BFO and lead based PZT to fabricate CNTs-FE nano structures. General properties of all the three selected FE are mentioned in Table 1-1.

1.2   Outline of the thesis

This chapter (*Chapter 1*) presents the motivation and the objective of the present work. In *Chapter 2* a detailed introduction of carbon nanotubes (CNTs) for electronics, to the basics of ferroelectricity and ferroelectric materials and the comprehensive discussion on ferroelectric behaviour at the nano scale and in nanostructures, passing by the fabrication of MWCNTs-FE composite is reported. *Chapter 3* describes the experimental details carried out along the work, including the purification and functionalization of the MWCNTs used in this work, followed by a concise description on the characterization techniques and conditions used in the present work. Some of the experimental details concerning materials preparation are detailed later in *Chapters 5 to 7* for each case study. The results obtained in this work and discussion are presented in next four chapters. *Chapter 4* is dedicated to the thermal degradation studies conducted on MWCNTs used in this work. The following chapters report the several cases studies of this work based of each of the FE material used to combine with MWCNTs. *Chapter*

5 reports on the structures of MWCNTs-PZT. *Chapter 6* describes the work on MWCNTs-BT and *Chapter 7* present the work on MWCNTs-BFO. General conclusions and future work are presented in *Chapter 8*.

Table 1-1 Physical properties of the selected ferroelectric materials to be studied in this work. The presented properties refer to performance as in 2D films.

Properties	$PbZr_{0.52}Ti_{0.48}O_3$ (PZT) on platinum coated silicon substrate [33]	$BaTiO_3$ (BT) on platinum coated silicon substrate [34]	$BiFeO_3$ (BFO) on $SrRuO_3$ coated silicon substrate [35]
$P_r(\mu C/cm^2)$	>30	~10	~45
Coercive field (E_c) (kV/cm)	~150	~35	~200
Crystallization temperature (^{o}C)	650-700	700-750	650-700
Curie temperature (^{o}C)	~390	~120	~830
Fatigue	$>10^{10}$	-	-

Chapter 2

2   *Fundamentals and state of the art*

Abstract

The purpose of this chapter is to provide the background of the current work by presenting a review on the state of the art of the most significant topics. It starts by emphasising the importance of carbon in microelectronics followed by the presentation of the most important concepts, nomenclature and knowledge on Carbon Nanotubes (CNTs), as synthesis, electrical properties and dependence on temperature and pressure of the physical properties of CNTs. The basic concepts and definitions of piezoelectricity are introduced after and followed by details on ferroelectrics. A brief review on ferroelectric behaviour and size effects of ferroelectrics is subsequently presented. The literature review on the CNTs-FE structures covers the available information on the topic. The chapter further includes details on the two major synthesis approaches, top- down and bottom up, used for the fabrication of nano structured materials, precisely nano ferroelectrics. The chapter ends with a summary of the presented concepts, indicates the opportunities and challenges if carbon-based electronics will be further exploited.

2.1 Carbon nanotubes for electronics

2.1.1 Why CNTs might be useful in microelectronics?

The Holy Grail for semiconductor industries is to keep following Moore´s law [2], in what concerns the scaling of conventional silicon based integrated circuits to even smaller feature sizes. The smallest element printed on the chip in repeatedly array or the half pitch of the DRAM is known as feature size. From the last 45 years the feature size has been reduced from 10 µm to 22 nm in silicon microelectronic devices [8]. The small features have been mainly fabricated by lithography processes, but it's getting difficult to further achieve small feature sizes without affecting the electrical properties of the devices. Continuous scaling of devices on silicon based microelectronics is getting difficult and companies are exploring new sets of nano-materials such as CNTs and graphene in order to go beyond silicon based microelectronics [36]. The global market revenue for CNTs is expected to reach $2,398.4 million by 2018 in various sector including microelectronics [37].

CNTs is the prime material under consideration due to its extraordinary electrical and mechanical properties. In addition to this, it has quasi one dimension (1D) structure which helps in unidirectional current flow and long mean free path (up to few hundred nanometer). CNTs can offer scattered free ballistic transportation for small channel devices, hence low power dissipation and has good thermal conductivity [38, 39]. The above properties make CNTs as a perfect channel material for Field Effect Transistors (FET). Digital circuits based on transistors fabricated from CNTs have the potential to outperform silicon by improving the energy efficiency of the product by more than one order of magnitude. Hence, CNTs are a promising complement to the existing semiconductor technologies [40].

The first potential use of semiconducting single wall CNTs (SWCNTs) with a diameter of 1 nm was demonstrated in 1998 by the University of Delft and IBM Corporation for field effect transistors (FET) (Figure 2-1) [41, 42]. In FET the SWCNTs are used as a channel material. They demonstrated that the conductance of semiconductor SWCNTs can be modified by an order of magnitude ($\sim 10^5$) by externally applying a gate

voltage, similar to that of a metal–oxide–semiconductor field-effect transistor (MOSFET). Transistors made from CNTs depict 20 times less switching resistance and 200 times more current handling capacities than conventional MOSFETs. This was a revolutionary finding among the scientific community that demonstrates the potential usefulness of CNTs FET. The reports on the first use of CNTs in digital circuit application came in 2001, when CNT - based logic gate by integrating n-type and p-type nanotube transistors was demonstrated. [43-45]. n and p type semiconductor CNTs can be prepared by the integration of metals with different work functions (smaller for the case of n-type and higher for p-type semiconductor, respectively) [46, 47]. The potential of CNTs was also explored for the Radio frequency (RF) applications as a planar RF transistors, self-aligned T-gate RF transistors and transistors with embedded bottom gate [48-50].
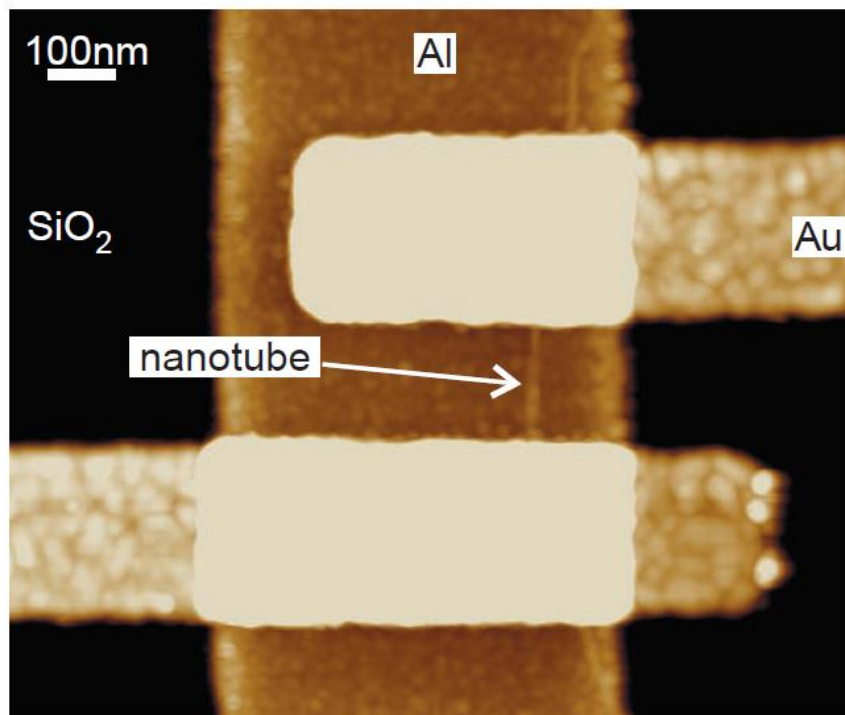
Figure 2-1 Atomic force micrograph of FET device constructed using single wall carbon nanotubes [41, 42].

CVD grown CNTs can be processed into thin films of CNTs by solution transfer methods. The thin films of CNTs have a great potential application for flexible devices. These films have excellent transparency which makes them a preferential material for future electronics displays. The potential of semiconducting CNTs for thin films

transistors (TFTs) was demonstrated [51-53]. CNTs TFTs have been employed as active matrix organic light-emitting diode (AMOLED) arrays [19]. The schematic diagram of one pixel of organic light-emitting diode (OLED) controlled by CNTs network based driver circuit is given in Figure 2-2 (a). This is the first demonstration of AMOLED arrays with 500 pixels driven by 1000 CNT TFTs. Figure 2-2 (b) depicts AMOLED arrays fabricated on glass substrates. Figure 2-2 (c) shows an optical image for the OLEDs lights on CNT TFTs with yield efficiency of 70 %. CNTs TFTs has also been employed in the control of circuits for pressure sensing elements in electronic skin (Figure 2-3) [54]. It was proved that this flexible CNTs network-based FETs can be processed at room temperature, hence less expensive what is indeed important from the industrial and consumer point of view [53].

More recently in 2013, Shulaker *et al.* [55] demonstrate the first CNTs based computer. This computer is entirely built on CNTs-based transistors in which CNTs are used as channel material. The CNTs computer runs an operating system that is capable of multitasking.

(a)

Ferroelectric – Carbon Nanotubes (CNTs) structures fabrication for advanced functional nano devices
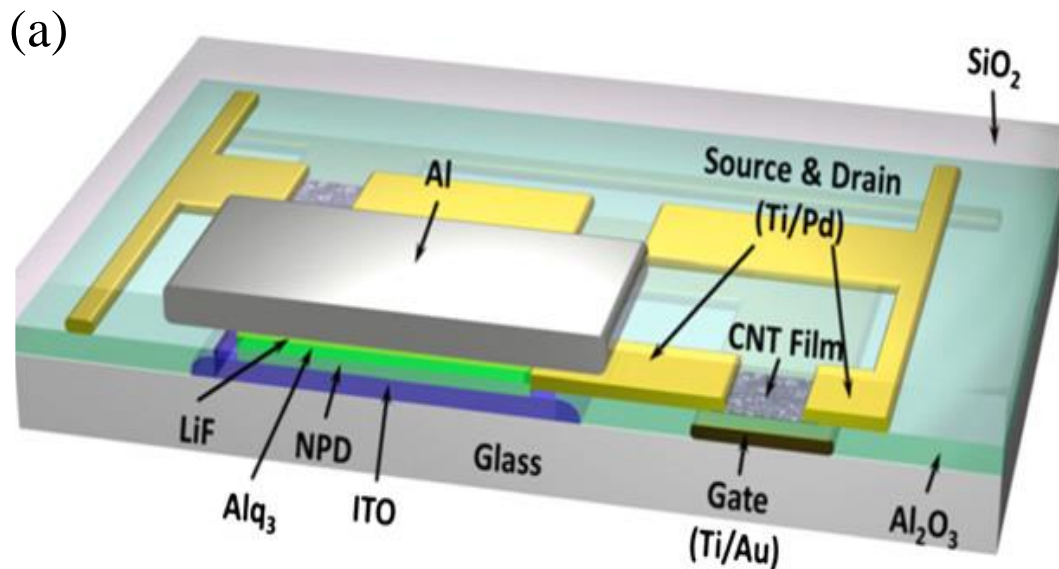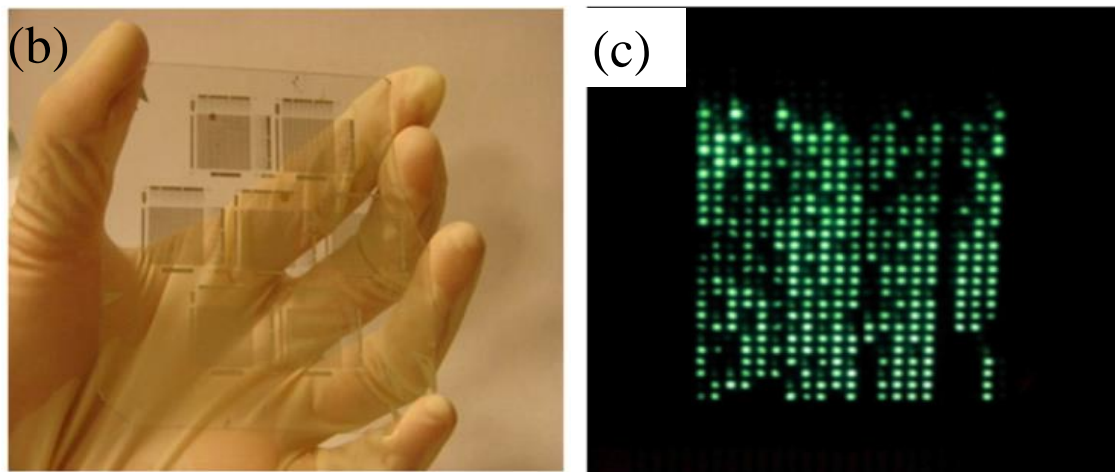
Figure 2-2 (a) Schematic diagram for the construction of one pixel of OLED controlled by CNTs, (b) Arrays of AMOLED fabricated on transparent glass substrate and (c) illuminating arrays of green light of AMOLED with the CNTs based network circuit [56].
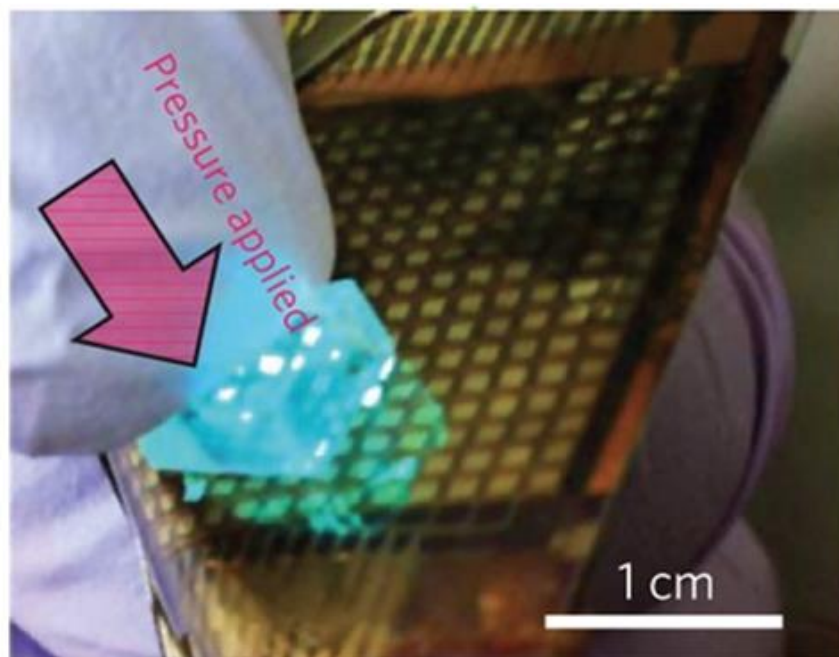
Figure 2-3 Represent the pressured OLEDs containing FETs where CNTs are used as channel material [54].

Other than FETs, CNTs have been studied for interconnectors applications due to its high current density up to 109 A/cm^2 which is more than 100 times that of copper and high surface area. In CMOS two kinds of interconnectors are used, named as horizontal and vertical interconnectors (Figure 2-4). Horizontal interconnectors join FETs in different parts of an integrated circuit. There are many layers of horizontal interconnectors in CMOS and each layer is separated by a dielectric. The vertical interconnectors called as vias, and they pass through holes in the dielectric to join horizontal interconnectors to the source and drain or gate electrode of a FET as shown in Figure 2-4 [11]. Defect free MWCNTs with sizes ranging from 20 to 100 nm in bundles or as individual have proven the potential to be used as metallic interconnectors. The high thermal conductivity of CNTs is also very useful for chip thermal management and dissipation of heat in devices [57]. Fujitsu Ltd. and Infineon Technologies AG have carried out extensive studies on the fabrication of interconnectors [58-60].

The high surface area of CNTs depicts, make them ideal material to fabricate sensors with high sensitivity. CNTs transistors was tested as sensor and depicts high sensitivity to low concentration of NO_2 and NH_3 [61].The CNT transistor shows the increase in conductance when come in contact with NO_2 and NH_3. The phenomena was interpreted by the charge transfer mechanism between gasses and CNTs. Further, development shows the CNT transistor based sensors can detect 100 ppm level of NO_2 gas [62].

Nantero Inc. demonstrated the use of MWCNTs sandwiched between two metallic electrodes to form resistive Nanotube based / Non-volatile random access memory (NRAM) cell. Figure 2-5 (a) shows the SEM micrograph of NRAM cell where CNTs are embedded inside the tungsten electrodes. Figure 2-5 (b) shows the various steps followed to fabricate the NRAM cells from the heterostructure of SiO/TiN/CNT/W. The memory works based on the principle of change in the resistance that occurs due to the interaction between CNTs attach on the top and bottom electrode shown in Figure 2-5 (c) [32].

The first commercial application for CNTs in microelectronics was realized as a composite with polymer (polycarbonate-ABS), which is used as electric discharge material in automobiles [63]. Other than electric discharge application composites based on CNTs can be used as electromagnetic interference shielding, as well [64].
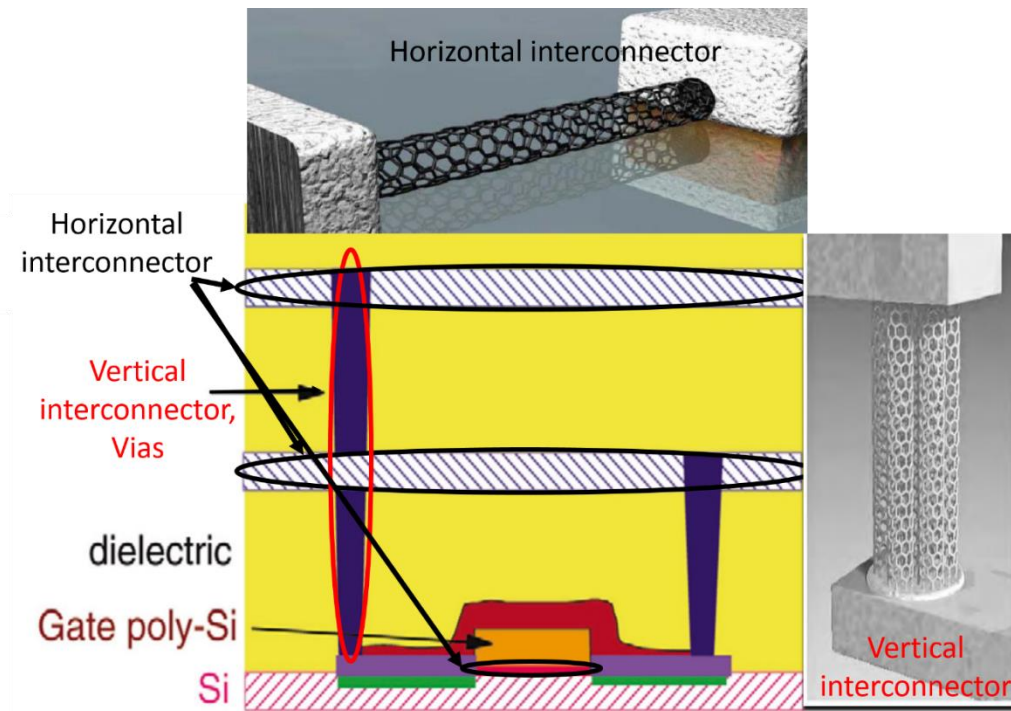
Figure 2-4 Schematic of the two kinds of interconnects in which CNTs can be used in CMOS circuitry design (adapted and modified from [11]).

One of the areas of microelectronics where further miniaturization is getting difficult is the area of memories, in particular Non Volatile Ferroelectric Random Access Memory (NV-FERAM) (detailed in Chapter 1). Therefore, there is need to move from 2D designs to 3D design which results in the high reliability and sensing of the signals due to the large contribution from bottom electrode. One way to achieve this 3D design is using CNTs. CNTs are tubular in geometry and have unique set of properties, including ballistic electron transportation and a huge current caring capacity, this make them of great interest for future FeRAM [11]. The idea of using CNTs covered with dielectric material for Nanoelectromechanical dynamic random access memory non-volatile was first put forward by Jang *et al.* [14], later followed for non-volatile ferroelectric memory [21].

To integrate CNTs with complex functional oxide such as ferroelectric there is need for detail and comprehensive assessment on various aspects, mainly on synthesis and properties. So that CNTs can be effectively used for microelectronic devices

applications. Some of initial investigation has been carried out and its details are mentioned in section 2.5.
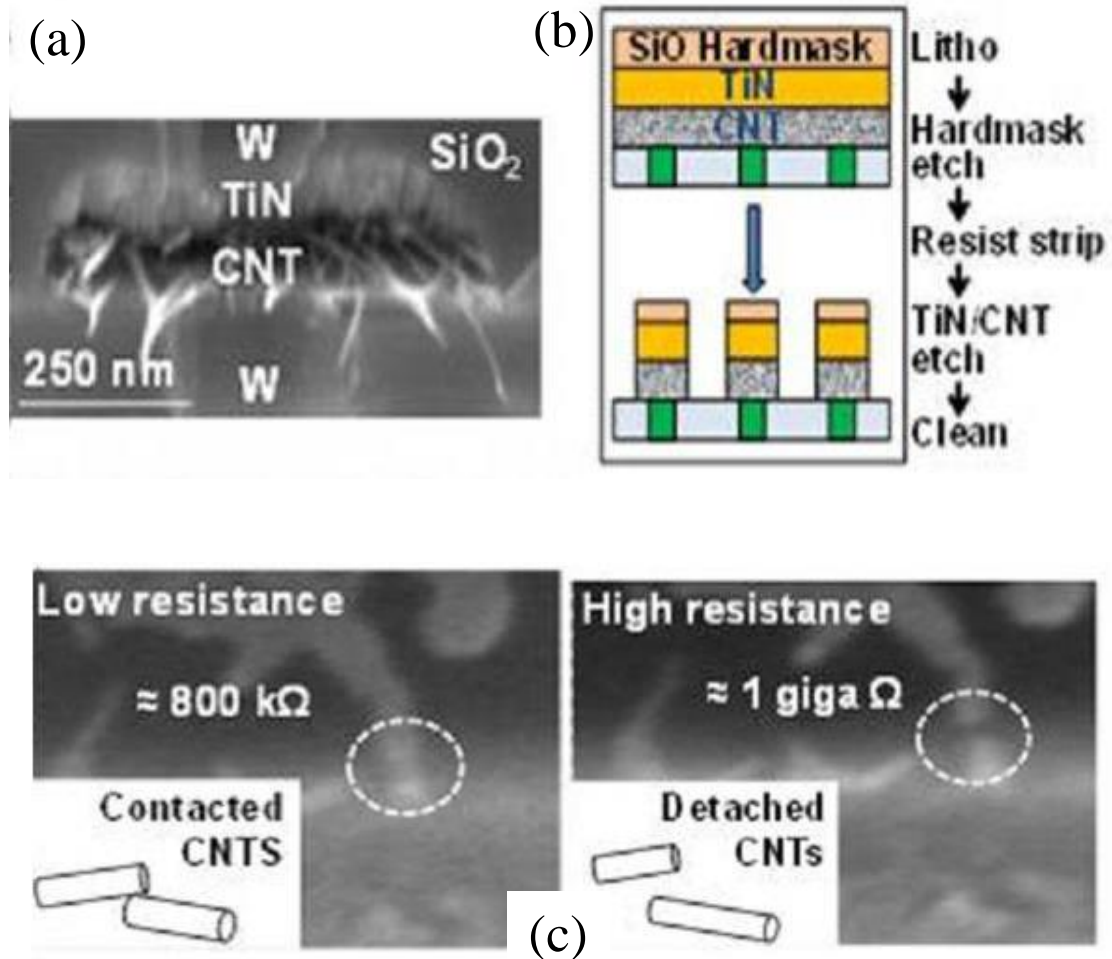
Figure 2-5 (a) Scanning electron micrograph of NRAM cell based on CNTs, (b) schematic of layer heterostructure of SiO, TiN and CNTs, which was litho followed by etching to obtained NRAM cells and (c) working of the CNTs based RAM on the principle of change in resistance; on left the CNTs are in contact so low resistance "on" state and on right CNTs are not in contact "off" state [32].

2.2 Introduction to carbon nanotubes (CNTs)

Most of the literature has been credited the discovery of carbon nanotubes (CNTs) to Sumio Iijima (1991). However, it know by now that first electron micrograph published back in 1952 by Radushkevich and Lukyanovich in the Journal of Physcial Chemistry of Russia [65]. The micrograph shows the carbon filaments exhibiting a inner cavity having

diameter of 50 nm. However, the work might be not highlighted due to the cold war and discouraging of citing articles written in Russian language by west. Iijima work has get maximum importance because of the fundamental physics and systematic growth mechanism discussed on the formation of CNTs [66].

In the following years, the properties of CNTs were studied theoretically and exploited by different experimental methods. CNTs show extraordinary charge carrier mobility (2 - 6) $\times$ 104 cm^2/(V·s)), with a band gap (1 eV) dependent on the specific ordering of carbon atoms in the nanotube, and a maximal electrical current density of >10^9 A/cm^2 (~100 times higher than copper wires). In addition CNTs has Young's modulus of 0.8 to 1.8 TPa and tensile strength of ~63 GPa far better than steel (Young's modulus ~0.2 TPa and tensile strength 1.55 GPa) [67-69]. The electrical properties of CNTs are mainly dependent on the chirality (tube diameter and wrapping angle determined by vector (m, n)), which creates a big challenge in terms of CNTs synthesis to develop a method by which one can control the chirality of the tubes. The task of producing samples containing CNTs of a specific chirality is difficult and is still open for further research [70]. In spite of that, CNTs have found already vast applications when used as fillers in composites to strengthen the mechanical properties of materials, especially oxides and polymers [71].

CNTs are formed by rolling a graphite sheet in to a seamless hollow cylinder. The CNTs are classified based on the rolling direction to get different diameter and helicity of the tubes. The circumference of CNTs is determined by the chiral vector $\vec{C}_h$, that is defined by $\vec{C}_h = m\hat{a_1} + n\hat{a_2}$, where m and n are integers and â$_1$ and â$_2$ are unit vectors as represented in Figure 2-6 [72]. The chiral vector of graphene sheet becomes a circumferential line of the tubes when they are rolled to form CNTs. The CNTs with a roll-up vector of the form n = m are called armchair tubes and chiral vector angle is 30º. Zigzag tubes are characterized by the roll-up vector, either n or m, being zero and the chiral vector equal to 30º. Both zigzag and armchair are achiral tubes and all other tubes are known as chiral tubes or helical, where n ≠ m and chiral vector angle lies between 0 and 30º. The diameter of the tubes, d, is defined as:

$$d = \frac{a\sqrt{m^2 + mn + n^2}}{\pi}$$

Equation 2-1

where a is the C-C bond length of the graphene sheet.

CNTs are further divided by the number of graphene sheets rolled to form concentric graphene sheets. If seamless tube form from the rolling of single sheet of graphene it is called a Single Wall CNTs (SWCNTs). If two sheets are rolled to form concentric circle these are known as Double Wall CNTs (DWCNTs). The third type are called Multi Wall CNTs (MWCNTs), where concentric graphene tubes are stacked one into the other (Figure 2-7). MWCNTs were the ones described in the landmark paper of Iijima [73]. The discovery of SWCNTs came later in 1993 [74, 75].
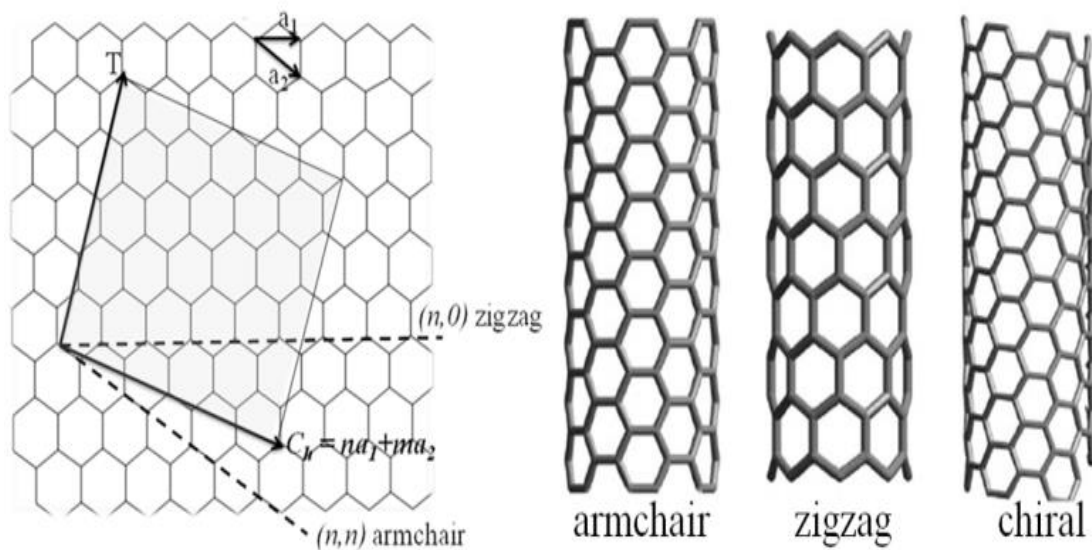
Figure 2-6 A sheet of graphene rolled to in particular directions to form three different kind of single walled carbon nanotubes, named as armchair, zigzag and chiral [72, 76].
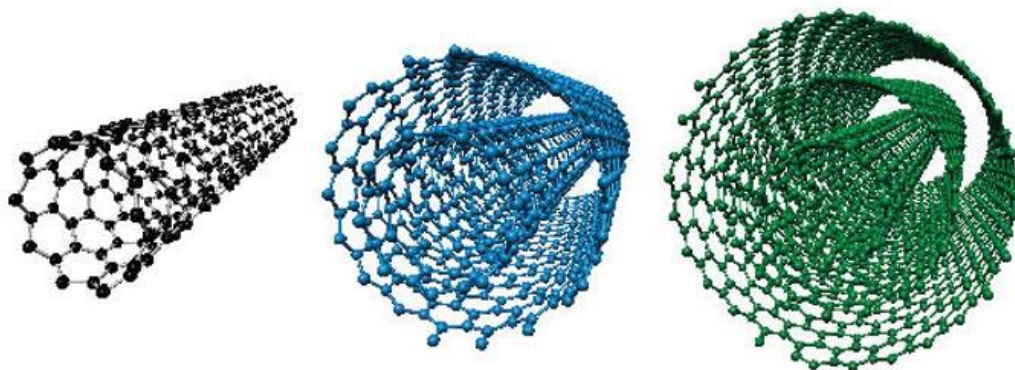
Figure 2-7 Classification of CNTs based on the no. of graphene sheets rolled concentrically single wall CNTs, double wall CNTs and multi wall CNTs (from left to right) [77].

2.2.1 Electronic properties of CNTs

CNTs depict metallic, semi metallic and semiconductor (with band gap of 1 eV) properties. The electrical properties are mainly dependent on the values of n and m, as first predicted by Saito [71, 72, 78, 79]. It was found that depending on the chiral vector $1/3^{rd}$ of the nanotubes are metallic and $2/3^{rd}$ of them are semiconducting. Armchair nanotubes are always metallic, while other chirality can be metallic or semiconducting. In CNTs C atoms form both σ and π bonds. In CNTs lattice the unhybridized π orbitals are responsible for the transportation of the π electrons through the nanotubes. In the axial direction the π electrons move freely throughout the lattice due to no constrictions [72], whereas in the radial direction electrons are confined by the monolayer thickness of the graphene sheet [69]. There is a destructive interface of electrons (as wave) by itself if the wavelength of the electron is not a multiple of the circumference of the nanotubes [80]. Therefore the dominant conduction path in CNTs is along the axis of the tubes. The rolling of the graphene sheet results in the π orbitals more delocalized outside the CNTs and σ bonds being slightly out of plane [77]. This results in CNTs more thermally and electrically conducting.

MWCNTs usually consists of the several tubes rolled one on other with interlayer distance in each layer of approximately 3.4 Å. The bending of the graphene sheet and its influence on the electrical and structural properties of MWCNTs are similar to SWCNTs.

However, even if the MWCNTs consist of rolling of semiconducting tubes they behave as semi-metallic due to their reduce band gap [77]. Due to their metallic nature and large number of walls they are potential candidates to be used as bottom conducting electrodes for future microelectronic devices.

2.2.2 Synthesis of CNTs

MWCNTs are the first CNTs synthesised by Iijima (1991) [73] by arc discharge method which was adopted from the early investigators on the synthesis of fullerenes [73, 75, 81, 82]. In arc discharge method, discharge between the two graphitic electrodes (6 - 12 mm diameter) separated by 1 - 4 mm takes place inside a chamber filled with an inert atmosphere. With the application of a bias across the electrode carbon is ejected from the positive electrode and deposited on the negative electrode, resulting in the formation of MWCNTs [83]. In order to synthesised SWCNTs by arc discharge method, the graphite electrodes are loaded with metallic catalysts (Fe, Co, Ni, Y, Mo). The graphite electrodes are vaporized along with the catalyst and carbon condenses in the form of SWCNTs [81, 84-87].

In the later years (1995) laser ablation method was used to produce CNTs, mostly SWCNTs [81, 83, 88, 89]. In laser ablation method, a graphite target is ablated by the powerful laser in inert helium or argon atmosphere (also acting as carrier gas) and results in the evaporation of carbon. These carbon atoms are carried by the carrier gas to the cold cooper collector on which they condense in the shape of nanotubes [88, 90].

However, both arc discharge and laser ablation method does not yield large amounts of CNTs as required for a full industrial adoption of CNTs. The breakthrough technique that enabled CNTs to become an industrial material was a route that involved Chemical Vapor Deposition (CVD) [91, 92]. In CVD process the hydrocarbon vapor thermally decomposed on the surface of catalyst and precipitate to form CNTs. Indeed, the catalytic decomposition of hydrocarbons was used well before the discovery of CNTs for the production of certain kinds of carbon fibres [93, 94]. Although slow, this method yield long and large amounts of CNTs. This synthesis route makes possible the production of CNTs in a continuous manner and enables a kind of control over the nanotube

parameters that other techniques do not offers [95, 96], including: the patterned growth of nanotubes [97], the growth of centimetre long nanotubes [98], doped CNTs [99], among others.

The MWCNTs used in the present studies were fabricated by CVD, therefore the procedure is explained here more comprehensively.

In a thermal CVD setup (Figure 2-8), the substrate (or holder) embedded with a catalyst is placed in the centre of the quartz tube, which was flashed with inert gas, like H_2 at 400 ºC for 30 min in order to reduce the catalyst. Transition metal nano particles are used as catalysts, usually Fe, Ni, Co, Mo either in the pure form or as an alloy [100, 101]. CNTs synthesis begins on the nano particles (used as catalyst) with a suitable source of hydrocarbon (methane, ethane, ethanol, benzene) [102]. The hydrocarbon source is heated at high temperature, in the range of 700 ºC to 1200 ºC [103], inside the quartz tube. The hydrocarbon gas at high temperature is thermally decomposed into hydrogen and carbon, the carbon atoms diffuse on the surface of the metallic nano particles, forming an amorphous carbon shell around the metal catalysts. This amorphous carbon rearranges itself into an hexagonal network and finally precipitates in the form of CNTs. The termination of CNTs occurs when the metal particles are fully covered with CNTs walls and future diffusivity of carbon as a feedstock on the surface of catalyst is constraints by already grown CNTs walls [104].

Two types of mechanisms for CNTs growth are known: base growth and tip growth. The type of growth depends mainly on the interaction between the catalysts and the base (substrate). If the interaction of the catalyst particles with the support (substrate) is strong it yields CNTs on the top of the particles and this is known as base growth type (Figure 2-9 (a)). Conversely, when the interaction is not so strong between the support and the particles CNTs grow between the support and the metal particles and this mechanism is known as tip growth (Figure 2-9 (b)). Both experimentally and theoretically it was proven that CNTs diameter is highly dependent on the catalyst size [105, 106]. It is important to mention that during the synthesis of CNTs there is the formation of secondary forms of carbon such as amorphous carbon, fullerene and graphene. The presence of these secondary phases affects markedly the quality of the CNTs. Therefore, post treatments based on chemical and thermal treatments are needed to remove unwanted

carbon allotropes. Still up to day it is a challenge to develop a technique by which only a particular chirality of CNTs is synthesised with a minimum amount of secondary phases.
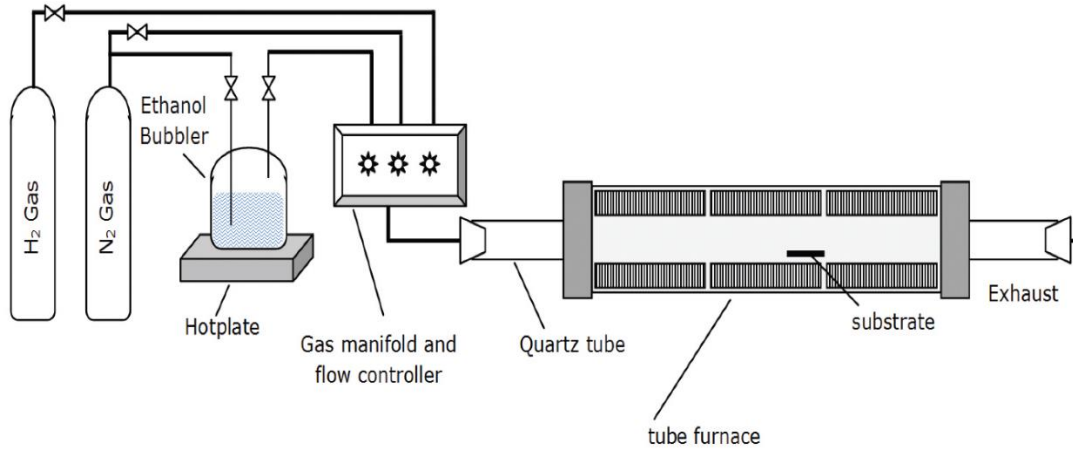
Figure 2-8 Schematic of a CVD setup for the synthesis of CNTs [107].
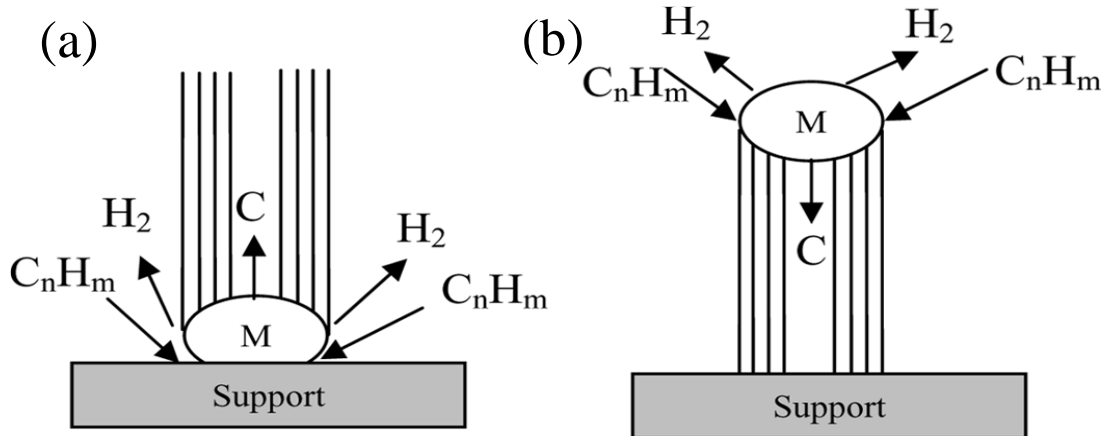
Figure 2-9 Illustration of two growth mechanisms of CNTs: (a) base growth and (b) tip growth. These growth mechanisms are dependent on the interaction of the catalyst and support (substrate) [108].

2.2.3 Functionalization of CNTs

Carbon nanotubes are naturally hydrophobic, and in order to optimised their surface for posteriori use or to alter physical and/or electrical properties, their outer surface needs to be modified and usually CNTs are functionalized by chemicals and physical methods [109-111].

Within the chemical functionalization, the modification of the CNTs surface can be categorised as: (a) covalent attachment of the chemical group to the side walls of CNTs, (b) non-covalent attachment of the chemical group to the side walls of CNTs, where the chemical species adsorbed or wrapped on the surface of the CNTs; and (c) the endohedral filling of CNTs inner empty cavity, as illustrated in Figure 2-10 [109, 112].

In covalent type the functionalized groups, like hydroxyl and carboxylic groups, are formed at defect sites of CNTs with π-conjugate. The attachment of functional groups to the nanotubes usually takes place at defect sites present at the walls or at the caps of CNTs. This is due to the lower activation energy for chemical reaction at defect sites (vacancies, non-hexagonal arrangement of C atoms, etc.) [110]. Covalent attachment always influence the properties of CNTs, for example in the case of fluorine atoms when attached they adopt the tetrahedral coordination and the sp^3 hybridization, which destroys the electronic band structure [113, 114]. In the non-covalent functionalization functional groups wrapped up the CNTs by Van Der Waals forces and π- π stacking. Some examples of chemicals which can be used for non-covalent functionalization are sodium dodecyl benzene sulfonate (NaDDBS), sodium dodecyl sulfate (SDS) and poly vinyl pyrrolidone (PVP).

Endohedral functionalization is the filling of the inner empty cavity of CNTs. This filling can be performed by two methods: i) physical and ii) wet chemical. In the physical one the open tubes are directly immersed in the molten materials (no solvent is used). The tubes are filled by the molten metals due to the capillary forces. Dujardin *et al.* [115] suggested that the filling of metals with high surface tension such as lead [116], bismuth [117] and cesium [115] occurred due to the formation of oxides or carbide compounds as a result of the reaction with oxygen and/or carbon. The carbides or oxides of those metals have a surface tension lower than the surface tension of pure elements, allowing

compounds to fill the nanotubes by capillary action. Therefore, the filling of tubes is may be related with oxides rather than pure metal particles.

Other method of filling CNTs is by wet chemistry. In 1994, Tsang *et al.* [118] filled nanotubes with metal oxide particles such as cobalt, nickel and iron. They used a nitric based metal solutions to open the end of the CNTs by refluxing CNTs in the nitric solution and, simultaneous filling took place with the metal salts. The tubes were annealed at 200 to 400 ºC, so that metal salt decomposes and forms the respective element. Gold, silver, platinum particles were also filled in CNTs by wet chemical method [119-122]. Other than oxides, biomolecules and liquids were also filled in CNTs for various biomedical and storage application; more details can be found in reference [71]. The CNTs inner cavity offers space for the storage of guest molecules which can be used to produce confined nano structures, for hydrogen storage and drug delivery applications [115, 123-125].
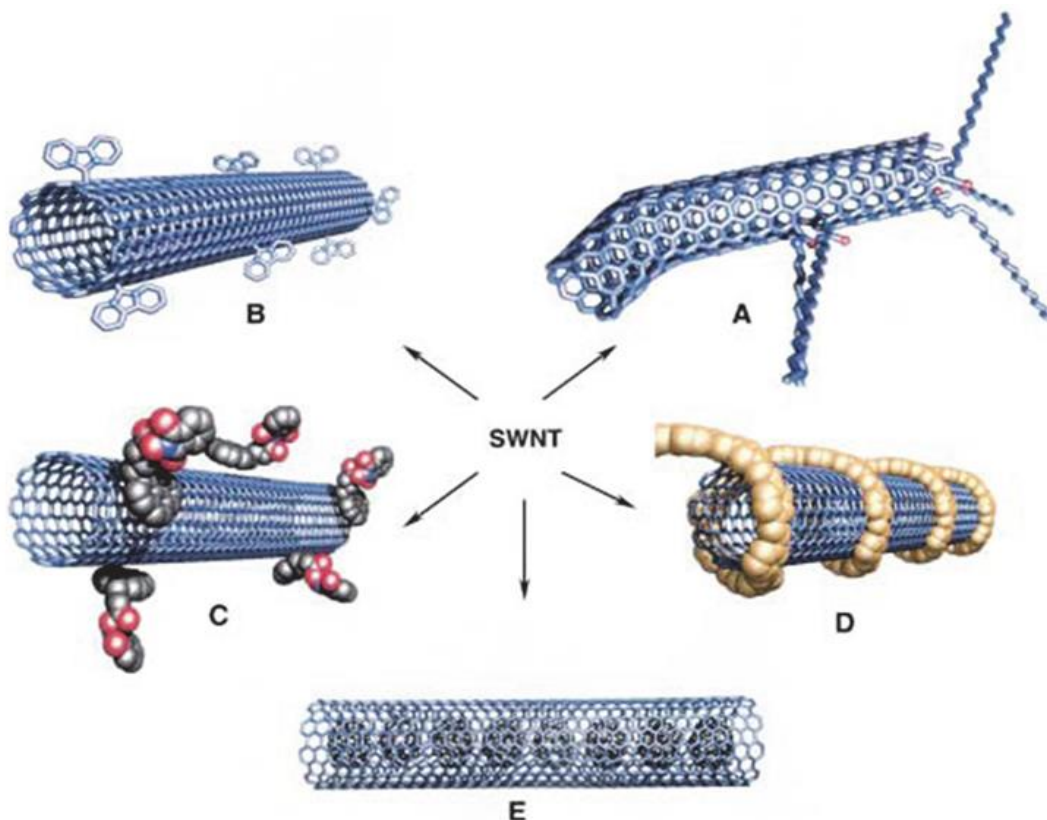
Figure 2-10 Scematic representation of the various types of functionlization of CNTs: (a-b) covalent, (c, d) non-covalent and (e) endohedral functionalization[126].

2.2.4 Effect of temperature and pressure on CNTs

As mentioned above one of the main objectives of this work is to cover MWCNTs with ferroelectric oxide layers. However, it is known that the ferroelectrics oxides have generally high temperature of crystallization of around 700 to 1000 °C. In this particular or any other application in which CNTs will be submitted to pressure and or temperature, requires knowledge on the effect of temperature and pressure on CNTs and their dependence on the type of CNTs.

According to the literature CNTs starts oxidizing around ~500 °C. Therefore, combining ferroelectric oxides with CNTs, for 1D structure might be quite challenging, especially, when CNTs are needed to be used as a bottom electrodes. There are various factors which affect the oxidation of MWCNTs. Here, is a brief literature review on the thermal oxidation of MWCNTs.

It is established that the thermal stability of CNTs depend on two main parameters i) type of CNTs and ii) diameter of CNTs [127-133]. The activation energy for oxidation of carbon nanotubes depends on the types of CNTs, here we listed activation energy from low to high as follow. The first species to start oxidize are SWCNTs (325 °C), closely follow by amorphous carbon (350 °C), then DWCNTs, MWCNTs (450 °C) and the most stable carbon form is graphite (starts oxidizing at around 700 °C). The second parameter is the size and diameter of the tube [131, 134]. Tubes with smaller diameters and lengths have higher surface energies and strains resulting in poor resistance to oxidation. Therefore tubes with small diameters and lengths oxidize first followed by tubes with bigger diameters.

As known, produced CNTs contain different carbon species (or impurities) such as amorphous carbon, graphite and fullerenes. All these species have different C-C bond lengths, curvature what influences the decomposition (oxidation) temperature of CNTs; therefore for any further application and maximization of their properties tubes need to be purified before being processed. Chemical and thermal treatments are the current procedures used for the purification of CNTs. The effect of purification on the thermal behaviour of CNTs has been part of many publications.

The thermal stability of the chemically purified CNTs (using acids as HCL, HF and nitric acid) was monitored by DTA/TG, HRTEM, Raman spectroscopy, Wide Angle X-ray Diffraction, among others [135-139]. It was demonstrated that there is an increase in the oxidation temperature of MWCNTs after the chemical purification due to the removal of amorphous carbon and metal catalysts. It was also reported that the treatment with nitric acid for 2 h results in the increase of the crystallinity of MWCNTs by 85 % and hence the thermal stability of the tubes by 5 to 10 ºC [140].

The other method for purification is a thermal treatment. The thermal treatments reported in the literature were carried out in air or in inert atmosphere. For tubes thermally treated in air at around 350 to 500 ºC the amorphous carbon was eliminated and resulted in improved thermal stability of the tubes [141, 142]. The other way to purify CNTs is to anneal in inert atmosphere [143] or in vacuum [143-145] at very high temperature (2000 ºC). By systematic studies of comparison of the activation energy of oxidation of MWCNTs using TEM and Raman it was found to be an effective method to remove impurities and enhance graphitization of CNTs and, as a consequence, to increase the thermal resistance of CNTs [146, 147].

For some particular applications the pressure stability of CNTs might be important. The best way to characterize the pressure effect on the CNTs is to monitor the shift in Raman radial and tangential modes (Raman peaks). It was found that with the increase in pressure there is a linear shift in the tangential mode 5.7 cm^{-1}/GPa up to 1.7 GPa, followed by the change in the value of the slope for further pressure increase up to 5 GPa [148]. On releasing the pressure tangential bands come back to its original position with small delay for all hollow nano structures. No significant change in the electrical transportation behaviour was observed for CNT$_S$ with applied pressure of 2 GPa [149]. Experiments carried out at high pressure and temperature showed that a pressure of 5.5 GPa and temperature of 950 ºC is needed for MWCNTs to deform and form other structure such as ribbon or onion like [150-152]. Further, increase in temperature to 1500 ºC results in the formation of diamond [153].

However, it was found that there is no systematic study on the effect of different atmosphere and heating conditions on the oxidation of MWCNTs. Therefore and within the aim of the present work, the effect of different atmospheres and temperature was

studied so that different experimental condition can be explored to obtain crystalline ferroelectrics on CNTs. These results will be presented in chapter 4.

2.3 Functional oxides: ferroics

2.3.1 Definitions, classification and application of ferroics

Functional materials are characterized as materials which possess particular native properties and functions [154]. The classification of functional materials is usually related to materials whose function is associated with electric, magnetic and optical properties. Functional materials are found in all classes of materials: ceramics, glasses, organic oxides and polymers. Ceramics functional materials mainly include dielectrics, pyroelectrics, piezoelectrics, ferroelectrics, ferroelectric relaxors, incipient ferroelectrics, semiconductors, ionic conductors, superconductors, electro-optics, magnetics and multiferroics. Application of these materials includes medical diagnostics such as ultrasonic imaging, aerospace such as accelerometers and micro positioners, automotive such as solid state piezoelectric fuel injectors, chemical and process control, which requires the use of thermal, strain and force sensors, in memories such as capacitor cell, magnetic sensors, and spintronics [155], among many others. The utility of functional materials in these applications reflects their unique properties, such as spontaneous polarization, piezoelectricity, superconductivity and magnetoresistance. All these properties are directly dependent on the chemical composition, singularities of the crystallographic structure and manufacture process.

Dielectric materials have high electrical resistivity, which means that ideal dielectrics do not conduct electricity, due to no or low density of free charge carriers; as a consequence dielectrics are used in insulating applications (e.g insulators used in high voltage transmission lines). However, dielectric materials exhibit polarization (P) when placed under an electric field. The mathematical derivation of polarization is presented below.

The electric flux density E_{flux} or electric displacement (charge per unit area, C m⁻²) at a given point of an insulator material is proportional to the electric field (E) and is given by following equation:

$$E_{flux} = \varepsilon_r \varepsilon_o E$$
Equation 2-2

where ε_o (F m⁻¹) and ε_r (F m⁻¹), are the dielectric permittivity of free space (vacuum) and relative dielectric permittivity of the material, respectively.

When an electric field is applied to the dielectric material, the trapped charges inside the material are displaced by some distance in the direction of applied electric field known as dipole moment. This displacement produces local dipoles throughout the material. The sum of all the individual dipole moments within the given volume is called as polarization (P) of the solid. Polarization measures the additional flux density and is represented by following equation:

$$E_{flux} = \varepsilon_o E + P$$
Equation 2-3

Polarization equation derived from Equation 2-2 and Equation 2-3 can be represented as:

$$P = \varepsilon_o (\varepsilon_r - 1)E$$
Equation 2-4

In addition, the polarization and dielectric permittivity of the material can be calculated from the capacitance of the material (the ability of the material to store charge) at a frequency well below mechanical resonances. The total polarization of a solid is the result of the contribution of four main mechanisms: atomic polarization, ionic polarization, dipolar polarization and space polarization (more details in reference [156]).

Dielectrics show a linear relationship between the applied field and induced polarization. For linear dielectrics when the applied field is removed the polarization disappears. Whereas, dielectric materials in which electric field develops due to mechanical stresses or strains develop due to applied electric field are known as piezoelectrics materials.

The piezoelectric effect was discovered by Jacques and Pierre Curie in 1880 in quartz, tourmaline and Rochelle Salt (RS) crystal (sodium potassium tartate tetrahydrate) [157-159], while studying the effect of pressure on the generation of electrical charges. They found that with the application of mechanical forces electrical charges are generated in the crystal; this is known as a direct effect and the degree of polarization is proportional to the applied stresses. Piezoelectric crystals also depict the converse effect, where a geometrical strain is produced by the application of an electric field. The name ´´piezoelectric`` derived from the combination of the two words: piezo and electric, where the prefix piezo comes from the Greek word meaning press, therefore piezoelectricity is the generation of electricity that results from a mechanical force, or vice versa. The necessary condition for a material to be a piezoelectric is to have a non-centro-symmetric structure, where the net movement of negative and positive ions in relation to each other produces an electric dipole i.e polarization. From the 32 classes of symmetry, 11 point groups possess a centre of symmetry hence, they are non-polar and 21 possess a non-centro-symmetric structure, hence they are polar or piezoelectric. Form these 21 non centro-symmetric 20 point groups materials shows piezoelectric effect. Figure 2-11 illustrates the interrelationship of piezoelectrics and subgroups on the basis of the crystallographic symmetry [160].

The mathematical expression for the piezoelectricity is expressed as:

$$\text{D} = dE + \varepsilon^T E \qquad generator, direct\ effect \qquad \text{Equation 2-5}$$

$$\text{S} = s^E T + dE \qquad motor, inverse\ effect \qquad \text{Equation 2-6}$$

where D is the dielectric displacement, S the strain, d a piezoelectric coefficient, s the material compliance, T the stress and ε the dielectric permittivity. The superscripts T and E represent the quantity held constant; in the case of ε^T the stresses are held constant and in the case of s^E the electric field is held constant in Equation 2-5 and Equation 2-6, respectively. Piezoelectricity is a directional property therefore expressed as follow:

$$D_3 = d_{33}T_3 \qquad (direct\ effect) \qquad \text{Equation 2-7}$$

$$S_3 = d_{33}E_3 \qquad (inverse\ effect) \qquad \text{Equation 2-8}$$

where d_{33} is a piezoelectric coefficient with the units (C/N) or (m/V). Figure 2-12 depicts the schematic of a direct (generator) and a converse effect (motor) of piezoelectric materials. The suffix of the piezoelectric coefficient d_{33} indicates the direction of polarization and the applied mechanical stresses. Where 1, 2 and 3 corresponds to Cartesian coordinate axis x, y and z, respectively. In case the piezoelectric coefficient given by d_{33}, it indicates the polarization generated in 3 (or z) direction (the first suffix) due to the application of mechanical stress in the 3 (or z) direction (the second suffix). For example in case of piezoelectric coefficient d_{31}, it indicates the polarization generated in the 3 (or z) direction with the application of stress in the 1 (or x) direction.

High d values are desire for piezoelectric materials used in motion or vibrational devices. Therefore, the piezoelectric materials which generate large amount of voltage per unit of input are evaluated by open circuit g coefficient, which is related with piezoelectric coefficient (d) by following equation:

$$g = \frac{d}{\epsilon_r \epsilon_o} \qquad \text{Equation 2-9}$$

The common application of these materials is in portable gas igniters and patio lighters.

There are 10 point groups with in a sub group of piezoelectrics which shows induced voltage or polarization when subjected to change in temperature and are known as pyroelectric materials. All pyroelectric materials show piezoelectric properties but the inverse is not true. Within the subgroup of pyroelectric materials, a group of materials which depicts spontaneous polarization at zero field conditions and that can be inverted by inverting the direction of the applied field are known as ferroelectrics. All the ferroelectric materials depict piezoelectric properties. A comprehensive detailed information on ferroelectricity is presented in next section, after the brief introduction to magnetoelectrics and multiferroics.
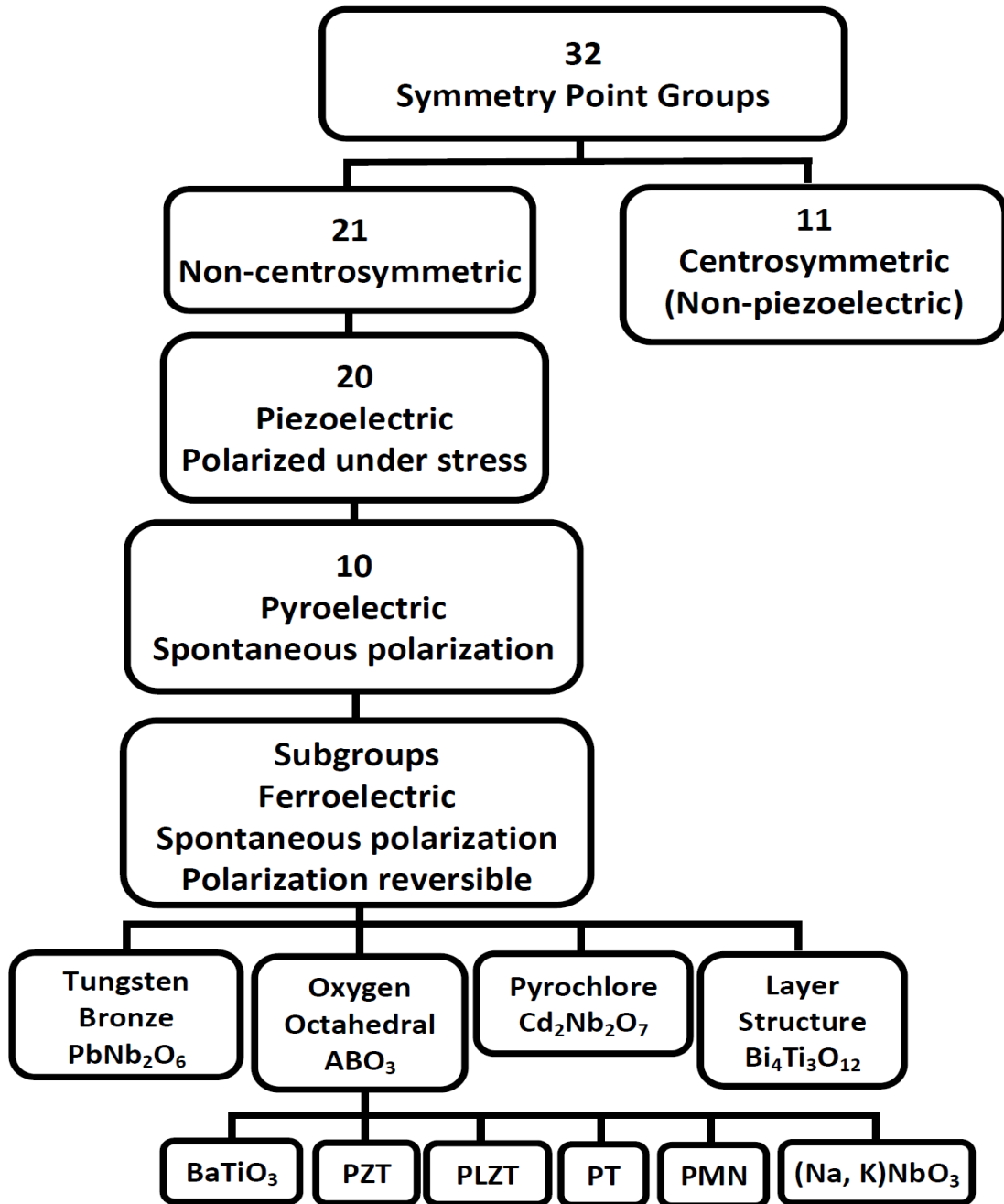
Figure 2-11 Interrelationship of piezoelectrics and subgroups on the basis of symmetry (adapted from [160]).
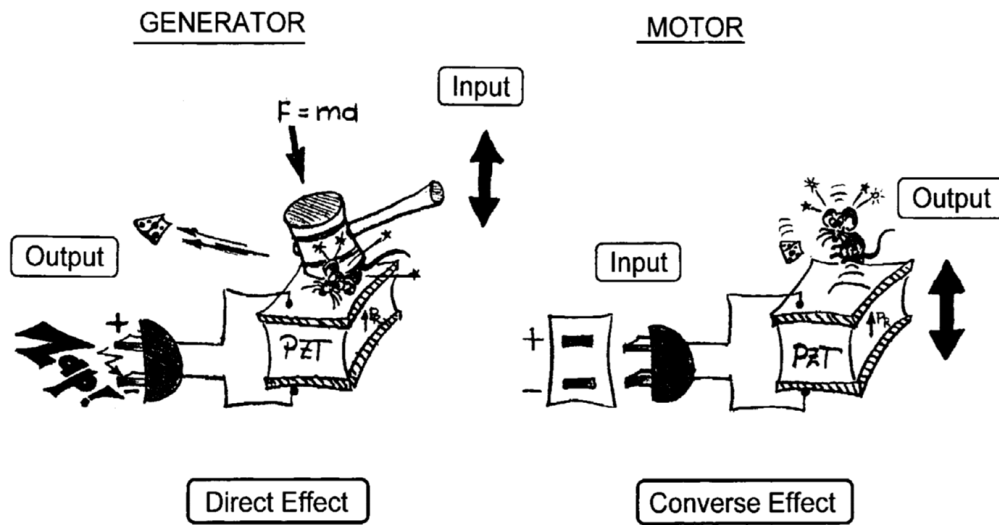
Figure 2-12 Schematic of piezoelectric effect direct (generator) on left and converse effect (motor) on right [160].

In the last decades and so, there has been an outbreak of research focused on a new class of materials known as magnetoelectrics and multiferroics [161, 162]. The major interest in this field of research is due to its hybrid functionalities, which make a material simultaneously ferromagnetic (FM) and ferroelectric (FE). In this case it is possible to control the magnetic response and/or electrical response (polarization) by the application of an electric field and/or magnetic field, respectively. This possibility opens a new whole range of interesting applications such as magnetic recording media, spintronics and sensors. Nevertheless, the study of multiferroics is also of scientific fundamental interest [163].

The term multiferroic is defined as a single-phase material that exhibits more than one fundamental functionality (ferroic - ferroelectricity, ferromagnetism, ferroelasticity [164] and ferrotoroidicity [164-166]). The definition can be further broadened if includes non-primary order parameters under consideration such as antiferromagnetism, ferrimagnetism and anti-ferroelectricity. On the other hand, magnetoelectric (ME) materials can be multiferroics or non-multiferroics, possessing the cross-coupling between electric and magnetic parameters under external stimuli. The subgroup of ME and multiferroic materials is given in Figure 2-13. The coupling between the electric and

magnetic order parameters can be realized by measuring the induced magnetization under the action of an external electric field or the vice versa [167]. In 2000, Hill *et al.* [168] demonstrated the conditions required for the existence of ferroelectricity and ferromagnetism in single-phase materials, which are hardly satisfied. Ferroelectricity needs broken spatial inversion with invariant time reverse symmetry. In contrast, magnetization (M) and magnetic field (H) change their signs upon time reversal and are unaffected by spatial inversion. Multiferroic system requires simultaneous breaking of both time and spatial symmetries. This is possible in spin frustrated systems which always prefer to have spatially inhomogeneous magnetization and lone pair effect, as in the case of $BiFeO_3$.

In the last 10 years, various patents have been registered, from synthesis, designing to applications, of new devices based on multiferroic and magnetoelectric materials [169-174]. In this work we used $BiFeO_3$ a single phase multiferroic to combine with MWCNTs for ferroelectric based applications, therefore a more comprehensive detailed description on ferroelectricity and ferroelectrics is presented hereafter.
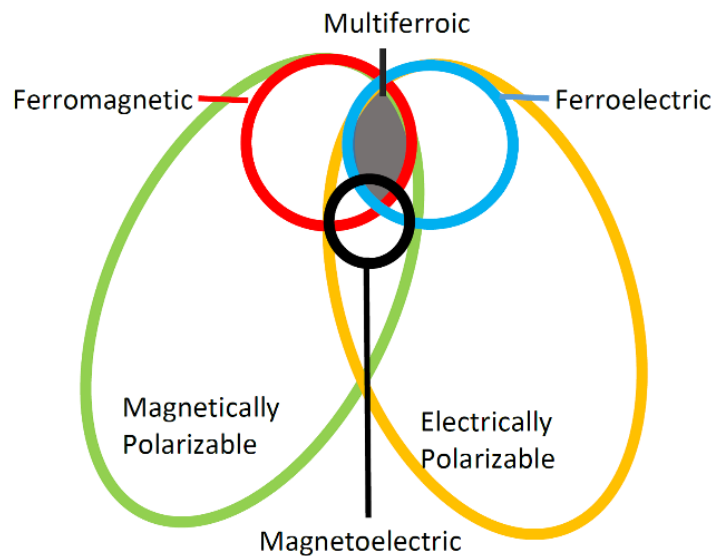
Figure 2-13 Relationship between multiferroic and magnetoelectric materials. Illustrates the requirements to achieve both in a material, imitated from [163].

2.4   Ferroelectrics

Discovery of the ferroelectric (FE) phenomena dates back to mid-16s century with the observation of ferroelectricity in Rochelle Salt (RS) crystals (sodium potassium tartate tetrahydrate) by Elie Sceignette in France for medical purposes [175]. It took approximately two centuries to measure the pyroelectric effect and further 60 years to find piezoelectric response in RS crystal. Later in 1921, Joseph Valsek [176] proved experimentally the ferroelectric nature of RS crystal that had been theoretical predicted in 1912 [177]. Several studies in the following years were carried out on the crystal structure and properties of RS crystals. However, due to its water solubility nature, soon the interest diminished. In the mid 40s with the development of high capacitance capacitors based on the ferroelectric barium titanate ($BaTiO_3$, BT) the interest in FE reappeared. In 1945 and 1946 the work of Wu and Goldman in USSR [178] and Hippel´s group in USA [179] established the high dielectric constant and FE behaviour of $BaTiO_3$ single crystals. However, the startling discovery came from Gray [180] in 1949, when he reported the ferroelectric nature of $BaTiO_3$ ceramics. The authors demonstrated that with the application of an external electric field it is possible to orient ferroelectric domains within the grains of the ceramics, in a similar way to the single crystals. These findings were the trigger factor that turned polycrystalline $BaTiO_3$ ceramics into one of the most important ferroelectrics of all the times with a great industrial and commercial use. Later, in 1952 the discovery of high T_c (Curie temperature) lead zirconium titanate (PZT, $Pb(Zr_{1-x}Ti_x)O_3$) ferroelectrics has given the field of piezoelectrics and ferroelectrics further importance, up to the current days. Indeed, at the present 50 % of the microelectronic devices used commercially contain lead based functional oxides. However, due to the toxicity of lead and regulations from Europe and USA there is a strong need to replace lead based materials by lead free dielectrics, piezoelectrics and ferroelectrics [181, 182].

As said above, ferroelectricity is a property of a material defined as the ability to switch the spontaneous polarization by the application of external field [183]. Due to a non- centrosymmetric structure, there are dipolar moments in the ferroelectrics that under zero field conditions originate a spontaneous polarization. For a material that contains electric dipoles, the local electric field will promote the dipole alignment in certain regions, contributing to the increase of the polarization, which, by itself, will promote the

increase of the local field [155, 160]. These co-operation phenomena will align the dipoles along the same direction, resulting in the spontaneous polarization of the material. Consequently, the electric polarization in ferroelectrics does not vary linearly with the applied field and hence they are called non-linear dielectrics. In ferroelectrics the relationship between the applied field and the polarization is described by a hysteresis loop, similar to the one exhibited by the ferromagnetic materials [155]. Ferroelectric hysteresis shows the nonlinear relation between the polarization (P) (on Y axis) and applied electric field (E) (on X axis) presented in Figure 2-14. When an electric field is applied to a ferroelectric material, the dipoles begin to align in the direction of the applied field, this phenomena is also know as switching. When saturation polarization (Ps) reaches the maximum value and do not further increase with the increase in applied field, a maximum number of domains are aligned in the direction of the applied field. If the field is reduced to zero, the polarization values will decrease, but do not fall to zero, at this point the polarization value lower than Ps known as the remanent polarization Pr (shown in Figure 2-14). To reduce the value of polarization to zero, it is necessary to apply a field in the opposite direction. The field at which polarization reaches to zero is called coercive field (Ec) and at this point all the domains are randomly oriented (as shown in Figure 2-14). If the applied field is further increased in the negative direction domains start to oriented in the direction of applied field and attain maximum polarization, also known as saturation polarization Ps, but in this case with a negative sign (-Ps). When the electric field is reduced again to zero, there is again a remanent polarization but in the negative direction (-Pr). Further increase of the field will bring the polarization back to +Ps and this creates the loop as shown in Figure 2-14. This loop is known as the ferroelectric hysteresis loop. The spontaneous polarization of ferroelectrics is used to store data in FeRAM as a encoded "0"s and "1"s (binary number for digital computing), as illustrated in Figure 2-14. Since no external field is required to maintain these states once reached, the memory device is known as non-volatile i.e. when the power is switched off the information is kept saved. Commercially FeRAMs use ferroelectric thin films (90 -200 nm) because they have low coercive field and can be switched from one spontaneous polarization state to other with the application of ~ 3 to 5 V. In order to miniaturize FeRAMs without affecting the properties, considerable efforts

are required to improve the fabrication techniques, explore new nano materials and new designs.
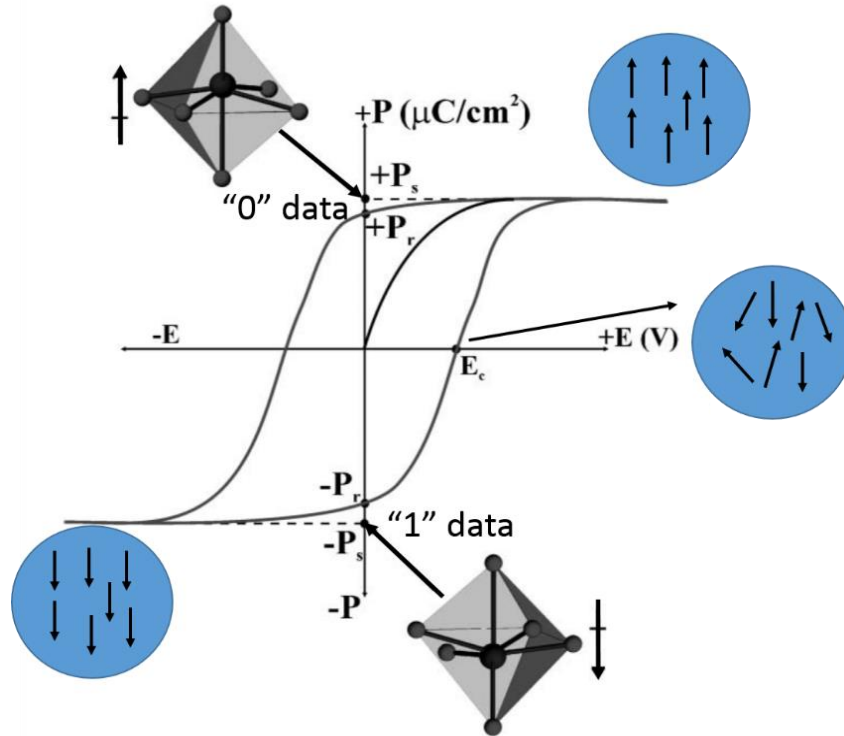
Figure 2-14 Hysteresis loop of ferroelectrics, where Ps and, Pr are spontaneous polarization and remanent polarization, respectively (adapted from [184]).

2.4.1 Crystal structure of ferroelectrics

In general ferroelectrics have four crystal structures, namely:

1. Tungsten-bronze

2. Perovskite (oxygen octahedral, ABO_3)

3. Pyrochlore

4. Bismuth layer-structure

From all the above structures materials that depict the perovskite structure are by far those that possess better properties and commercially more in use [185]. Some of the most important compositions having a perovskite-type structure are $BaTiO_3$, $PbTiO_3$, $Pb(Zr_xTi_{1-x})O_3$, $(Pb_{1-x}La_x)TiO_3$, $Pb(Zn_{1/3}Nb_{2/3})$-$PbTiO_3$ (PZN-PT), $Pb(Mg_{1/3}Nb_{2/3})$-

$PbTiO_3$ (PMN-PT) and $K_xN_{1-x}NbO_3$ (KNN), which represent the bulk of ferroelectric ceramics manufactured in the world today.

An ideal perovskite has a centrosymmetric structure with a cubic space group Pm3m and chemical formula ABO_3, where A^{2+} and B^{4+} atoms are cations and O^{2-} the anion. The perovskite crystal structure can be described based on either a body centre cubic (BBC) and face centre cubic (FCC) lattice. In case of BCC lattice, the perovskite structure consists of twelve oxygen ions (O^{-2}) placed at the middle of all the edges of a cube and A^{2+} ions placed at the centre of the unit cell surrounded by four B^{4+} ions placed at each corners. In case of FCC lattice, the perovskite structure consists of B^{4+} ions at the body centre position surrounded by six oxygen ions (O^{-2}) at the face centre positions and A^{2+} ions occupy all the four corner positions (Figure 2-15 (a)) . Perovskite structure with cubic symmetry are at the non-polar state where A, B and O ions coincide, depicts no polarization (P = 0). When the A and B ions are displaced from their position with respect to O^{2-}, a net polarity of the lattice (P ≠ 0) is established (Figure 2-15 (b)) [155]. Moreover, many different cations can be substituted in both A and B sites of the perovskite to improve the physical response of the materials, namely the electrical properties [186].
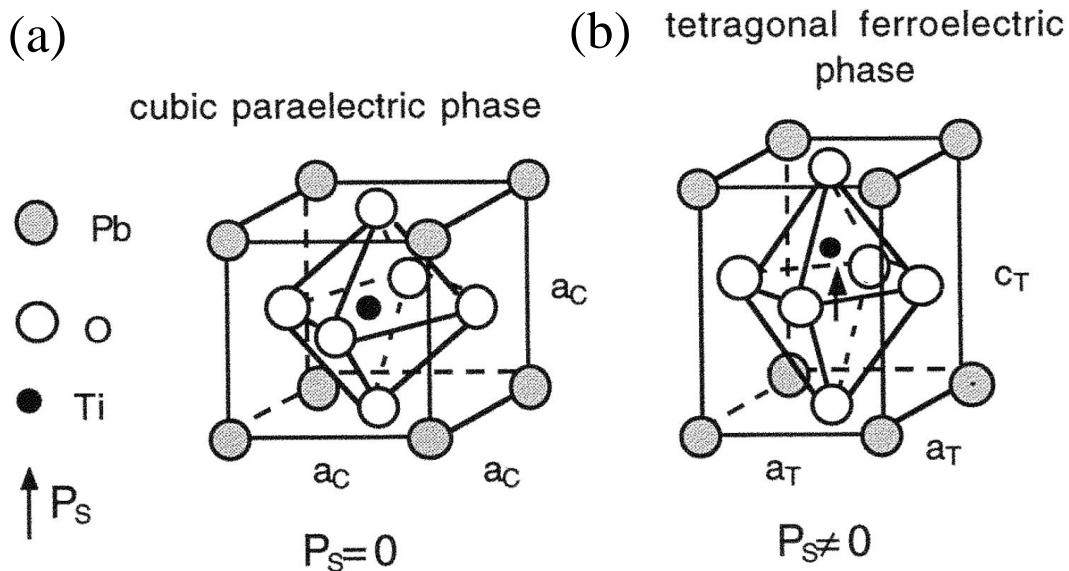
Figure 2-15 (a) Ideal perovskite structure at temperature above T_c, (b) below T_c a non-centrosymmetric structure results in the B site atom displacement, where a_C, a_T, c_T, are the length of the unit cell, where suffix C and T stand for cubic and tetragonal structures, respectively [184].

The ideal perovskite structure is rarely obtained at ambient temperature/pressure due to the strict constraints placed by the ionic sizes. The Goldschmidt tolerance factor, t [187], based on the geometrical packing of charged spheres, can be used to describe the distortion of the perovskite structure from the ideal configuration, by the following equation:

$$t = \frac{r_A + r_O}{2(r_B + r_O)} \qquad \text{Equation 2-10}$$

where r_O, r_A and r_B are the ionic radius of the O, A and B site ions. Figure 2-16 depicts list of compounds with t value from 0.95 to 1.08. For t = 1, the cubic paraelectric phase is stable. For t > 1, since the B-site ion is too small for its site, it can shift off-centre, leading to the occurrence of a displacive-type ferroelectricity in the crystal; $BaTiO_3$ and $Pb(Zr,Ti)O_3$ are some examples. For t < 1, perovskite oxides are in general not ferroelectrics, but exceptions are found for Bi based materials (e.g. $BiFeO_3$), in which large A-site displacement is observed that results in ferroelectric behaviour.
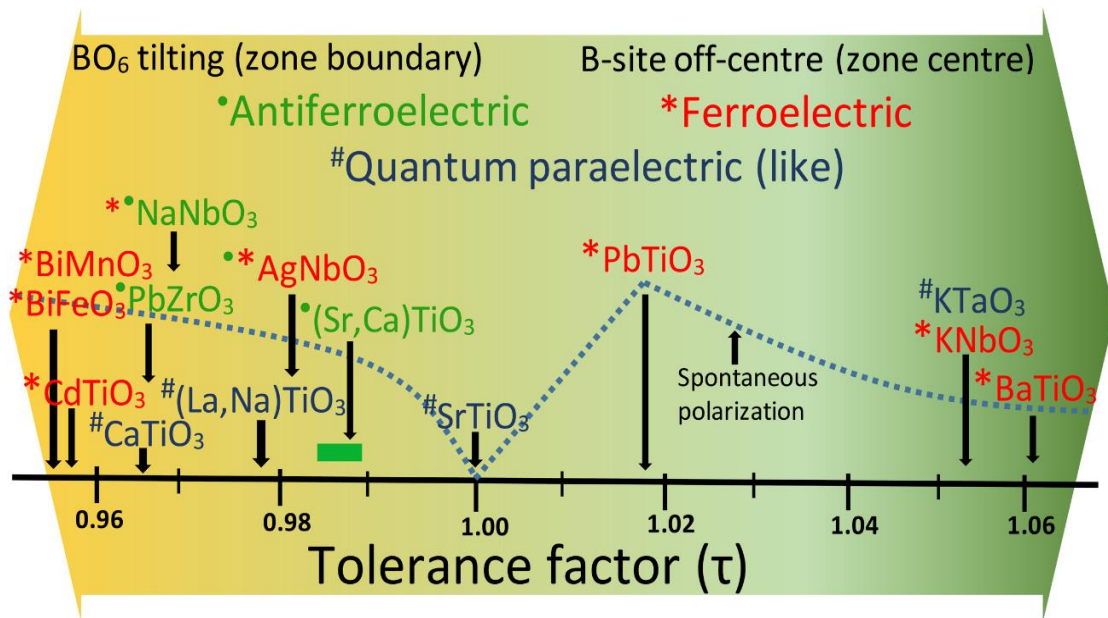
Figure 2-16 Distribution of ferroelectric oxides based on tolerance factor (adapted from [188]).

2.4.2 Ferroelectric phase transition

A ferroelectric material can undergo a phase transition adopting a non-polar centrosymmetric structure at a temperature called Curie temperature (T_C). Above T_C, with the loss of the polar structure, the material does not exhibit spontaneous polarization and it is said to be paraelectric. Below T_C, due to the appearance of the spontaneous polarization and to the mutual interaction between the dipoles, which causes a significant increase of the local field, the material exhibits ferroelectricity. The structural phase transition from the paraelectric to the ferroelectric phase is reversible. Near T_C due to a distortion in the crystalline lattice as the phase structure changes, the thermodynamic properties, including dielectric, elastic, optical, and thermal constants show an anomalous behaviour; the permittivity raises, reaching a maximum at T_C [189].

The theoretical explanation for the phase transition is the concept of a soft mode, which was proposed by W. Cochran *et al.* [190]. According to which, the ferroelectric order is based on the instability of a transverse vibrational mode, referred to a soft mode or a ferroelectric mode. Blinc *et al.* [191] have reported detailed lattice dynamic calculations for several ferroelectric crystals and more rigorous mathematical treatments of the soft mode in ferroelectrics. In the proximity of T_C the crystalline lattice is also soft and can be strongly polarized with a relatively small coercive field, this results in very high permittivity values for some ferroelectrics near T_C. This phenomenon is generally known as a dielectric anomaly. The temperature dependence of the dielectric permittivity above T_C can be described by a simple law called the Curie-Weiss law [192] given by following equation:

$$\varepsilon = \varepsilon_o + \frac{C}{T - T_c} \qquad \text{Equation 2-11}$$

where C is Curie Weiss constant.

2.4.3 Ferroelectric domains

When a ferroelectric material is cooled down from the paraelectric state to the ferroelectric one, there is the formation of uniform aligned electric dipoles in certain

regions of the crystals; regions that are known as ferroelectric domains. These ferroelectric domains are formed in order to minimize the electrostatic energy of the depolarization field (Ed) and the elastic energy associated with mechanical constraints. At the transition temperature, with the onset of the spontaneous polarization there is the formation of surface charges, the field due to this surface charge is known as a depolarization field. The direction of the depolarization field is opposite to the direction of spontaneous polarization (Ps) (Figure 2-17 (lower half of the image). Depolarization fields occur in regions where non homogeneous distribution of the spontaneous polarization takes place such as at the surface of the crystal, at grain boundaries where the direction of the polarization in neighbour grains is in the opposite orientation. Depolarization fields (mV/m) can be so high that they may affect the single domain state of ferroelectrics [186, 193, 194]. The electrostatic field associated to the depolarization field can be minimized by splits into ferroelectric domains with oppositely oriented polarization, this resulting in the formation of 180° domains; or alternatively the depolarization charge is compensated by electrical conduction with the surrounding materials.

The formation of domains in ferroelectrics also occurs due to mechanical stresses as illustrated in Figure 2-17 (upper half of the image). Assuming that part of the crystal is under compression in one direction, as it is cooled down through the phase transition temperature, in order to minimize the elastic energy associated with the compression stress, polarization develops perpendicularly to the direction of the stress, where in unstressed region the polarization may remain parallel to the stress direction, this resulting in the formation of 90° domains.

Domain walls therefore separate regions in which polarization oriented is antiparallel (180°-walls) or perpendicular (90°-walls) to each other. Both 90 and 180° domain walls may reduce the effects of the elastic strain and depolarization electric fields. In a real scenario when crystal cools through the ferroelectric phase transition it undergoes a combination of electric and elastic boundary conditions and results in the formation of complex domain structure with an interplay of 90° and 180° walls. Domain walls with orientations that differ from the spontaneous polarization are called ferroelectric domain

walls and those with orientations that differ from spontaneous strain tensor are called ferroelastic domain walls [184].

It was understood from above description that the directions along which the polarization will develop depend on the electrical and mechanical boundary conditions imposed on the material. The type of domain walls formed in ferroelectric materials depends on the non-ferroelectric and ferroelectric phase of the crystal. In the rhombohydral crystal, the direction of the polarization occurs along the body diagonal (111) direction. This leads to the formation of 180º, 71º and 109º domain walls with eight possible direction of the spontaneous polarization. Fousek and Janovec [195] derived a mathematical expression which gives the possible criteria by which it is possible to predict the type of domain walls existing in ferroelectric materials.
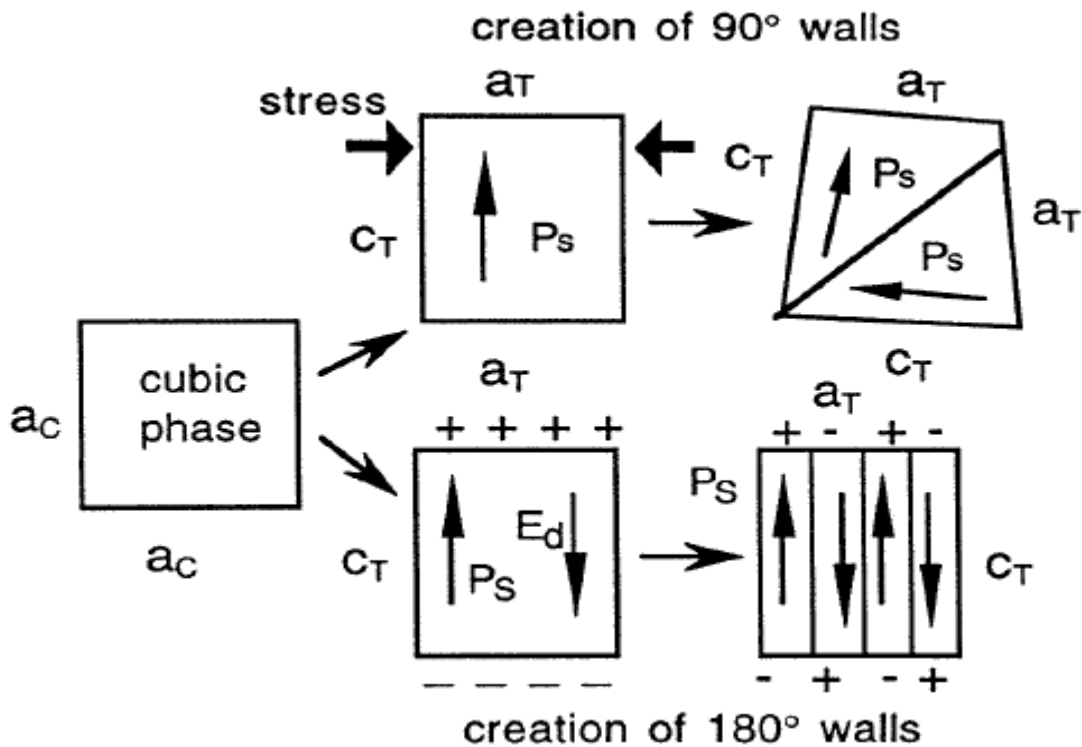
Figure 2-17 Schematic illustrating the phenomena of domains formation: (upper part) formation of 90º and 180º domains due to mechanical stresses, (lower part) formation of 180º domains due to electric field, during the cooling down from high temperature to lower temperature in a crystal, where aC, aT, cT, are length of unit cell, where suffix C and T for cubic and tetragonal structure, respectively. Ps and Ed are spontaneous polarization and depolarization field, respectively [184].

2.4.4 Ferroelectric applications

Ferroelectric materials found applications not only due to ferroelectricity but also due to the related properties such as pyroelectricity and piezoelectricity. These properties are of great interest in a vast range of applications. Pyroelectrics are useful for imaging and thermal detection applications where as piezoelectrics are used in electromechanical devices, such as sensors and actuators. In particular in microelectromechanical systems (MEMS), the large piezoelectric coefficients of ferroelectric solid solutions such as PZT allow for novel miniature electromechanical devices [196]. In the last three decades, the development made in the ferroelectric fabrication and processing of ceramics and thick and thin films for integrated–circuit applications have served to keep the industry growing to the current maturity [160]. Ferroelectrics in the form of bulk are used in dielectric capacitors, infra-red (IR) sensors, piezo sensors and actuators, electo optic shutters and electro optic displays. In form of films they are used in Nov-volatile memories, as a buffer layer for FET, integrated optics and reflective coatings. Figure 2-18 illustrates the possible use of ferroelectrics in form of bulk ceramics and/or films. More details on ferroelectric application are out of the context of this work and can be found in reference [160].
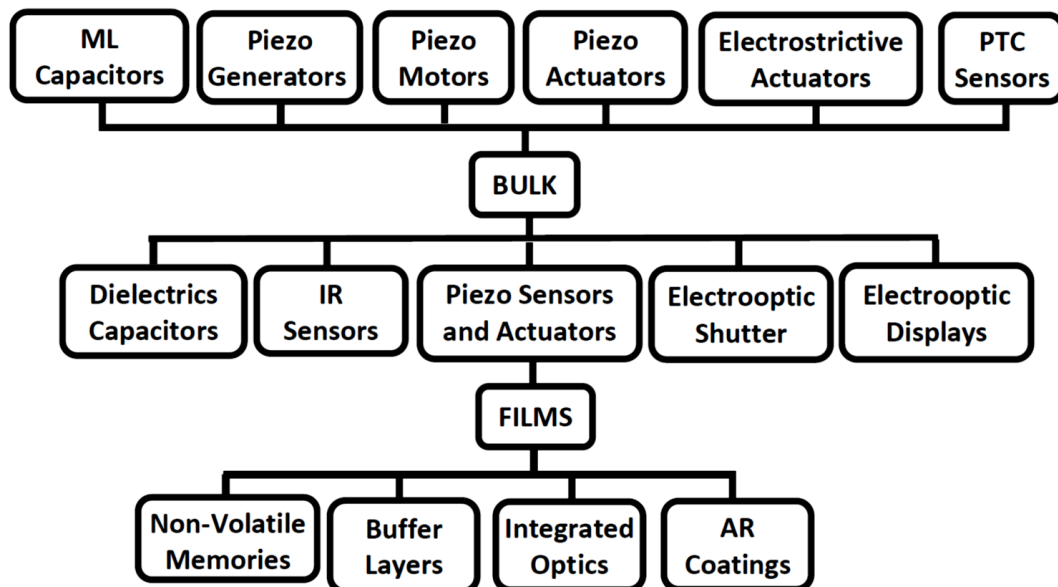
Figure 2-18 Various application fields of ferroelectric oxides ceramics and films are identified in the flow chart [160]. Abbreviations used in the figure are ML (multilayer), PTC (positive temperature coefficient), IR (infra-red) and AR (anti-reflective).

2.4.5 Ferroelectric memories

The ferroelectric hysteresis is a unique characteristic of ferroelectrics that can be explored from the practical point of view (described above). A ferroelectric material with a square hysteresis loop has stable remanent polarization (Pr) values for small changes of the electric field (E) and the switching of polarization occurs for high applied electric fields. These are ideal features for the binary code and NV-FERAMs (as stated above).

In 1951, Dudley Allen Buck [197] proposed the use of ferroelectrics as Random Access Memory (RAM) in his master thesis. At that time ferroelectrics started to be considered as promising candidates, however lack of reliability, fatigue of the switching cycles, imprint (the shift of the hysteresis loop along the origin axis due to self-polarization), high operation voltages and leakage currents limited their practical implementation. Magnetic and later semiconductor memories were used [198]. More recently, due to the ability to prepare high quality films (epitaxial grown, defect free and with controlled stoichiometry) a renewed interest in ferroelectric memories appear. The work on the development of ferroelectrics as RAM started in late 1980´s and the concept was proved in 1991 at NASA´s Jet Propulsion Laboratory [199]. In the 1990´s a FeRAM consisted of two transistors - two capacitors (2T - 2C) with the storage capacity of 512 b to 16 kb. The first FeRAM with capacity of 256 b using one capacitor - one transistor (1T – 1C) was demonstrated in 1994 [200]. In order to compete with magnetic Dynamic Random Access Memory (DRAM) there was a need to increase the storage capacity and reliability of the signals and to miniaturize the device. Many efforts have been carried out to shrink the FE memory cell and new architectures and circuits/devices technologies have been developed. The major breakthrough came with the development of chain FeRAM in 1997. The first prototype of 16 kb chain FeRAM was fabricated in 1999. This was followed by 8 Mb in 2001 [201], 32 Mb in 2003[202], 64 Mb in 2006 [203] and 128 Mb in 2009 [204]. The average cell size including blocked selector region (region combined with memory cell and transistor) has been shrunk from 13 to 0.32 mm^2. 128 Mb FeRAM consists of 90 nm thick PZT film in a capacitor cell to store the information based on remanent polarization (discussed above) [204].

Table 2-1 illustrates the development of chain FeRAM with capacity and design rule (layout rules required to obtain optimum yield of the device without compromising circuit reliability). This development leads to improve the scope of usage of FeRAMs in various memory devices as illustrated below [205].

The continuous development made it plausible to use ferroelectrics in commercial memory devices, especially in the low power consumption devices such as smart cards. Since then different companies such as Ramtron, Fujitsu Ltd., Texas Instruments, Samsung, Sony, among others have been working on the fabrication and development of the FeRAM.

The commercial available FeRAMs are Fujitsu 8-kb made of PZT used in Sony play station 2, 32 Mb PZT FeRAM fabricated by Samsung and 4 Mb FRAM by Matsushita made from strontium bismuth tantalate (SBT) [206]. Bismuth ferrite ($BiFeO_3$, BFO), one of the true single phase multiferroic materials, is used for FeRAMs by Fujitsu [207].
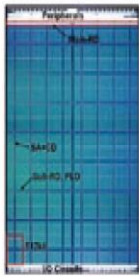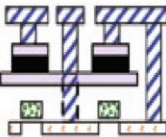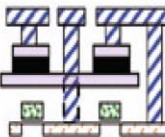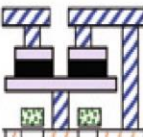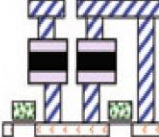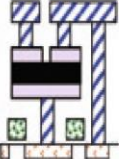
Applications of non-volatile memories include a display of highly consumable multimedia equipment (digital cameras, video cameras and digital audio) and portable products (mobile phones, notebooks, Palm PCs, among others) [155]. A comprehensive review on FeRAMs can be found in reference [208].

Further miniaturization of FeRAMs is still an area of active research as suggested by the International Technology Roadmap for Semiconductors (ITRS) for NV-FeRAM (non-volatile FeRAM) (Table 2-2) [209]. According to this road map the cell structure will go from planar (2D) to a three dimensional designs (3D) using nano structures such as nanotubes, nano trenches, among others and capacitor size of 0.08 μm^2 or below up to few nano meter dimension. There is also need to look for materials with high current caring capacity such as carbon nanotubes and graphene, in order to replace expensive metal electrodes.

Two fundamental questions are raised here: i) one more scientific and related with the need to know if ferroelectricity will still exist at the nano scale, and ii) a second one
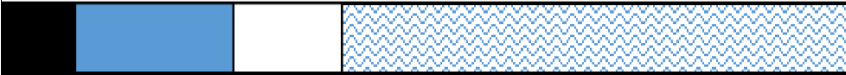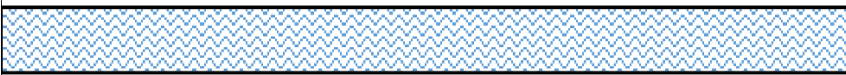
more technological and related with the existence of available technologies that will allow to fabricate the required nano size geometries.
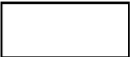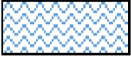
Table 2-1 Development of chain FERAMs as a function of capacity [210].

Design Rule	0.5um	0.25um	0.2um	130nm	130nm +DualOx
Capacity	16Kb	8Mb	32Mb	64Mb	128Mb
Chip	ISSCC1999	ISSCC2001	ISSCC2003	ISSCC2006	ISSCC2009
Cell Structure	Offset Cell	Offset Cell	Stacked Cell	1-Mask Cell	Non-separated PZT film
Cell Size(Ave.)	$13.26um^2$	$5.2um^2$	$1.875um^2$	$0.7191um^2$	$0.32um^2$
Chip Size	$1.9mm^2$	$76mm^2$	$96mm^2$	$87.5mm^2$	$87.7mm^2$
R/W Cycle	80ns	70ns	75ns	60ns	75ns
Page/Burst	80ns	40ns	25ns	10ns	1.25ns

The answer to the first question about the existence of ferroelectricity at nano scale is addressed in the next sub section with a comprehensive literature review on the topic and the answer to the second one related with the fabrication techniques is addressed in section 2.6.

Table 2-2: International Technology Roadmap for Semiconductors (ITRS), suggest potential solutions for future non-volatile memory [3].

Non-Volatile Memory potential Solutions						
Year of IC production	2011 2012 2013	2014 2015 2016	2017 2018 2019	2020 2021 2022	2023 2024 2025	2026
NAND Flash Poly ½ Pitch	22 nm	17nm	13nm	10nm	8nm	8nm
3D stacking						
Non-charge storage device Ferroelectric (FeRAM)						
Enhanced transport with alternate channels: CNT, Nanowires and graphene						

This legends represents the time during which research, development and qualification/pre-production should be taking place for the solution	
Research Required	
Development Underway	
Qualification/Pro-production	
Continuous Improvement	

2.4.6 Scaling of the ferroelectrics

Effect of size on ferroelectric properties of nano structure ferroelectrics

As indicated before, further improvements in terms of storage capacity are needed; these can be accomplished by miniaturization of the cell size into nano dimensions and/or the development of new nano structures based on nanotubes, nanorods or nanowires as described by J. Scott *et al.* [211]. These 1D structure seems to be the new

direction for decreasing the existing size of memory devices. So it is pertinent to know if at nano scale ferroelectrics preserve ferroelectricity; i.e are there size effects in the ferroelectric response of nanostructures? How quantum effects affect the ferroelectric behaviour? What are the mechanisms responsible for the modification of ferroelectricity at the nano scale. Indeed, it is well accepted now, that properties of a material can drastically change at the nano scale due to quantum confinement effects. New properties have been even discovered for many nano sized materials. The effects of size reduction in the ferroelectric properties have been also addressed from the experimental and theoretical point of view.

Size effects in ferroelectrics have two distinct origins: intrinsic and extrinsic. In terms of intrinsic effects contributing to the ferroelectric instability phenomena to be considered are: depolarization phenomena [212], the absence of long-range cooperative interactions, elastic constraints and new ferroelectric polarization. In terms of extrinsic effects to be considered are: domain structure, free carriers, lattice defects and interface phenomena [213-217].

Theoretical determination of the stability of the spontaneous polarization with the decrease of size was given by Landau theory [218] and by *Ab Initio* models [219-221]. Ghosez and Rabe *et al.* [221] studied the critical thickness for $PbTiO_3$ films using atomistic simulation and first principle calculations. The authors found that in (001) films with thickness as low as three unit cells (~1.2 nm) the ferroelectricity persist. Later, Junquera and Ghosez [219] determined the critical thickness using first principle on more real scenario where interface between the $BaTiO_3$ thin films and the metallic electrodes ($SrRuO_3$) was taken in to account. The authors found that $BaTiO_3$ thin layers lose the ferroelectric properties below 24 Å (2.4 nm), due to the depolarization electrostatic field.

To verify the theory on the critical thickness several systematic experimental studies were carried out on powder particles of different sizes [222, 223] and thin films [224-226]. Here we present the most important works on experimental evidences for the persistency of ferroelectric properties for nano particles and thin films. Later, comprehensive details on the existence of ferroelectric ordering in nanotubes and nano rods is also discussed.

Ishikawa *et al.* [223] determined the critical size for $PbTiO_3$ nano particles below which ferroelectricity might not exist, using Raman and XRD. Raman results indicate that the critical size is ~ 10.7 nm below which Raman scattering was not observed. Whereas, the c/a ratio determined by XRD pattern indicates critical thickness of 11.7 nm. According to the authors the critical size effect is due to the weakening of dipole-dipole interaction with the decrease in particle size. The experimental difficulties to fabricate small size (> 10 nm) constrain the experimental investigation on critical size effects in ferroelectrics. However, this constrain has been overcome and critical size of particles was studied for ~5 nm $BaTiO_3$ particles by Polking *et al.* [227]. High quality mono domain $BaTiO_3$ (BT) particles prepared by hydrothermal method were studied by aberration corrected transmission microscopy with holographic polarization imaging and piezo force microscope (PFM). The maps of ferroelectric structure distortions indicate the persistence of a linearly ordered and monodomain polarization at nano dimension. Further, the switching of mono domains for 5 nm BT particles were proved by PFM. These results point the way to fabricate ferroelectric memories with the storage capacity of multi-Tbit/in^2. From these studies it can be concluded the ferroelectric critical size for particles is well below 5 nm.

The first experimental proof for the existence of ferroelectricity for thin films came from the work of Tybell *et al.* [225]. Epitaxial $Pb(Zr_{0.2}Ti_{0.8})O_3$ (PZT) thin films, with thickness from 800 to 40 Å (up to 10 unit cells) were grown on Nb-doped $SrTiO_3$ metallic single crystal substrates by off centre RF sputtering. Using scanning probe and electric field microscopy the ferroelectric state was found for PZT films of 40 Å (4 nm to 10 unit cells). Fong *et al.* [228] studied critical thickness for ultra-thin films of $PbTiO_3$ synthesised by metal organic chemical vapor deposition (MOCVD) on $SiTiO_3$ substrate. Films with thickness of 4 to 12 nm were studied by synchrotron x-ray scattering maps *in-situ* (during the growth of films) as a function of temperature. The satellite peaks obtained from the in plane domains were used to study the ferroelectric transition as function of temperature. Satellites peaks persist down to 12 Å (approximately three unit cells). This result seems to indicate that the effect of depolarisation in theory is overestimated. Indeed, in theoretical studies 180º domains were not considered however they were present in the experimental samples and it is well known that this domain configuration produces a natural mechanism (described above) for reducing the depolarising fields across the

thickness of the film. It is clear from the experimental results that stable ferroelectricity exists in nano particles and thin films up to 5 nm and 1.2 nm, respectively.

Various theories have been used to investigate the ferroelectric behaviour and critical thickness for 1D ferroelectrics [229-242]. Here, we described the most relevant works.

Ebenezer and Ramesh theoretically evaluated the percentage of piezoelectric-response on the cylinder structure (such as nanotubes) having diameter of 5 mm and length of 10 mm using finite element methods. The result proved that the polarization lay along the long axis z or radially through the wall, but piezoelectric response around the tube circumference (θ) was not calculated.

Euler-Lagrange equation was used by Morozovska *et al.* [230] to derive the analytical expression for dependence of paraelectric-ferroelectic transition temperature on the radii of nonotubes, while considering the influence of effective surface tension and depolarization field. In their studies they found the enhancement of spontaneous polarization for $BaTiO_3$ and $Pb(Zr,Ti)_3$ nanotubes and the noticeable increase of transition temperature which the authors suggest to be due to the radial stresses coupled with polarization via electrostriction effect.

Geneste *et al.* [232] used the first principle calculation and found that the critical thickness below which ferroelectric distortion does not exist for $BaTiO_3$ nanowires is about 1.2 nm. The authors suggested that the disappearance of distortion is due to low coordination at the wire surface. Later in 2008, Hong *et al.* [234] used Landau-Ginzburg-Devonshire theory to study the ferroelectric properties for $Pb(Zr_{0.5}Ti_{0.5})O_3$ nanowires. It was proposed that Curie temperature, coercive field, remanent polarization, dielectric permittivity and piezoelectric coefficient are size dependent. These properties disappear below the critical thickness (2 nm) but can be recovered if appropriate axis tension is applied. The same authors studied the size dependent ferroelectric properties for $BaTiO_3$ nanowires using the same theory. They found the Curie temperature, polarization and width of the ferroelectric loops decrease with the reduce diameter of the noanowires below 20 nm. The critical thickness for $BaTiO_3$ where hysteresis loop disappear is estimated to be 3.6 nm [235]. The effect of the surface curvature of $PbTiO_3$ nanowires

was also theoretically studied [238]. The nanowires depict enhancement of spontaneous polarization due to the tension induced by nanowires surface curvature at the surface. This induced tension counteracts the surface depolarization and $PbTiO_3$ nanowires with 1.8 nm diameter depicts 1.26 times higher spontaneous polarization than bulk counterpart.

The effect of surface termination for $BaTiO_3$ [236] and $PbTiO_3$ [237] nanowires were also theoretically investigated. It was found that the critical thickness for $BaTiO_3$ nanowires regardless of stoichiometry and nanowires side wall termination is about 12 Å. However, the nanowires with Ba-O termination depict polarization below critical thickness. In the case of $PbTiO_3$ nanowires the ferroelectricity is enhanced at the edge of the Pb-O terminated nanowire because Pb-O covalent bond that predominates strengthened ferroelectric distortions locally. Whereas, it is found considerable suppression of ferroelectricity for Ti-O terminated nanowires. Critical thickness for $PbTiO_3$ nanowires with Ti-O termination is around 17 Å. Zheng *et al.* [240] use thermodynamic models and Ginsburg - Laudau equation to determine the effect of surface tension and the near –surface eigenstrain relaxation on the ferroelectric properties. The authors found that the transition temperature and polarization are enhanced due to the effective radial pressures induced by the surface tension. This results in high remanent polarization and coercive field in comparison with bulk values for $BaTiO_3$ nanotubes. Ma *et al.* [239] use Landau–Ginzburg–Devonshire phenomenological approach to investigate the surface tension associated internal pressure on the phase transition in $BaTiO_3$ nanowires. The surface tension inside 1D structures induces the internal pressure along the radial direction which influences the ferroelectric properties. It was concluded that if the polarization is oriented along the axis of the nanowires the polarization and transition temperature are expected to increase with the decrease in diameter, until the long –range ordering favouring ferroelectricity. In the case of polarization normal to the axis of the tubes transition temperature decreases with diameter.

From the theoretical point of view it is somehow clear that the critical size of 1D structures to present ferroelectricity is dependent on many factors as size, polarization direction, stress at curvature, termination and so on. Hence it is difficult to predict or indicate an exact critical size; however from the above mentioned works, the maximum critical size theoretically calculated for 1D ferroelectricity is estimated to be around ~3

nm. A clear picture on the critical size can be obtained if one considers experimental studies, as well.

In last decades, experimental studies have been carried out on 1D nano ferroelectrics to understand the existence of ferroelectricity and domain formation in nanowires, nanotubes and nanorods and also to verify the theoretical predictions. Here, we detailed the most important experimental investigations carried out accordingly.

The first experimental investigation about ferroelectric properties on $BaTiO_3$ nanowires prepared by solution based methods was carried out in 2002 [243]. The ferroelectric properties were investigated by Electron Force Microscope (EFM) on $BaTiO_3$ nanowires having diameters ranging from 10 to 35 nm. 10 nm $BaTiO_3$ nanowires retain ferroelectric properties and depict a coercive field of ~7 kV/cm and retention time for the induced polarization >5 days.

In 2003 Morrison and co-workers obtain nanotubes of strontium bismuth tantalate (SBT), BT and PZT with wall thickness of ~200 nm, using Si porous template assisted chemical solution deposition (CSD) [211, 244, 245]. SBT and PZT tubes exhibit good rectangular hysteresis loops acquired by SPM [246].

Nanorods of Rochelle salt (RS) single crystals were synthesised inside alumina templates with pore size of 30 nm by Yadlovker *et al.* [247]. The electrical measurements were carried out by Sawyer-Tower circuit from temperature ranges from 21 - 60 ℃. They found there is an enhancement of the spontaneous polarization from 0.25 up to 2 $\mu C/cm^2$ in nanorods as compare to bulk.

In 2006, Zhaoyn e*t al.* [248] characterized $BaTiO_3$ nanowires synthesised by chemical based methods having diameter of 50 - 200 nm and length up to 10 mm. PFM studies were carried out both in plane and out of plan mode. The authors have found that the ferroelectric polarization switching along the axis of nanowire, whereas ferroelectric response normal to the axis was strongly suppressed. In the same year Spanier *et al.* [213] investigated the ferroelectric phase transition in $BaTiO_3$ nanowires synthesised from solution-phase decomposition of barium titanium isopropoxide. In this case $BaTiO_3$ nanowires have diameters ranging from 30 to 100 nm with lengths up to 10 μm. The

influence of depolarization fields on the stability of written domains perpendicular to the nanowire axis was demonstrated by Electrostatic Force Microscopy and the enhancement of ferroelectricity was attributed to the presence of molecular adsorbents on the surface of the wires. Curie temperature (T_c) variation as a function of the nanowire diameter is shown in Figure 2-19. Based on the experimental results it was predicted that the Curie temperature for $BaTiO_3$ nanowires falls below room temperature for nanowire with diameter of 3 nm and ferroelectricity can be retained in the $BaTiO_3$ nanowires up to 0.8 nm below the room temperature. The suppression of ferroelectricity for nanowires with decrease in diameter is the result of the depolarization fields as it is known that the depolarization is an inverse to the thickness of the material.

Focused ion beam was used by Schilling *et al.* [249-251] for the synthesis of different sizes of 1D $BaTiO_3$ structures. The domain study on these 1D $BaTiO_3$ structures were carried out after cooling the wires below the Curie temperature and imaged by Scanning Tunnelling Electron Microscopy. The authors found that the orientation of polarization exists both in parallel and vertical axis of the nanowires. By changing the aspect ratio of the wires, it allows local variations of the polarization direction.

Nanorods of $PbTiO_3$ with width of 30-100 nm and length of 100´s nm were fabricated by hydrothermal method and characterized by Piezo Force Microscope. These rods exhibit ferroelectric hysteresis loops with the applied dc bias of ±10 V. The orientation of the domains can be altered from perpendicular to parallel by heating the nanorods above Curie temperature. Heat treatment also results in the formation of 90º domains what might be caused by the rearrangement of the surface as stated by the authors [252].

The above studies suggest the size is not a constraint for 1D nano structures and possess sufficient ferroelectricity along the axis of 1D structure as well in the perpendicular to axis.

In 1984 Ginzburg *et al.* [253] theoretically predicted that anomalies in magnetic response of CdC and CuCl are due to the presence of toroidal ordering and this ordering can be found in ferroelectric material as well.

Fu *et al.* [254] investigated BaTiO$_3$ colloidal quantum dots and wires using first principle based approach. They found that large ferroelectric off centred displacement exists in 5 nm nanodots, where ferroelectric domain ordered in spontaneous vortex ordering. This theoretical demonstration of spontaneous toroidal moment open the possibility of fabricating high density ferroelectric memory based on spontaneous toroidal moment. Later, Naumov and co-workers [6, 255] used ab initio studies to investigate the ferroelectric behaviour of Pb(Zr,Ti)O$_3$ nanodisks and nanorods. Nanodisks of 3.2 nm diameter show the structural stability at low temperature and possess spontaneous polarization in the form of clockwise and anticlockwise vortices (Figure 2-20) which is not similar to the bulk. The toroidal movement and T$_C$ for nanorods increases with diameter at low temperature where in the case of nanodiscs T$_C$ is insensitive to the diameter. The authors also explained numerically that there is a critical diameter under which vortex do not exist.
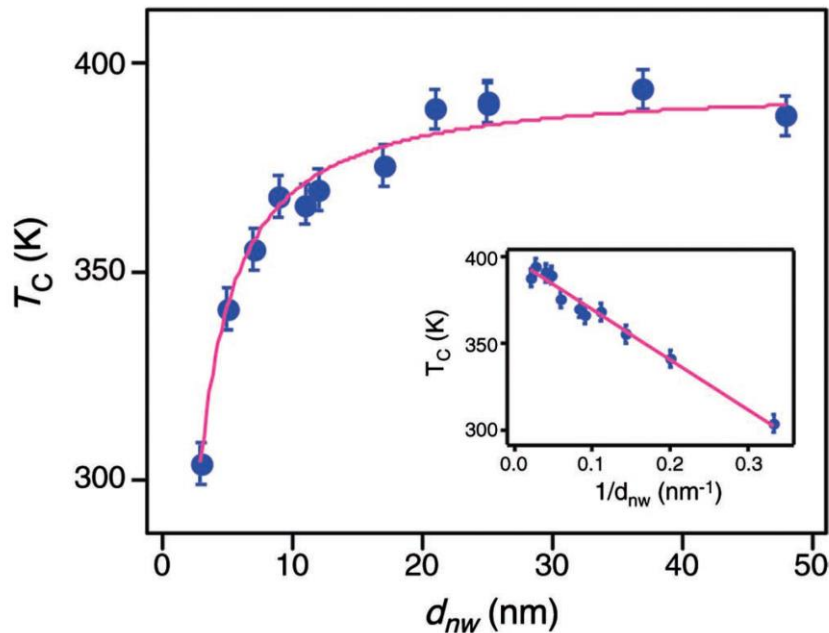
Figure 2-19 Ferroelectric phase transition temperature (T$_C$) as a function of the diameter of BaTiO3 nanowires (d$_{nw}$). The solid circles are the experimentally determined T$_C$ and magenta solid line is the fit to the data. The inset plots T$_C$ as a function of 1/d$_{nw}$ [213].
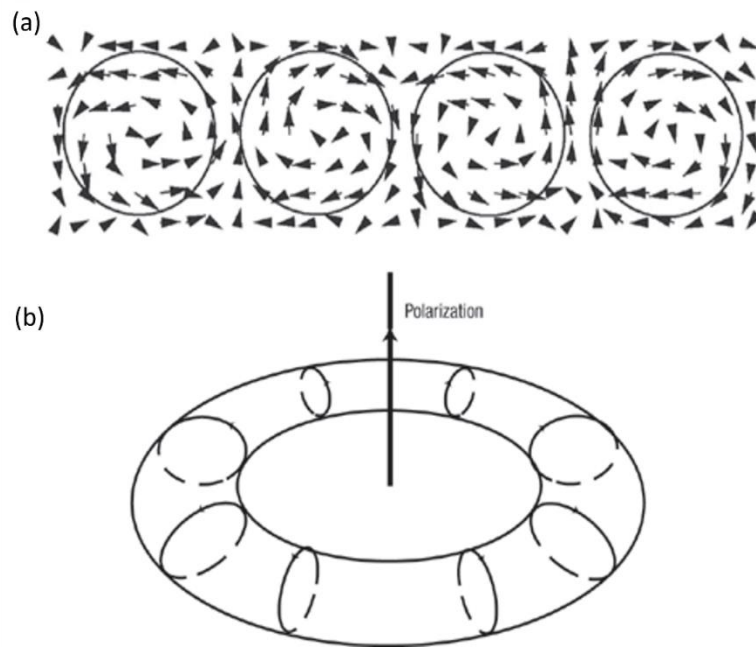
Figure 2-20 Schematic of the possible polarization phenomena pattern that occurs at the nano scale (a) circular and [6] (b) toroidal spontaneous moment [256, 257].

2.5 CNTs and ferroelectrics

A key requirement for the miniaturization of FeRAM capacitor cell (or memory cell) is to have large electrode surface area so that reliability of the switching and sensing of the signals can be improved. These requirements cannot not be achieved in the present 2D planar structure. Therefore, alternative structures and circuit designs are needed. 3D type structures appears as a promising alternative. It is expected that these 3D capacitor cells for FeRAMs will allow to fabricate RAMs with the storage capacity of 1 - 10 Gbit without exceeding the total area of the memory cell i.e. more than 0.08 μm^2 [258, 259]. This means that the memory cell should be of lateral dimension of 100 nm or less up to 20 nm.

3D FeRAM cells can be design by two different approaches based on the design of bottom electrode (BE) [4]. The schematic of the two designs that are currently being proposed are represented in Figure 2-21; the first one is named as pin shaped (Figure 2-21 (a)) and the second one as cup shaped (or trench). In pin shaped the BE is deposited on a flat substrate and shaped in the form of rods or tubes. These tubes are then conformally

covered with the ferroelectric material and top electrode (TE). In the cup shaped geometry (Figure 2-21 (b)) the BE is shaped in the form of a trench that is later covered with the ferroelectric and on the top of it with the TE. The whole cell size needs to be less than 10 F^2 (where F is feature size) to accumulate the high storage density.
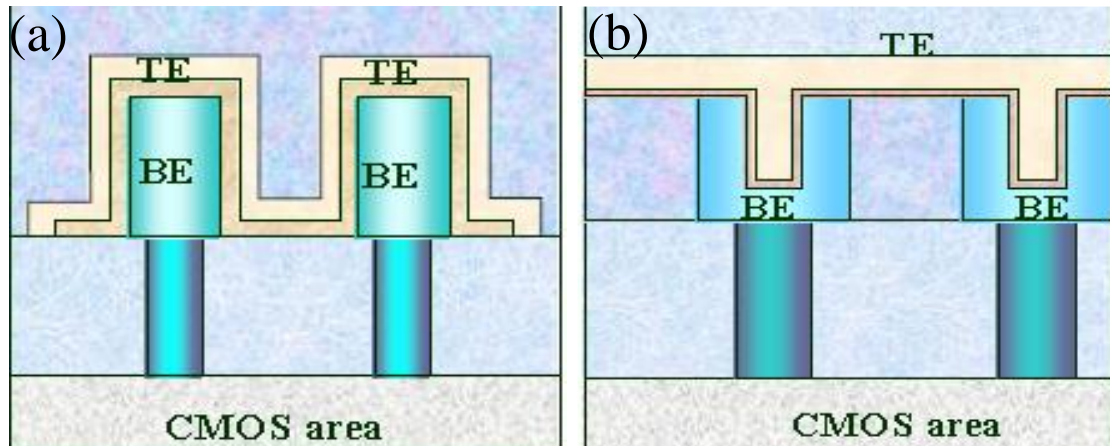
Figure 2-21 3D FeRAM capacitor cell: (a) pin shaped and (b) cup (or trench) shaped [4].

The major developments on 3D shaped FeRAM capacitors have been mainly performed by three different research groups. The group of Funakubo from Japan used silicon trenches to fabricate 3D FeRAM capacitor cells [258, 260]. The group of Wouters from Belgium used pin shaped bottom electrodes covered with strontium bismuth tantalate (SBT) [261-263] and the third group of Scott from United Kingdom and Katiyar from USA used CNTs as a BE for the synthesis of 3D capacitor cells [13, 21].

Cup (or trench) shaped bottom electrodes were first investigated by Funakubo *et al* [260] in collaboration with Samsung-Tokyo Institute of Technology (Figure 2-22). The authors used $SiO_2/TiAIN/Ti/SiO_2/Si$ trench substrates as a bottom electrode for the fabrication of 3D shape FeRAM capacitors. By pulsed–metal organic chemical vapor deposition (MOCVD) Si trenches were coated with Ru electrode followed by the ferroelectric layer of PZT by pulsed-MOCVD at 540 °C. SEM and EDS analysis evidenced the good conformal covering of Si trenches with Ru and PZT, demonstrating the success of using MOCVD to fabricate trench bottom electrode capacitor cells for high

density FeRAMs. However, this work reveals some concerns about the variation of the PZT composition throughout the structure and thickness of PZT layer in the trench.

Kim *et al.* [258] did similar investigations on the fabrication of 3D capacitors using Si trench, but in this case atomic layer deposition (ALD) was the chosen technique. Si trenches were covered with ~ 15 nm layers of Ir conducting electrodes using TiAlN as buffer layer between the PZT and Ir which improves the stability of Ir electrodes. The ferroelectric PZT layer deposited after by MOCVD depicted a uniform covering throughout the trench with compositional uniformity of PZT throughout the trench. However, structural non-uniformity of the PZT layer on the bottom and on the side walls was observed by TEM.

These results are preliminary investigations on using Si trenches as templates for the fabrication of 3D capacitors; more systematic investigations using different FE materials and electrical characterization are necessary to be carried out.

In 2003, pin shaped electrodes were first investigated by Zambrano *et al.* [4] in STMicrelectronis. The authors illustrates the pin shaped electrodes have some advantages over cup shaped ones because there is no need of uniform covering of BE with FE, moreover no need of masking required during the deposition process of BE and/or FE and the size of the capacitor cell was not controlled by parasitic components as in trench shape cells. In this work Zambrano and co-workers used MOCVD to cover Pt/IrO$_2$/Ir/TiAlN (BE) with strontium bismuth tantalate (SBT) (Figure 2-23 (a)). However, structural non-uniformities of SBT grains were found at the bottom electrode. In following works [261-264] this same group fabricated SBT films on pin shaped Pt/IrO$_2$/Ir/TiAlN (BE) with the technology node of 0.35 µm and 0.18 µm using MOCVD. A 70 % increase in the remanent polarization was reported for these 3D capacitors in comparison with similar 2D capacitor cells due to the contribution of the sidewalls of BE (Figure 2-23 (b)). The authors also found that remanent polarization values increase with the miniaturization of the cell size as illustrated in Figure 2-23 (c). These 3D capacitor cells show fatigue after 10^{13} cycles.

These innovative works clearly show that the use of 3D structures results in improving polarization of 3D capacitors due to the increase in the surface area of the

bottom electrode. These findings triggered the further research with the use of metallic 1D materials with enhanced conducting properties such as CNTs, to fabricate 3D capacitor cells for future 3D FeRAMs.
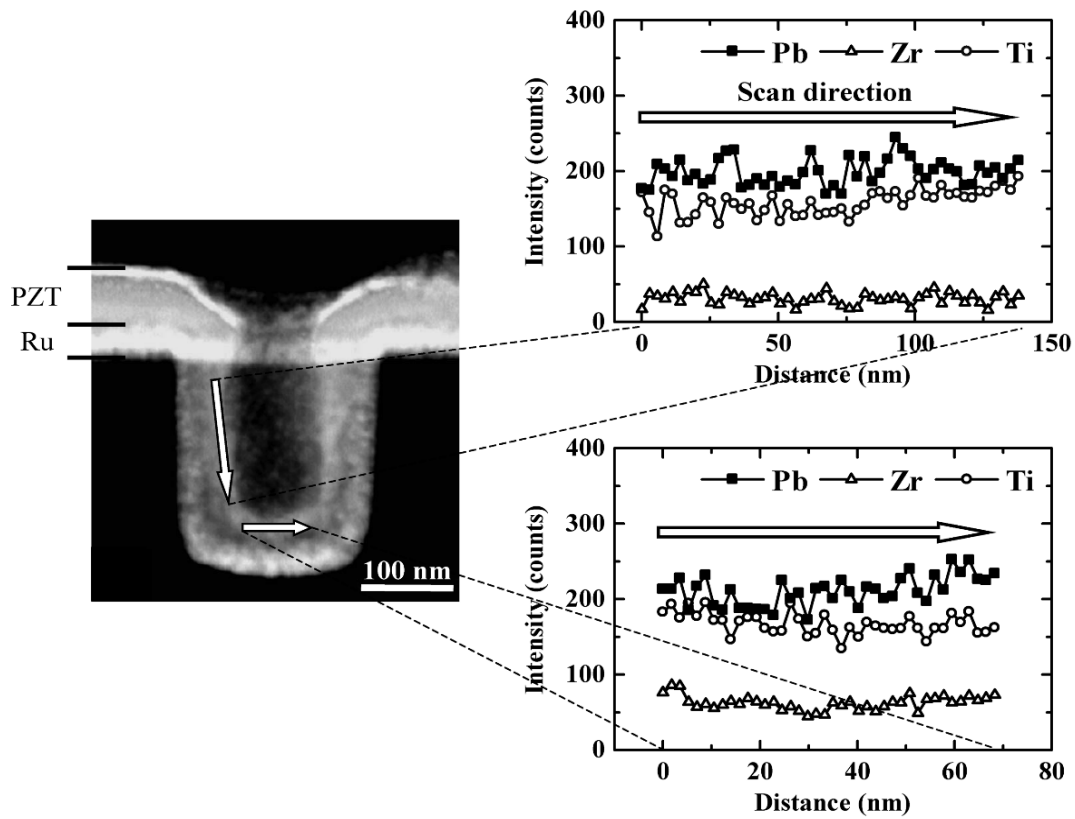
Figure 2-22 SEM micrograph of 3D trench shaped capacitor, Si trench covered by PZT for 3D capacitor cell for FeRAM (left side image). The EDS analysis from side walls and bottom of the trench reveals the presence of Pb, Zr and Ti elements (right side image) [260].

(a)

W-plug
deep
M1-Si
contact

Isolation

H-seal

Pt

SBT

Bottom
electrode

Pt/IrO$_2$/Ir/TiAlN

W-plug
BE contact

Si

1 µm

(b)

P (µC/cm^2)

3-D

5 V

2-D

3 V

5 V

3 V

E (kV/cm)

25
20
15
10
5
0
-5
-10
-15
-20
-25

-400 -300 -200 -100   0   100   200   300   400

(c)
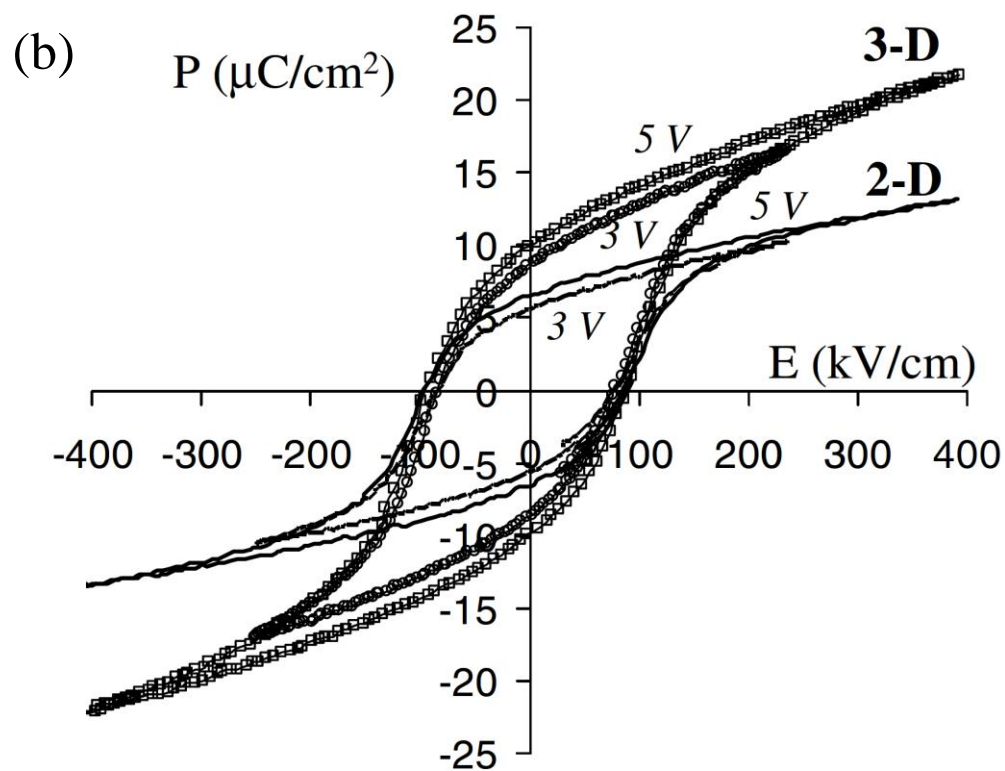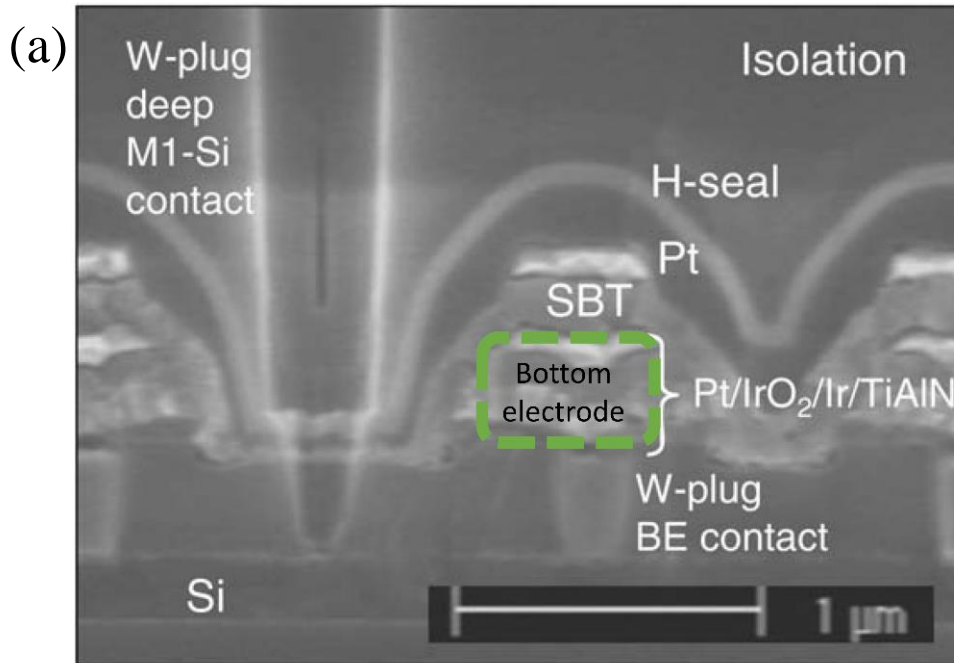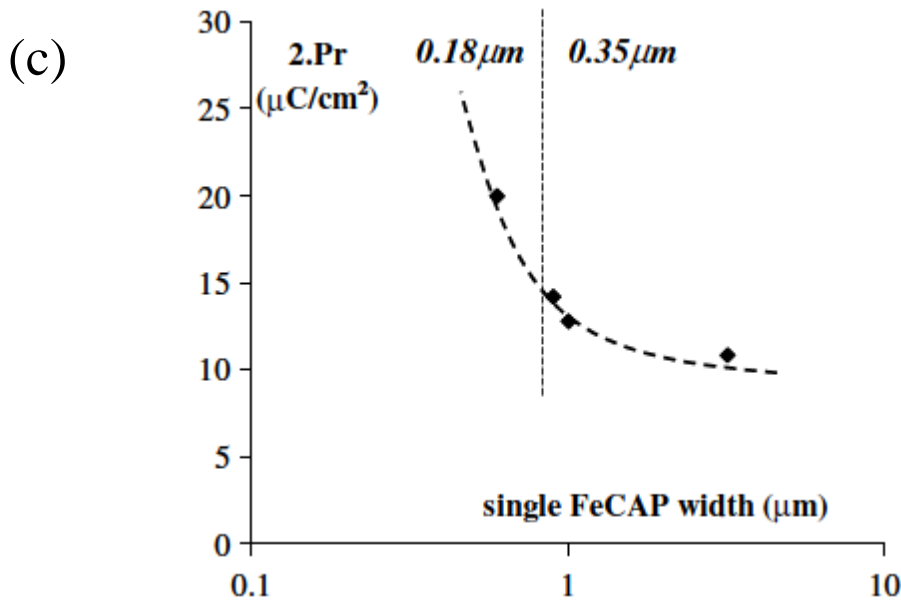
Figure 2-23 (a) 3D pin shaped capacitor cell in which the BE is covered with SBT; (b) caparison of hysteresis loops of 3D and 2D capacitors, 3D capacitor depicts high remanent polarization; and (c) size dependence of the remanent polarization of 3-D capacitors measured at 5 V, in 0.18 and 0.35 µm technology [265].

The first use of CNTs as bottom electrode for pin shaped memory application came from the work of Jang *et al.* [14, 16, 17] in which the potential of using vertical aligned CNTs coated with Si_3N_4 targeted to the development of ultra large scale integration (ULSI) memory based on DRAM or nano electromechaical RAM (NEMRAM) was proved. The working principle of NEMRAM memory is based on the mechanical movement of the nanotubes, due to the charging of capacitor as in DRAM. The main advantage of vertical structure design using CNTs is to decrease the cell dimension and improve the storage capacity. CNTs were vertically grown by CVD on the substrate and then coated with Si_3N_4 layer by direct current plasma enhanced chemical vapor deposition system (DC-PECVD) (Figure 2-24 (a)).

Later in 2007, based on a similar idea Kawasaki *et al.* [13, 21] have employed CNTs as bottom electrodes for the development of pin shaped 3D capacitors cells for FeRAM. In this work CNTs were vertically grown on silicon substrates and vertical MWCNTs were coated with PZT by liquid source misted chemical deposition (LSMCD) (Figure 2-24 (b)). After PZT deposition on MWCNTs the samples were pyrolysed at 300

ºC for 3 min followed by annealing at 650 ºC in oxygen atmosphere. TEM and STEM studies show that the tubes are not uniformly coated and also that the MWCNTs did not burn due to the protective coating of the oxide on the top of the tubes. However, EDS analysis clearly reveals the contamination of CNTs surface with platinum. These studies were the initial step and proved the feasibility of producing CNTs – FE structures. In these studies the ferroelectric behaviour of CNTs-FE was not demonstrated.

Following this pioneer work, Katiyar and co-workers demonstrated the covering of Bamboo–CNTs (BCNT) (diameter of 100 to 150 nm) with pulsed laser deposition (PLD) method at low oxygen pressure of 70 to 80 mTorr and temperature ranges from 600 ºC to 700 ºC with ferroelectrics as PZT and $Ba_{0.7}Sr_{0.3}TiO_3$ (BST) [27] and ferromagnetic $La_{0.67}Sr_{0.33}MnO_3$ [31]. PZT on the surface of BCNTs was analysed by Raman that confirms no damage to the BCNTs up to 650 ºC and confirms the formation of crystalline PZT at 650 ºC. However with the increase in the deposition temperature to 700 ºC, no RAMAN peaks corresponding to BCNTs were observed, point to the possible disappearance of BCNTs by oxidation. The structural morphology of the PZT grown on BCNTs studied by HRTEM depict nano sized crystal beads of PZT across the CNTs (Figure 2-25 (a)). PZT layer thickness on the surface of CNTs is varying from 50 to 80 nm. The local piezoelectric response shows ferroelectric behaviour of 1D BCNTs-PZT (Figure 2-25 (b)) [28, 29]. The leakage current maps were also obtained using conduction AFM reveals the variation in conductivity throughout the structure. According to author this may be associated with the presence of defects associated with the fabrication. BST deposited on BCNTs by PLD at 650 ºC with oxygen pressure of 80 mTorr were characterized by HRTEM and Raman [27]. HRTEM analysis shows the BST-BCNTs structure has diameter of 150 to 250 nm. BST layer consists of maize like nano beads having thickness of 15 to 25 nm. Raman analysis confirms the presence of BCNTs with little damage fabricated at 650 ºC. No electrical measurements were performed on the BST covered BCNTs structure. Later, the same group deposited $La_{0.67}Sr_{0.33}MnO_3$ (LSMO) [31] on CNTs using PLD. The thickness of the LSMO layer on the surface of MWCNTs is ~50 nm. The *in-situ* I-V measurement in TEM and modelling of the data states the electron transport properties of LSMO-BCNTs outperform those from CNTs alone.

Yang *et al.* [25] fabricated co-axial nano structures (or core shell) of MWCNTs and oxides using PLD. $CoFe_2O_4$ layers on MWCNTs were deposited by PLD followed by BT layers. The authors found that increasing the deposition temperature (above 700 ℃) and oxygen concentration (100 mTorr) improved the crystallinity of BT but the surface morphology of the tubes becomes affected at these conditions. No electrical measurements were reported.
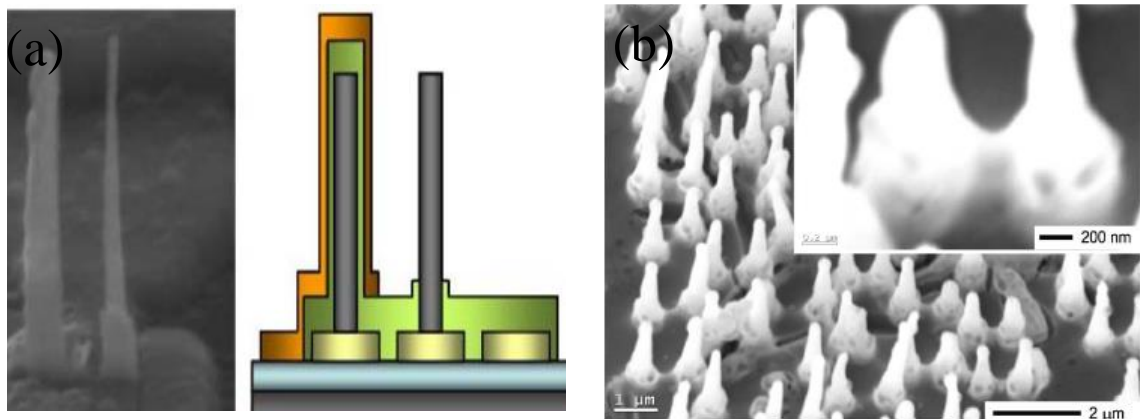
Figure 2-24 (a) MWCNTs coated with Si_3N_4 for NEMRAM [15] and (b) MWCNTs coated with PZT by liquid mist technique [21].
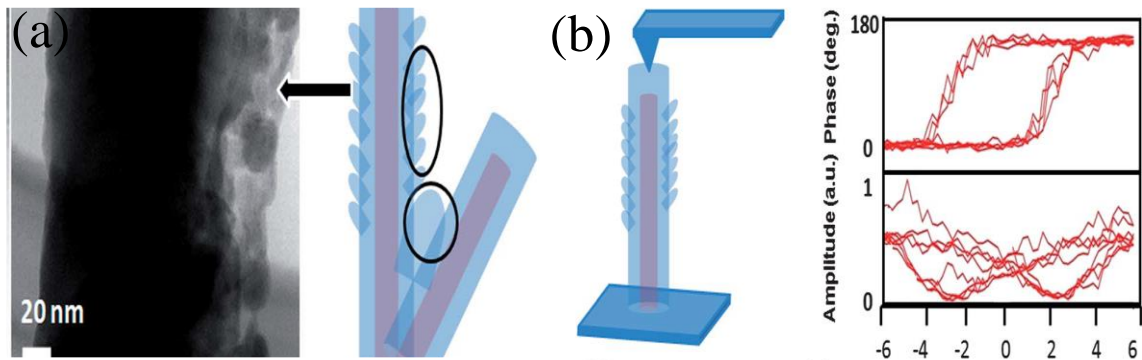
Figure 2-25 (a) HRTEM micrograph shows nano beads of PZT on the surface of PZT coated MWCNTs. (b) Piezo-electric response from a PZT nanotube [28, 29]. It was demonstrated that MWCNTs can be conformally covered with PZT by PLD and a ferroelectric response was measured.

Vertical Aligned (VA) MWCNTs covered with $SrTiO_3$ layers by RF sputtering to control the field emission from the VA-MWCNTs has been demonstrated by Pandey *et al.*[30]. Author, prove the high dielectric constant dielectric ($SrTiO_3$) on VA-MWCNTs can reduce Coulomb repulsion forces between electrons in neighbouring CNTs. This leads to lower the drifting of electron flows in CNTs and thus reduce electron phonon scattering and Joule heating. No information is disclosed on structure or interfaces of MWCNTs-$SrTiO_3$. The possible application of this heterostructure was proposed for field emission devices such as X-ray generation, and wave amplification application.

The above mentioned works use physical/chemical vapor deposition methods to cover CNTs with FE, but there are some reports on use of chemical solution deposition methods to cover MWCNTs with FE detailed below.

The first work on the use of chemical methods to cover MWCNTs with FE was reported in 2010, where Bedekar *et al.* [23, 24] reported coatings of MWCNTs with $BaTiO_3$ (BT). The BT layer on the surface of MWCNTs was formed by dispersing the CNTs in to the commercial sol gel solution of BT. MWCNTs covered with BT precursor were heat treated in nitrogen atmosphere at 700 ºC for 2 h to obtained MWCNTs covered with BT layer. HRTEM and EDS revealed uniform covering of tubes with layer thickness from 10 to 20 nm. However in this study information on oxide phase formation process, crystallinity and electrical measurements are lacking.

Mohammadi *et al.* in 2012 [26] used MWCNTs as sacrificial templates for the growth of PZT nanotubes. Here, MWCNTs were coated with PZT sol gel solution and annealed at >450 ºC for different time periods to oxidized MWCNTs. Without explanation the authors stated that the presence of MWCNTs promoted the early PZT phase formation. The activation energy for the PZT phase formation was calculated by Kissinger equation and found to be 103 kJ/mol. TEM analysis demonstrate the formation of PZT tubes with thickness of 50 to 60 nm. Electrical measurements were not performed on these PZT nanotubes.

Vertical aligned MWCNTs were covered with BST particles using low cost electrophoretic deposition (EPD) process for 3D capacitor cell. Commercial $Ba_{1-x}Sr_xTiO_3$ (BST) nano particles (average size of 10 nm) were used for the deposition in aqueous

media. Vertical aligned MWCNTs synthesised by CVD were used as a working electrodes and deposition of BST particles were carried out with electric fields of 5 V/cm and 100 V/cm [22]. Although BST particles covered MWCNTs, a non-uniform surface of BST granules on the MWCNTs is the main limitation of this fabrication process. The electrical properties of these MWCNTs-BST structures were not measured.

Other than covering CNTs with FE there are other studies which are focused on the fabrication of MWCNTs-FE composites for various electrical application. Here are some of the most important ones, which are somehow related with the present work.

Hydrothermal synthesis was used to fabricate MWCNTs-BT composite structures in which MWCNTs were used as metallic fillers to improve the thermal and electrical properties of the composites [18, 19, 266]. The MWCNTs-BT composites were hydrothermally synthesised in two steps. In the first step TiO_2 was initially immobilized on the surface of MWCNTs using sol gel method. These MWCNTs-TiO_2 structures were reacted with barium acetate solution to get MWCNTs-BT composite powders. [18-20] Using these powders MWCNTs-BT sintered bulk ceramics with different wt% of MWCNTs were fabricated by spark plasma sintering (SPS). Composite depicts decrease in thermal conductivity and electrical conductivity from 3.06 to 2.46 W/mK and 20.3 to 6.5 S/cm, respectively, whereas specific heat capacity increases from 425 to 465 mJ/gK.

In 2008, Ruangchalermwong *et al.* [267] synthesised MWCNT-PZT thin films on Pt (111)/TiO_2/SiO_2/Si(200) substrates by spin coating. The films were prepared by mixing different wt% (0 to 1) of MWCNTs in the PZT sol. The deposited films were pyrolysised at 400 ºC for 2 h and then annealed at 650 ºC for 30 min. During the annealing process MWCNTs oxidized and leave open porosity. The effect of porosity on the dielectric properties of porous PZT films was investigated. As expected it was found that the dielectric response degrades with the increase of porosity.

Table 2-3 and Figure 2-21 summarizes the above literature review and the most important contributions to this field of covering of MWCNTs with ferroelectrics up to now. In the Figure 2-21 the green ovals and square represent the major aim and specific aims for the present work carried out.

Most significant progress on covering MWCNTs with FE has happened in last five years; most of this work relates with covering MWCNTs for 1D structure by physical/chemical vapor deposition methods and just a few studies are related to the use of chemical solution deposition methods;

-except the work of Kumar *et al.* [29], no other works studied the ferroelectric properties of the CNTs-FE.

-there are no systematic studies on the coverage of MWCNTs with low cost chemical solution methods has been reported, especially for BFO.

-it is clear that developing and understanding the covering process of CNTs with FE is an important aspect for 3D FeRAM capacitors.

From the above discussion it is clear there is need to pursue this idea and to develop techniques by which the short come of previous studies can be overcome, such as stoichiometry control, carbon lattice damage and siphoning of the using CNTs as a substrate material. It is also necessary to conduct more systematic characterization of ferroelectric properties.
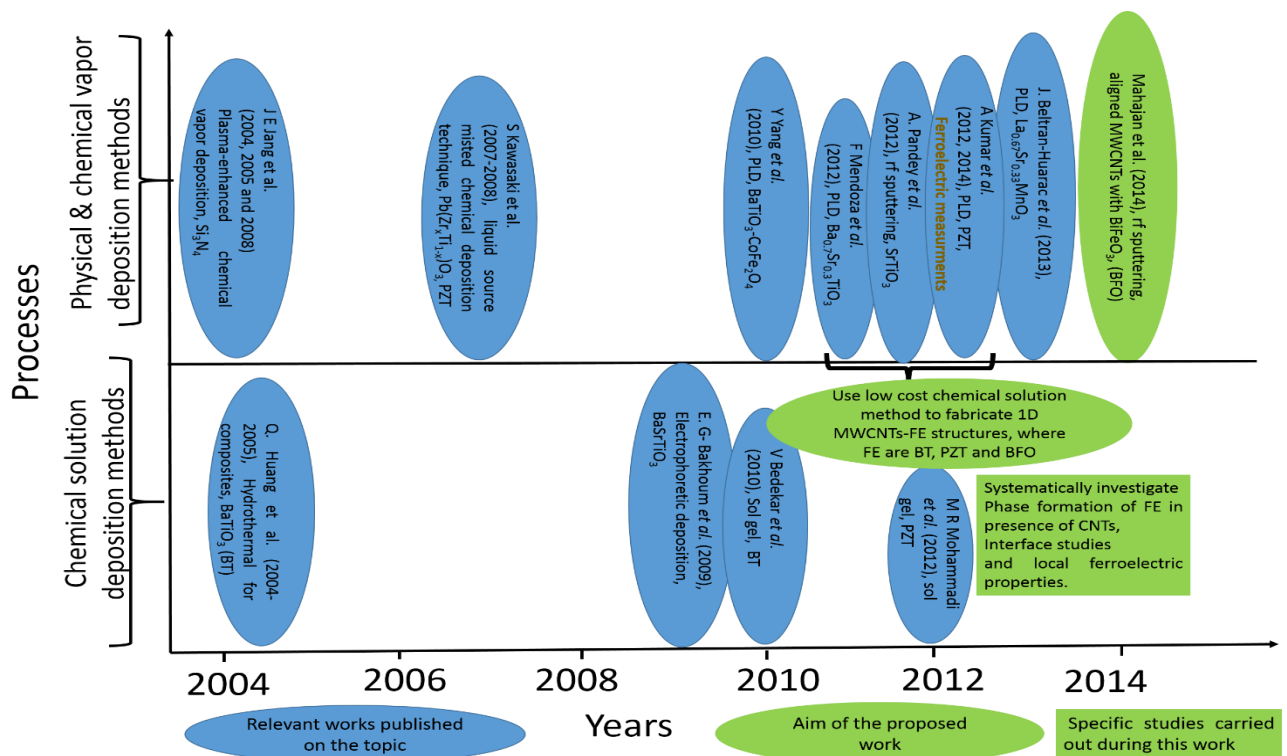
Figure 2-26 Plot illustrates the important works published on covering of CNTs with FE by physical/chemical vapor deposition and chemical solution deposition methods.

Table 2-3 Literature review on the development of CNTs-FE.

Group	Material/Process	Characterization	Conclusions	Reference
J E Jang *et al.* (2004, 2005 and 2008)	Si_3N_4-MWCNTs/ Plasma-enhanced chemical vapor deposition (PECVD)	SEM, electrical measurements	Proof the concept of using 3D geometry for Ultra large scale integrations and nanoelectromechanical DRAM	[14-17]
Q. Huang *et al.* (2004-2005)	$BaTiO_3$–MWCNTs/ Hydrothermal method followed by sintering using RTP furnace, bulk	XRD, SEM and electrical measurements	Transfer n-type $BaTiO_3$ semiconductor to p-type with the inclusion of CNTs	[18-20]
S Kawasaki *et al.* (2007-2008)	MWCNTs-$Pb(Zr_xTi_{1-x})O_3$ /liquid source misted chemical deposition (LSMCD) technique	SEM, EDS mapping	MWCNTs damaged at 650ºC in air. Also, there is reaction between substrate material and CNTs	[13, 21]
Ezzat G Bakhoum *et al.* (2009)	$BaSrTiO_3$-MWCNTs / Electophoretic deposition (EPD)	SEM, deposition parameters	Non uniform coating of MWCNTs with BST particles	[22]
V Bedekar *et al.* (2010)	$BaTiO_3$-SiCN-MWCNTs Use MWCNTs as Template/ solution method	XPS ,SEM,TEM, EDS	Successfully coated BT on SiCN/MWCNT	[23]
V Bedekar *et al.*(2010)	$BaTiO_3$–MWCNTs/ solution method	FTIR ,SEM ,TEM , EDS, Contact Angle	Coating thickness of 5-15 were obtained by solution method	[24]
Y Yang *et al.*(2010)	$BaTiO_3$-$CoFe_2O_4$–MWCNTs/ Pulsed Laser deposition (PLD)	SEM ,TEM ,XRD	Proved PLD is effective technique for coating MWCNTs	[25]
M R Mohammadi *et al.*(2012)	$PbTiO_3$ Nanotubes Use MWCNTs as Template/ Solution method	DTA/TG ,XRD ,RAMAN, SEM, TEM, EDS Mapping	PZT nanotubes were successful obtained using MWCNTs template	[26]
F Mendoza *et al.*(2012)	$Ba_{0.7}Sr_{0.3}TiO_3$ (BST)-CNTs/ PLD	XRD, RAMAN , SEM, HRTEM	Demonstrate the possible strategy for the conformal coating of MWCNTs	[27]
A Kumar *et al.* .(2012, 2014)	PZT-CNTs/ PLD	XRD, RAMAN , SEM, HRTEM, PFM	Demonstrate the possible strategy for the conformal covering of MWCNTs with PZT without major damage to CNTs and Local ferroelectric measurements	[28, 29]
A. Pandey *et al* .(2012)	Strontium Titanate on Vertical Aligned CNTs/RF sputtering	Raman, XPS, SEM, HRTEM and Current (I) -Electric field (E)	Field emission properties has been improved	[30]
J. Beltran-Huarac *et al.* (2013)	$La_{0.67}Sr_{0.33}MnO_3$-CNTs/ PLD	XRD, RAMAN , SEM, HRTEM, I-V Curve	Demonstrate the possible strategy for the conformal coating of MWCNTs with ferromagnetic oxide	[31]

2.6 Introduction to the nano fabrication methods

Since the last 20 years and related with the expectations on nano technologies, a key enabling technology, synthesis and fabrication of nano structured materials have been consistently studied. Indeed novel properties expected for many nanostructures, nano materials and nano devices and the market needs for small, smart and mobile electronic gadgets have been the driving force behind these developments. Extensive efforts have been on going to prepare nano particles, ultrathin films, nanowires, nanotubes and 3D arrays of nano structures. Among all of these, 1D nano structures and their arrays as 3D structures are been seen as highly promising to be used in various electronic applications, due to their electron caring capacity, large surface area and high strength. As mentioned before, 1D nano structures are expected to play a prominent role as interconnectors, 3D memories cells, as a gate material for transistors, in optoelectronics and as electrochemical and electromechanical devices with nano scale dimensions, among others [206, 268].

So far fabrication strategies can be divided in to two main groups: top down and bottom up approach.

In top-down methods the feature size is obtained by etching or removal of materials from a large surface. The methodology mainly relies on lithography processes that utilize highly energised particles such as photons, ion or electron beam to erase material. Top down methodologies employ physical methods such as lithography, etching, ball milling and probe-based methods to downsize large macro structure to micro sized ones. The main advantage of top down methods comprise high-precision positioning and size control and disadvantages include: effect the crystallographic orientation of the materials, introduced impurities and imperfections and time [269].

In the case of bottom up approaches the nano structures are fabricated from the atomic level to the molecular one, as building blocks, up to a nano or micrometre size. As a consequence, advantages of the bottom up processes include better chances to obtain defect free nano structures, high homogeneity in the structure, epitaxy and possibility to be used for coatings; the main disadvantages of bottom up approaches include: toxicity of precursors, difficulties in controlling uniformity of size and morphology of the nano

structures and complexity of the process in some cases. Table 2-4 summarises the most common top down and bottom up approaches used for the fabrication of ferroelectric films and nano structures with their advantages and disadvantages [270].

Table 2-4 List of top down and bottom approaches and their advantage, disadvantages and limitations, adapted from [270]

Approach	Technique	Advantages	Disadvantages	Minimum size (nm)	References
Top-Down	FIB	High resolution, Use of High quality films, Uniform size and array	Surface damage, Low throughput, Volume shrinkage, Shape change	70	[259, 271-274]
	EBDW	No etching process, High resolution and Uniform size and array	Low throughput, Etching process	70	[271, 275-277]
	EB-lithography	High resolution and uniform size and array	Low throughput, Etching process	100	[278, 279]
Bottom-up	CSD (solgel, hydrothermal)	Easy Process, Easy to generate various size and to access extremely small size	Difficulty in uniform size array, and shape	<10	[224, 271, 280-287] [288, 289]
	MOCVD	Easy Process, Easy to generate various size and to access extremely small size	Difficulty in uniform size array, and shape	<10	[271],[282],[290], [291, 292]
	PLD	Easy process, Access to extremely small feature	Difficulty in uniform size array, and shape	<10	[271, 282]
	Sputtering	Easy process, conformal coating	Difficult in uniformity	<10	[30, 293]

Top-down approaches mainly rely on lithography processes that utilizes highly energised particles such as photons, ions or electron beam to remove material. Within these methodologies the most important techniques used to fabricate ferroelectric nano structures are Focused Ion Beam (FIB) and Electron Beam Direct Writing (EBDW).

These techniques are currently used in modern commercial nano technology, because they provide high-precision positioning and excellent size control [294]. The working principles of these techniques are described below.

The working principle of FIB is based on bombardment of high energy ions on the surface in order to remove the atoms. In FIB the Gallium ions are generated form the gallium metal placed in contact with tungsten needle. The produced gallium ions are accelerated towards the samples using electrostatic lenses with the acceleration energy from 1 - 50 keV. FIB is carried out under high current (~4 nA) to remove the material up to sub-micrometres to nanometre [295]. FIB has the same experimental setup as scanning electron microscope except in the case of FIB focused beam ions (namely gallium ions) are used instead of electrons. FIB is one of the most popular techniques for the fabrication of ferroelectric nano structures from already deposited metal organic crystalline films. 70 nm FE nano structures can be fabricated from FIB. FIB can be used in three different ways for micro fabrication, named as FIB lithography, FIB milling and FIB deposition milling. The main advantages of FIB are: high resolution, uniform size and the ability to fabricate arrays. Low throughput and high cost are however major limitations.

As an example, Ganpule *et al.* [259] successfully demonstrated the use of FIB to achieve ferroelectric nano structures with sizes ranging from 1 to 0.01 μm^2 of $Pb_{1.0}(Nb_{0.04}Zr_{0.28}Ti_{0.68})O_3$. A protective layer of Pt is coated on the top LSCO electrode previously deposited on $Pb_{1.0}(Nb_{0.04}Zr_{0.28}Ti_{0.68})O_3$ film (Figure 2-27 (a)). FIB ion beam was operated with an acceleration voltage at 50 kV, dose of 8 x 10^{17} ions/cm^2 and beam spot size of 6 - 12 nm to fabricate nano structures as small as 100 nm. The obtained ferroelectric nano structures show ferroelectric hysteretic response. However, there are major concerns regarding the damage of the oxide lattice at the etching surface by the high energy electron milling. Therefore, it is not possible at this stage of the technology to obtained feature sizes below 70 nm, for which ferroelectric oxides will not damage.

E-Beam Direct Write (EBDW) is a massless lithography process used to fabricate patterns of metallic and oxide nano structures using metal organic precursors [296]. It uses electrons as a source for patterning the surface of the substrate covered with the metal organic precursors. Chemical reactions are locally induced in a metal-organic film by irradiation the film with the electron beam. The unexposed area is dissolved by etching

or firing process and further heating at high temperature yields nano pattered structures of metal or oxides. A feature size around 20 nm can be achieved by this process. This technique is widely used for making photo masks for integrated circuits [296]. However, EBDW is not economically viable to make patterns, besides being very time consuming, the fabricated nano structures are highly defective.

Alexe *et al.* [275] used EBDW to fabricate $SrBi_2Ta_2O_9$ and $Pb(Zr_{0.70}Ti_{0.30})O_3$ nano structures; the experimental steps followed during this process are shown in Figure 2-27 (b). The metal organic films of $Pb(Zr_{0.70}Ti_{0.30})O_3$ and $SrBi_2Ta_2O_9$ on $SrTiO_3$/Nb substrates were exposed to the electron doses varing from 600 to 1500 mC/cm^2 and 600 to 1200 mC/cm^2, respectively. The films were then immersed in toluene for 1 min and dried with nitrogen. Nano structured patterns (as shown in Figure 2-27 (b)) were obtained with lateral dimensions between 1 and 0.125 μm. After this the substrates were heat treated to obtained crystalline nano structures of $Pb(Zr_{0.70}Ti_{0.30})O_3$ and $SrBi_2Ta_2O_9$ ferroelectric. The local ferroelectric switching proved the ferroelectric nature of 100 nm $Pb(Zr_{0.70}Ti_{0.30})O_3$ nano structures.

Bottom up approaches are divided into three categories i) Physical Vapor Deposition (PVD) and ii) Chemical Vapor Deposition (CVD) and iii) Chemical Solution Deposition (CSD).

In PVD process a vapor phase from a pure material is created by laser ablation or ion bombardment. This vaporized material condenses on the substrate to create the desired ferroelectric layer. In the case of CVD, the source material, in the form of volatile precursors and together with the carrier gases are injected into the CVD chamber, where the vaporized precursors adhered to the hot substrate, eventually undergoes chemical reaction and leaves the desired ferroelectric oxide layer on the substrate. Both PVD and CVD are widely used in microelectronic industries to fabricate thin film based devices [297, 298].

In comparison to the previous PVD and CVD, Chemical Solution Deposition (CSD) methods are high-throughput, well suited to the deposition of large areas and low cost. Due to these assets CSD has recently started to be used in the industry to fabricate ferroelectric thin films and/or nano structures. In CSD process liquid precursors of desire

material are transferred/deposited on the substrate to form films and or nano structures of ferroelectrics [299, 300].
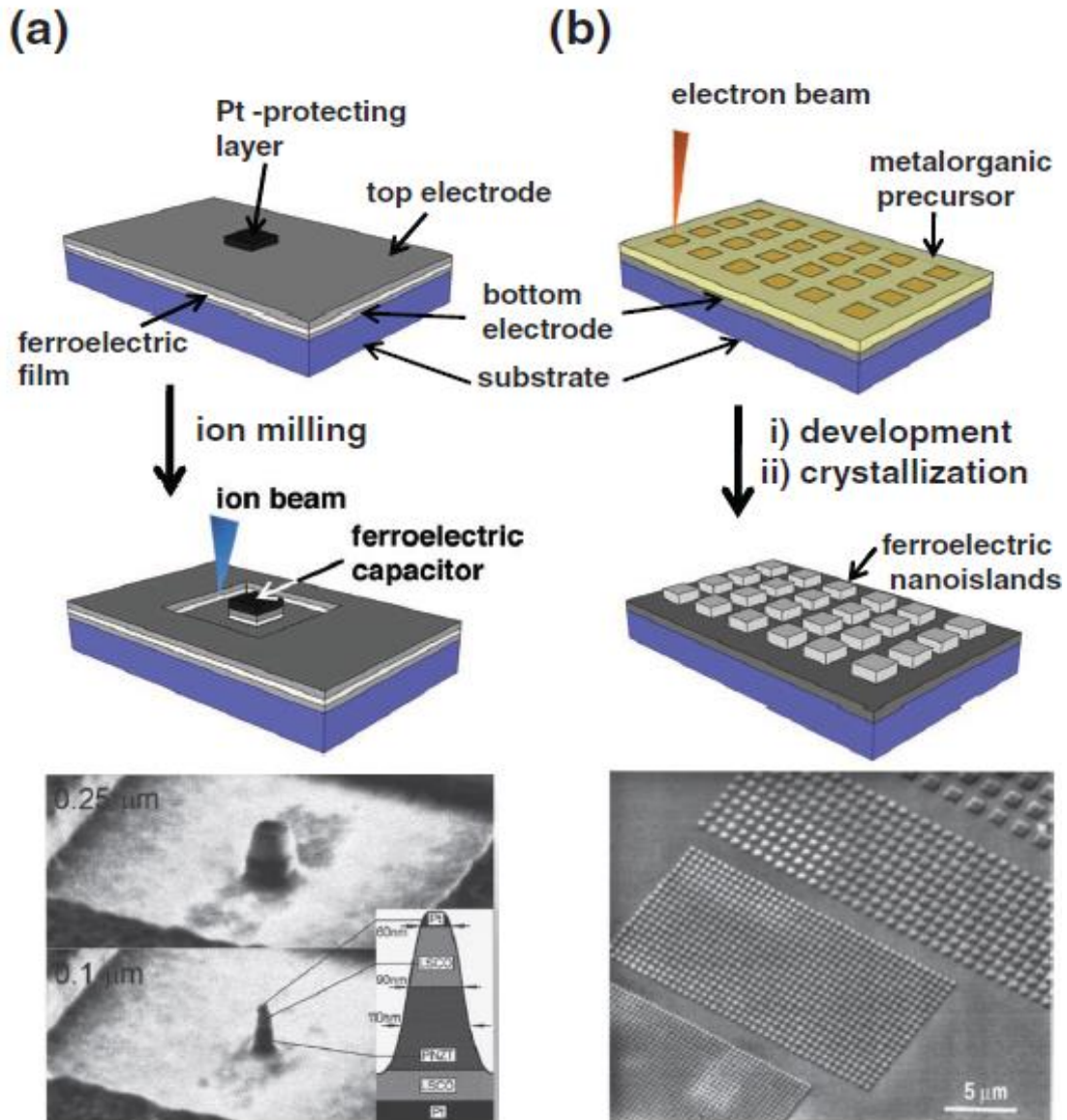
Figure 2-27 Top down methodologies for the fabrication of ferroelectric nano structures: (a) focused ion beam milling (FIB) and (b) EB direct writing [259, 275].

Important processing methods used for the fabrication of ferroelectric nano structures by PVD are Pulse Laser Deposition (PLD) and sputtering. Within CVD methods, Metal Organic Chemical Vapor Deposition (MOCVD), because it combines chemical reactions at the gas phase, has a prominent place. In what concerns CSD

methodology sol gel and hydrothermal are some of the most versatile methods to fabricate ferroelectric nano structures at low costs and low temperature.

PLD involves ablating a target material with a high energy focused laser beam to produce a highly forward directed plasma plume (normal to the target surface) that subsequently condenses and deposits onto the substrate. The PLD method is of interest due to its relative simplicity when compared to other PVD techniques, its relative good capacity to transfer stoichiometric amounts of the target material to the substrate, and its ability to control the stoichiometry of the growing thin film with the aid of a background gas atmosphere. Usually an excimer or Nd-YAG laser, producing an intense pulsed (repetition rate 0-100 Hz) laser beam in the UV range, is used. Typical wavelengths are 193 nm for ArF, 248 nm for KrF and 308 nm for XeCl excimer lasers and 355 nm for Nd:YAG. For every material there exists a set of optimal deposition parameters that requires some systematic previous work. The main advantage of PLD is related to the possibility of getting conformal covering and very small dimension structures (>10 nm). The main disadvantage includes the difficulties in getting uniform size, arrays and shapes [301].

Sputtering is also a PVD technique. It works on two modes, named as DC mode used to deposit metallic films mainly and Radio Frequency (RF) mode use for depositing oxide films. The working principle of sputtering is based on the bombardment of a target (cathode) with high energy positively charged ions. In the sputtering chamber the inert gas is introduced at a pressure of 1 to 10 mTorr. A DC voltage is applied between the target (cathode) and the substrate (anode), which ionizes the inert gas and results in the formation of a plasma. The charged ions of the inert gas accelerate towards the target and the forced collisions of the ions with the target results in the ejection of atoms from the target into the space. These ejected atoms move towards the substrate (anode) where they condense to form a film. During the ionization of the inert gas the electrons are released and accelerate towards anode substrate. During electron journey to anode, it collides with the inert gas and create more ions and electrons in the process, so that cycle of sputtering continues. Inert gases, as Ar and Xe, are used to form a plasma and prefer for the fabrication of metallic films [194].

For the deposition of oxide films RF sputtering is preferable because it can be operated in low gas pressure (< 1mTorr) at RF of 13.65 MHz, nevertheless the RF sputtering can be operated from 0.5 -30 MHz. In the RF sputtering a permanent magnet is fixed behind the target to accelerate the ionization process. With the application of magnetic field parallel to the target surface, the secondary electrons drift in circular path very near to the target surface. The advantage of RF sputtering is the plasma confined near to the target without causing any damage to the film (on anode). As particles are drifting in circular motion it increases the traveling distance and the probability of ionization of the inert gas molecules. This process tends to generate large amount of ions, therefore, increasing the efficiency of the sputtering process. Although sputtering techniques are very good for growth of 2D films, there are limitations especially in what concerns the control of the microstructure, crystal structure and stoichiometry for complex multicomponent systems. Moreover, it is implies the use of expensive equipment. For the synthesis of oxides, reactive gases such as nitrogen and/or oxygen mixed with argon are used. It is also possible to deposit multicomponent systems, but it requires system and target modifications [302]. In the present work RF magnetron sputtering is used to deposit BFO film on the surface of aligned CNTs. The important parts of the sputtering unit used in the work are marked in Figure 2-28.

MOCVD is a chemical vapor deposition process used to fabricate thin films and coatings, especially for manufacturing III-V compound semiconductors and mainly based on nitrates. MOCVD working principle is simple. Pure gases of the desired processed material along with carrier gases are introduced into the CVD chamber by pumping. The atoms of desired oxides are deposited on the substrate by decomposing organic molecules while they are passing over the hot substrate. The deposited atoms undergoes crystallization process to form thin oxide film on the surface of substrate. MOCVD is used for manufacturing light-emitting diodes (LEDs), lasers, transistors, solar cells and other electronic devices, and is one of the key enabling technologies for future markets with high growth potential [298]. The advantages of MOCVD process include a high output and versatility to generate a wide range of sizes up to very small sizes <10 nm, whereas the disadvantages encompass difficulties to have uniform coverings and the use of toxicprecursors.
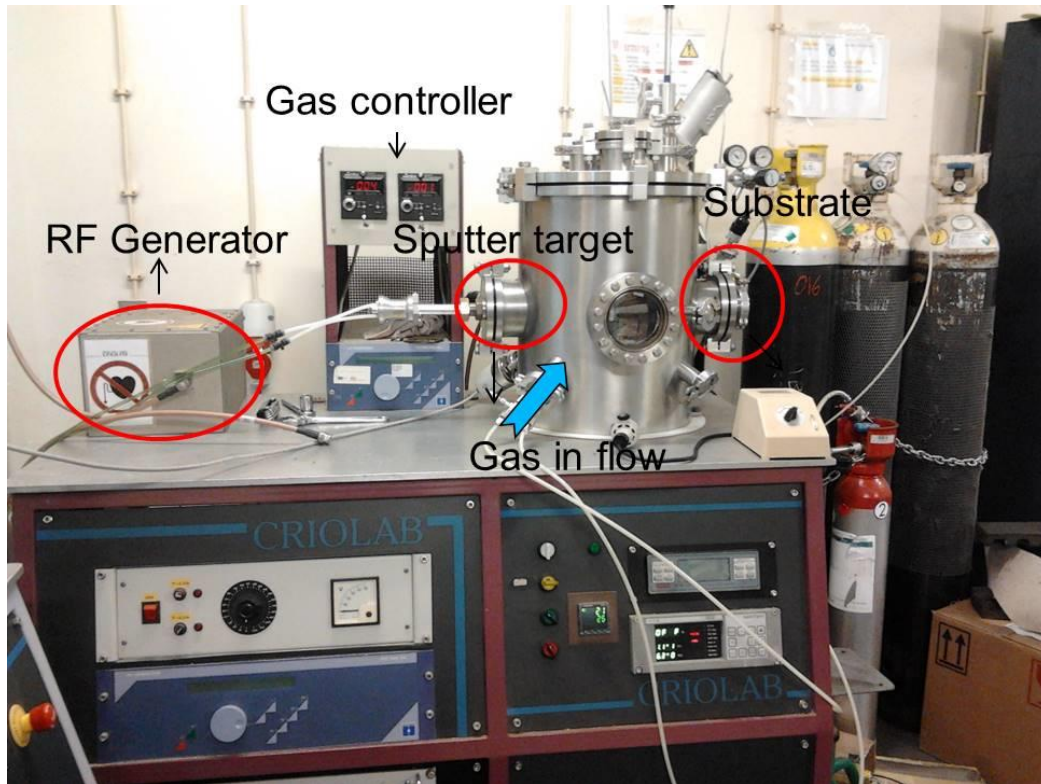
Figure 2-28 RF Sputtering unit from CRIOLAB, the important parts are marked with circles.

Sol gel processing is known as wet chemical method, through which nano sized particles and/or thin films of simple and complex compounds can be obtained at the molecular level (Figure 2-29). The term sol refers to a colloidal suspension of solid particles of nano metric size, where gravitation forces are negligible and interactions are dominated by short range forces, like Van Der Walls [303]. The term gel is used to define a porous three dimensional network of clusters or particles that result from the hydrolysis and condensation of the sol.

The steps involved in the formation of inorganic networks from a solution are dependent on the structure of the sol. Metal alkhoxides ($M(OR)_z$, (where R is an alkyl group C_xH_{2x+1}, and Z is the oxidation state of the metal) and metal salts are the most commonly used starting reagents for sol-gel processing of oxides. Many chemical

parameters affect the reaction process such as pH, temperature. type of solvent, concentration of the metal in solution, acid and base catalysis, order of addition of reagents, among others [304].

Hydrolysis and poly condensation are the two steps towards the formation of the gel. This reaction can be described by a S_N2 mechanism (bimolecular nucleophilic substitution) [305].

$$\begin{array}{c} H \\ \diagdown \\ \quad\ O^{\delta-} + M^{\delta+} \text{-}O^{\delta-} R \Rightarrow \end{array} \begin{array}{c} H^{\delta+} \\ \diagdown \\ \quad\ O\text{-}M\text{-}O^{\delta-} R \Rightarrow HO\text{-}M\text{-}O \\ H \diagup \end{array} \begin{array}{c} H^{\delta+} \\ \diagdown \\ \quad\ \Rightarrow HO\text{-}M\ + ROH \\ R \end{array}$$
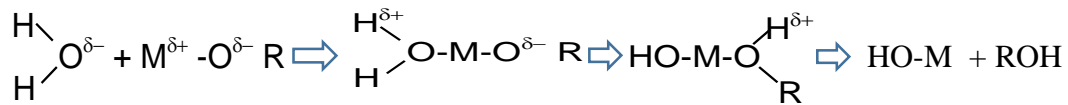
The reaction occurs with the nucleophilic addition of a negatively charged $HO^{\delta-}$ group on to positively charged metal $M^{\delta+}$, leading to an increase of the coordination number of the metal atom in the transition state. The positively charged proton then transferred towards an alkoxy group and the positively charged protonated ROH ligand is finally removed.

The simple way of describing the whole reaction of hydrolysis and condensation is given below:

$$M(OR)_x + H_2O \Leftrightarrow (RO)_{x-1}M\text{-}OH + ROH \qquad \text{Equation 2-12}$$

$$(RO)_{x-1}M\text{-}OH + (RO)_xM \Leftrightarrow (RO)_{x-1}M\text{-}O\text{-}M(OR)_{x-1} + \qquad \text{Equation 2-13}$$
$$ROH$$

$$RO)_{x-1}M\text{-}OH + HO\text{-}M(RO)_{x-1} \Leftrightarrow (RO)_{x-1}M\text{-}O\text{-}M(OR)_{x-1} \qquad \text{Equation 2-14}$$
$$+ HOH$$
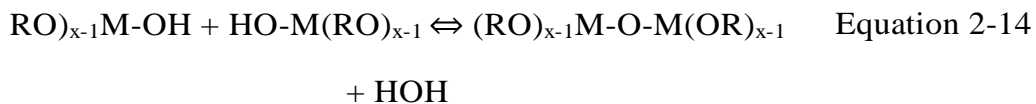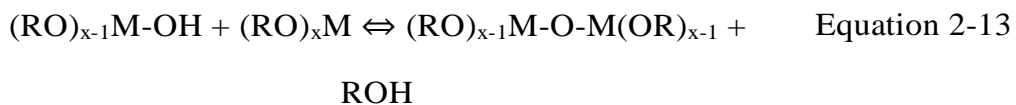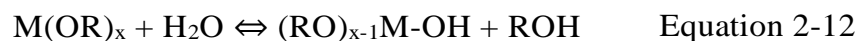
In reaction Equation 2-12, hydrolysis of the metal alkoxide bond (M-OR) results in the formation of a metal hydroxyl bond (M-OH). In the second step (Equation 2-13), the condensation between the hydroxyl and an alkoxide ligand or between two hydroxyl ligands (Equation 2-14) results in the formation of a metal-oxygen-metal (M-O-M)

bridge, which constitutes the backbone of any oxide structure. Continuous condensation leads to increase in metal-oxygen-metal crosslinks, eventually results in gelation or precipitation.

The final structure contains an inorganic network of oxygen bridged metal, hydroxyl and alkoxy groups [303, 306]. The network branching, molecular size and number of alkoxide groups depends on the reaction kinetics. In order to have small molecules and precipitates it is advised to have a fast hydrolysis step.

One of the claimed advantages of sol gel method is the possibility to synthesised nano powders and thin films at relatively low temperatures compared to solid state method. Some of the disadvantages of the sol-gel process include: relative high cost and toxicity of precursors and solvents and crack formation in the case of thin films, resulting from the decomposition of the organics prior to the oxide formation.
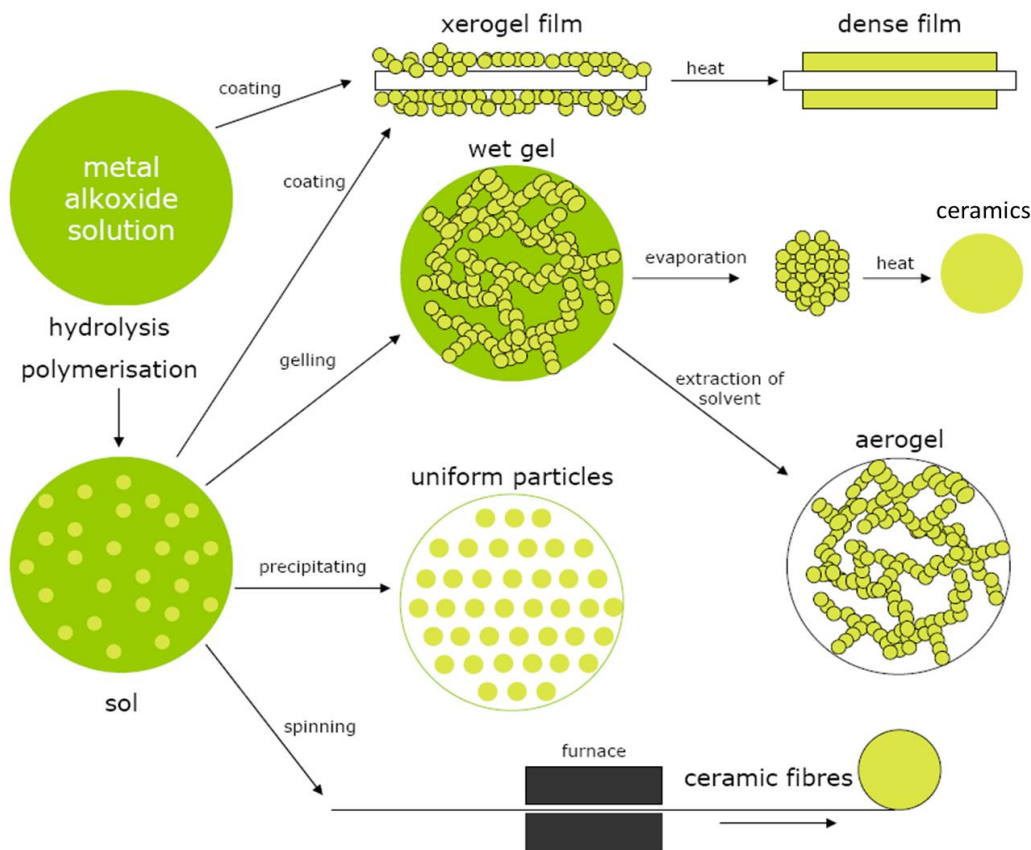
Figure 2-29 Sol-gel process to obatin different nano structure materials such as films, fibers, glass, ceramics xerogel and aerogel [307].

Hydrothermal is a process by which fine organic or inorganic materials are obtained using single or heterogeneous phase reaction in aqueous media above room temperature (T > 25 $^{\circ}$C) and above atmosphere pressure. Synthesis is usually conducted above the boiling temperature of the solvent, which results in the generation of an autogeneous pressure which is the saturated vapor pressure of the solution. This condition provides optimum conditions to increase solubility and reactivity of the precursors used in the material synthesis. If water is used as the solvent the process is known as hydrothermal and when nonaqueous solvent is used it is known as solvothermal [308]. Upper limit of hydrothermal temperature and pressure used commercially are 1000 $^{\circ}$C and 500 MPa respectively [299].

Figure 2-30 demonstrates the effect of filling factor (of teflon jar used for hydrothermal process) on the autogeneous pressure and temperature for water based process. The doted curve represents the line where the liquid and gaseous phase coexists. Below this dotted line the liquid water is not present and the vapor phase is not saturated. The compressed liquid phase is presented above the dotted line. The solid line represents the pressure inside the vessel due to different filling factors. For example when the filling factor is 70 % the vessel is completely filled with liquid water at a temperature of ~ 300 $^{\circ}$C, with the increase in temperature the pressure inside the vessel also increases and follows the 70 % line [309].

The properties of the water changed with the addition of mineralizers. This mineralizers are used to improve the solubility limits of different precursors, diffusion and reaction rate. The precursors used in hydrothermal synthesis also influence the composition of the liquid and gas phase equilibrium in the autoclave.

The hydrothermal synthesis is an economical and environmentally friendly method to synthesised organic and inorganic materials with different shapes and sizes.
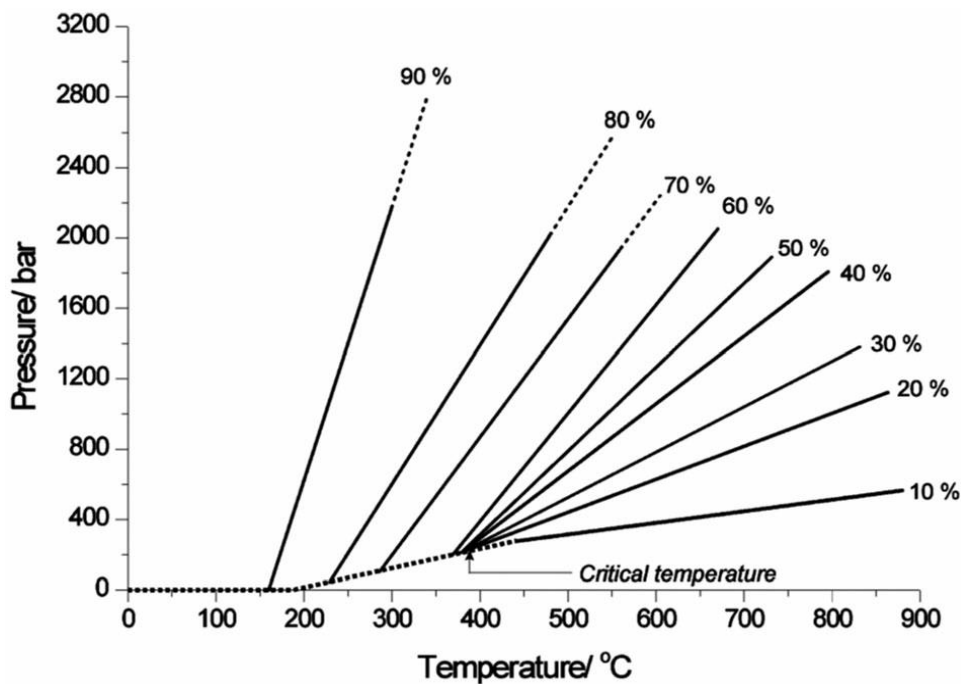
Figure 2-30 Pressure – temperature dependence for different degrees of filling of the autoclave with water during hydrothermal process [309].

The nucleation and growth mechanisms of formation of oxides in hydrothermal synthesis can be dissolution-precipitation [310] or phase boundary chemical reaction [311]. Dissolution-precipitation mechanisms involve the transportation of the solute through the suspension, surface adsorption and dehydration of the solute species, surface diffusion between precursors and finally crystallite formation and growth (Figure 2-31 (a)). In dissolution-precipitation the solubility of the precursors is important and in some cases it might not be sufficient for the reaction process to occur. Therefore different precursors with different reactivity should be used; for example in the hydrothermal synthesis of $BaTiO_3$, anatase has a higher reactivity than rutile. Not only precursors but also pH is major factor, therefore different mineralizers needs to be added to increase the solubility of the precursors. The choice of the optimal mineralizer should consider the chemistry of the oxide and precursor species needed to be dissolved. Strong bases (NaOH or KOH) have a high solubility under the hydrothermal synthesis conditions, therefore frequently used [312].

The phase boundary controlled mechanism occurs for the amorphous gels, exhibits a porous network structure, which is believed to be infiltrated by the aqueous solute and solvent under hydrothermal conditions Figure 2-31 (b); because of that the diffusion process is very rapid for the phase boundary mechanism in comparison to the dissolution- precipitation one. The nucleation of small particles occurs with the addition of basic solution followed by the growth at hydrothermal conditions.

Different crystallite size and shapes can be obtain by controlling the various parameters, such as concentration of precursor in the solution, pH of the solution, temperature and type of precursors. In order to obtained 1D nano structured materials with anisotropic crystal structures, the appropriate organic additives or surfactants to aid directed growth or 1D templates [313] are usually used.
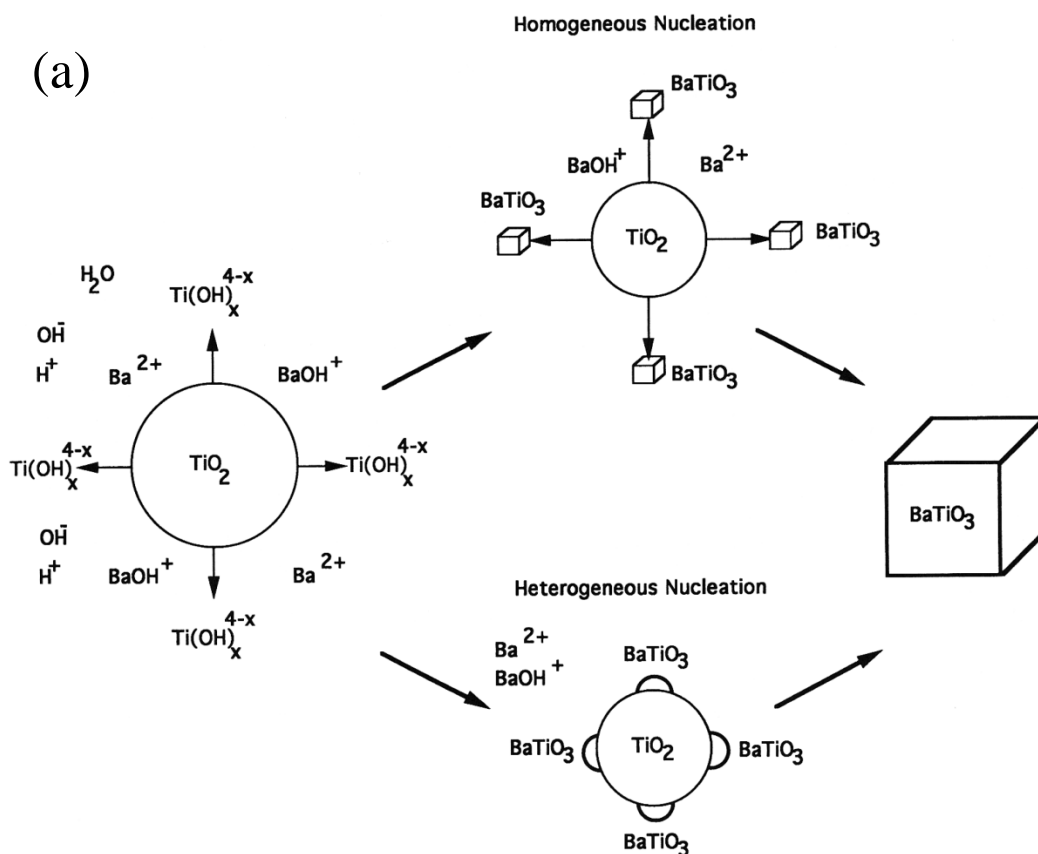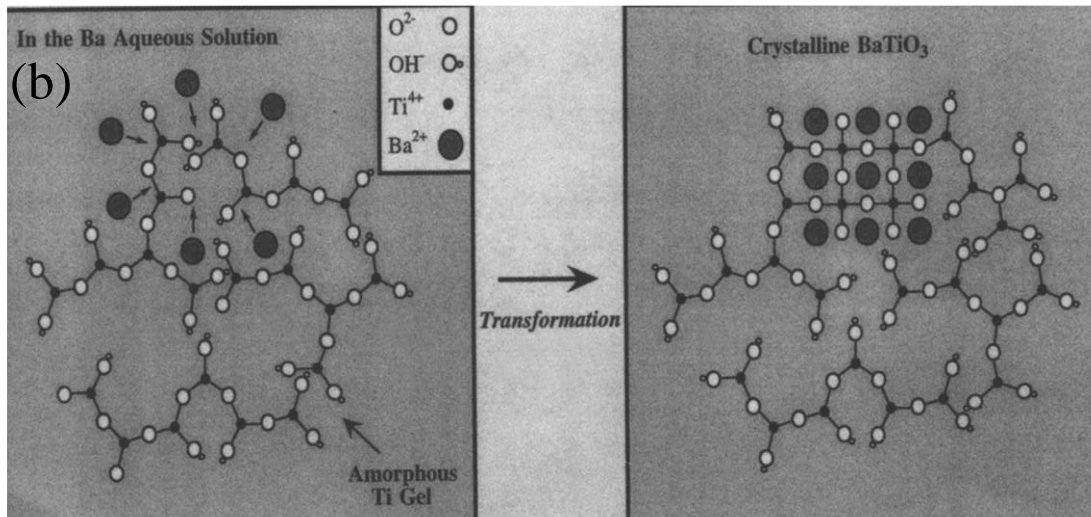
Figure 2-31 Schematic of (a) dissolution-precipitation and (b) phase boundary control reactions [310, 311].

Hydrothermal synthesis is performed in stainless steel autoclaves as illustrated in Figure 2-32. The used precursors can be oxides, nitrates, hydroxides or other salts of the desire material. The precursors, additives and mineralizers are added together with the solvent in the teflon jar, before putting it into the stainless steel autoclave. The filling factor of the teflon is always lower than 80%. Moderate temperatures in between 80 to 300 °C are used for the synthesis, which are lower than supercritical conditions. The heating time varies from system to system and can differ from 0.5 to 72 h. The hydrothermal synthesis is carried in teflon jars to avoid contaminations [309]. The fabricated powder is washed with water and in some cases with alcohols to remove the ions deposited on the surface of the product. The advantages of hydrothermal methods over other methods are: use of low working temperature, the materials which have high vapor pressure near the melting point can be grown by hydrothermal method and different shapes of the same material can be obtained.
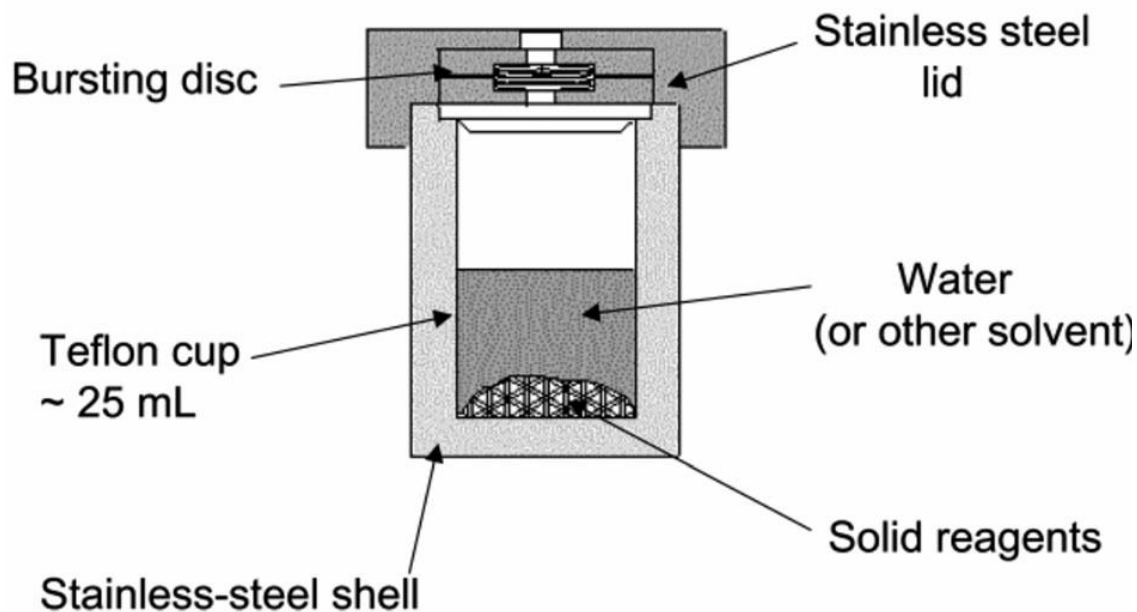
Figure 2-32 Schematic of a teflon lined stainless steel autoclave, used for hydrothermal synthesis [309].

There are various different mechanisms and strategies by which 1D ferroelectrics can be fabricated by CSD and can be classified as template assisted synthesis and template free synthesis.

In template assisted synthesis, 1D negative templates made of porous alumina (AAO, anodic aluminium oxide) and positive templates such as nanotubes, nanorods or nanowires are used to fabricate 1D nano structures. Sol-gel solution of the desired compound is introduced into the pores or channels by capillary forces and/or use of vacuum pumps. This is followed by an heat treatment to obtained crystalline tubes similar to the geometry of the formation channels [314]. The template of AAO is removed by basic solution such as NaOH, in some cases removed by heating the template at elevated temperature Figure 2-33 (a)).

Positive templates has been used to fabricate 1D nano structures, the nano wires and nanotubes of ferroelectrics. Mohammadi *et al.* [26] used MWCNTs as a positive sacrificial templates to fabricate $Pb(Zr_{0.52}Ti_{0.48})O_3$ nanotubes. MWCNTs covered with $Pb(Zr_{0.52}Ti_{0.48})O_3$ solution was heat treated at elevated temperature to obtained $Pb(Zr_{0.52}Ti_{0.48})O_3$ 1D nanotubes with diameter of 80 to 100 nm. CNTs can be used as non-

sacrificial positive template to fabricate FE-CNTs structures, where CNTs will be used as bottom electrodes for microelectronic devices. The use of CNTs for non-sacrificial template was described above in the work of Kumar *et al.* [29].

Electrospinning is also a template assisted synthesis in which the shape of the final nanofibre is confined by the shape and size of the nozzle. A viscous polymeric solution of the desired material is uniaxial stretched under an electrified jet to get thin fibres (Figure 2-33 (b)) [315]. Hollow fibres can also be produced using co-electrospinning method [316]. Alkoy *et al.* [317] used sol-gel based PZT solution and polyvinyl pyyrolidone polymer to fabricate PZT nanofibres heating at 700 ºC. PZT fibres having diameters ~230 nm were obtained from this process.

(a)   (b)
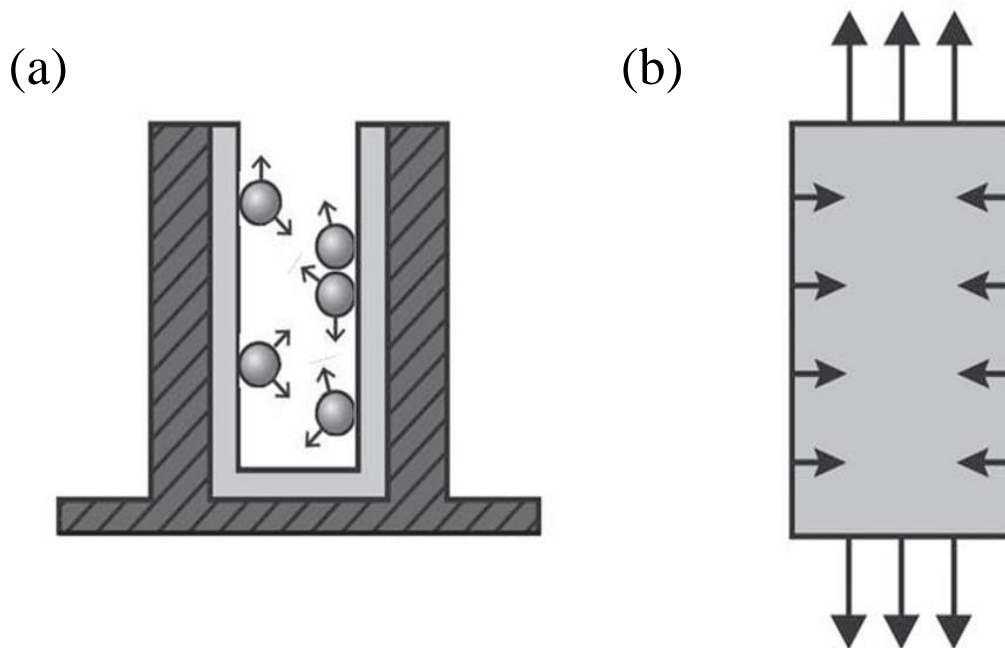
Figure 2-33 (a) Template growth using AAO templates and (b) uniaxial stretching during the electro spinning process for the fabrication of 1D ferroelectrics(adapted from [318]).

In template free method the 1D structures are formed due to kinetically favouring or controlling of crystallographic facets. Template free synthesis methods are better in many aspects when compared with template methods, especially because no post treatments are required. The most common mechanisms of template free growth are: 1)

crystallographic orientation preferences and 2) growth of preferential crystal facets by the use of appropriate capping reagents.

In case of materials with anisotropic crystal lattice. There is an energy differences between the crystal faces, faces with high surface energies show the fastest growth rate in contrast to others, resulting in 1D structures Figure 2-34 (a)). Orientated attachment for piezoelectric ZnO was reported by Pacholski *et al.*[319]. 1D ZnO structures were formed by the attachment of the quasi-particles with perfectly allied lattice planes along c direction. The attachment between the particles occurred by the conventional mechanism of dissolution and growth. The other mechanism for the growth of 1D is adsorption of capping reagents on preferential surfaces of the crystal. These capping agents stabilized that surface triggering the differences in the growth rate between capping and non-capping sites resulting in the formation of 1D structures Figure 2-34 (b)). Yang *et al.*[320] fabricated nanowires of $BaTiO_3$ by hydrothermal method using polyethylene glycol (PEG) as a surfactant. PEG molecules have specific surface adsorption on to the selective crystallographic planes of the oxide crystals. This limits the growth of the crystal to specific orientation resulting in the formation of 1D BT nanowires under hydrothermal conditions.
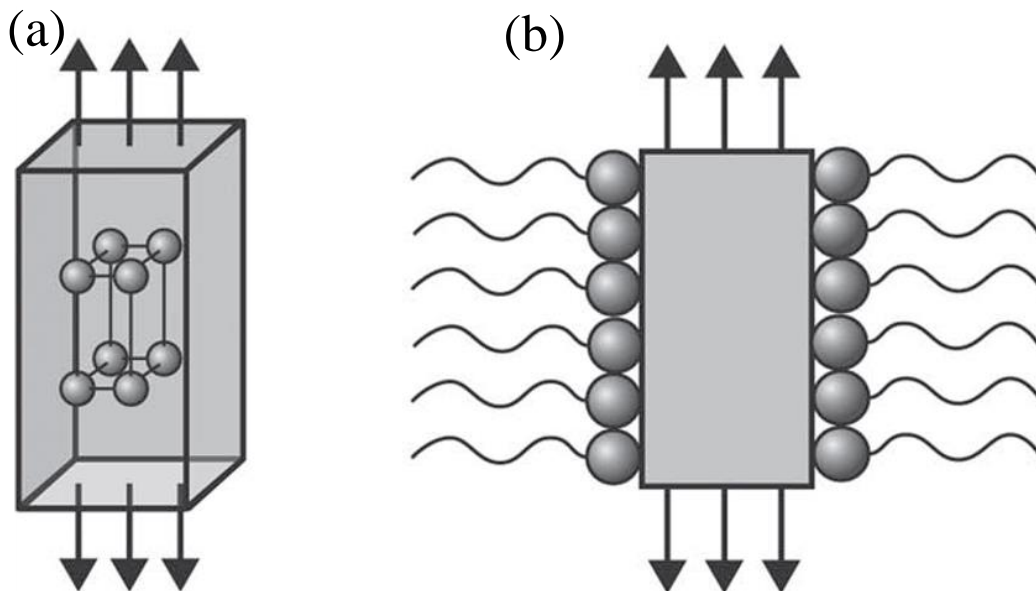
Figure 2-34 Growth of 1D nano ferroelectric structures due to (a) use of anisotropic crystallographic structure of a solid and (b) use of surfactant [318].

2.7   Conclusions

This chapter detailed important aspects related with the proposed work on the fabrication of CNTs-FE nano structures. It is evident from the literature that CNTs is the optimum material for microelectronics due to its extraordinary physical, chemical properties and unique geometry. With the evolution of electronic world there is urgent need to have high data storage devices which can be also achieve if FeRAM are redesign from capacitor planar structure to 3D one, as suggested by ITRS 2011. One way to achieve this 3D design FE capacitors is to combine CNTs with FE. However, this is not a trivial task as mentioned above and, currently there are no systematic studies on the fabrication and characterization of CNTs-FE structures, and in particular exploiting the use of low cost and low temperature synthesis methods.

This is the ground where this work is set, aiming to explore the potential of using low cost, low temperature process to construct MWCNTs-FE nano structures and to check their ferroelectric behaviour towards potential applications, namely as FeRAMs.

Chapter 3

3   *Experimental details*

Abstract

This chapter describes the experimental strategy followed to fulfil the defined objectives of this thesis. The materials under study include MWCNTs and as ferroelectrics, Lead Zirconate Titanate ($Pb_{1-x}Zr_xTiO_3$, (PZT)) and Barium Titanate ($BaTiO_3$) and as a multiferroic Bismuth Ferrite ($BiFeO_3$). The synthesis techniques used comprise low temperature chemical solution methods as sol gel and hydrothermal and physical deposition, as RF sputtering. The different fabricated MWCNTs-FE structures were characterized by a variety of techniques that include, X-Ray diffraction, thermal analysis (DTA/TG), Infra-Red spectroscopy, Raman spectroscopy, Scanning Electron Microscopy (SEM), Transmission Electron Microscopy (TEM), High Resolution (HR) TEM, Atomic Force Microscopy (AFM) and Piezo Force Microscope (PFM). As received MWCNTs are impure, and for the purpose of this work MWCNTs were purified and functionalised. For each MWCNTs-FE system the particularities of the experimental procedure are described in detail later in the corresponding chapters.

3.1   Introduction

The experimental work carried out during this work is illustrated in Figure 3-1. In this work two ferroelectric compounds (PZT and $BaTiO_3$, BT) and one multiferroic ($BiFeO_3$, BFO) were used to cover MWCNTs. In the first phase of the work and since ferroelectrics usually require high crystallization temperature the thermal resistance of MWCNTs was studied as a function of temperature, heating rate and atmosphere. In the next phase, MWCNTs were purified and functionalised. For that two different functionalization processes were used: covalent bonding and non-covalent bonding functionalization. Using these functionalised MWCNTs the combination between PZT, BT and BFO, as ferroics with MWCNTs was conducted using sol gel and hydrothermal methods to obtain 1D ferroelectric structures. In the last phase of the work, BFO was deposited on the Vertical Aligned (VA) MWCNTs using sputtering to investigate the potential use of VA-MWCNTs as conducting bottom electrodes. The physical properties of the nano structures were characterized by various techniques such as DTA/TG, XRD, Raman, FTIR, SEM and HRTEM. The electrical response for MWCNTs-FE were investigated by PFM.
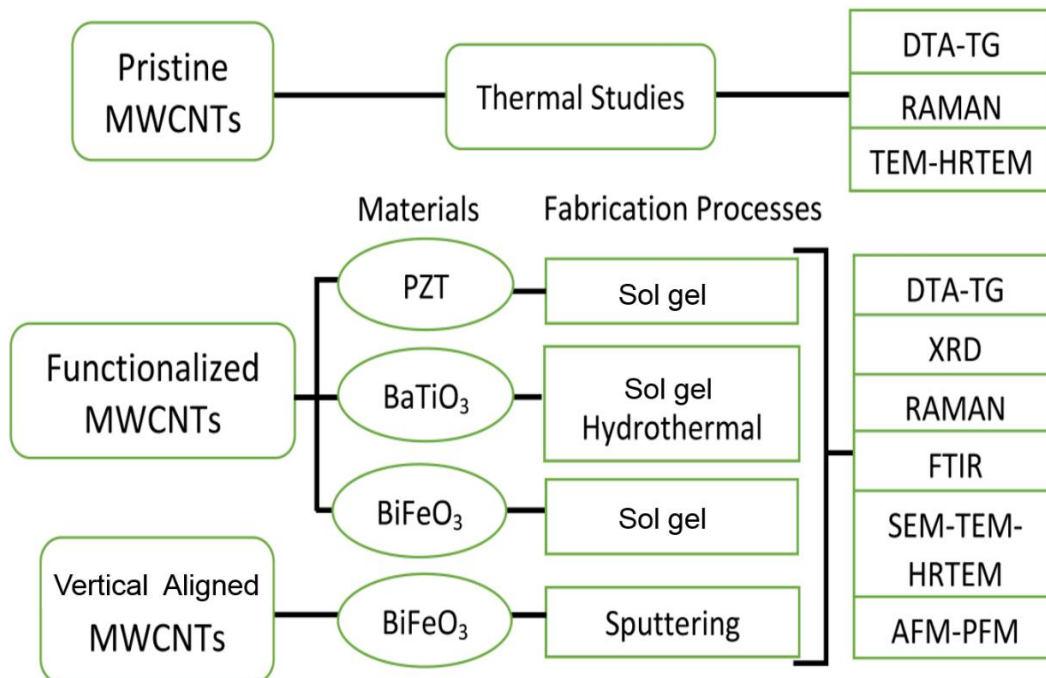
Figure 3-1 Flow chart of the experimental strategy followed during this work.

3.2 Multiwall carbon nanotubes used in the present work

3.2.1 As-received MWCNTs

MWCNTs used in this work were synthesised at the University of Scientirarum Szegediensis (University of Szeged) in Hungry, by Chemical Vapor Deposition Technique (CVD). Briefly, alumina supports impregnated with Co-and Fe-acetate (catalyst) were used as substrates to grow MWCNTs. The substrates are placed on quartz boats in the reaction chamber. In the first step, furnace and catalysts are degassed at 750 ℃ in flowing nitrogen. After 30 min, the gas stream is changed for a mixture of acetylene-nitrogen and the catalytic chemical vapor deposition takes place for 1 h. At this stage the CNTs grown on the catalyst particles with amorphous carbon. After the reaction, the system is cooled under nitrogen flow. As prepared MWCNTs are removed from the alumina support by boiling in concentrated sodium hydroxide (NaOH) solution [321]. The thermal studies were performed on the as-received MWCNTs.

Vertical aligned (VA)-MWCNTs grown on Si substrates with diameter and length of 5-20 nm and 1-2 mm, respectively, were also used to fabricate MWCNTs-FE structures. VA-MWCNTs were purchased from CVD Materials Corporation, USA. They were used to exploit the potential of CNTs as bottom electrode in order to replace the expensive metal electrode such as platinum.

3.2.2 Purification and functionalization of MWCNTs

As received MWCNTs contain impurities such as amorphous carbon, metal particles and so on, that compromise the final properties of the MWCNTs. To remove the impurities and to functionalize the tubes for improved wettability they were thermally and chemically treated. MWCNTs were functionalised both covalently and non-covalently, as described below.

The steps followed for the purification of as-received MWCNTs are illustrated in Figure 3-2. As-received MWCNTs were cleaned by thermal heating at 350 °C for 1 h to remove the amorphous carbon and other chemical groups attached on the surface of the tubes. This was followed by a chemical refluxing step in 6 M of hydrochloric acid (HCl)

for 6 h at 125 °C; this resulted in the removal of metallic catalysts. The refluxed MWCNTs were washed with deionized water using ultrasonic bath and repeated filtration until pH come close to neutral. Vacuum filtration was performed using PVDF membrane filter (Membrane Solution) having diameter ~ 47 mm and pore size 0.22 μm. At the end of this step purified MWNTs were dried at ~100 ˚C overnight in the oven. This purification process removed almost all the carbonaceous (amorphous carbon) along with metal catalyst particles. After this step MWCNTs are designated as purified MWCNTs.

The purified MWCNTs were acid treatment with 5 M of nitric acid (HNO_3) and a mixture of 5 M and 10 M of HNO_3 and sulphuric acid (H_2SO_4) for different periods of time. The nitric acid results in the functionalization of the tubes by induction of hydroxyl and carboxyl ion groups on the defect sites, whereas H_2SO_4 cuts the tubes into small segments. In the present work, MWCNTs tubes functionalized with 5 M HNO_3 where used for the fabrication of MWCNTs-FE structures. It was verified that functionalization with mixtures of 5 M and 10 M of HNO_3 and H_2SO_4 induced severe damages to MWCNTs and because of that tubes treated with this process were not further used in this work.

Non covalent functionalization was carried out on purified MWCNTs using Sodium Dodecyl Sulfate (SDS, Sigma, ≥ 98.5%). The MWNTs (~300 mg) were dispersed in SDS aqueous solution (1:10 volume ratio) using ultra-bath sonicator for 2- 5 h. This solution was further magnetically stirred overnight so that as much as complete reaction between SDS and MWCNTs occurs. The SDS functionalized MWCNTs were filtered and dried in oven for 24 h at 80 °C. SDS functionalized MWCNTs are referred as SDSMWCNTs. The non-covalent functionalization is more conformal and has less damage to the structure of MWCNTs. Figure 3-2 illustrate the steps followed for the functionalization of MWCNTs both covalently and non-covalently.
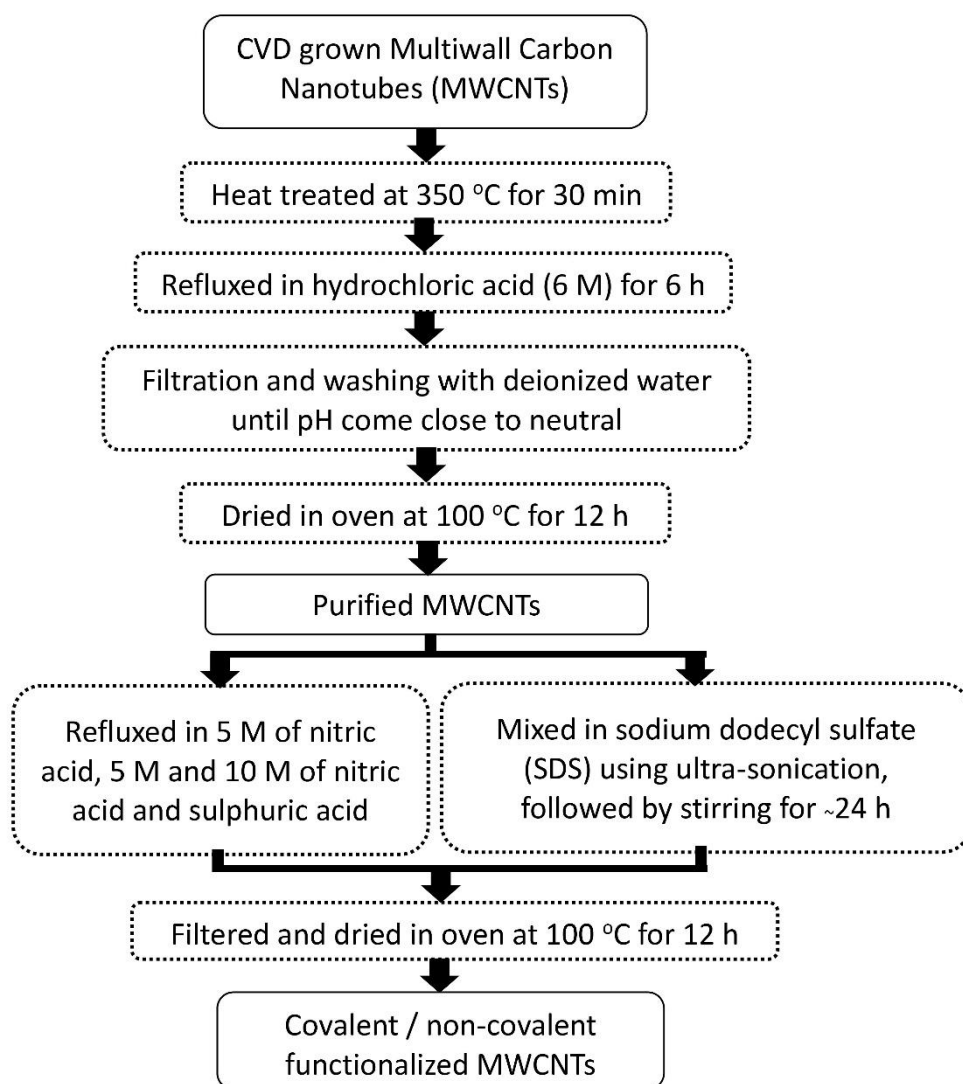
Figure 3-2 Flow Chart illustrating the steps followed for the purification and functionalization of MWCNTs.

3.3   Characterization techniques

3.3.1   Contact angle

In this work the wettability of the MWCNTs is an important aspect, since one aims at the complete coverage of the tubes by the ferroelectric oxide. To measure the

wettability of surfaces there are different methods (quantitative and qualitative) and among the quantitative ones, contact angle method is one of the best when pure fluids are used.

The contact angle was defined for the first time by Thomas Young *et al.* [322], the angle formed between the liquid drop contact with the solid surface where the mechanical equilibrium of the drop under the action of three interfacial tensions, namely liquid vapor (γ_{lv}), solid-vapor (γ_{sv}) and solid-liquid (γ_{sl}) given in Equation 3-1. The Young equation for the contact angle (θ) is given below.

$$\gamma_{lv}cos\theta = \gamma_{sv} - \gamma_{sl} \qquad \text{Equation 3-1}$$

The facile way to measure contact angle is a direct measurement of the tangent angle at the three phase contact point on a sessile drop profile also known as sessile method. The set-up used for measuring contact angle by sessile method is referred as telescope-goniometer. It consists of a horizontal stage to mount the sample of interest and a micro meter pipette or motor driven syringe is attached on the overhead of horizontal stage (as in the present work). A digital camera and illumination source are placed in both sides of the horizontal stage so that camera, horizontal stage and illumination source are horizontally aligned. The water/liquid drop of desired volume is transfer to the surface of interest and image is acquired after the drop come in stable configuration. The contact angle is measured between the solid-liquid interfacial tensions and liquid-vapor interfacial tensions as shown in Figure 3-3. If the contact angle is >90° the surface has poor wetting, if it is equal to 90° then incomplete wetting and good wetting is obtained when θ is <90°. The direct measurement of sessile drop contact angles with a telescope-goniometer can yield an accuracy of approximately ±2° [323].

The contact angle was measured on purified and functionalized MWCNTs using sessile drop method (Dataphysics, OCA 25). A drop of water (~3 μl) is delivered on the surface of MWCNTs films. The water droplet on MWCNTs is allowed to come in stable configuration before taking the images to measure contact angle using software (SCA 20) provide with the equipment.
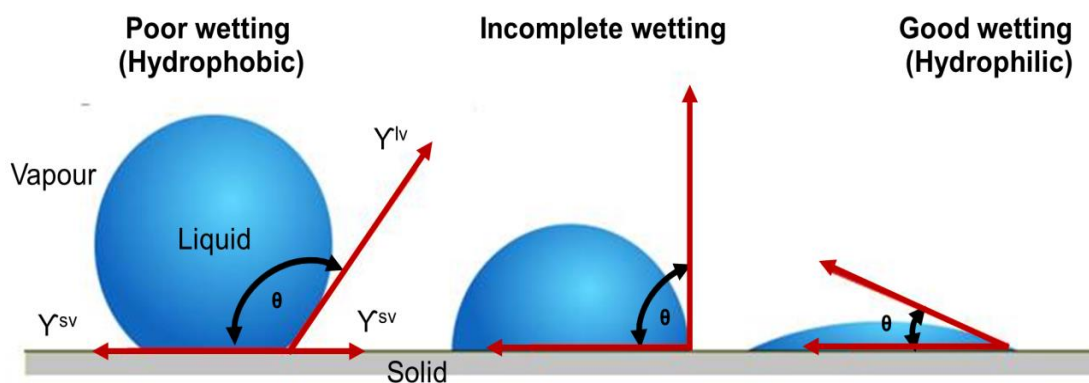
Figure 3-3 Contact angle (θ) formed by sessile liquid drops shows the wettability of the substrate on (left) θ > 90º poor wetting, (in middle) θ = 90º incomplete wetting (right) θ < 90º good wetting (adapted from [323]).

3.3.2   Differential Thermal Analysis (DTA) – Thermo gravimetric (TG)

DTA and TG analysis are one of the most basic and powerful tools to evaluate the behaviour of a material as a function of temperature. From the DTA and TG plots, various information can be extracted, among them: thermal stability, chemical and physical reactions (exothermic or endothermic), phase formation and transition, glass transition temperature, melting temperature, among others.

The working principle of DTA is based on the heat loss or gain due to the structural changes in material as a function of temperature or time. DTA equipment uses two set of identical columns, one for the reference (generally, empty alumina crucible) and other for the sample. Both the columns undergoes similar thermal cycle, while recording any temperature difference between reference and sample by thermocouples equipped with in the chamber. This temperature changes occurs due to the endothermic or exothermic reactions taking place in the sample. A DTA curve provides vital information on the phase formation especially in case of ferroelectric oxide synthesis by chemical methods. This information can be used to synthesise material with the desire phase or can be used to predict the reaction evolution for the formation of oxide.

The working principle of TG is based on the weight change occurred as function of temperature or at isothermal conditions. The weight loss that occurs in amorphous gels prepared by solution are mainly due to the evaporation of water, solvents, releasing of carbon dioxide and, in some cases, phase formation. In the particular case of carbon nanotubes, the weight change in ambient atmosphere is typically a superposition of the weight loss due to oxidation of carbon into gaseous carbon dioxide and the weight gain due to oxidation of residual metal catalyst into solid oxides. TG and DTA data can be obtained simultaneous in the same equipment, under various atmospheres and various heating rates.

For oxidation studies of MWCNTs and phase formation of ferroic oxides, DTA/ TG was performed in a SETARAM, Labsys, TG-DTA12. The samples were heated in aluminum crucibles from temperature ranging from 80 ºC to 900 ºC in air at different heating rates (2, 5, 10, 20 and 40 ºC/min). Base line was measured for all the experiments for each heating rate and deducted from the calculated data for each analysis.

3.3.3 X-Ray Diffraction (XRD)

The physical properties of all the solids are dependent on the crystal structure as is the case of FE. Therefore it is important to know the crystallographic structure of oxides under study and how the crystallographic structure is affected by the preparation conditions, and presence of foreign elements such as CNTs (present work scenario). X-ray diffraction is one of the most important and used characterization tool to study the crystalline structure of materials.

The working principle of XRD is based on the diffraction of X-ray from Bragg plane. When a beam of X-ray interacts with the atom and electrons in the crystal, they will oscillate under the X-ray impact and emit a large number of electromagnetic waves in particular directions. The direction of the emissions will be in phase in certain directions, which depends on the incident X-ray (Figure 3-4), on the wavelength and on the spacing between atoms in the crystals. The relation between all of these parameters is given by Bragg relation Equation 3-2:

$$n\lambda = 2d.\sin\theta \qquad\qquad \text{Equation 3-2}$$

where n is an integer and λ is the wavelength of the x-ray used, d is the inter planar spacing, and θ is the angle made by the incident ray with the crystal plan.

Diffracted rays are detected by a diffractometer; the obtained diffraction patterns are then compared with the reference standards for identification. Each solid has its unique crystallographic characteristics and X-ray powder patterns can be used as a "fingerprint" for crystal identification. Once the material has been identified, X-ray diffraction may be used to determine its crystalline or microcrystalline structure, i.e. the relative orientation of atoms in the crystal or crystallite and interatomic distances. Furthermore, it is possible to determine the size of the crystallites using Scherrer equation [324].
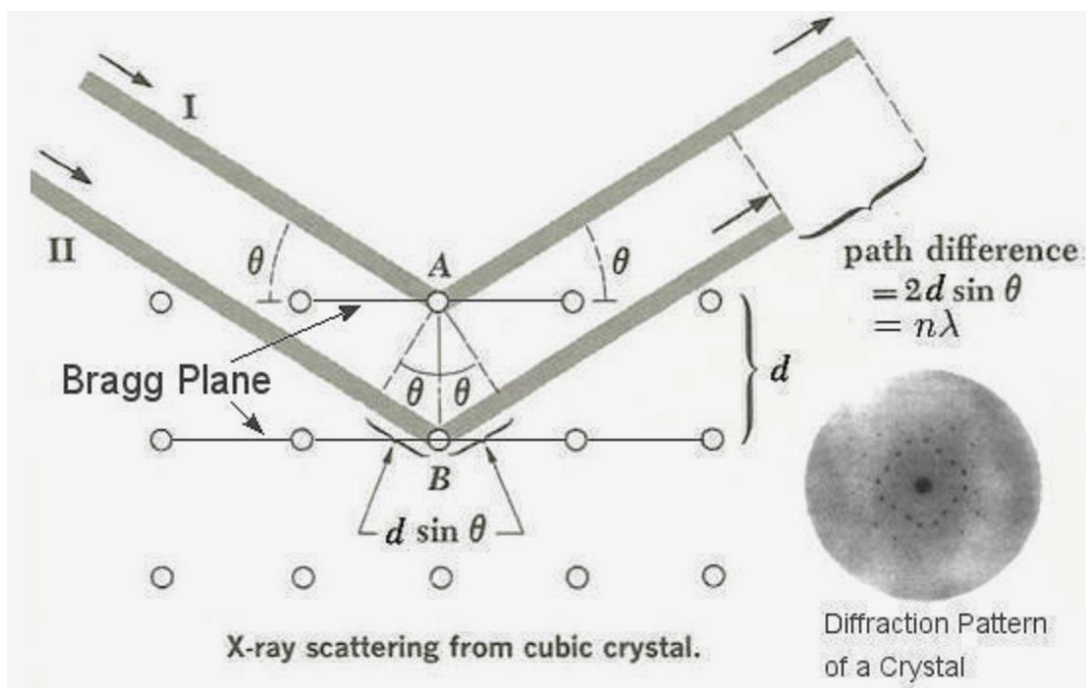
Figure 3-4 X-ray diffraction from the Bragg plane of cubic crystal with path difference equal to 2d sinθ, diffraction pattern is shown on the bottom right of the figure[325].

Two sets of XRD equipment were used in the present investigation. For the phase identification studies conducted at room temperature Rigaku diffractometer with Cu-Kα radiation filtered by Ni was used. The diffraction patterns were acquired from 10 to 80° (2θ) with a step length of 0.04 °. For the *in-situ* phase formation studies as a function of the temperature Philips X'Pert diffractometer with Cu-Kα radiation was used to analyze samples for phase formation studies with temperature. In this case the diffraction patterns were acquired from 10° to 60° (2θ) with a step length of 0.02°.In order to obtain reliable quantitative data for kinetic analysis, the scan time and the samples weight were always the same. Variable-temperature X-Ray diffraction measurements were performed using Panalytical X'pert-Pro powder diffractometer equipped with an incident beam monochromator (Cu Kα1 radiation), Pixcel position sensitive detector, and Anton Paar TTK-450 temperature stage having an operating range from -190 °C to +1300 °C.

3.3.4 Vibration spectroscopy

3.3.4.1 FTIR Spectroscopy

FTIR stands for Fourier Transform Infra-Red. As an infrared spectroscopy (IR), it gives information about chemical and bonding environment of the molecules. At room temperature the organic molecules are always in motion. The energy of the molecules are quantized rather than continuous. This means the molecules can only stretch and bend at certain allowed frequencies. When, molecules interact with the electromagnetic radiation, if the radiation frequency matches with the frequency of one of the vibrational modes, it will absorb energy (in most cases) from the radiation and jump to higher energy state. The difference between the lower vibration state and higher vibration state is equal to the energy associated with the wavelenght of the radiation that was absorbed. This results in the infrared spectrum as a function of transmission or absorption of energy. In a FTIR spectra the abscisa axis corresponds to the IR wavenumber, which are expressed in cm^{-1}. This is the number of waves in a length of one centimetre. The ordinate axis represents the percentage of transmittance or absorbance, denotes the amount of light that was absorbed at each frequency [326]. The wave number ($\bar{v}$) is expressed by the following relation given in Equation 3-3:

$$\overline{v} = \frac{1}{\lambda} = \frac{v}{c} \qquad\qquad \text{Equation 3-3}$$

where λ stands for the wavelength, c for the speed of light in vacuum (c = 2.997925 $\times$ 108 ms^{-1}) and **v** wave frequency.

There are different possible modes of vibration. The number of fundamental modes of vibration of a molecule can be predicted by the degrees of freedom of the vibrational energy which for linear and non-linear polyatomic molecules containing N atoms are 3N-5 and 3N-6, respectively [327]. The stretching vibration can be described by the movement when the bond length vary, and the bending vibration is the movement when one atom can move out of plane and so the bond angle is changed. Some bonds can stretch in-phase (symmetric stretching) or out-of-phase (asymmetric stretching). More detailed description of modes of vibration is presented in Figure 3-5.
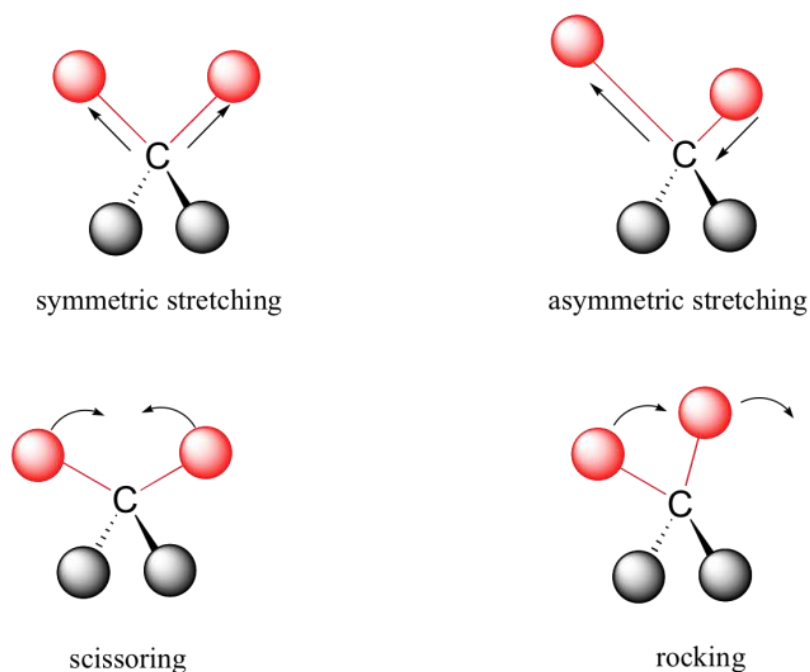
Figure 3-5 Four vibration modes for molecues [328].

In this work Fourier Transformed Infrared (FTIR) spectra in transmittance mode was acquired with a Mattson Mod 7000. FTIR spectra in the range 400-4000 cm^{-1} was obtained from the pellets. The pellets were prepared by mixing the sample with KBr (150

mg) and pressed uniaxial with the pressure range from 10-20 MPa. The spectra is typically an average of 64 scans with 4 cm^{-1} resolution.

3.3.4.2   Raman Spectroscopy

Raman spectroscopy was discovered by an Indian scientist C.V Raman for which he was awarded the Nobel Prize in physics in the year 1930. Raman spectroscopy is also known as vibrational spectroscopy, it is used to study various modes such as vibration, rotation etc. in the system by means of inelastic scattering. Laser light is used as a source for Raman spectroscopy in visible, infrared and near ultraviolet range. Laser light interacts with the phonons from the sample and results in the shift of energy. These shifts in energy give the information about the electronic environment of the molecules [329].

The working principle of Raman is based on the inelastic scattering of light when interact with molecules. When a monochromatic light from the source interacts with the molecules or bonds inside the sample it gives rise to different scattering phenomena, namely Rayleigh, Stokes Raman and Antistoke Raman scattering. During this interaction the photon excites the molecules from ground state to the virtual energy states (Figure 3-6), where it stays for some time and return to the ground state in different or same vibration levels after emitting the photon. The molecule if excited from first vibrational level returns back to the same vibrational level then it is known as Rayleigh scattering or elastic scattering (no change in frequency of photons) (Figure 3-6). If the molecule returns to different vibrational level, then the difference between the original state and the new state leads to a shift in the emitted photon's frequency, away from the excitation wavelength. When the photon frequency is shifted towards lower wavelength then it is known as Stoke scattering, otherwise it is known as Antistoke scattering. Energy of scattered phonons is discrete for every bounding and electronic environment; therefore it shows typical frequency for all Raman active molecules [330].
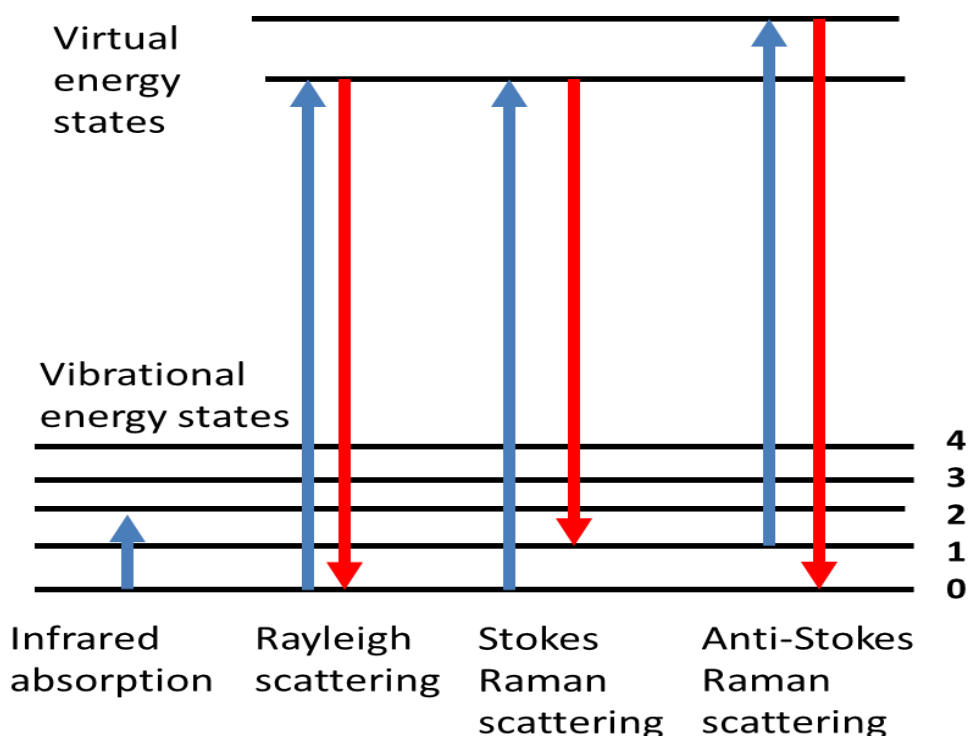
Figure 3-6 Diagrammatic representation of an energy transfer model of Rayleigh scattering, Stokes Raman and Anti-Stokes Raman scattering, adapted from [329].

Raman spectroscopy gives very valuable information, which is useful for chemical identification, characterization of molecular structures, effects of bonding, environment and stress on a sample. Due to these features, Raman spectroscopy is widely used for polymers, oxide films, ceramics, and semiconductors and for the analysis of fullerene structures.

Raman spectroscopy is most important tool for the characterization of MWCNTs. The Raman spectra of MWCNTs usually exhibit two characteristic bands, the tangential stretching G mode (1500 -1600 cm^{-1}) and the D mode (~1350cm^{-1}). The D band is a double resonance Raman mode, which can be understood as measurement of structural disorder coming from amorphous carbon and any defect. The G band originates from tangential in plane stretching vibration of the C- C bonds within the graphene sheets related with sp^2 bounding. The intensity ratio of the D and G bands is represented by R (R = I_D/I_G, calculated from Raman spectra), can be used to evaluate disorder density of

nanotube walls. The graphitized MWCNTs exhibit a lower value for R with an average of ~1.1 [331].

Raman spectra for isothermally heated MWCNTs were recorded on a Bruker RFS 100/S FT Raman spectrometer using a 1064 nm excitation of the Nd/YAG laser. The spectra were collected on powder samples in a range of wavenumber from 100 and 2000 cm^{-1}. However, for better resolution, the spectra was also acquired by HR 800, Jobin Yvon spectrometer, using the excitation lines of 532 nm for MWCNTs-FE and MWCNTs.

3.3.5 Electron microscopy

The transmission electron microscope operates on the same basic principles as light microscope but instead of light it uses electrons. The use of electrons as the light source is related with its lower wavelength which gives high resolution, thousands of times better than light microscope. TEM works under high vacuum created by different pumps such as ionic, diffusion and rotary pumps.

TEM is divided into three main parts: the first one is the electron source, the second one is the column consisting of electromagnetic lenses, sample holder and aperture and the third one is the detector where one will have the final image (fluorescent screen) (Figure 3-7). The electrons are generated by three known mechanisms, field emission, thermionic emission and schottky emission. To guide these electrons through the column the electromagnetic lenses are used that focuses the electrons into a very thin beam. The electron beam then travels through the specimen to the detector where it gives the final image [332].

There are different image modes in which the TEM can work. The most common mode is bright field and in which TEM generally starts. In this mode, contrast is formed directly by blockage and absorption of electrons in the sample. Thicker regions of the sample or regions with a higher atomic number appear dark, whereas regions with no sample in the beam path appear bright, hence the term bright field.

In dark field mode the objective aperture (a metallic plate with different sizes of holes) is placed in back focal plane that blocks the direct beam from the interacted

electrons and allow only scattered electrons to produce an image, due to which the image appears to be dark. In this mode it is possible to identify if the particles are crystalline or amorphous. The crystalline particles appear dark in this mode.

The diffraction mode also known as selected area electron diffraction (SAED) is obtained by adjusting the magnetic lenses such that the image comes from back focal plane of the lens rather than the image plane, the spots in case of single crystal and rings in case of polycrystalline are observed.
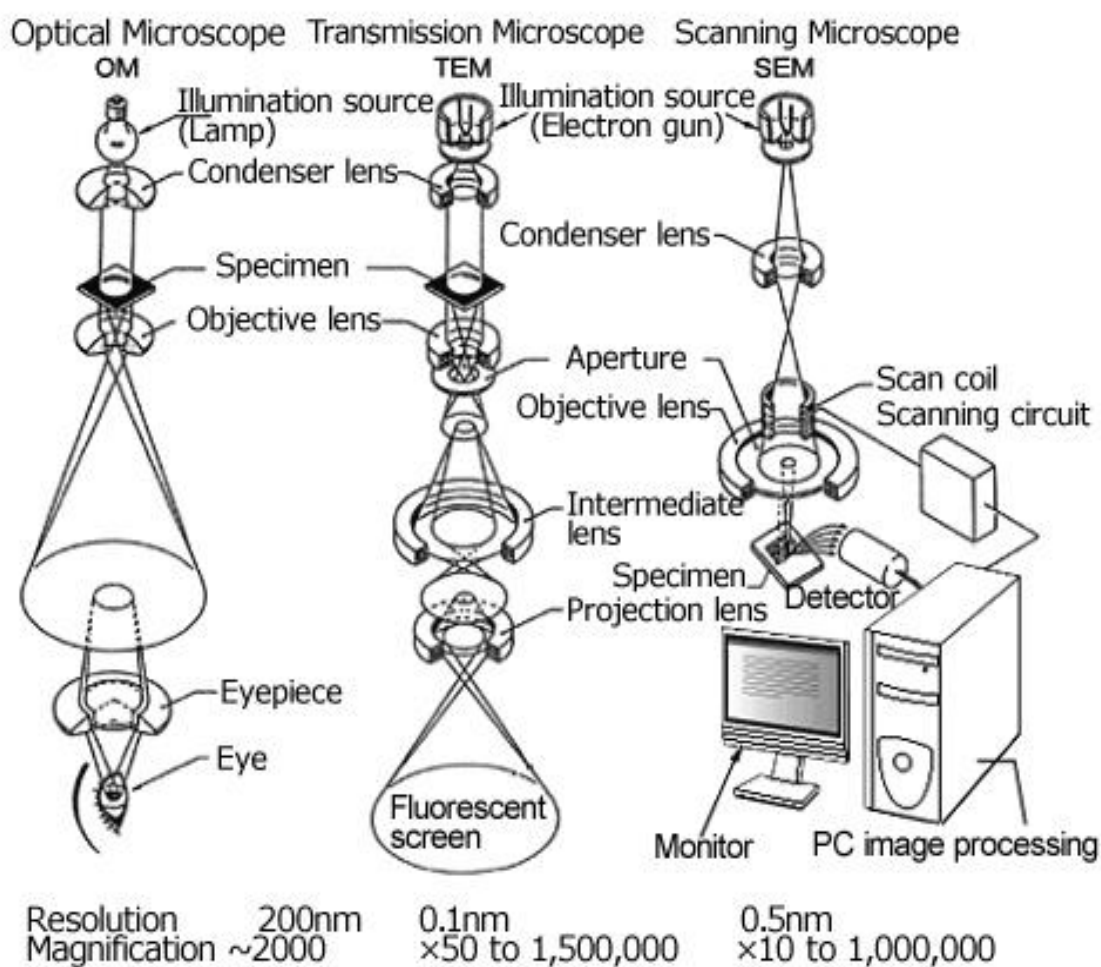
Figure 3-7 Schematics of optical microscope, TEM and SEM (from left to right) with important parts are named [333].

The major application of TEM is to study the morphology of materials, and to obtain crystallographic and compositional information (if so equipped). TEM can also give information about structural aspects, phases, impurities, elemental analyses and dislocations. SAED is also required to calculate the lattice parameter and to observe the crystallinity of the composites.

The resolution of the TEM is limited primarily by spherical aberration. By the reduction of the spherical aberration (by aberration correctors), an increase of the mechanical stability and the use of high voltages has led to the development of High Resolution TEM (HRTEM) which allows the production of images with sufficient resolution to show carbon atoms in diamond separated by only 0.89 Å and atoms in silicon at 0.78 Å [334]. The ability to determine the positions of atoms within materials has made HRTEM an important tool for nano-technologies research and development.

In this work, the microstructures were analysed by TEM with a 300 kV Hitachi, H9000-NA instrument and HRTEM manufactured by a Jeol 2200FS microscope worked at 200 kV. MWCNTs-BFO samples were observed in King Abdullah University of Science and Technology (KAUST), Saudi Arabia using FEI Titan, 300 kV.

For TEM analysis powder samples were dispersed in chloroform. One drop of the formed suspension was then put on a lacy carbon grid supported on a copper grid (Agar Scientific). The sample were dried in air for few hours before investigated for morphology, elemental analysis, interface and d spacing of the MWCNTs and MWCNTs-FE by TEM.

Scanning Electron Microscope (SEM)

Most of the electronic systems of scanning electron microscope is similar to the ones of TEM. However, here the sample image is formed from the secondary electrons, which reflect from the sample rather than transmitted and detected by the detector (Figure 3-7).

The samples characterized by SEM were prepared as follows: MWCNTs and MWCNTs-FE powders were dispersed in ethanol or chloroform and few drops of the suspension were spread on aluminium sample holders. After drying the samples were

covered with a thin layer of carbon in order to make them conductive. The carbon deposition process was performed using an Emitech K950 carbon deposition chamber equipped with a turbo pump. The outgas time and evaporated time were 30 and 2 seconds, respectively. The SEM analysis were performed using Hitachi SU- 70 (S-4100) (FCT: REDE/1509/RME/2005).

3.3.6 Atomic force microscopy and Piezo force microscope

After the invention of the Scanning Tunnelling Microscope (STM) it quickly became obvious that other physical processes could be used to map surfaces, not just a tunnelling current. Indeed, physical forces (Van Der Wall forces, electrostatic forces and so on) between the sample and the tip were proved to be used for image surfaces, and this technique named as atomic force microscopy (AFM) [335].

AFM works on two basic modes: contact mode and non-contact mode. In contact mode AFM, the tip (scanning probe) mounted on the cantilever is brought in contact with the sample and scanned using piezoelectric actuators. The deflection of the cantilever is accurately monitored by laser spot reflected from the cantilever to the mirror and photo diode, refer Figure 3-9 (a). These signals are passed to the feedback system which allow the mapping of the sample surface [336]. During the interaction between the tip and the sample surface, the tip experiences rapidly changing forces. As the function of the magnitude of these interaction forces the vibrational characteristics of the tip changes: amplitude, frequency, magnitude etc. These signals are converted to get topography profile of the samples.

The other mode of AFM operation is non-contact or tapping mode (TAFM). In this mode the cantilever is placed at some particular Z distance from the sample (knows as set point), where the tip oscillates close to its resonance frequency (with free amplitude). When the tip comes in contact with the sample forces the amplitude of the tip vibration reduces or increase by nm. This change in amplitude is monitored by the photo diode similar to contact mode to acquire the topography of the sample. The major advantages of the tapping over contact mode are the better resolution due to the negligible lateral forces and less wear of the tip.

AFM images are not a true representation of the sample topography due to the complex dynamics of the vibration tip and surface system. Therefore, there are limitations in achieving atomic resolution. This limitation can be overcome by using tips with very small (1-2 nm) tip diameter and having high aspect ratio. However, the tip used for AFM imaging are not ideally sharp and having low aspect ratio as shown in Figure 3-8 (a and b). Therefore, an AFM image does not reflect the true sample topography, but rather represents the interaction of the probe with the sample surface. This is called tip convolution. Nevertheless, the tip convolution does not affect the height of the feature only affects the lateral resolution.

In the present work, this remark was kept in mind and the values mention in the text for the size of MWCNTs-FE was related with the vertical measurements rather than lateral measurements.
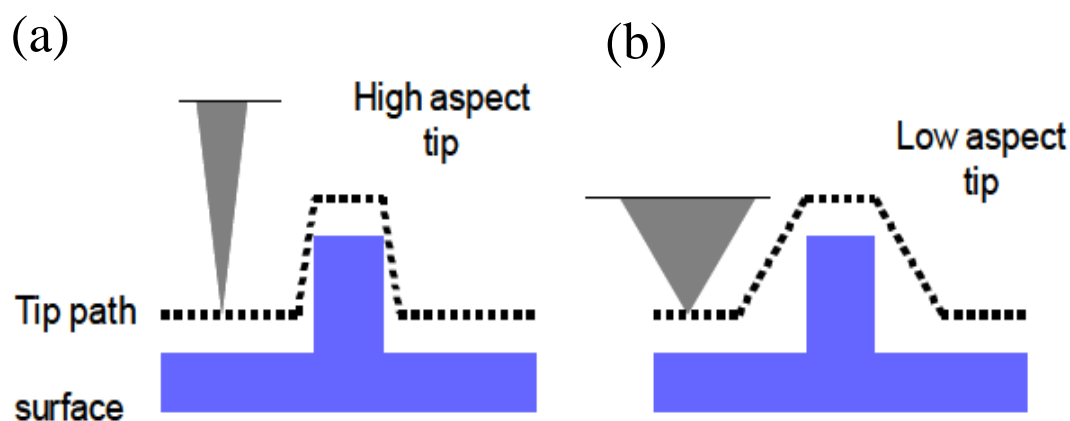
Figure 3-8 Schematic illustrates the topography acquired from (a) a high aspect ratio and (b) a low aspect ratio tip. A high aspect ratio tip is the ideal probe (tip) to acquire best resolution. Whereas, with low aspect ratio will results in the convolution. This does not often influence the height of a feature but the lateral resolution [337].

It was addressed in the previous chapter, that the nano scale ferroelectrics are of technological interest and therefore there is need to study the various aspect of ferroelectric and piezoelectric properties at nano meter scale. Therefore, PFM was used to study the local ferroelectric properties of MWCNTs-FE. Schematic of experimental setup for PFM is shown in Figure 3-9 (a) [155, 335].

In general, the PFM is carried out in contact mode using a conductive tip, used as a moveable nano electrode. The PFM response image is created from the deformation of ferroelectric domains due to the applied external field. This deformation can be in the form of contraction, elongation or shear depending upon the polarization vector and direction of the applied field. The PFM works on the converse piezoelectric effect where electric field- induce strain (S). It is expressed as follow:

$$S_j = d_{ij}E_i \qquad \text{Equation 3-4}$$

where E_i is the applied field and d_{ij} piezoelectric tensor. For a single–domain ferroelectric the piezoelectric coefficient relates to the spontaneous polarisation P_s via the following expression:

$$d_{ij} = \varepsilon_{im}Q_{jmk}P_s \qquad \text{Equation 3-5}$$

where ε_{im} is the dielectric constant, Q_{jmk} is the electrostatic coefficient and d_{ij} piezoelectric tensor.

The above equation states linear coupling between piezoelectric and ferroelectric parameters and can be used to determine the domain polarity from the sign of field induced strain. The electric field along the polarization direction results in the elongation of the domain. The contraction of the domains is observed when the direction of the polarization is opposite to the applied field direction. The relation between induced strain (S) and changes in thickness (ΔZ) is given by following equation:

$$S = \frac{\Delta Z}{Z} = \pm d_{33}E \qquad \text{Equation 3-6}$$

where ΔZ is the sample deformation, Z thickness of the sample, d_{33} effective piezoelectric constant. The above equation can be further rewritten as follow:

$$\Delta Z = \pm d_{33}V \qquad \text{Equation 3-7}$$

where V is applied voltage. The contribution related to the electrostriction (given in Equation 3-5.) is typically much smaller than the piezoelectric response in a polarized state and vanishes if no dc field is applied to the sample. In the dynamic piezoresponse imaging method, an AC voltage is applied and the surface displacement is measured by the change in the vertical vibration of the cantilever, this response is know as vertical piezoresponse (VPFM), and amplitude is given by Equation 3-7.

When domain polarization direction is parallel to the surface, the imaging of that domain is represented by detecting the torsional vibration of the cantilever Figure 3-9 (b) known as lateral PFM (LPFM). This surface vibration translates via friction forces to the torsional movement of the cantilever. The amplitude of the in-plan oscillation is given by

$$\Delta X_o = d_{15} V_o \qquad \text{Equation 3-8}$$

where ΔX_o is the change in the deflection along the X axis and V_o is the applied voltage and d_{15} is piezoelectric coefficient. Single-point piezoresponse force spectroscopy (PFS) is a technique which allows to probe the domain growth by detecting the changes in area of domain orientation as a function of time. It is mainly used to study the domain growth. The local ferroelectric hysteresis of the materials can be performed at the single point mode also known as switching spectroscopy (SS) PFM. Where the switching response of the domain is measured as the function of applied dc bias from positive to negative cycle. The characteristic local hysteresis response from the ferroelectric materials is shown in Figure 3-9 (c).

(b)

(c)
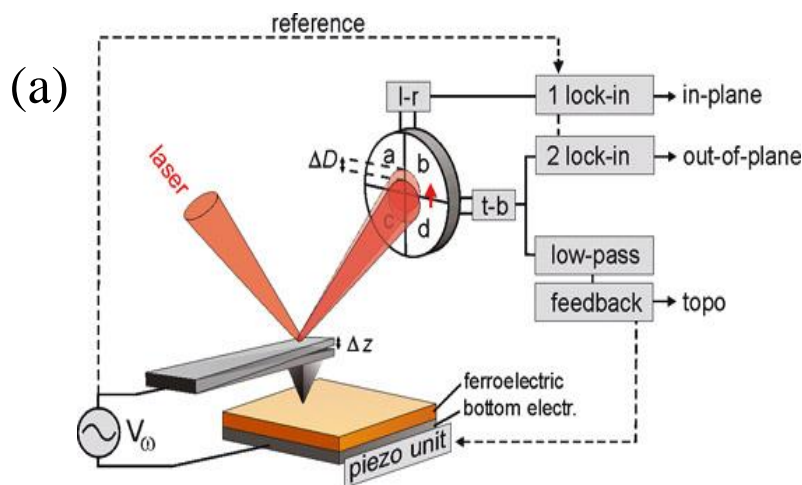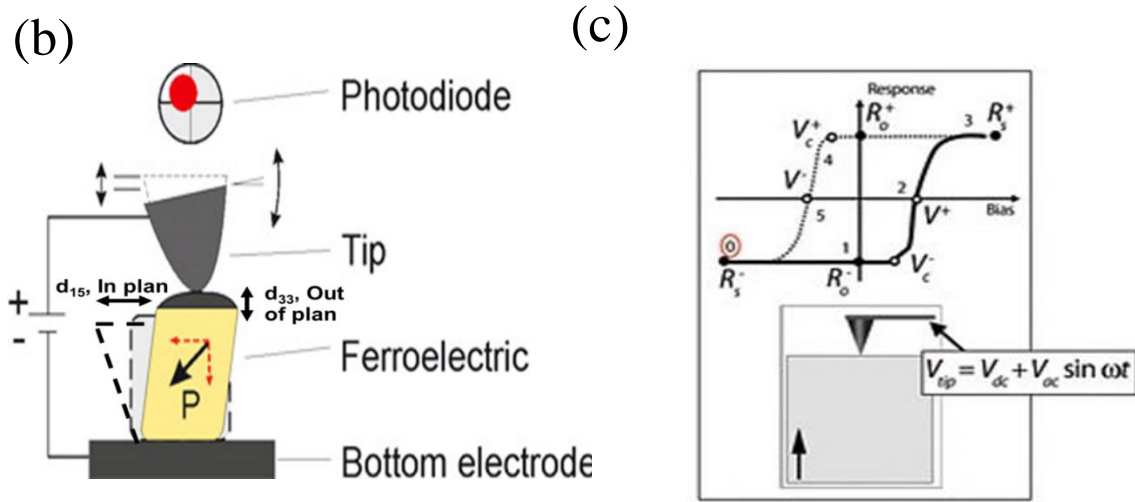
Figure 3-9 (a) Schematic of PFM setup to simultaneously acquire the topography and the in- and out-of-plane component of the polarization. A function generator is used to apply an alternating voltage V_w between the tip and the bottom electrode of the ferroelectric, (b) schematic illustrates how PFM signals is acquired by the deformation of ferroelectric under the applied field; the voltage induced cantilever deflection is detected by a reflected laser beam on a four sector photodiode and (c) a hysteresis loop acquired by switching spectroscopy (SS-PFM)[338].

In this work, the topography and simultaneously piezoelectric response was obtained by Standard Asylum SPM (at the University College Dublin (UCD), Ireland). The vertical PFM was obtained when the mechanical oscillations were induced by alternating current (ac) voltage at frequency away from resonance frequency of the tip. MikroMasch series XSC11/Pt (cantilever no. B) silicon nitrate platinum coated tips were used, having a resonance frequency of 60 to 100 kHz and spring constant of 1.1 to 5.6 N/m. The PFM response was also obtained using an Atomic Force Microscope (AFM, Multimode Nanoscope III A), equipped with external lock-in amplifier. Si AFM tips with platinum coating (force constant 2.8 Nm^{-1} and resonant frequency 70 kHz, MikroMasch series NSC18/Pt) were used with an applied voltage. As the effective piezoelectric coefficient ((d_{33})$_{eff}$ is proportional to the amplitude signal, this can be defined as (d_{33})$_{eff}$ $\propto$ (amplitude signal . cos(phase signal)) / Vac, where Vac is the ac voltage applied. The local hysteresis measurement were carried on individual grains by applying dc bias in 20 steps, with 0.3 s duration of each step and 0.2 s delays after the step.

3.3.7 Electrical characterization

In this work, the capacitance and dielectric losses were measured using an impedance bridge (HP 4284A, Agilent, USA) over a frequency range of 100 kHz to 1 MHz. The oscillation level of the applied voltage was set to 0.1-0.5 V. The analysed electrical properties include the capacitance and loss tangent. The macro level electrical response on $BiFeO_3$ deposited on top of Vertical Aligned (VA) MWCNTs was measured using Metal-Insulator-Metal (MIM) configuration, where MWCNTs-cloth (cloth fabricated by vacuum filtration method) as top electrode and aligned MWCNTs as bottom electrode was used (as presented in Figure 3-10).

To confirm the ferroelectric behaviour of MWCNTs-BFO, polarization-electric field (P-E) hysteresis loop were measured at room temperature using a Sawyer-Tower circuit [157]. The loops were acquired at two set of frequencies 50 and 100 Hz using a ferroelectric tester, Aixact, TF analyzer 1000. Current vs Voltage (I-V) measurements were carried out on the pressed MWCNTs (as received and functionalized) from 0 to 3 V to study the conducting nature of the tubes. The distance between the probes is fixed at 10 mm, approximately.
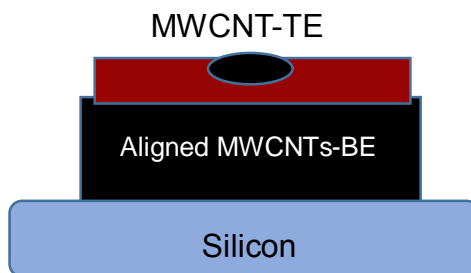
Figure 3-10 Schematic representation of BFO in between aligned MWCNTs and MWCNTs cloth, where MWCNTs act as electrode for measuring dielectric properties and P-E loop.

3.3.8 Vibration sample magnetometer (VSM)

VSM was invented by Simon Foner at Lincoln Laboratory MIT, in 1955. The working principle of VSM is based on Faraday's law of induction, according to which the change in the magnetic field results in induced electric fields. In VSM, the sample is placed under a constant magnetic field. If the sample is magnetic, the domains of the sample are aligned in the direction of applied magnetic field and higher the magnetic field higher is the magnetic moment. The magnetic dipoles of the sample create a magnetic field around the sample and as the sample is moved (using piezoelectric actuators) up and down there will be a change in the induced magnetic field as a function of time (change in induced emf) that can be sensed by pick up coils, in the form of electric field, according to Faradays law as induction electric fields. The induced voltage is amplified and signaled to a lock-in amplifier, where the piezoelectric signal is a reference signal. After the mathematical calculations, the induced magnetization as a function of applied magnetic field can be monitored. From this measurement it is possible to plot a magnetic hysteresis loop. It is possible to detect very small moments about 10^{-4} to 10^{-6} emu. Various measurements can be made in a uniform magnetic field as a function of temperature and field intensity [339]. In this work, Cryogenic VSM (Cryogenic Inc., UK) was used to measure the magnetic behaviour of samples up to 10 T at room temperature and at 5 K. The flakes of MWCNTs-BFO placed inside the gelatin capsule was placed inside a non-magnetic straw and is attached to the VSM vibrator for magnetic measurements.

Chapter 4

4   Thermal studies, functionalization and characterization of MWCNTs

Abstract

Carbon Nanotubes (CNTs) have unique physical properties. This has been the driver for the current exploitation of their use in different advanced applications, such as in composite nano scale structures or devices. If a thermal treatment is required for the fabrication of the composite, the thermal decomposition behaviour of the tubes is a key aspect in this process. Within this context the thermal decomposition behaviour under different conditions of the MWCNTs used in this work was studied by DTA/TG, X-Ray, Raman spectroscopy and electron microscopy.

Our studies revealed that purified MWCNTs are stable up to 420 ℃ in air, as no weight loss occurs in TG/DTA analysis under non isothermal conditions but morphology changes were observed for isothermal conditions at 400 ℃ by Raman spectroscopy. In oxygen-rich atmosphere MWCNTs started to oxidize at 200 ℃. However in argon-rich atmosphere and under a high heating rate MWCNTs remain stable up to 1300 ℃ with a minimum sublimation. The activation energy for the decomposition of MWCNTs in air was calculated to lie between 80 and 108 kJ/mol. These results have broad implications for the expanded use of MWCNTs in composites with functional complex oxides that usually require synthesis temperature above 650 ℃.

MWCNTs are hydrophobic in nature and to cover MWCNTs with FE, they were functionalized covalently and non-covalently. The FTIR studies confirms the attachment of functionalized groups on MWCNTs. The linear variation of current with voltage depict the CNTs are metallic in nature. Vertical Aligned (VA) MWCNTs were also characterized for morphology and electrical properties. The microstructure of MWCNTs reveals well crystalline layer of graphene with presence of small amount of amorphous carbon. I-V curve from VA-MWCNTs confirms the metallic behaviour.

4.1   Introduction

As described in chapter 2 scaling of electronics is no longer only about reducing dimensions; instead, it currently encompasses the development of emerging devices that incorporate new and combined functionalities. Carbon- based nano devices are expected to be integrated into nano electronics during the next decades [209]. MWCNTs were discovered in 1991, by Iijima [73] and since then have attracted tremendous interest in all fields of research and engineering. Due to its graphene structure CNTs have hydrophobic behaviour and inert nature. So, a successful combination of CNTs with different materials (organic and inorganic) may require a process to modify the tube's surface through surface functionalization [126]. Additionally, as-produced MWCNTs contain different carbon species (or impurities), namely amorphous carbon, graphite and fullerenes. These species have different C-C bond length, curvature and strains that influence their surface and decomposition behaviour. Amorphous carbon acts as low temperature pre-ignition sites, and therefore as-prepared CNTs typically decompose at low temperatures. Therefore by removing the amorphous carbon the thermal resistance of the tubes improves [138]. Chemical and thermal treatments are current procedures used to purify and improve the thermal resistance of CNTs.

On the other hand and from a different point of view, for composites in which thermal treatments at elevated temperatures during the synthesis are required, the thermal behaviour of CNTs is a key feature. The high firing temperatures and controlled atmospheres needed to synthesize and densify functional oxides used in microelectronic applications can be detrimental to the CNTs, compromising their role in the composite. In spite of the previous studies on the thermal behaviour of MWCNTs towards their purification, the literature is still incomplete in the description and understanding of the thermal behaviour of MWCNTs under different atmospheres.

In this chapter the oxidation of MWCNTs and its dependence on the atmosphere is studied. The activation energy for the decomposition is calculated. The condition in which these MWCNTs can be used in combination with ferroic oxides are defined. In addition to improve the compatibility and liaison between MWCTs and ferroic oxides different tubes functionalization was conducted. Since one of the main purposes of these MWCNTs is as possible bottom electrodes their metallic nature was investigated.

4.2   Experimental

As received MWCNTs (93% purity) were used to investigate the thermal stability. Differential thermal and thermo gravimetric analysis (DTA/ TG) were carried out in a SETARAM Labsys TG-DTA12 system. The samples were heated in alumina crucibles up to 1400 °C in air and flowing oxygen and argon atmospheres (0.4 L/min in both cases) for different heating rates (2, 5, 10 and 20 °C/min). For isothermal studies MWCNTs heat treated inside DTA/TG equipment at particular temperature as a function of time. The morphology of MWCNTs heat-treated at different temperatures, in different atmospheres were analyzed by Raman (Bruker RFS 100/S FT) and TEM (Hitachi Microscope, Model H9000-NA).

As received MWCNTs were purified followed by functionalization by nitric acid and Sodium Dodecyl Sulfate (SDS), detailed procedure on functionalization is mentioned in chapter 3.

These functionalized MWCNTs were characterized by Fourier Transform InfraRed (FTIR) spectroscopy (Mattson Mod 7000 FTIR spectrometer).). The contact angle was measured on purified and functionalized MWCNTs using sessile drop method (Dataphysics, OCA 25). The morphology of the functional MWCNTs were investigated by Scanning Electron Microscopy (SEM) and TEM. I-V curves were obtained on purified and functionalized MWCNTs by Aixact, TF analyzer 1000.

4.3   Results and Discussion

TG and DTA curves of MWCNTs conducted in air are depicted in Figure 4-1. In air MWCNTs are thermally stable up to 420 °C, i.e. no phase change or any oxidation reaction took place. Above 420 °C, weight loss starts to occur due to the oxidation of the amorphous carbon and of MWCNTs themselves Figure 4-1 (a)). DTA curves from the as-received MWCNTs are characterised by an exothermic peak between 500-600 °C depending on the heating rate, and an endothermic one above 700 °C. For the heating rate of 20 °C/min (Figure 4-1 (b)) two maxima between 510–580 °C were observed which demonstrate the presence of two different forms of carbon having similar oxidation

behaviour; i.e. amorphous carbon and MWCNTs. Similar observations were also noticed in the DTA behaviour of SWCNTs [128].
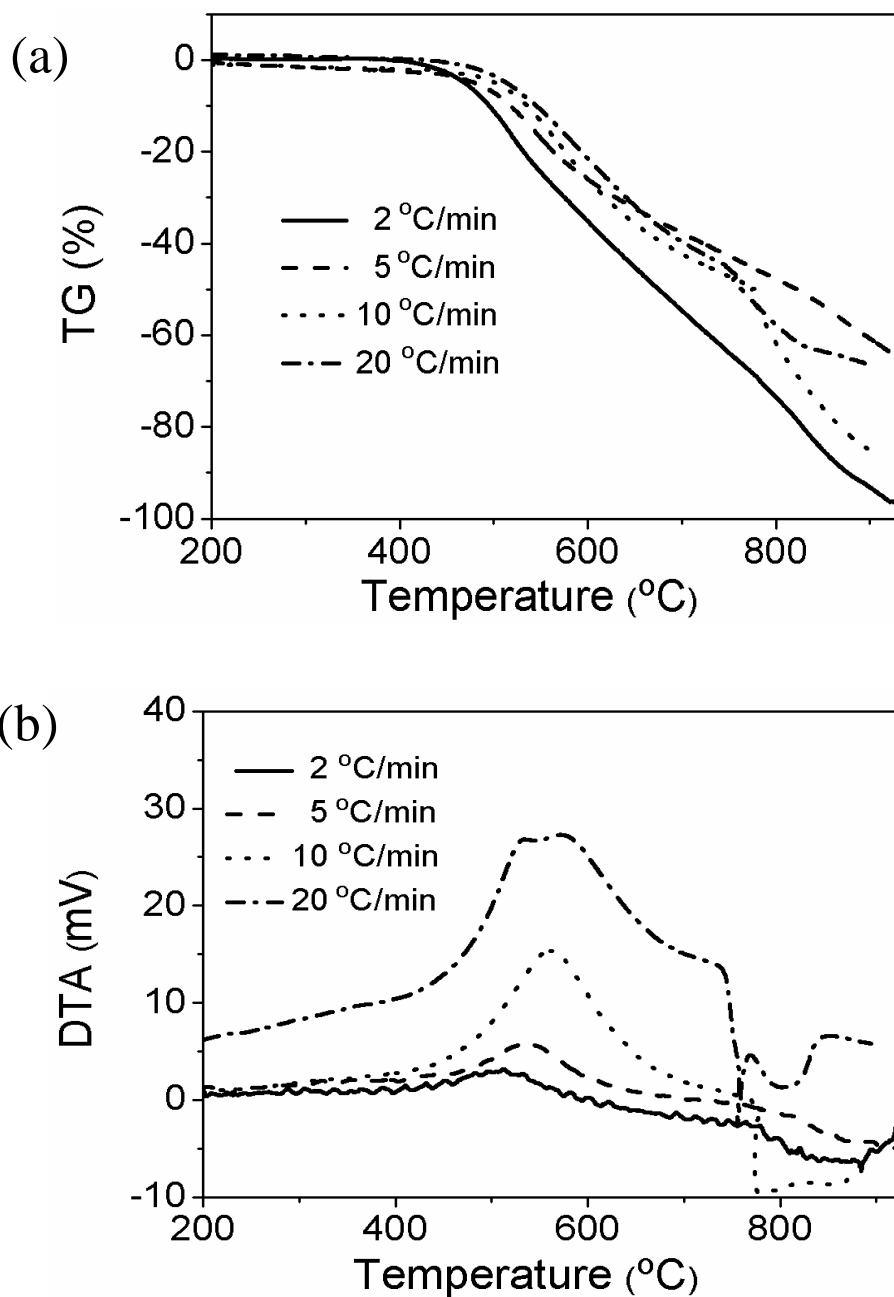
Figure 4-1: TG (a) and DTA (b) of as received MWCNTs conducted at different heating rates (2, 5, 10 and 20 °C/min) in air. MWCNTs are thermally stable up to 420 °C in air.

For the evaluation of the activation energy for a oxidation process two models were used, Kissinger´s [340] and Coat and Redfern [341].

Kissinger´s model assumes that the decomposition reaction is of first order and irreversible in nature. The calculation of the activation energy is based on the temperature at which the maximum mass loss change occurs, for different heating rates and is expressed as [340]:

$$In\ \frac{\beta}{T_p^2} = \ \frac{E}{RT_p} + In\ \left[\frac{df(\alpha)}{d\alpha}\right]\frac{AR}{E}$$

Equation 4-1

where β stands for the heating rate, $f(\alpha)$ for the conversion function, A for the pre-exponential factor, E (kJ/mol) for the activation energy for the reaction, R(J/mol K) for the gas constant and T_p (K) for peak temperature where the mass change is maximum. The activation energy for the decomposition was calculated from the slope of the variation of $ln\ (\beta/(T_p)^2$ as a function of $1/T_p$, to be 108kJ/mol.

In the Coat and Redfern model, in contrast to the previous one, the activation energy is calculated based on the change in the mass fraction for a single heating rate, according to the Equation 4-2 [340]:

$$In\ \left[-In\ \frac{(1-\alpha)}{T^2}\right] = \ In\ \left[\frac{k_0 R)}{\beta E}\right] - \frac{E}{RT}$$

Equation 4-2

For single heating rates of 2, 5, 10 and 20 ºC/min, the activation energy was calculated by plotting $ln[-ln(1-\alpha)/T^2]$ against $1/T$, where α is the fraction of reactant, and calculated by the formula $((m_i-m_t)/(m_f-m_i))$ from the TG data, where m_i is the initial mass, m_t is the mass at a given temperature and m_f is the final mass. In this case, the activation energy was calculated to be 80 kJ/mol.

The thermal behaviour of MWCNTs under partial oxygen and argon atmospheres is depicted in Figure 4-2. The tubes started to decompose at 200 ºC under partial oxygen and at 430 ºC under argon. The enhanced amount of oxygen increases the reaction rate at lower temperature and results in the oxidation of the amorphous carbon at 200 ºC. The major losses occur above 420 ºC in partial oxygen atmosphere, which is similar to the

oxidation of MWCNTs in air where both amorphous carbon and MWCNTs oxidizes simultaneously. Even at higher heating rates of 40 °C/min, under which MWCNTs kept unchanged until 540 °C/min, the excess amount of oxygen accelerates the oxidation of MWCNTs resulting in the total oxidation of the tubes below 670 °C (Figure 4-2 (a)).

In partial argon atmosphere (Figure 4-2 (b)), no sublimation occurs before 430 °C for both 2 °C/min and 40 °C/min heating rates. For 2 °C/min a first 20 % weight loss occurs before 800 °C, which may be due to the amorphous carbon, and the rest of the MWCNTs were sublimation between 800 - 1280 °C. Heating in argon makes possible to retain the maximum amount of MWCNTs until 800 °C, even for a low heating rate. For the heating rate of 40 °C/min the sublimation of MWCNTs starts just at 500 °C which is mainly from amorphous carbon, and until 1400 °C only ca. 25% loss occurs. For this high heating rate MWCNTs were kept up to 1300 °C with very negligible sublimation.
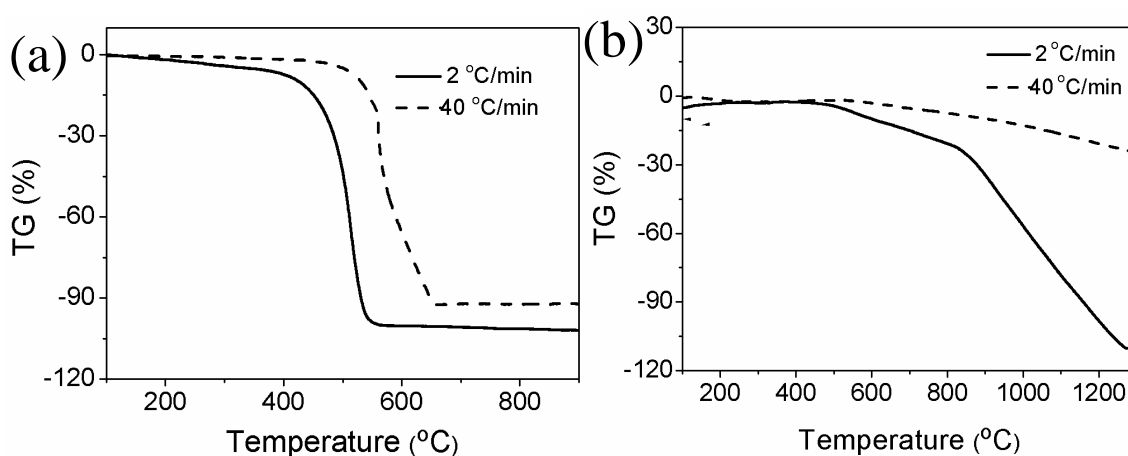
Figure 4-2: TG of as received MWCNTs in partial oxygen (a) and in partial argon (b) atmospheres. The tubes started to decompose at 200 °C under partial oxygen with the total oxidation occurring below 670 °C. Under a reducing atmosphere, even for a low heating rate, the tubes remain intact up to 800 °C.

As received MWCNTs contain impurities (amorphous carbon, metal particles, etc.) and the graphite layers are not uniform along the tube, which results from point defects and faults between graphite layers. MWCNTs heat treated at 400 °C in air for different periods of time do not show any visual changes in the morphology corroborating the TG analysis, where no weight loss was noticed at 400 °C. However, MWCNTs heated at 500 °C show an increase in the tubes diameter and ruptures of walls clearly indicating

the oxidation process that results in breaking of MWCNTs (marked by circles in Figure 4-3 (a)). With the further increase in temperatures (600 ºC) MWCNTs formed bundles due to the reduction in the free energy of the system, as previously reported for Double Wall Carbon Nanotubes (DWCNTs) [342] and the morphology were severely affected presented in Figure 4-3 (b).

The morphology of MWCNTs treated in argon at 800 ºC with heating rate of 2 ºC/min is depicted in Figure 4-3 (c). The TEM micrograph shows uniform and intact tube walls with no presence of amorphous carbon. The decomposition of the MWCNTs cap (i.e. end) was observed (marked by a circle in the Figure 4-3 (c)), which is due to the high reactivity of the sp^3 bonds associated with the cap, and the high local curvature strain. Figure 4-3 (d) depicts the Raman spectra for MWCNTs heat-treated at 600 and 800 ºC in argon with R (defined in Chapter 3) values of 1.01 and 1.005, respectively. The R value of MWCNTs heat treated at 600 ºC is higher than the one of MWCNTs heat treated at 800 ºC, due to the presence of a relative high amount of impurities, in this case amorphous carbon and metal particles, which results in a high intensity of the disorder band (D) for 600 ºC. After heat treated at 800 ºC the amount of impurities in the tubes decreases and the D band intensity decreases, as well.
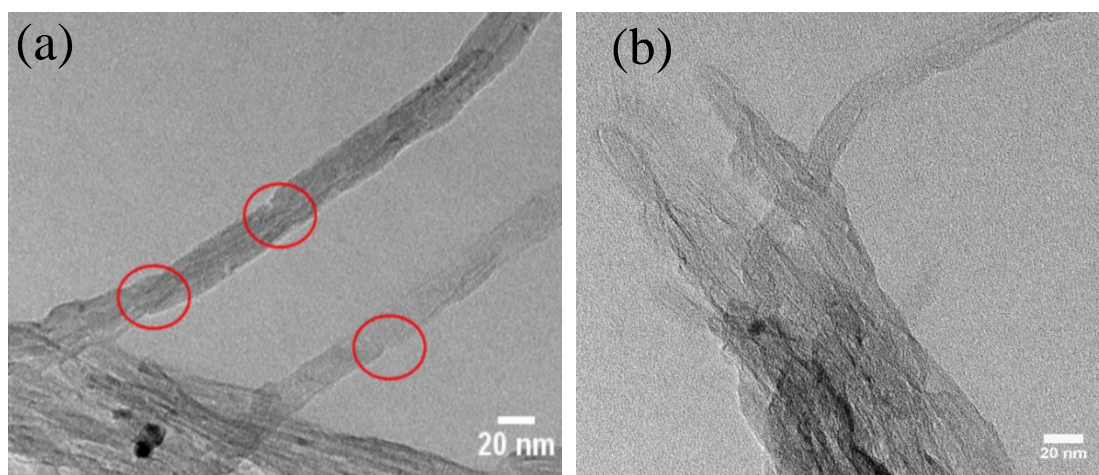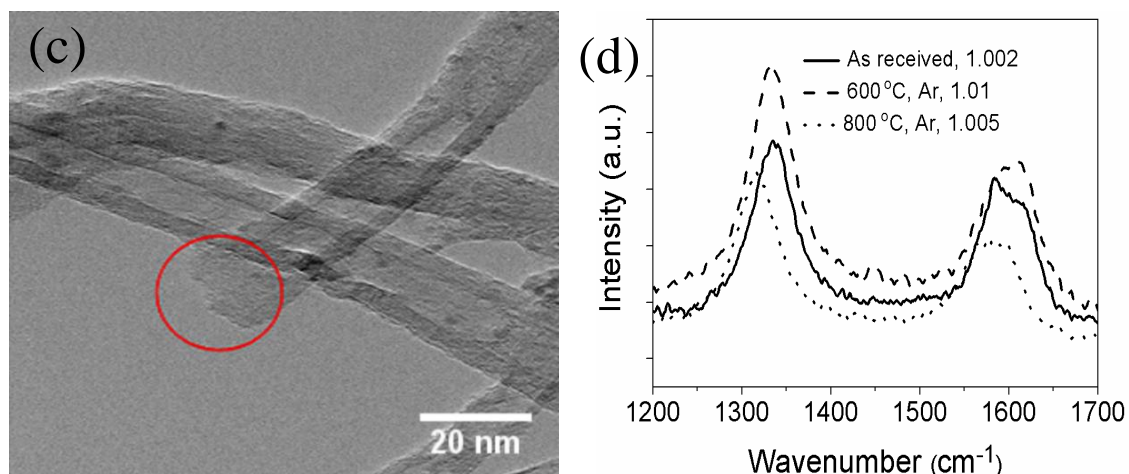
Figure 4-3: TEM micrograph (a) of MWCNTs heat treated at 500 ºC and (b) MWCNTs heat treated at 600 ºC in air; (c) TEM micrograph of MWCNT heated at 800 ºC at 2 oC/min in argon and (d) Raman spectra for as received, heat-treated at 600 ºC and 800 ºC MWCNT with R values in argon with heating rate of 2ºC/min (c).

4.4   Functionalization and characterization of MWCNTs

MWCNTs are hydrophobic in nature which results in poor wettability. In order to improve the wettability of the MWCNTs prior to be used for the fabrication of MWCNTs-FE structures they were functionalized by chemical processes. The MWCNTs were refluxed in nitric acid (detailed description mentioned in Chapter 3) to create defects site by breaking the sp^2 and sp^3 carbon bonds and induce hydroxyl and carboxyl groups at those sites. This type of functionalization in known as covalent functionalization.

MWCNTs were also functionalized with SDS, where the aliphatic chains of SDS adsorbed on the surface of MWCNTs with week forces such as Van Der Waals forces. This type of functionalization is known as non-covalent functionalization. Both covalent and non-covalent functionalized MWCNTs were used in this work. Figure 4-4 represents the schematic of covalent and non-covalent functionalize CNTs.
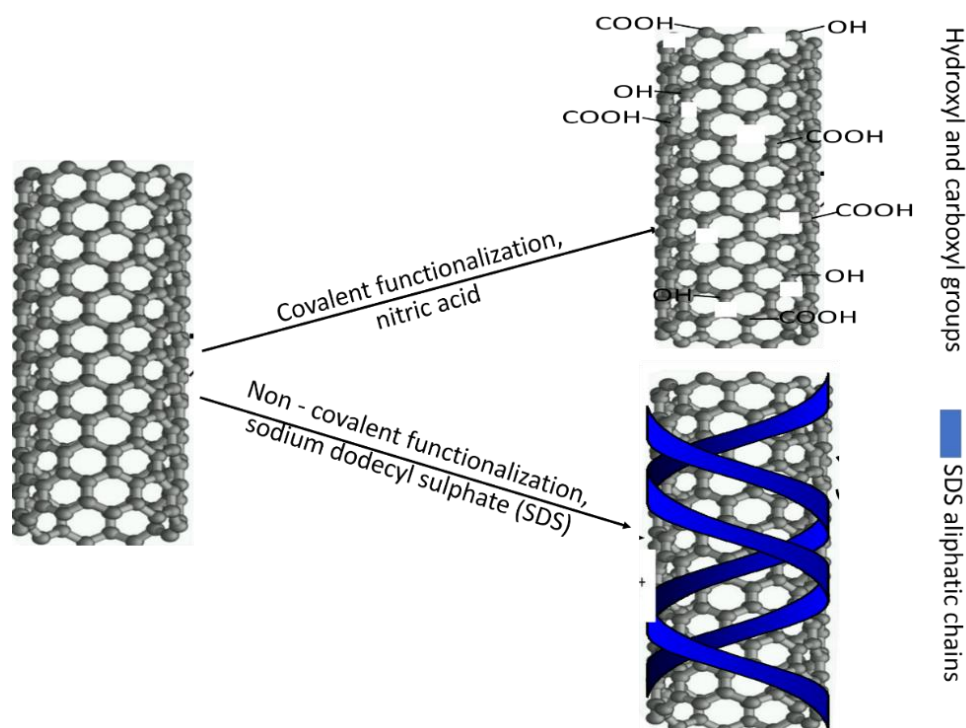
Figure 4-4 Schematic depicts covalent (on top right) and non-covalent (on bottom right) functionalization carried out using acid treatment by nitric acid and sodium dodecyl sulphate (SDS), respectively. The covalent functionalization took place on defect sites and very local, whereas, non-covalent functionalization with SDS molecules adsorbed along the nano tube, covering maximum surface.

The purified and covalent functionalized MWCNTs were characterized by vibrational spectroscopy (FTIR) in order to identify the functional groups attach to the surface of MWCNTs, given in Figure 4-5. Purified MWCNTs depict the characteristic peak at 1629 cm^{-1} that is associated with the vibration of the carbon skeleton from the carbon nanotubes. The peaks at 3446, 2977 and 2971 cm^{-1} for purified MWCNTs are assigned to hydroxyl groups (-OH), asymmetric stretching of CH$_2$ groups and symmetric stretching of CH$_2$ groups [343] which might result of some structural or point defects on CNTs. FTIR spectra of covalent functionalized MWCNTs shows an increase in absorption band 3446 cm^{-1}, attributed to the hydroxyl group (-OH) that clearly indicates the increase in number of OH groups attach to the surface of CNTs. The bending deformation for -COOH and bond stretching of CO in the functionalized-MWCNTs are

observed at 1447 cm $^{-1}$; and 1048 cm $^{-1}$, respectively; indicating the presence of carboxyl groups on the surface of MWCNTs[344, 345].
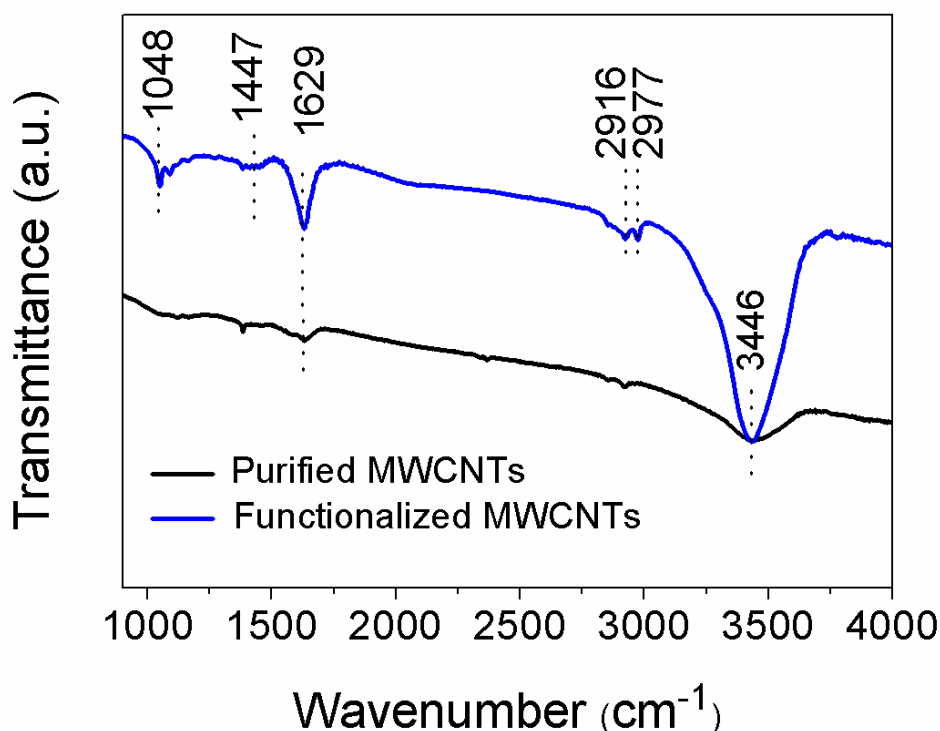
Figure 4-5 FTIR spectra of purified and functionalized MWCNTs with 5 M nitric acid, FTIR bands at 3446, 2916, 2977 and 1447 cm^{-1} depict the presence of hydroxyl and carboxyl groups. The characteristic band from MWCNTs is present at 1629 cm^{-1}.

Further the wettability of the MWCNTs were assessed by measuring the contact angles between MWCNTs and water droplets. The optical micrograph for purified MWCNTs and functionalized (HNO$_3$) with water droplet on the surface is given in Figure 4-6. The contact angle for purified MWCNTs is 150º, which decreases to 52º for the functionalized MWCNTs. This results clearly corroborates the FTIR observation on the presence of carboxylic and hydroxyl groups on the surface of MWCNTs which results in the improved wettability.

(a) (b)
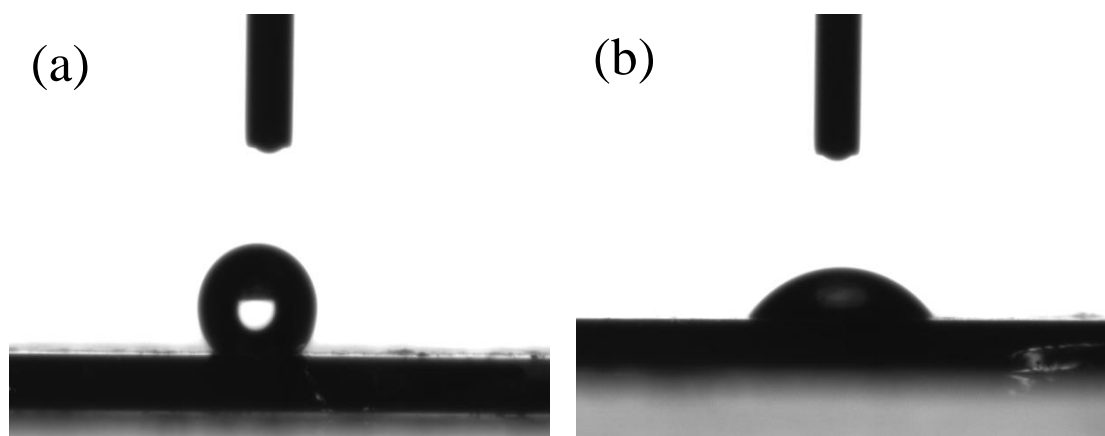
Figure 4-6 Optical micrograph of the water droplet on the surface of (a) purified MWCNT and (b) nitric acid functionalized MWCNT, the contact angle decrease from 150 º to 52 º after functionalization of MWCNTs, confirm the improvement in wettability of MWCNTs.

The MWCNTs tubes as-received, purified and functionalised were characterized by SEM and TEM (Figure 4-7). SEM micrographs for as-received MWCNTs show the presence of amorphous carbon and the metal particles (appears bright in the micrograph) Figure 4-7 (a). Whereas, after the purification process the MWCNTs are almost free from amorphous carbon and metal particles. The purified MWCNTs are more agglomerated and hence difficult to distinguish them in SEM (Figure 4-7 (b)). After functionalising MWCNTs (with 5M HNO_3) shows less agglomeration with few impurities as presented in Figure 4-7 (c). The TEM micrograph of the functionalised MWCNTs depicts a well crystalline carbon lattice with fewer defects and having interlayer distance between carbon walls around 0.34 nm. The MWCNTs depicted in this micrograph have diameters ranges from 12 to 30 nm (Figure 4-7 (d)).
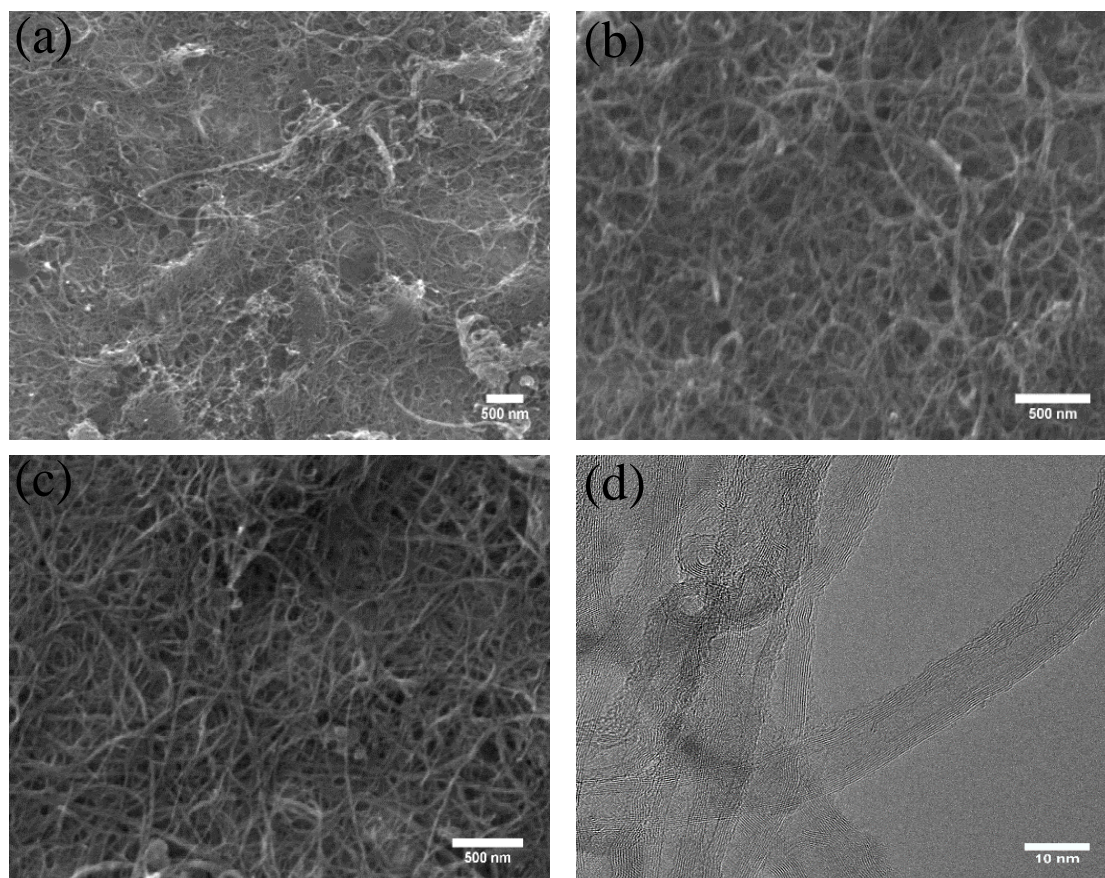
Figure 4-7 SEM micrographs of MWCNT films (a) as-received (b) purified (c) functionalized 5M HNO₃ and (d) TEM micrograph of functionalized MWCNTs.

As stated above, the non-covalent functionalization (by SDS) was also performed on MWCNTs in order to increase the functionalized area on MWCNTs. To confirm the functionalization of MWCNTs with SDS they were characterized with FTIR (Figure 4-8). Peak at 1629 cm^{-1} is associated with the vibration of the carbon skeleton from the carbon nanotubes, this peak is very clear for both MWCNTs and SDS functionalized MWCNTs. For SDS functionalized tubes two more peaks are present in comparison to as received MWCNTs; one at 1058 cm^{-1} assigned to the symmetrical stretching vibration of S=O and second at 881 cm^{-1} assigned to the asymmetrical stretching vibration of C–O–S [346, 347]. This peaks confirms the functionalization of CNTs with SDS.
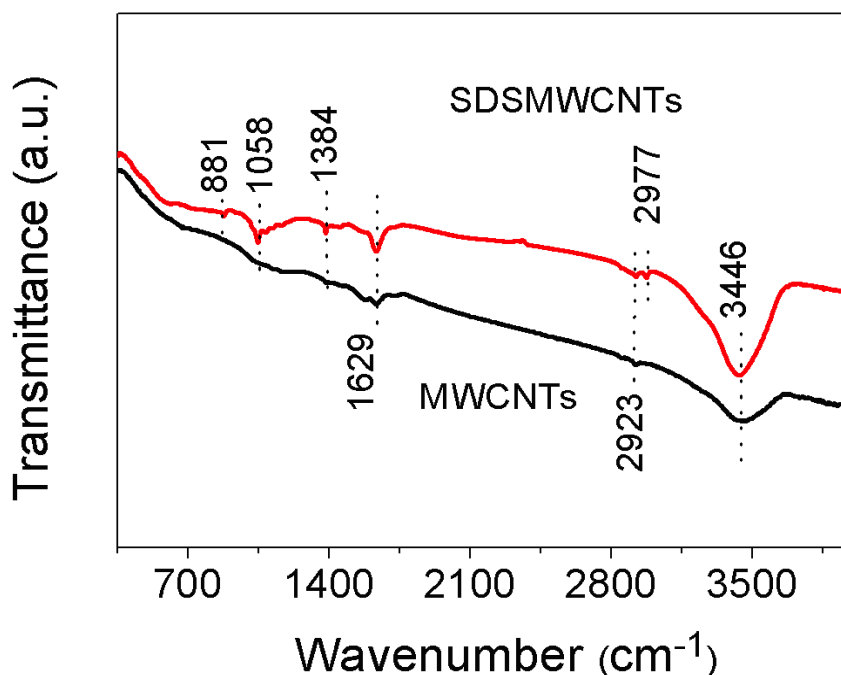
Figure 4-8 FTIR spectra of MWCNTs and SDS functionalized MWCNTs confirm the covering of MWCNTs with SDS molecules with the presence of peaks at 881 and 1058 cm^{-1}.

The metallic nature of the MWCNTs used in this work were investigated by the I-V curves (Figure 4-9). I-V curves were measured with the application of dc bias up to ± 3 V. I-V curve for as received, nitric acid functionalized (covalent functionalization) and SDS functionalization (non-covalent functionalization) depicts the linear change in current with the application of the applied voltage. This states the ohmic nature of the tubes as shown by metals, hence they are metallic in nature. Whereas, as-received MWCNTs depicts less current values (~0.5 mA) at 3 V in comparison to nitric acid (1.5 mA) and SDS functionalised MWCNTs (1.7 mA). This is due to the presence of impurities such as amorphous carbon and metal particle for the as received MWCNTs which affects the electron flow path in the tubes.

The current values in the case of SDS functionalized tubes are slightly better in comparison to the nitric acid functionalized tubes (at 3 V for SDS MWCNTs 1.7 mA and for nitric acid MWCNTs 1.5 mA). This indicates that during the covalent functionalization the breaking of carbon lattice occurs (defects). This defects hinder the

electron flow and as a consequence effect the current flow. In case of non-covalent functionalized MWCNTs the defect sites were not induce because the functionalize molecules are adsorbed on the surface of the MWCNTs rather than making covalent bonding as in case of covalent functionalized MWCNTs. Therefore the current flow for SDS functionalised MWCNTs is slightly higher in comparison to covalent functionalized MWCNTs.
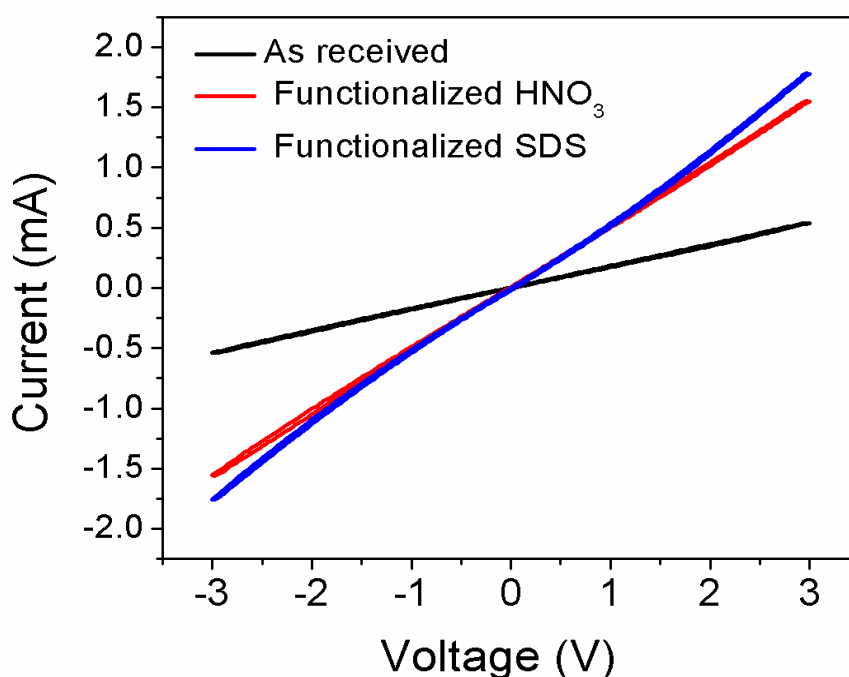
Figure 4-9 I-V curves for as received, oxidative treatment with nitric acid (covalent functionalization) and SDS functionalized (non.-covalent functionalization) MWCNTs. I-V curves illustrates the improvement of current flow after functionalization of MWCNTs.

The VA-MWCNTs were used to explore the potential of MWCNTs as conducting bottom electrode for FeRAM. The morphology and electrical characterizations are presented below.

SEM micrograph of VA-MWCNTs grown on the silicon substrate is illustrated in Figure 4-10 (a). They are densely packed and having length up to 1-2 mm. TEM micrograph of VA-MWCNTs depicts the presence of amorphous carbon along the walls. The tubes have well crystalline carbon lattices and having diameters ranging from 5 to 20

nm (Figure 4-10 (b)). I-V curve of VAMWCNTs depicts the linear increase of current with the applied voltage, proving the metallic behaviour of the tubes (Figure 4-11).
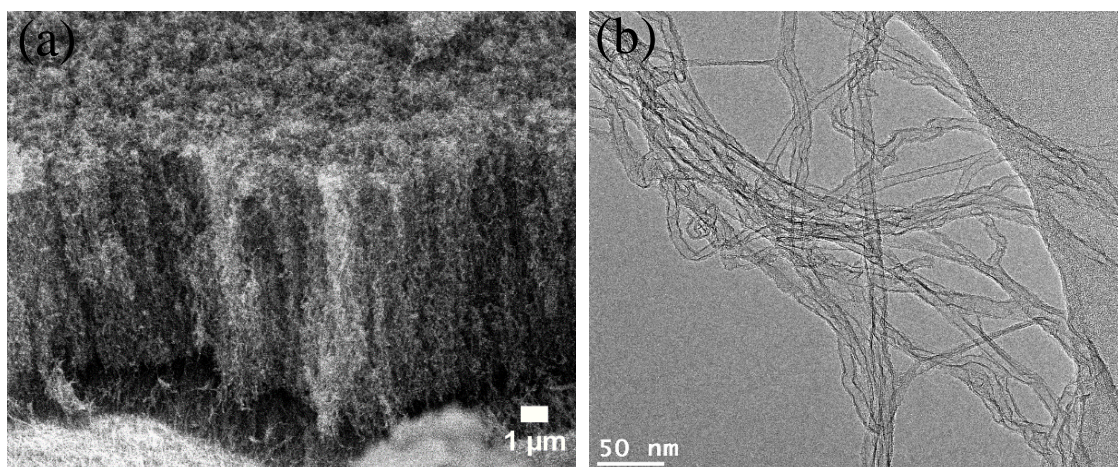
Figure 4-10 (a) SEM micrograph of VA-MWCNTs and (b) TEM micrograph of MWCNTs depicts the presence of amorphous carbon on the walls and high crystalline carbon walls with thickness of CNTs between 5-20 nm.
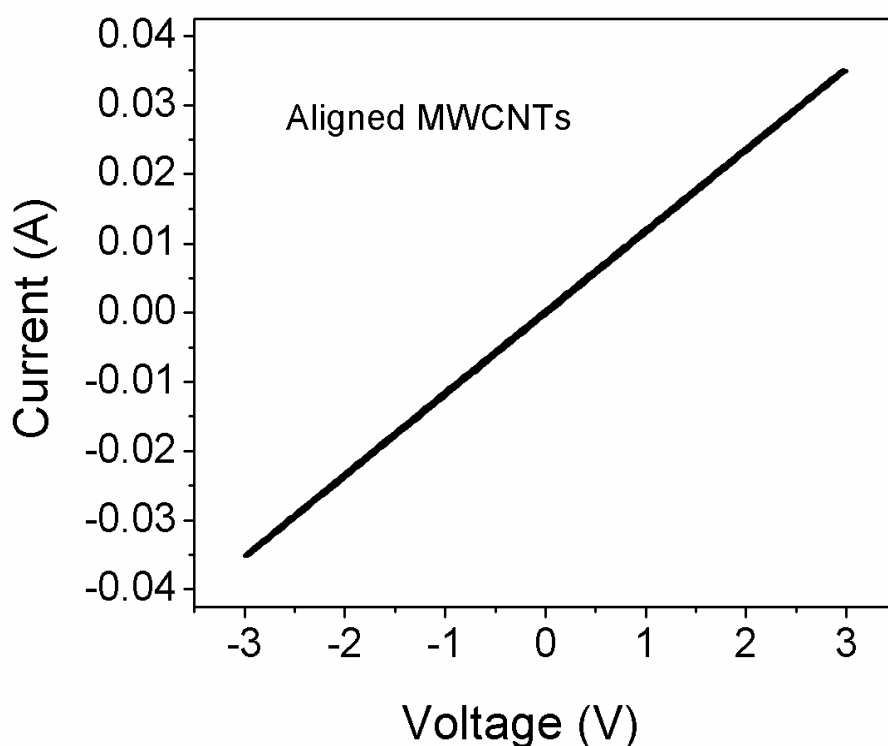
Figure 4-11 I-V curve for VA-MWCNTs, depicts the metallic behaviour of the tubes.

4.5 Conclusions

According to thermal analysis, when heat-treated in air the MWCNTs used in this work are stable up to ~400 ºC and start degrading after the initial combustion of amorphous carbon. Under these conditions the activation energy for the decomposition of the tubes lies between 80 and 108 kJ/mol. The decomposition of MWCNTs is accelerated in oxygen and decelerated in argon, as expected. The tubes start to decompose at 200 ºC and at 430 ºC at oxygen and argon atmosphere, respectively. The MWCNTs heat treated at 800 ºC with heating rate of 2 ºC/min in argon atmosphere are well intact without major physical damage of the walls. However, under a reducing atmosphere and for high heating rates MWCNTs are kept stable up to 1300 ºC with very negligible decomposition. These are relevant results for the further utilization of MWCNTs in composites with functional complex oxides with synthesis temperature usually above 650 ºC. FTIR and I-V curves for covalent and non-covalent functionalized MWCNTs confirm that the MWCNTs are functionalised and metallic in behaviour.

Chapter 5

5 Multiwall carbon nanotubes (MWCNTs) – Lead zirconium titanate (PZT)

Abstract

In this chapter we prove that it is feasible to utilise MWCNTs as electrodes for the formation of 1D $Pb(Zr_{1-x}Ti_x)O_3$ (PZT) nano ferroelectrics. In addition we unveil the role of CNTs on the phase formation of nano ferroelectrics.

Growing a ferroelectric on the surface of CNTs is a non-trivial task. Previous works have clearly demonstrated the damage of the CNT lattice after the annealing of the oxide. In this work we demonstrate that MWCNTs decrease the time and temperature for formation of lead zirconium titanate PZT by ~100 ºC commensurate with a decrease in activation energy from 68±15 kJ/mol to 27±2 kJ/mol. As a consequence, monophasic PZT was obtained at 575 ºC for MWCNTs-PZT whereas for pure PZT traces of pyrochlore were still present at 650 ºC, where PZT phase formed due to homogeneous nucleation. The piezoelectric nature of MWCNT-PZT synthesised at 500 ºC for 1 h was verified.

5.1 Introduction

As mentioned before PZT is commercially used in a large number of microelectronic devices such as ferroelectric memories (FeRAMs), electromechanical sensors and actuators, due to its high dielectric constant (~800) and polarisation (40 $\mu C/cm^2$) and large piezoelectric (d_{33} > 300 pC/N) and electromechanical coupling coefficients (k_{eff} = 0.42) [348]. Hence PZT was one of the targeted materials in this PhD work.

However, PZT from conventional solid state reaction requires high temperature, between 900-1000 °C [349] and care must be taken to compensate for the volatilization of lead oxide [350, 351]. PZT has been prepared by chemical methods such as hydrothermal synthesis[352, 353], sol gel [354-356] and co precipitation [349]. These routes guarantee compositional homogeneity at the molecular level and reduce crystallization temperature.

As described in Chapter 2, the use of CNTs as templates or as bottom electrodes is a potential strategy to realise 3D ferroelectric nano structures [4, 21, 28, 90, 357]. However, the practical use of CNTs as bottom electrodes depends on the ability to retain their geometry and integrity during fabrication. In the last years, only a few reports on the investigation of MWCNTs covered with ferroelectrics for 3D capacitors and related applications have been published (referred in section 2.5). In 2007 Kawasaki *et al.* [21] was the first to report the coverage of aligned MWCNTs with PZT by Liquid Source Misted Chemical Deposition (LSMCD). The authors found that annealing at 600 °C resulted in the damage of the CNT lattice and reaction between the substrate and the tubes. In 2012, Mohammadi *et al.* [26] used MWCNTs as a sacrificial template to synthesise 1D PZT tubes by sol gel. The early decomposition of CNTs between 400 - 500 °C was observed and the authors refer to early formation of perovskite (at ~ 450 °C) but no further information or discussion was provided.

In this work, we coated MWCNTs with PZT via a chemical solution process, which offers crystallisation of the perovskite phase at low temperature. Interaction between the PZT and CNTs as a function of the temperature is studied using thermo gravimetric (DTA/TG), X-Ray diffraction and microscopy characterisation. The

activation energy for the perovskite phase formation is calculated and the role of CNTs in perovskite crystallization addressed. The piezoelectric and ferroelectric responses of MWCNTs coated with PZT are reported.

5.2   Experimental

A diol-based sol-gel was utilised to coat the MWCNTs used in this work. The tubes were functionalized with 5 M nitric acid to improve their wettability (as described in Chapter 2). Lead(II) acetate trihydrate (99.5%, Sigma-Aldrich) was mixed with 1, 2 propanol diol and acetic acid for 30 min at 60 ℃. Titanium(IV) isopropoxide (97 %, Fluka) stabilized with acetylacetone (1:2 mol ratio) was then added to the lead acetate solution followed by mixing for 30 min at 60 ℃. Zirconium(IV) propoxide (70 %, Fluka) stabilized with acetyl acetone (1:2 mol ratio) was subsequently added followed by dilution with acetic acid to obtain a 0.2 M solution containing the correct proportions of Pb, Zr and Ti.

5 wt. per cent (approximately) of MWCNTs were immersed in the PZT solution and ultra sonicated for >2 h (Branson, USA, 40 kHz). During the sonication process temperature stay well below 50 ℃ and no bubbles or precipitations occurred. The solution was then stirred on a hot plate at 70 ℃ for ~ 1 h and gelation occurred. The gel was dried at 120 ℃ for 24 h to obtain MWCNTs-PZT composite powders. Similar steps were followed to obtain PZT powders. A flow chart representing the steps followed to fabricate PZT and MWCNTs - PZT are illustrated in Figure 5-1.

PZT and MWCNTs-PZT powders were characterized by differential thermal and thermo gravimetric analysis (DTA/ TG), carried out in a SETARAM Labsys TG-DTA12 system in air up to 700 ℃ with heating rate of 5 ℃ /min. The phase formation of PZT with and without MWCNTs was followed by *in-situ* XRD (Philips X´´ Pert. Cu, *Kα*), carried out in air at 5 ℃/min up to 650 ℃. *Ex-situ* XRD (Rigaku, Geigerflex D/Max-C, Cu *Kα*) was used to characterize MWCNTs-PZT powders heated for 1 h at various temperatures. All the samples investigated in the present studies were heat treated in alumina crucibles covered with platinum foils. These MWCNTs - PZT composites were further studied by Fourier Transform InfraRed (FTIR) spectroscopy (Mattson Mod 7000

FTIR spectrometer) and transmission electron microscopy (TEM) (Hitachi Microscope, Model H9000-NA and JEOL, Model 2200 FS).
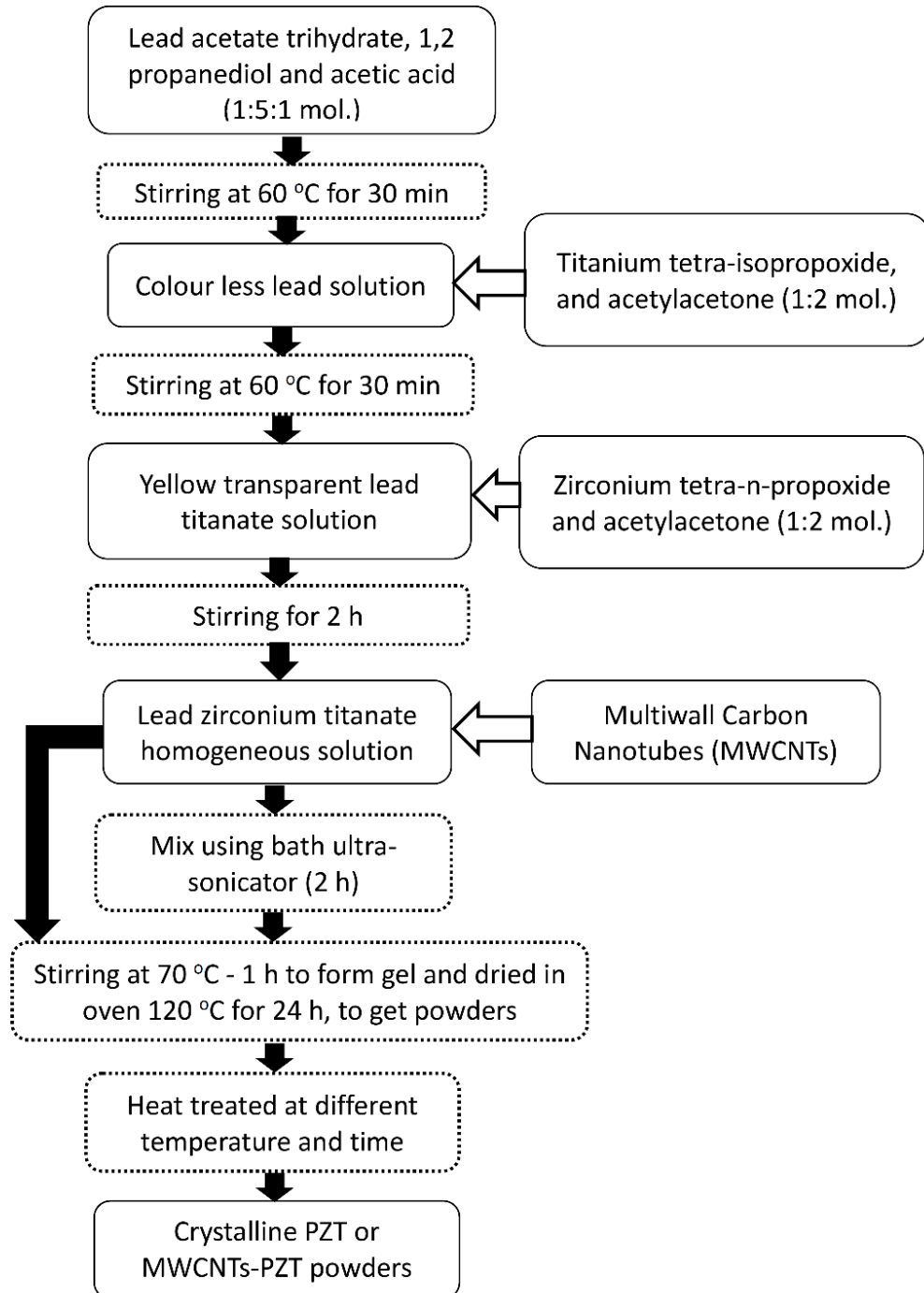
Figure 5-1 Flow chart illustrates the steps followed to fabricate PZT and MWCNTs-PZT.

The piezoelectric and ferroelectric response of MWCNTs-PZT were investigated by Atomic Force Microscope (AFM, Multimode Nanoscope III A), equipped with external lock-in amplifier for measuring piezo response. Si cantilevers with platinum coating (force constant 2.4 N/m and resonant frequency 80 kHz, MIKROMASCH) were used with an applied voltage of 5 V. Topography signals of the surface were taken simultaneously with the amplitude and phase signals and were collected in contact mode. Several hysteresis loops with dc bias from - 40 to + 40 V were obtained for MWCNTs-PZT to ensure the reproducibility of the results, and representative loop is presented. Switchable polarization corresponds to the difference between the positive saturation polarization and negative ones ($R_m = (R_S)^+ - (R_S)^-$). As the effective piezoelectric coefficient ($(d_{33})_{eff}$) is proportional to the amplitude signal, this can be defined as $(d_{33})_{eff} \propto$ (amplitude signal . cos(phase signal)) / V_{ac}, where V_{ac} is the ac voltage applied.

5.3   Results and Discussion

Figure 5-2 (a) illustrates the DTA analysis conducted in air at different heating rates (5, 10, 20 and 30 ^{o}C/min) for PZT (continuous line) and MWCNTs-PZT samples (dashed line). For PZT heated at 5 ^{o}C/min., there is a small broad exothermic peak at ~200 ^{o}C related to the release of low temperature organics. Between 200 and 350 ^{o}C, a further broad exothermic peak occurs, attributed to the combustion of organic solvents. On increasing temperature, the next broad exotherm lies between 420 ^{o}C - 570 ^{o}C and corresponds to the formation of pyrochlore phase [358] followed by transformation to perovskite observed as a small shoulder at 505 ^{o}C.

However, for MWCNTs-PZT heated at 5 ^{o}C/min, the broad exothermic peak corresponding to the formation of the pyrochlore phase begins at ~ 350 ^{o}C, ~ 80 ^{o}C lower than PZT. Moreover, the transformation to perovskite is complete by 480 ^{o}C for MWCNTs-PZT as opposed to 570 ^{o}C for PZT. According to our previous studies, the exothermic peak for the oxidation of MWCNTs starts at ~ 420 ^{o}C [359] but in the present study this peak is not observed since it overlaps with that of pyrochlore and perovskite phase formation. From the TG analysis of PZT and MWCNTs-PZT samples, four major weight loss events (I, II, III and IV) are identified (Figure 5-2 (b)). The first (I), an

exothermic event with ~2 - 10 wt% loss, occurs below 200 ℃ due to the evaporation of water and solvents. The second (II), also exothermic but with ~25% and 20% wt% loss for PZT and MWCNTs-PZT, respectively, occurs in the range 200 to 300 ℃ due to the combustion of organics. The third (III), ~6% for PZT between 300 ℃ and 450 ℃, may relate to the decomposition of residual organics. For PZT, a small additional weight loss, ~3% is observed up to 560 ℃ (IV). For MWCNTs-PZT above 400 ℃, the weight loss is higher than that observed for PZT and is continuous up to 750 ℃. According to our previous studies, oxidation of MWCNTs occurs up to ~750 ℃. In comparing the TG spectra of PZT and MWCNTs-PZT the observed difference in the weight loss is ~5 %, which is approximately the wt% MWCNTs added in the MWCNTs-PZT samples. Nonetheless, it is evident that the formation of pyrochlore and perovskite phases takes place at lower temperature for the case of MWCNTs - PZT in comparison with PZT.

To study further the phase formation, *in-situ* XRD was carried out on both PZT and MWCNTs-PZT powders (Figure 5-3). For PZT, peaks attributed to pyrochlore appear at ~500 ℃ and with perovskite at 550 ℃ (Figure 5-3 (a)). However, for MWCNTs-PZT small peaks ascribed to pyrochlore and perovskite appear at 450 ℃ (Figure 5-3 (b)). Moreover, for MWCNTs-PZT perovskite peaks become sharper as temperature increases with monophasic PZT obtained at 575 ℃. In contrast, for PZT, traces of pyrochlore are still identifiable at 650 ℃.

Ex-situ XRD analysis of samples calcined for 1 h at different temperatures are presented in Figure 5-4. For MWCNTs-PZT annealed at 400 ℃, the volume fraction of PZT perovskite phase is enhanced when compared with *in-situ* XRD of MWCNTs-PZT at 400 ℃. For MWCNTs-PZT annealed 1 h at 500 ℃, only peaks associated with perovskite are present. Further increasing the annealing temperature to 550 ℃ sharpens the perovskite peaks, presumably due to an increase in scattering coherence length related to grain growth.
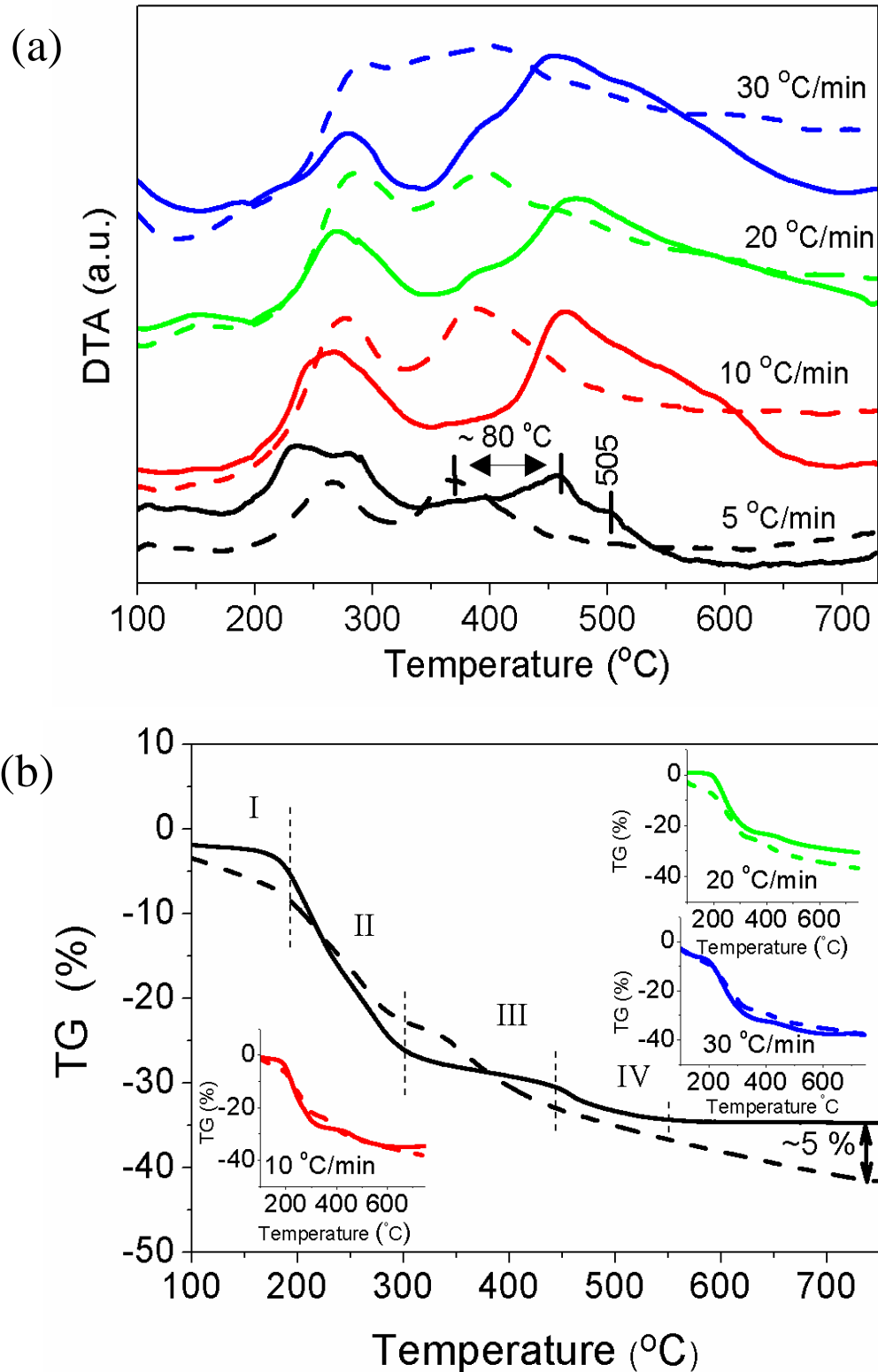
Figure 5-2 (a) DTA and (b) TG analysis of PZT (continuous line) and MWCNTs-PZT (dashed line) heat treated at different heating rates: 5, 10, 20 and 30 ºC/min. DTA clearly evidences the early appearance of exothermic peaks associated with the formation of pyrochlore and perovskite around 350 ºC for MWCNTs-PZT samples in comparison to PZT (420 ºC).
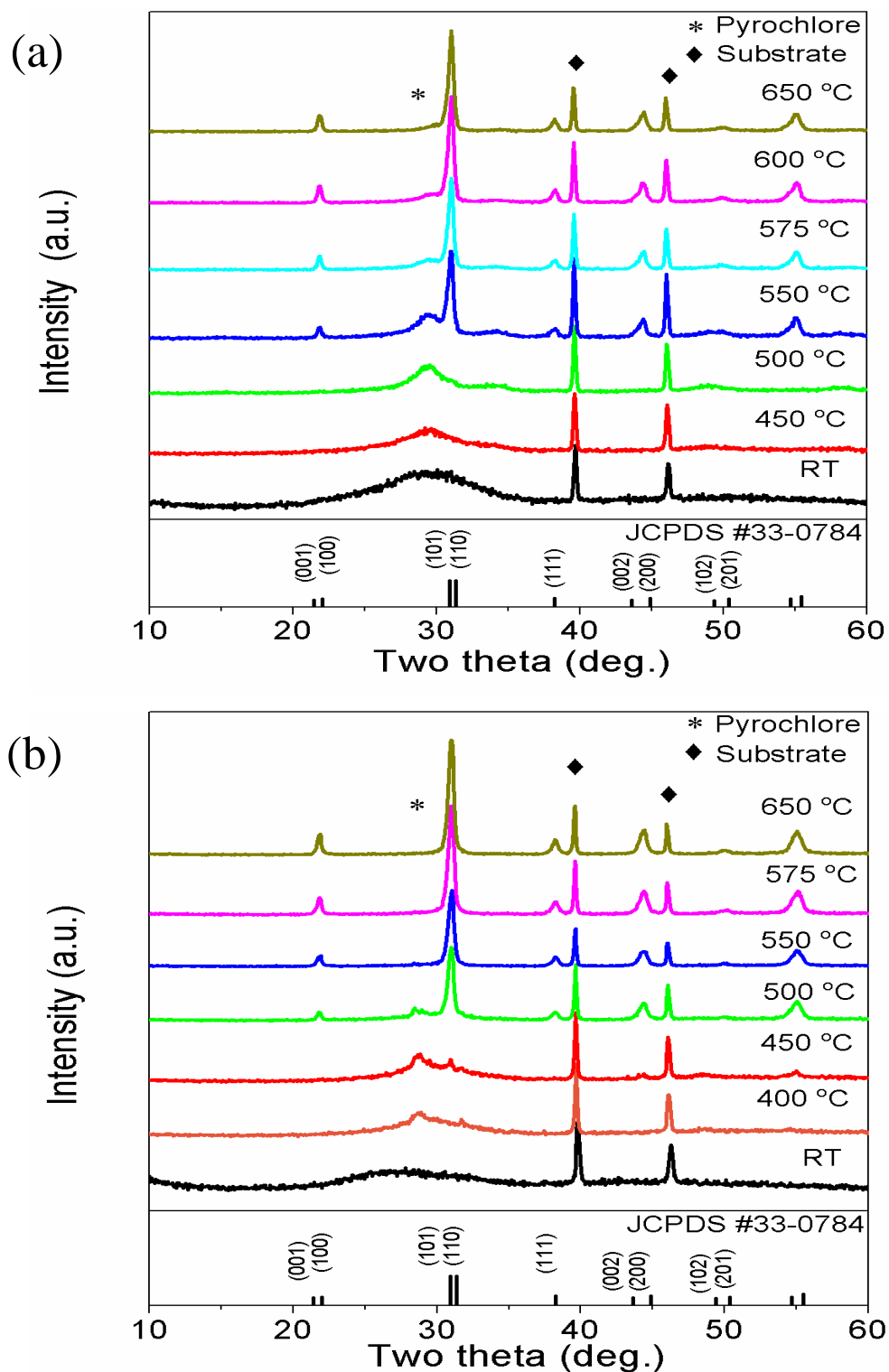
Figure 5-3 In-situ XRD patterns of (a) PZT and (b) MWCNTs - PZT acquired from room temperature to 650 ºC with an heating rate of 5 ºC/min. Monophasic perovskite phase was obtained at 550 ºC for MWCNTs - PZT samples but was not obtained up to 650 ºC for PZT.
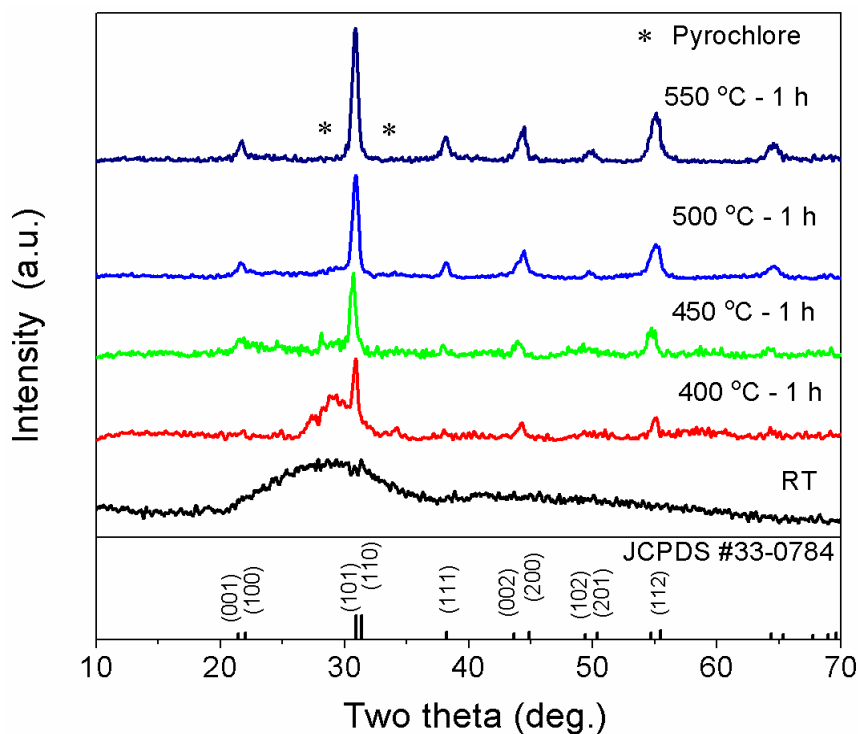
Figure 5-4 Ex-situ XRD patterns obtained for MWCNTs-PZT samples, annealed 1 h at 400, 450, 500 and 550 °C. Note the simultaneous appearance of pyrochlore and perovskite phase after 1 h at 400 °C and monophasic perovskite after 1 h at 550 °C.

FTIR spectra of MWCNTs and MWCNTs-PZT samples (annealed 1 h at 400, 450, 500 and 550 °C) are shown in Figure 5-5. The spectrum of MWCNT has one major characteristics peaks at 1630 cm^{-1}. The transmittance bands at 3448 cm^{-1} and around 1580 cm-1 correspond to the stretching of O-H and C-H bonds and its occurrence in all the samples confirms the presence of organics. For MWCNT-PZT the bands at 1640 cm^{-1} and 1315 cm^{-1} correspond to acetic acid or acetate [360] and bands at 1436 and 1560 cm^{-1} are attributed to symmetric and asymmetric -COO stretching modes of the acetate groups [361].

MWCNTs-PZT heat-treated at 400 - 450 °C exhibit additional peaks identified as an intermediate acetate salt whose bands occur at 1050, 1020, 940, 860, 666 and 620 cm^{-1}. The intensity of these peaks diminishes for MWCNTs-PZT samples heated 1 h at 500 °C but there are additional peaks at ~588 cm^{-1} and 349 cm^{-1}. These two transmittance peaks are attributed to TiO_6 and ZrO_6 stretching and bending of the octahedra, respectively, confirming the formation of perovskite [362]. MWCNTs-PZT sample

heated 1 h at 550 °C do not depict characteristic peaks of MWCNTs and intensity of octahedral peaks further strengthen. The combination of XRD (*in-situ* and *ex-situ*), DTA/TG and FTIR studies clearly indicates that the presence of MWCNTs facilitates the crystallization process of PZT and reduces the crystallization temperature by ~100 °C. However, the mechanism of PZT formation and the growth of the perovskite phase required further study using TEM.
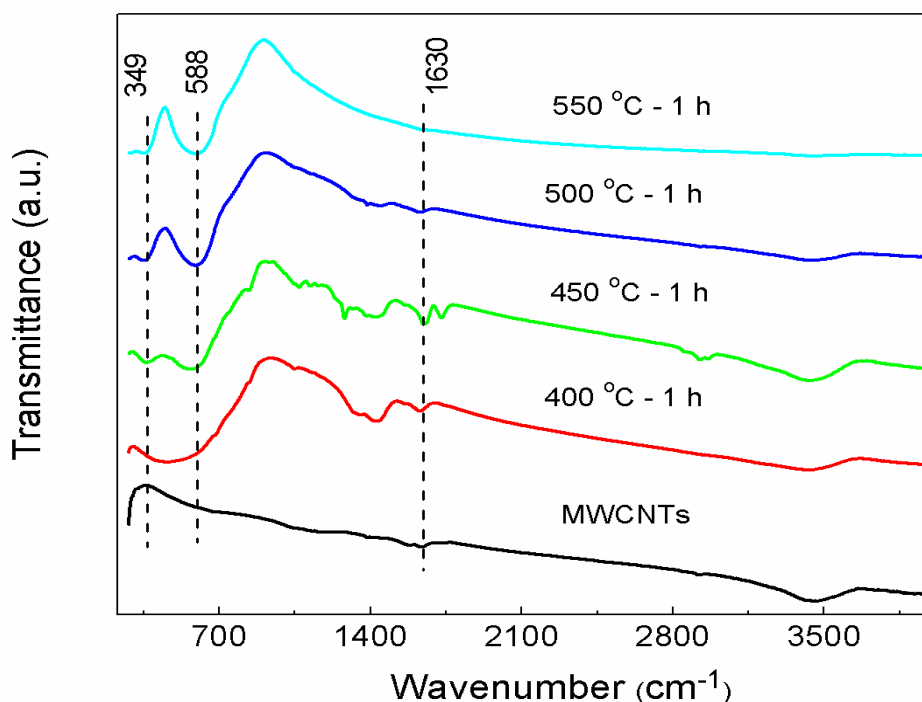
Figure 5-5 FTIR spectra of MWCNTs and MWCNT-PZT samples annealed 1h at 400, 450, 500 and 550 °C. The characteristic peaks of CNTs at 1630 cm^{-1} and at 349 and 588 cm^{-1} are from octahedra of Zr and Ti and indicate the formation of a crystalline PZT.

Figure 5-6 (a) is a TEM micrograph of MWCNTs-PZT, dried 24 h at 100 °C, which illustrates the conformal covering of MWCNTs with an amorphous PZT sol and also depicts the presence of some particulates. This sample was further analysed under high resolution (HR) TEM. Crystalline particles of lead ions with d spacing of ~ 0.30 nm surrounded by an amorphous network of zirconium and titanium are observed (Figure 5-6 (b)). EDS spectra confirmed the presence of lead, zirconium and titanium (inset of Figure 5-6 (b)). Similar observations have been previously reported in the literature for the growth of BaTiO$_3$ and ZnO. In these studies *in-situ* HRTEM indicated that Ba and Zn

ions were entrapped in the amorphous network of the respective organics prepared by sol gel [363, 364].

In TEM micrographs of MWCNT-PZT annealed 1 h at 400 °C (Figure 5-6 (c)), amorphous and crystalline phases are observed which corroborates previous XRD and FTIR analyses and confirmed the presence of perovskite and PZT. The MWCNTs (diameter ~100 nm) have been coated with a crystalline phase of dark contrast, presumably perovskite.

The TEM micrographs of MWCNTs-PZT samples annealed 1 h at 500 °C reveal crystalline tubes of ~50 nm having d spacing = 0.28 nm consistent with d_{110} PZT, Figure 5-6 (d). EDS spectra (inset in Figure 5-6 (d)) confirm the presence of lead, zirconium and titanium. HRTEM micrographs from one of the CNTs covered with PZT is illustrated in Figure 5-6 (e) and reveal the CNT lattice (inset Figure 5-6 (e)) with d spacing ≈ 0.34 nm and d_{001} PZT ≈ 0.40 nm. After annealing at 500 °C, HRTEM proves the tubes are intact, covered in a crystalline phase with d spacing characteristic of d_{001} and d_{110} PZT.
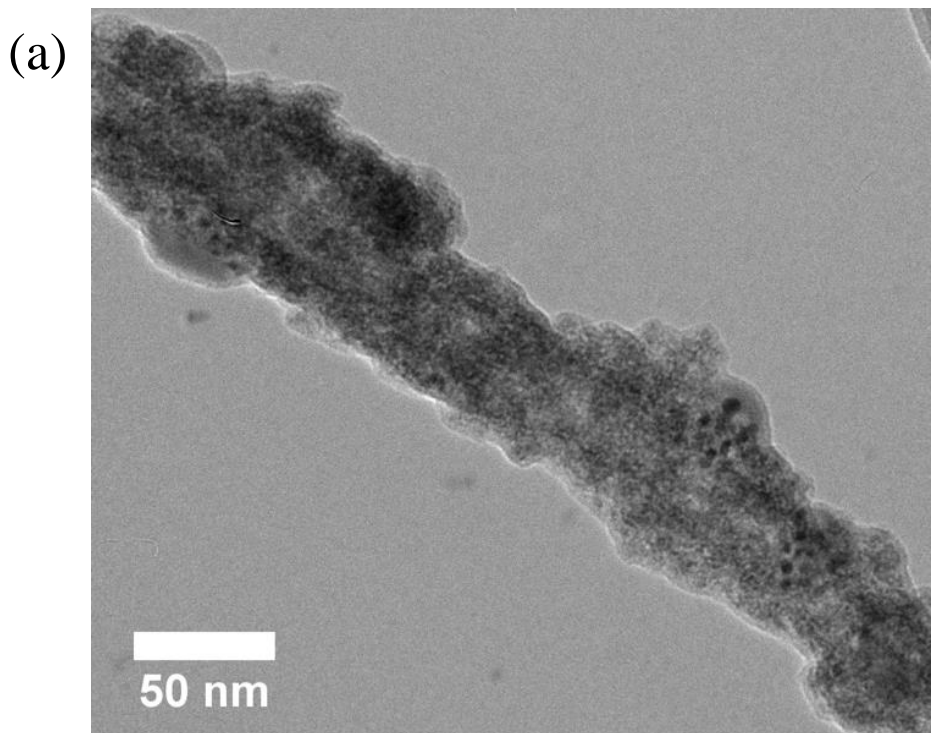
(b)
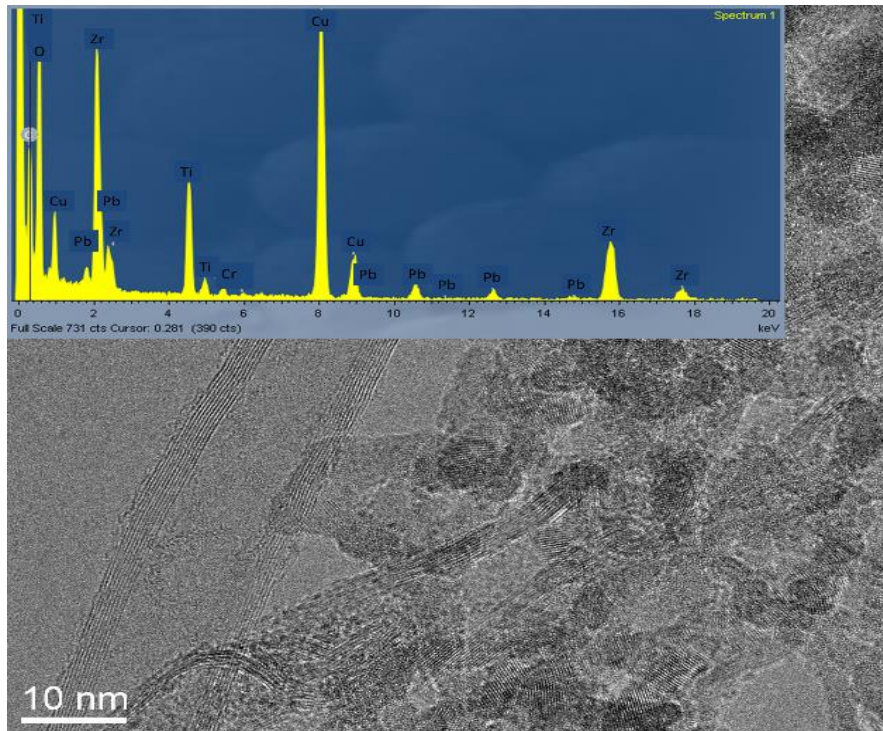
(c)
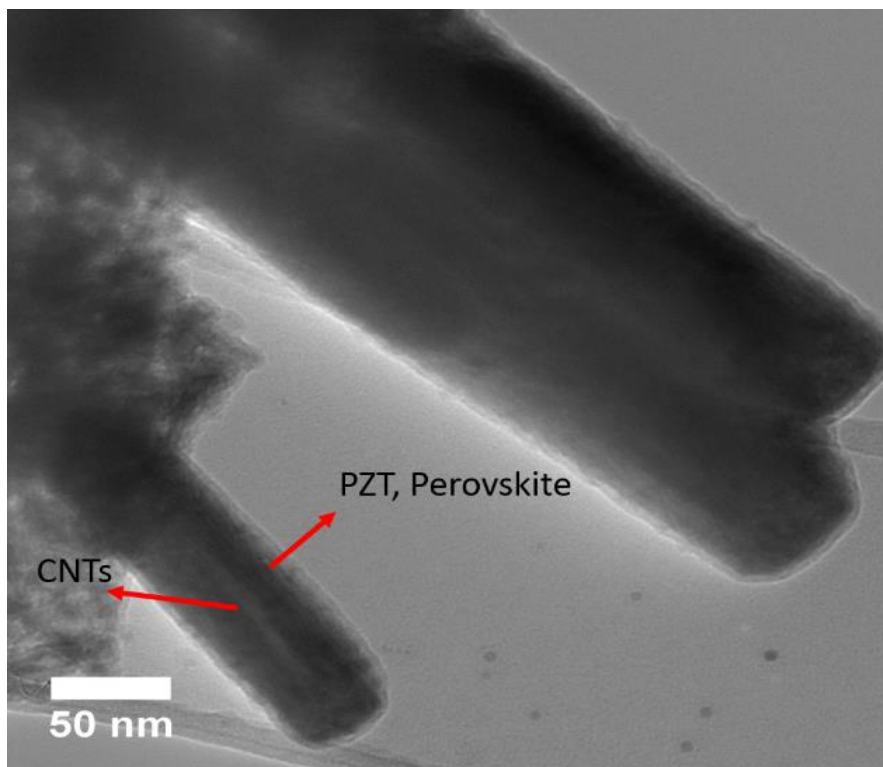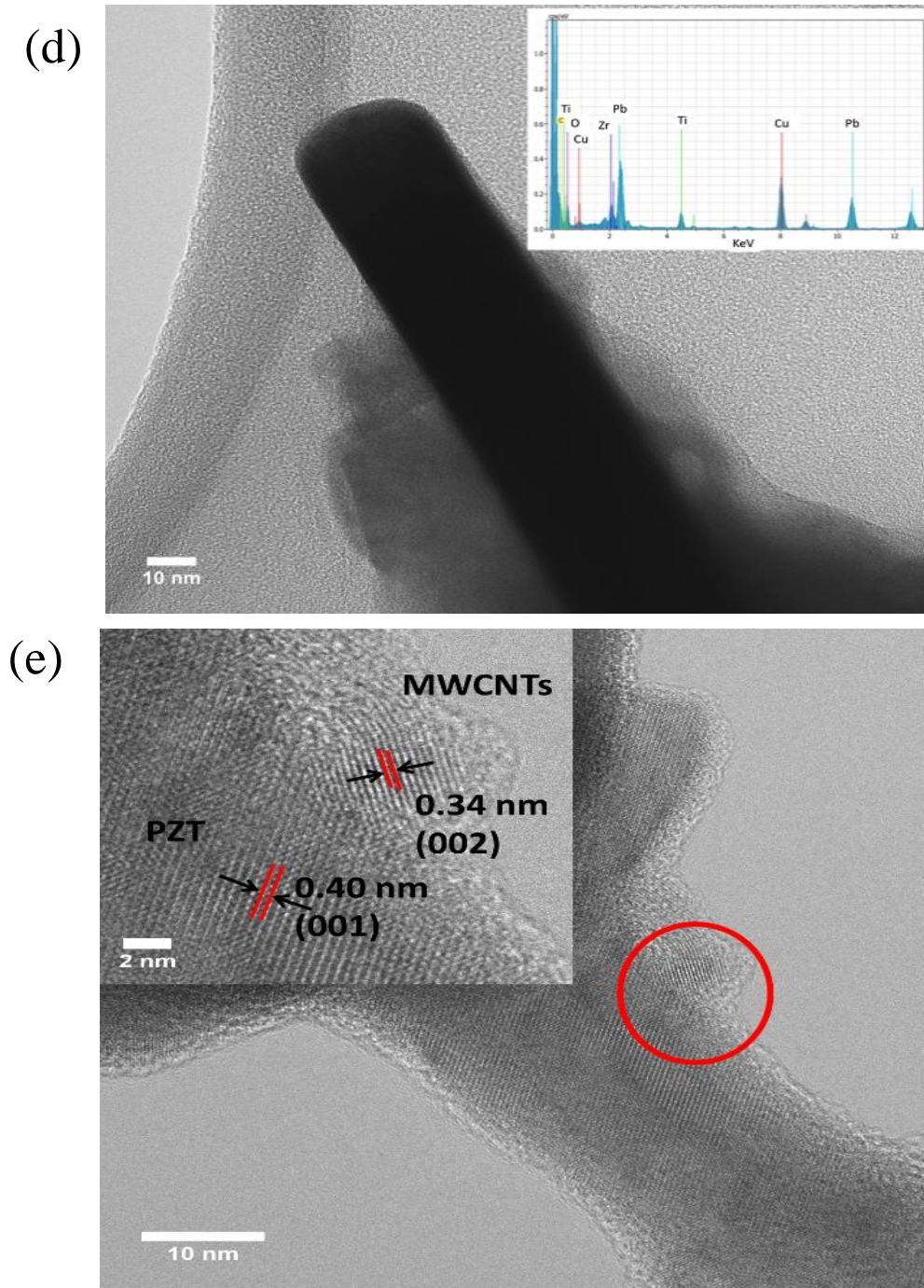
Figure 5-6 TEM micrographs of MWCNT-PZT samples showing: (a) as dried sample with a conformal covering of amorphous PZT on MWCNTs; (b) HRTEM micrograph of an amorphous sol accompanied by an inset EDS spectra confirming the presence of Pb, Zr, O and Ti (Cr and Cu are from sample holder); (c) a micrograph of sample annealed 1h at 400 ºC showing tubular shaped rods of ~100 nm with dark contrast; (d) a sample annealed 1 h at 500 ºC illustrating long range crystalline regions of perovskite along with an inset EDS spectra confirming the presence of Pb, Zr, O and Ti and (e) a HRTEM micrograph illustrating coated MWCNTs (the red circle and the inset magnified view depicts the CNT lattice spacing of 0.34 nm and d_{100} for PZT (0.40 nm)).

From the above TEM images, it is evident that the crystallisation of PZT is triggered by the MWCNTs whose surfaces act as nucleation sites for the perovskite phase. This mechanism implies that the MWCNTs lower the activation energy for perovskite PZT formation. The activation energy of phase formation of PZT and MWCNTs-PZT may be calculated by applying the Kissinger equation [340] to data from DTA (Table 5-1). The maximum energy change associated with the combustion of organics, formation of pyrochlore and perovskite phase is calculated from the DTA peaks (heating rate of 5 ºC/min), marked as: i) A (combustion of organics), B (pyrochlore) and C (perovskite), corresponding to 254, 453 and 505 ºC, respectively for PZT (Figure 5-7 (a)) and ii) A', B' and C', corresponding to 265, 366 and 395 ºC, respectively for MWCNTs-PZT (Figure 5-7 (b)). A Gaussian function was used to fit the DTA data for different heating rates and the associated maximum energy change (together with measurement error) are indicated in Table 1.

Kissinger´s model assumes that the reaction is of first order and irreversible in nature. The calculation of the activation energy is based on the temperature at which the maximum mass loss occurs, for different heating rates and is expressed as [340]:

$$\frac{d(In\alpha/T_p)}{d(T_p)} = \frac{E}{R} \qquad \text{Equation 5-1}$$

where α stands for the heating rate (5, 10, 15 and 20 ºC/min in the present study), E (kJ/mol) for the activation energy for the reaction, R (J/mol K) for the gas constant and T_p (kelvin) for peak temperature. The T_p was calculated from peak fitting and the activation energy from the slope of the variation of In (α $\alpha/(T_p)$ as a function of $1/T_p$. The activation energy for pyrochlore and perovskite phase for PZT is 248±29 kJ/mol and 68±15 kJ/mol, respectively and for MWCNT-PZT is 158±25 kJ/mol and 27±2 kJ/mol, respectively. As anticipated, the activation energy for the formation of both the pyrochlore and perovskite phase is lower for MWCNT-PZT in comparison to PZT. As shown in Figure 5-7 (a) good fitting is obtained for all the peaks. A certain uncertainty may be associated with peak A fitting, due to the combustion of the different organics present in precursor powders, still the error associated is limited.

The origin of the lower of activation energy may be explained by a combination of factors. The presence of high surface area of the tubular CNTs may act as heterogeneous nucleation sites for the oxide crystallization at low temperatures, reducing the activation energy for PZT in the presence of MWCNTs.

The perovskite formation in PZT is a sequential transition through an intermediate pyrochlore/fluorite phase. The transformation of pyrochlore into perovskite is a nucleation-controlled process where the perovskite nucleation is the rate-controlling step [365, 366]. If the nucleation energy is reduced the crystallization temperature of the perovskite phase is lowered. Indeed, low processing temperature can be obtained if the underlayer provides heterogeneous nucleation sites [367-373]. However, this seeding effect of CNTs has not been previously reported. In fact, the result is somewhat unexpected, as C-based compounds have not traditionally been considered for nucleation or for substrates for these perovskite materials. In addition, the local increase in temperature in the vicinity of the MWCNTs due to exothermic oxidation may also contribute to the overall lowering of the activation energy. MWCNTs start to oxidize at 420 ℃ and around this temperature there is the simultaneous appearance of pyrochlore and perovskite phase. Nevertheless, the major part of the CNTs remain intact up to ~500 ℃, which indicates they may be only locally oxidized, confirming the TG observations. The schematic of possible scenarios is given in Figure 5-8.
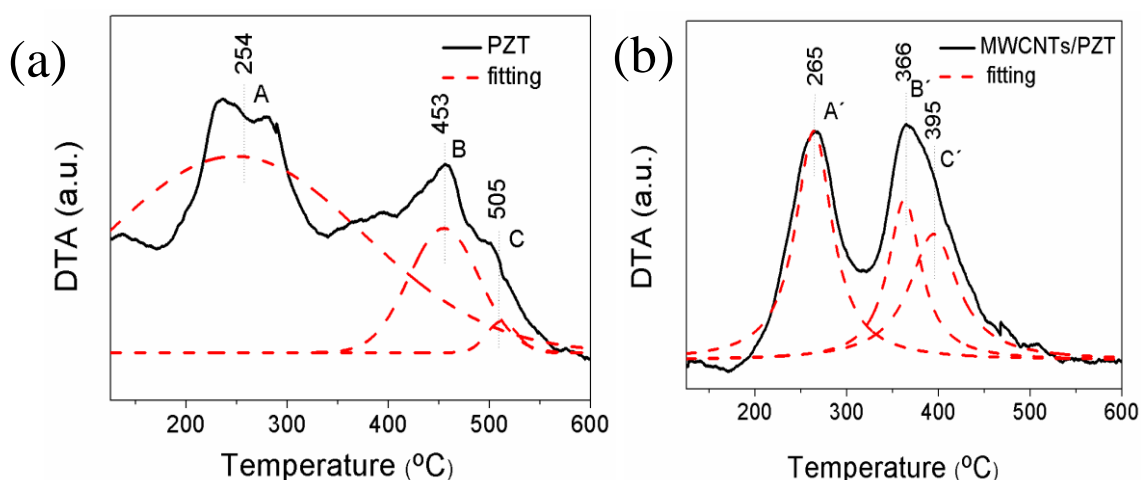
Figure 5-7 Gaussian fitting of differential thermal analysis peaks of (a) PZT and (b) MWCNT-PZT samples with an heating rate of 5 ℃/min, marked with A (A´), B (B´) and C (C´) that corresponds to the maximum energy change during the combustion of organics, formation of pyrochlore and perovskite, respectively.

Table 5-1 DTA peaks for PZT and MWCNTs - PZT samples and activation energy calculated from Kissinger equation for oxidation of organics, pyrochlore and perovskite.

Heating Rate (°C/min)	Phase	Temperature of maximum energy change for PZT	Temperature of maximum energy change for MWCNT-PZT
5	Organic	254	265
	Pyrochlore	453	366
	Perovskite	505	395
10	Organic	266	276
	Pyrochlore	464	386
	Perovskite	587	484
15	Organic	272	279
	Pyrochlore	467	390
	Perovskite	596	523
20	Organic	278	286
	Pyrochlore	476	395
	Perovskite	613	582
Activation Energy (kJ/mol) for PZT			
	pyrochlore		perovskite
	248±29		68±15
Activation Energy (kJ/mol) for MWCNTs - PZT			
	pyrochlore		perovskite
	158±25		27±2

From the application point of view the electrical response of MWCNTs-PZT is important, therefore the local piezoelectric and ferroelectric behaviour of MWCNTs-PZT annealed at 500 °C for 1 h were investigated through vertical piezoresponse force microscopy (VPFM). Figure 5-9 (a) represents VPFM phase response of MWCNTs-PZT

tube with domain of 80 nm in width and 180 nm in length and inset in Figure 5-9 (a) depicts the topography micrograph. Phase response depicts the clear dark contrast from the tube, indicating that polar domains are aligned in the opposite direction to the applied field. MWCNTs-PZT annealed at temperatures below 500 ºC do not present piezoelectric response related to their incipient degree of crystallinity. The line profile analysis, corresponding to the topography and phase signals rules out topography effects on the acquired PFM signal Figure 5-9 (b)). The local hysteresis loops obtained from MWCNTs -PZT depict the typical ferroelectric polarization behaviour, though with poor saturation up to the applied dc bias of 40 V (Figure 5-9 (c)). Various ferroelectric loops were acquired in different areas and a similar behaviour was observed. PFM measurements prove the piezoelectric and ferroelectric nature of the obtained MWCNTs-PZT and that the polarization direction can be reversed with the applied field as needed for memories.
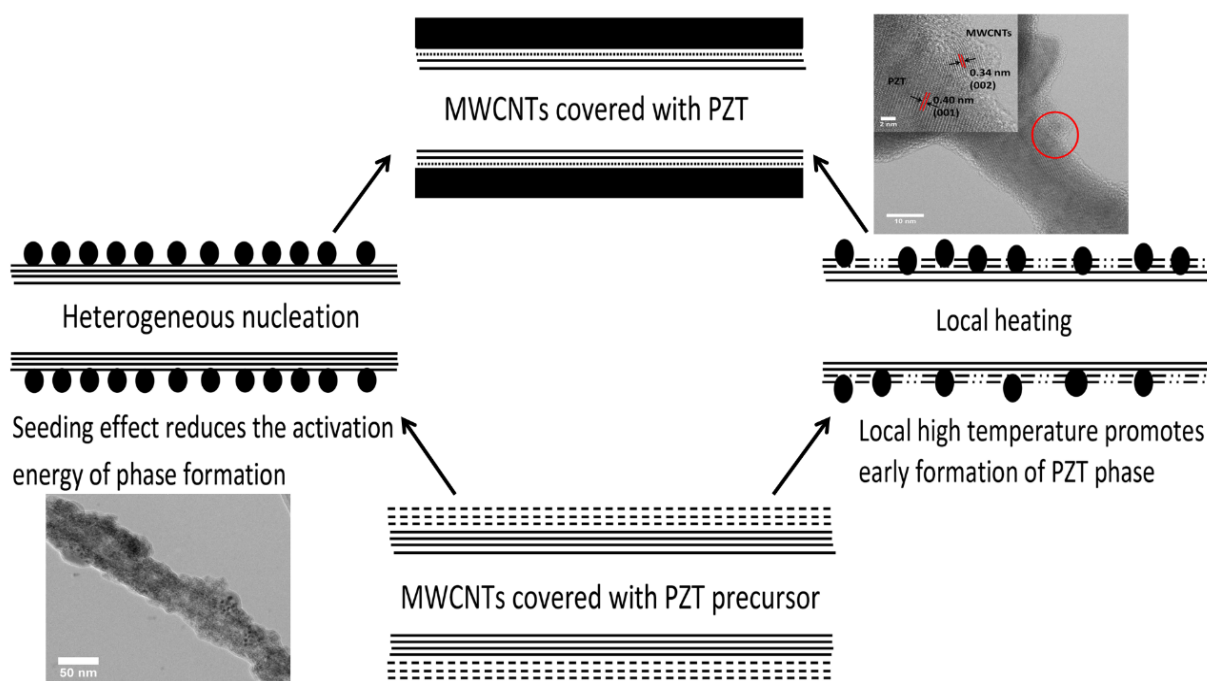
Figure 5-8 Schematic represent the two possible scenarios heterogeneous nucleation and local oxidation of MWCNTs which result in the early formation of PZT phase.
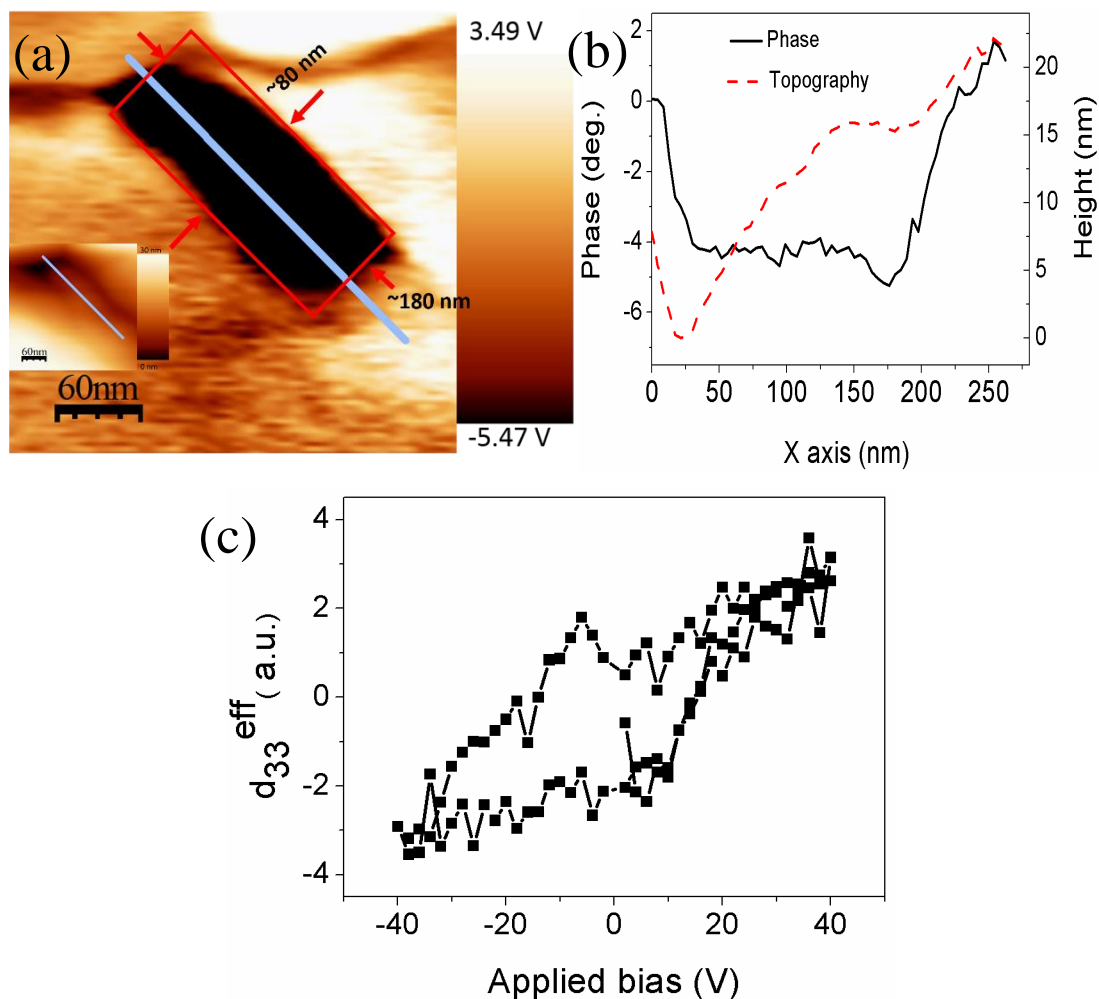
Figure 5-9 Topography (a) and VPFM phase images (b) of individual MWCNTs-PZT nanotube with domain 80 nm in width and 180 nm long, annealed at 500 ºC 1 h. Representative remanent local hysteresis loops (c). PFM measurements prove the piezoelectric and ferroelectric nature of the obtained MWCNTs-PZT.

5.4   Conclusions

The use of MWCNTs as electrodes for the formation of 1D $Pb(Zr_{1-x}Ti_x)O_3$ (PZT) nano ferroelectrics is demonstrated. For sol gel based MWCNTs-PZT structures a systematic study on the phase formation process by *in-situ* and *ex-situ* XRD, DTA, FTIR and HRTEM detected perovksite phase formation in the presence of the MWCNTs at ~100 ºC lower than without, accompanied by a decrease in activation energy from 68±15 kJ/mol for PZT and 27±2 kJ/mol. As a consequence, monophasic PZT was obtained at 575 ºC for MWCNT-PZT whereas for PZT traces of pyrochlore are still identifiable at

650 ℃. We proposed that MWCNTs act as seeds to reduce the nucleation barrier of perovksite phase formation by providing the low energy nucleation sites and the exothermic oxidation of MWCNTs. In addition the piezoelectric nature of MWCNT-PZT synthesised at 500 ℃ for 1 h was proved. Though further work is necessary, these results are of particular relevance in 3D ferroelectric nano capacitors in which CNTs are proposed as bottom electrodes.

Chapter 6

6   Multiwall carbon nanotubes (MWCNTs) – Barium titanate (BT)

Abstract:

In this chapter MWCNTs-BaTiO$_3$ (BT) structures fabricated from hydrothermal method are described. Two strategies for the functionalization of MWCNTs have been used: covalent and non-covalent functionalization.

Using covalent functionalized MWCNTs, the conventional hydrothermal synthesis, in which TiO$_2$ is previously deposited on the surface of MWCNTs prior to the reaction with Ba precursors to form BT, proved to be ineffective. However, when using a sol gel hybrid hydrothermal process BT layers > 100 nm thick conformally covered the MWCNTs. MWCNTs-BT structures synthesised at 160 ºC are ferroelectric and exhibit an electromechanical response of 15 pm/V.

However the process can be further improved if the MWCNTs are non-covalent functionalized, with sodium dodecyl sulfate (SDS). In this case the formation of carbonates is very residual and the SDSMWCNTs-BT structures obtained are typically 20 to 200 nm in diameter with lengths up to ~5 μm. These nano structures exhibit ferroelectric and piezoelectric behaviour, with an effective piezoelectric coefficient of ~2 pm/V, as assessed by piezo force microscope (PFM).

This work not only demonstrates how to adapt the hydrothermal process to successfully cover CNTs with ferroelectric oxides, but also proves the concept of 3D nano capacitors based on carbon nanotubes prepared by a low temperature and low cost process. This strategy can be used for many different ferroelectric oxides.

6.1 Introduction

In the previous chapter the feasibility to synthesise MWCNTs-PZT ferroelectric nano structures was proved.

Up to now, compositions within the solid solution between $PbZrO_3$ and $PbTiO_3$, designated as PZT ($Pb_{1-x}Zr_xTiO_3$), have been widely used in ferroelectric memories, piezoelectric actuators, sensors and transducers, and more recently as promising energy harvesters. However, the use of PZT that contains more than 60 wt% of lead will soon be severely restricted, due to lead toxicity [182]. Among the several possible lead free candidates to substitute PZT, $BaTiO_3$ based compositions are of relevance.

BT is a well-known lead free perovskite with high dielectric constant (~2000, at 1 kHz), low dielectric loss (0.02, at 1 kHz) and Curie temperature at ~125 ℃ [374, 375]. BT is used in many applications such as multilayer ceramic capacitors (MLCCs), temperature coefficient resistors, ultrasonic transducers, piezoelectric devices, and tuneable phase array antennas. BT synthesis by solid state reaction is typically performed around 1100 to 1300 ℃ [376]. BT can however be synthesised at around 650 ℃ to 900 ℃ by chemical solution methods such as sol gel [377] and co-precipitation [378] but these temperatures are still too high to avoid oxidation of MWCNTs (which is around 500 ℃). Therefore, for BT and other lead-free ferroelectrics, there is a need to explore low temperature processes for their crystallization on MWCNTs.

Hydrothermal synthesis is a low temperature chemical synthesis process by which crystalline oxides particles [379] and/or thin films [380] can be obtained from reaction in aqueous media at relative elevated temperature (> 25 ℃) and pressure (> 100 KPa) [379]. A wide range of different oxides have been fabricated from 80 to 300 ℃, such as $BaTiO_3$ [320, 381, 382], PZT [383] and ZnO [313]. Hence hydrothermal synthesis might be suitable for the synthesis of ferroelectric oxides in combination with MWCNTs. In previous reports, hydrothermal synthesis was used in the fabrication of MWCNTs-BT composite in which MWCNTs acted as metallic fillers to improve the thermal and electrical properties of the composites [28,29]. The MWCNTs-BT composites were hydrothermally synthesised in two steps. First, TiO_2 was immobilized on the surface of MWCNTs using a sol gel method. The TiO_2-MWCNTs structures were then reacted with barium acetate to obtain MWCNTs-BT powders [18-20] but conformal coverage of individual tubes was not the main objective of the research. MWCNTs-BT have also been fabricated by the sol gel method [23, 24, 384]. In this

method, MWCNTs-BT were annealed at 700 ºC in N_2 subsequent to deposition to achieve a final BT layer, ~5-10 nm thick. Phase formation and interfacial aspects were not reported nor did any of the above studies address the ferroelectric properties of MWCNTs-BT.

Within this context, in this work we exploit two different approaches to cover covalent functionalized MWCNTs with BT by hydrothermal method. In the first methodology MWCNTs are covered with a titanium based solution, followed by hydrothermal reaction with a Ba precursor to obtain BT on top of the MWCNTs. In the second methodology, a BT sol was used to cover MWCNTs followed by a hydrothermal reaction. A systematic study of the fabrication conditions and aspects of the synthesis is presented and the ferroelectric properties reported.

With the use of sol gel hybrid method we demonstrate the localized covering of covalent functionalized MWCNTs with BT using hydrothermal method. However, there is difficultly in conformal covering of MWCNTs up to large area. Therefore, we use non-covalent functionalize MWCNTs with SDS in order to improve the coverage area of MWCNTs with BT. The advantage of non-covalent functionalization is: it provides the large functionalized area and do not infer the electrical properties of the MWCNTs. In this context, the SDSMWCNTs-BT were fabricated via sol gel hybrid hydrothermal method and various aspects from synthesis to ferroelectric properties are discussed.

6.2   Experimental

MWCNTs used in this work were synthesised by a chemical vapor deposition technique (CVD). Prior to the coating with $BaTiO_3$, the tubes were purified and acid treatment with 5 M HNO_3 results in covalent functionalization. The average diameter and length of the tubes is around 15 - 60 nm and ~ 10 μm, respectively (for more detail refer Chapter 3 and 4).

Two synthesis methodologies were used to cover MWCNTs with BT.

Methodology One: Based on the previously reported methodology [19], 0.1 M of titanium solution was prepared from titanium(IV) isopropoxide (> 97 % purity, Fluka) mixed with deionized water, acetylacetone (> 99% purity, MERCK) and ethanol (> 99.5 % purity, Panreac) in the mol. ratio of 1:3:3:20. To minimize the presence of CO_2, which may promote the formation of $BaCO_3$, deionized water was boiled prior to being used throughout this work.

MWCNTs (40 mg, 4 wt. %) were dispersed in the titanium solution using a probe ultra-sonicator (UP200S, FORLAB) for 15 min followed by bath ultra-sonication (Branson, USA, 40 kHz) for 2 h. To encourage complete reaction, the solution was stirred at 70 ℃ for 2 h, followed by a filtrating and heating (100 ℃ - 24 h) until MWCNTs-TiO$_2$ powders were obtained. The amorphous powders were heat treated at 400 ℃ for 1 h to obtain MWCNTs covered with crystalline TiO$_2$ (MWCNTs - TiO$_2$). In the second step, as-prepared MWCNTs-TiO$_2$ were mixed with the Ba precursor solution in 1:1 mol. ratio. 0.1 M solutions of Ba acetate (99 % purity, ACS), Ba hydroxide (98 % purity, ACS) and Ba acetate with Na hydroxide (5 M) (NaOH, 98 % purity, ABCR) were used as the Ba precursors. MWCNTs-TiO$_2$ particles were dispersed in the Ba solution by stirring for 1 h at 30 ℃. The pH of the MWCNTs-BT solution was ~10 (for the acetate and hydroxide precursors) and ~13 in case of Ba acetate with NaOH. The solutions prepared from the different Ba precursors were transferred to 70 ml teflon-lined stainless-steel autoclaves, 40 % full. The hydrothermal reaction was carried out in the autoclave at 160 ℃ for 12 h to obtain the final MWCNTs-BT. The MWCNTs-BT particles were filtered and washed with distilled water until the pH of the solution came close to neutral. The powders were dried overnight at 100 ℃ before characterization.

Methodology Two: In the second methodology, 0.1 M of BT solution was used for the synthesis of MWCNTs-BT. Initially, a stabilized titanium solution was prepared by mixing titanium(IV) isopropoxide (> 97 % purity, Fluka) with acetylacetone (> 99% purity, MERCK) and ethanol (> 99.5 % purity, Panreac) in mol. ratio of 1:2:5. Ba acetate solution, prepared from barium acetate (99% purity, ACS) dissolved in deionized water (5 wt. ratio of Ba), was added to the previously prepared titanium solution. A clear and stable solution of BT was obtained after mixing for 1 h at 70 ℃. 25 mg of MWCNTs were added to the BT solution which was mixed by using an ultra-high sonicator (UP 200S) for 5 min, followed by 1 to 2 h in an ultrasonic bath (Branson 1510). The MWCNTs-BT solution was stirred and heated at 70 ℃ for 2 h to obtain homogeneity (a black solution, with no white precipitation). 5 M potassium hydroxide solution (KOH, ≥ 85 % purity, Sigma Aldrich) was added to the MWCNTs-BT solution to promote the nucleation of BT, which was observed as the formation of white amorphous precipitates.

The precipitated MWCNTs-BT solution was transferred to a teflon lined stainless-steel autoclave, ~ 40 % full. Hydrothermal treatment was carried at time and temperatures, ranging from 0.5 to 24 h and 100 to 250 ℃. Growth and crystallization occurred under autogenous

pressure inside the autoclave after being subjected to various temperatures. The crystalline MWCNTs-BT powders were filtered and washed with distilled water until the pH was neutral. The powders were dried overnight in the oven at 100 °C. The various steps to obtain MWCNTs-BT in Methodologies One and Two are illustrated in Figure 6-1.

(a)

Titanium isopropoxide, deionized water, acetylacetone and ethanol (1:3:3:20 mol.)

↓

Stirred at 60 °C for 2 h

↓

Add Multiwall Carbon Nanotubes (MWCNTs) ⟹ Transparent titanium solution

↓

Mixed the solution using ultra high probe sonicator (5 -15 min.) and bath ultra-sonicator (1-2 h), followed by mixed for 2 h at 70 °C

↓

Dark black MWCNTs-TiO$_2$ solution

↓

Barium salts dissolved in deionized water (1:5 mol.)

↓

Solution filtrated and dried in oven at 100 °C for 24 h

↓

Stirred at 25 °C for 30 min

↓

Heat treatment at 400 °C for 1 h

↓

Add transparent barium solution ⟹ MWCNTs-TiO$_2$ crystalline powders were obtained

↓

Mixed for 1 h

↓

Solution transferred to autoclave and then to oven at 160 °C for 12 h

↓

Filtered the solution and washed with deionized water

↓

MWCNTs-BT powders

(b)

```
┌─────────────────────────┐        ┌─────────────────────────────┐
│ Barium acetate dissolved │        │  Titanium isopropoxide,     │
│   in deionized water     │        │ acetylacetone and ethanol   │
│       (1:5 mol.)         │        │        (1:2:5 mol.)         │
└───────────┬─────────────┘        └──────────────┬──────────────┘
            ▼                                      ▼
┌─────────────────────────┐        ┌─────────────────────────────┐
│ Stirred at 25 °C for 30 │        │  Stirred at 60 °C for 2 h   │
│          min            │        │                             │
└───────────┬─────────────┘        └──────────────┬──────────────┘
            ▼                                      ▼
┌─────────────────────────┐        ┌─────────────────────────────┐
│  Transparent barium     │───────▶│ Transparent titanium solution│
│      solution           │        │                             │
└─────────────────────────┘        └──────────────┬──────────────┘
                                                   ▼
                                   ┌─────────────────────────────┐
                                   │   Stirred at 70 °C for 2 h  │
                                   └──────────────┬──────────────┘
┌─────────────────────────┐                       ▼
│  Multiwall Carbon       │        ┌─────────────────────────────┐
│  Nanotubes (MWCNTs)     │───────▶│  Stabilized transparent     │
│                         │        │  solution of BT was obtained│
└─────────────────────────┘        └──────────────┬──────────────┘
                                                   ▼
                                   ┌─────────────────────────────┐
                                   │ Mixed using ultra high probe│
                                   │ sonicator (5 min.) and bath │
                                   │ ultra-sonicator (2 h),      │
                                   │ followed by stirring for    │
                                   │ 2 h at 70 °C                │
                                   └──────────────┬──────────────┘
┌─────────────────────────┐                       ▼
│  Potassium hydroxide    │        ┌─────────────────────────────┐
│  (5 M) solution         │───────▶│  Dark black MWCNTs-BT       │
│                         │        │  solution                   │
└─────────────────────────┘        └──────────────┬──────────────┘
                                                   ▼
                                   ┌─────────────────────────────┐
                                   │ White precipitated MWCNTs-BT│
                                   │ formed, nucleation occurred │
                                   └──────────────┬──────────────┘
                                                   ▼
                                   ┌─────────────────────────────┐
                                   │      Stirred for 5 min      │
                                   └──────────────┬──────────────┘
                                                   ▼
                                   ┌─────────────────────────────┐
                                   │ Precipitated MWCNTs-BT      │
                                   │ transferred to autoclave    │
                                   │ and then to oven            │
                                   └──────────────┬──────────────┘
┌─────────────────────────┐                       ▼
│ Filtered the solution   │◀──────┌─────────────────────────────┐
│ and washed with         │       │  Heat treated at different  │
│ deionized water         │       │  temperature and time       │
│                         │──────▶│  MWCNTs-BT powders          │
└─────────────────────────┘       └─────────────────────────────┘
```

Figure 6-1 Flow chart illustrates the steps followed to obtained MWCNTs-BT via (a) Methodology One and (b) Methodology Two.

In order to have better wettability, the MWCNTs were non-covalently functionalized with sodium dodecyl sulfate (SDS), named as SDSMWCNTs. Procedure for functionalization detailed in Chapter 3.

For covering SDSMWCNTs with BT methodology two was used (sol gel hybrid hydrothermal method). Two different concentration of BT solution (0.1 and 0.01 M) were used

to cover SDSMWCNTs. The SDSMWCNTs (10 mg) were added slowly to the BT solution and the solution was mixed using a probe ultra-high frequency sonicator (UP 200S) for 5 min, followed by sonication using a ultra-sonication bath (Branson 1510) for 2 h. SDS MWCNTs-BT solution was heated at 70 ºC for 2 h to get homogenous solution (a dense black solution, with no white precipitation). The potassium hydroxide (KOH, ABCR, 85 %) solution (5 M) was added to the SDSMWCNTs-BT solution to increase pH to 13 or above, this results in supersaturation and nucleation occurs in the form of a white precipitate. The precipitated SDSMWCNTs-BT solution was transferred to a teflon lined stainless-steel autoclave, which was filled up to 40 % of the total capacity and the autoclaves exposed to hydrothermal treatment to obtain SDSMWCNTs-BT powders. The obtained SDSMWCNTs-BT powders were filtered and washed by distilled water until the pH value come close to neutral. The deionized water was boiled prior to be used throughout the experiments, in order to minimize CO_2 presence, which may contribute to the formation of $BaCO_3$. The obtained powders were dried in an oven at 100 ºC for 12 h, before being used for the characterization of the phase formation, morphology and electrical properties.

The obtained powders were dried in an oven at 100 ºC for 12 h, before being used for the characterization of the phase formation, morphology and electrical properties. Figure 6-2 schematic illustrates the steps followed for the synthesis of SDSMWCNTs-BT.

The phase formation of BT for all samples and degree of crystallinity were assessed by X-ray diffraction (Philips, X´Pert diffractometer and Cu-Kα radiation), Raman spectroscopy, (RFS100/S FT using a 534 nm excitation source) and Fourier Transform InfraRed (FTIR) spectroscopy (Mattson, Madison, WI, USA, 7000 FTIR spectrometer). The microstructures of the composites were analysed by Scanning Electron Microscopy (SEM) (Hitachi SU-70 (S-4100)), Transmission Electron Microscopy (TEM) (300 kV Hitachi H9000-NA) and High Resolution Transmission Electron Microscope (HRTEM, JEOL 2200 FS). SDSMWCNTs-BT powders for TEM were prepared by dispersing them in to the chloroform and later a drop from the solution was transferred to TEM lacey gird (Agar).

The topography of MWCNTs-BT and SDSMWCNTs-BT was determined using atomic/piezo-force microscopy whilst simultaneously obtaining local piezoelectric response (MFP-3D Asylum Research Atomic Force Microscope (AFM)). The measurements were carried out using soft Pt-coated cantilever with spring constant of 0.1-0.4 N/m and resonance frequency of 12 - 18 kHz (MikroMasch, XSC11). Samples for AFM/PFM were prepared by

dispersing MWCNTs-BT and SDSMWCNTs-BT structures in ethanol, and depositing them on platinised silicon substrate by spin coating. To calibrate the AFM deflection sensitivity, the force-curve method is used- which is also used to calibrate vertical PFM. This is done by taking the slope (in nm/V) of the linear (contact) region of a force curve, giving the distance moved by the tip, per voltage change on the photo detector.
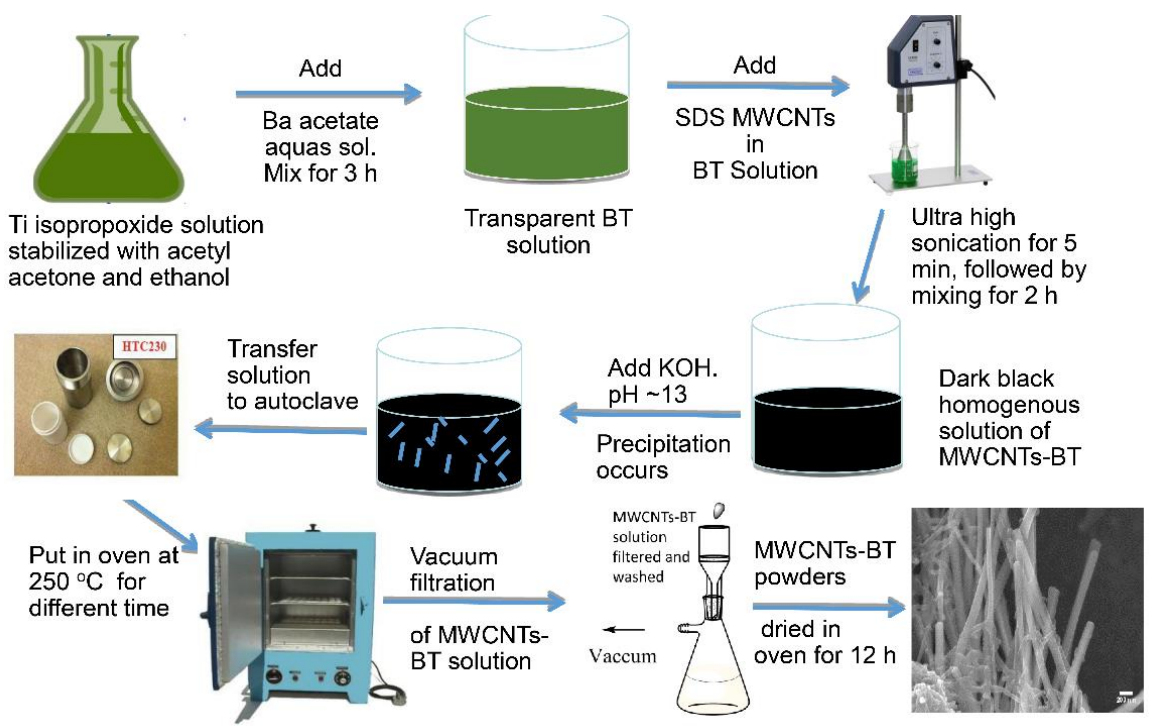
Figure 6-2 Schematic illustrates the processing steps to obtained MWCNTs-BT (SDSMWCNTs-BT) tubes.

6.3   Results and discussion

6.3.1   Covering covalent functionalized MWCNTs with BT

To follow the phase formation, MWCNTs-BT obtained from Methodology One were studied by XRD, SEM and TEM. Figure 6-3 (a) presents the XRD pattern of MWCNTs-TiO$_2$ heat treated 1 h at 400 ºC. XRD peaks match with the JCPDS #21-1272, confirming the formation of anatase. Figure 6-3 (b) shows the XRD pattern of MWCNTs-BT obtained from different Ba precursors at 160 ºC for 12 h. The MWCNTs-BT fabricated from Ba hydroxide precursor results in the formation of mainly BaCO$_3$ with only a few peaks with low intensity

that match cubic BT. XRD peaks corresponding to TiO_2 were not identified, which may be due to the dissolution of TiO_2 crystalline particles into Ti(OH)aq. XRD pattern obtained from MWCNTs-BT with Ba acetate precursor still exhibited $BaCO_3$ albeit with a higher volume fraction of $BaTiO_3$ (Figure 6-3 (b). However, with the addition of NaOH as well as Ba acetate, the reactivity increased [385] and monophasic BT was obtained, with no traces of carbonate in XRD pattern.

SEM micrographs of MWCNTs-TiO_2 show the presence of TiO_2 crystalline particles about 10 -30 nm on the surface of the MWCNTs Figure 6-4 (a). TEM micrographs from MWCNTs-BT obtained from Ba acetate-NaOH solution depict agglomerates of BT particles (150 nm) in contact with MWCNTs after hydrothermal reaction at 160 °C for 12 h (Figure 6-4) but not nucleating directly on their surface. Moreover, when Ba acetate and Ba hydroxides solutions were used, areas with no TiO_2 particles promoted the formation of $BaCO_3$. The detachment of TiO_2 from MWCNTs during the synthesis of MWCNTs - BT can be explained by a mechanism of homogeneous dissolution and recrystallization [310] in which TiO_2 dissolution into Ti(OH)aq results in the removal of TiO_2 particle from the surface of MWCNTs and formation of $BaTiO_3$ away from the surface of MWCNTs. A further reason for the detachment of TiO_2 might be weak bonding between MWCNTs and TiO_2. The schematic of the possible steps during the dissolution and recrystallization is presented in Figure 6-5.
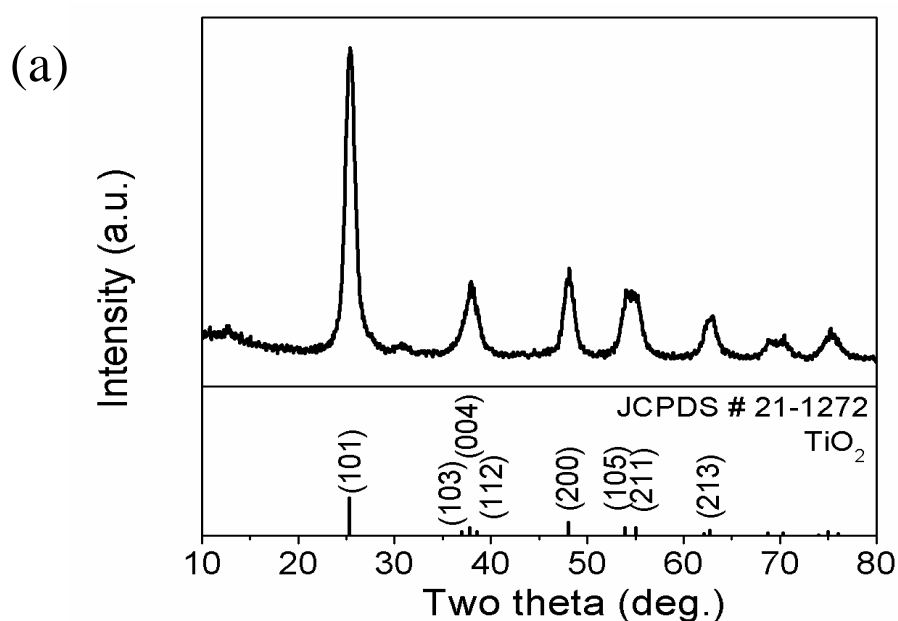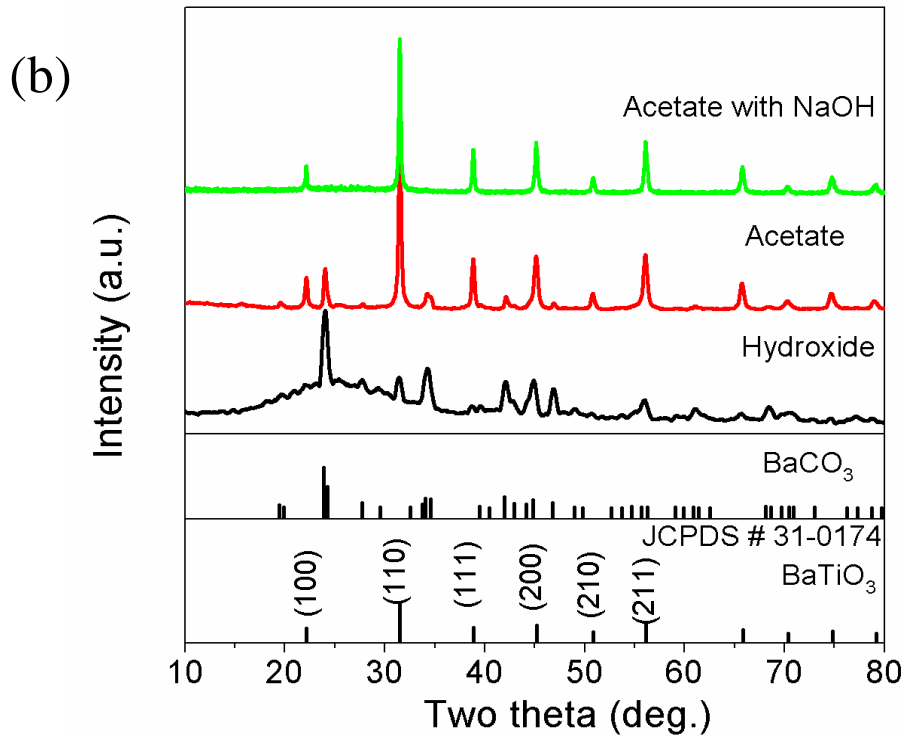
Figure 6-3 XRD patterns of (a) MWCNTs-TiO₂ particles synthesised at 400 ºC, JCPDS #21-1272 and (b) MWCNTs-BT obtained from the reaction of MWCNTs-TiO₂ with different barium precursors at 160 ºC for 12 h (Methodology One). The XRD patterns reveal monophasic BT (without BaCO₃) only when Ba acetate with NaOH was used.
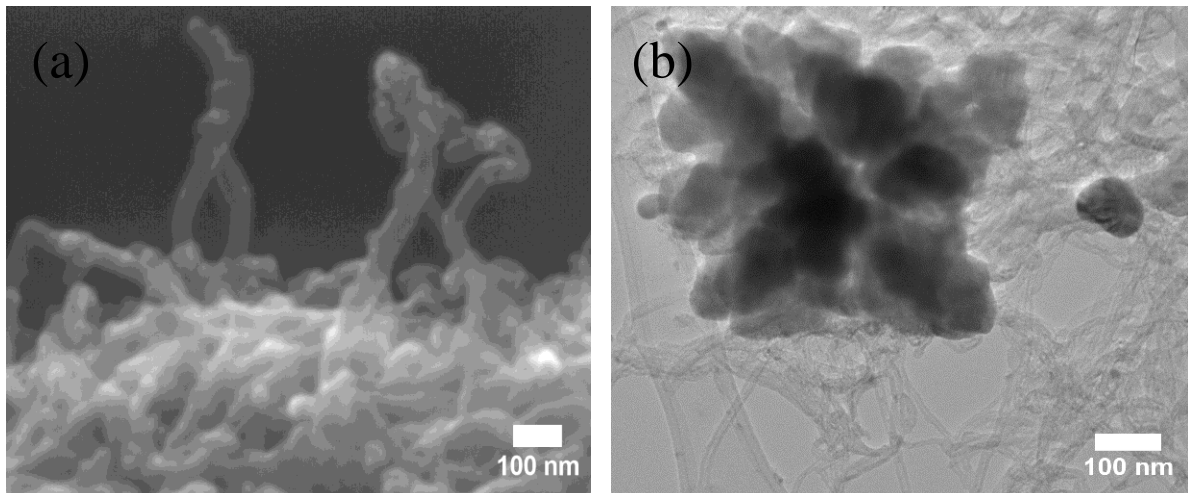
Figure 6-4 (a) SEM micrograph depicting the coverage of MWCNTs with TiO₂ particles, after synthesis for 1h at 400 ºC and (b) TEM micrograph of MWCNTs-BT powders obtained from Ba acetate and NaOH solution with a hydrothermal reaction at 160 ºC for 12 h (Methodology One). An aggregate of BT particles (150 nm) is formed, not attached to the surface of MWCNTs.
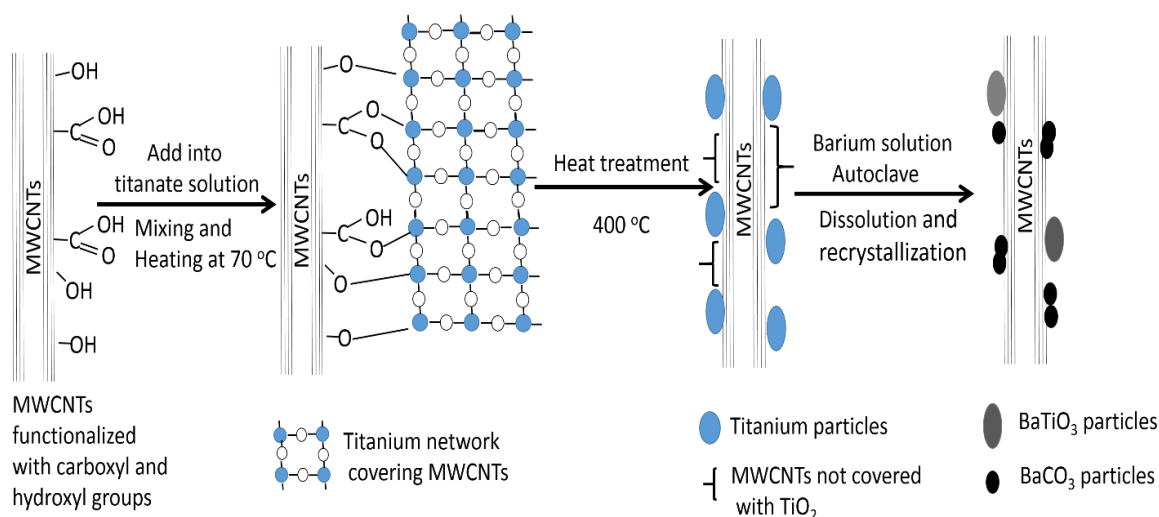
Figure 6-5 Schematic representation of the formation of BT from dissolution and recrystallization. TiO₂ particles detach from the MWCNTs surface, which results in the formation of BaCO₃ due to the exposure of MWCNTs surface to Ba precursors.

As a consequence of the poor results obtained by pure hydrothermal synthesis, a second (Methodology Two) sol gel/hydrothermal hybrid processing route was devised. MWCNTs were dispersed in a BT solution and exposed to hydrothermal conditions to obtain MWCNTs-BT. The phase formation of MWCNTs-BT fabricated from the hybrid sol gel / hydrothermal method was characterized by XRD as a function of synthesis time (Figure 6-6). All the diffraction peaks were indexed as cubic BT (JCPDS No.: #31-0174) with lattice parameter, *a* = 4.031 Å. As-precipitated MWCNTs-BT powders consisted of $BaCO_3$ phase with no crystalline BT phase. With the processing time of 0.5 h the crystalline BT formed and its crystallinity increased with processing time. With the increase in the synthesis time from 0.5 to 5 h the amount of $BaCO_3$ decreased significantly, as indicated by the disappearance of the $BaCO_3$ peak $2\theta = 23.09$. Monophasic BT is formed at ≥ 10 h at 160 ºC.

The cubic versus tetragonal BT phase assemblage as a function of synthesis time can be studied from splitting of the (200) peak at $2\theta \sim 45$ º. For MWCNTs-BT obtained at 160 ºC (0.5 and 2 h) the cubic phase is dominant. With the increase in the synthesis time from 5 to 24 h the peak of $BaTiO_3$ become broader and shifts towards the right, indicating the presence of a doublet (002 and 200) consistent with tetragonal BT (Figure 6-6 (b)). However, broadening of the 200 peak in comparison to solid state synthesised BT [386] indicates low tetragonality (c/a

→ 1), possibly associated with intrinsic size effects. The largest c/a ratio was obtained for MWCNTs-BT synthesised 10 h at 160 °C.

The evolution of BT phase assemblage as a function of temperature from 100 to 250 °C for a synthesis time of 2 h was also investigated, Figure 6-6 (c-d). Almost pure BT phase on the surrounding of MWCNTs were obtained at 250 °C for 2 h, whereas for lower reaction temperature the presence of $BaCO_3$ diffraction peaks are visible in XRD pattern (Figure 6-6 (c)). The formation of $BaCO_3$, during the synthesis of $BaTiO_3$ is inevitable due to its low activation energy, in comparison to BT. However, with the further input of energy in terms of synthesis time and temperature $BaCO_3$ converts to BT [382]. The transformation from pseudocubic to tetragonal phase was also monitored using the (200) peak at 2θ ~ 45, Figure 6-6 (d). MWCNTs-BT synthesised ≤200 °C are dominated by cubic BT but at 250 °C the peak is shifted to the right, indicating the presence of tetragonal BT phase.

(d)
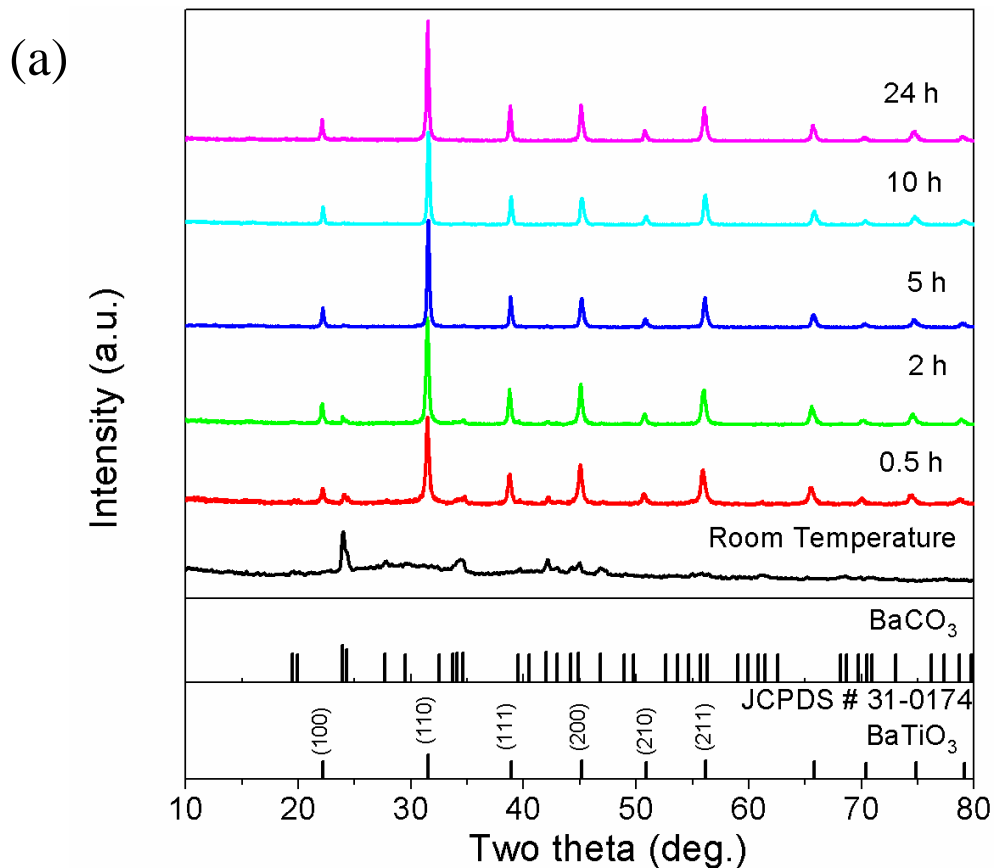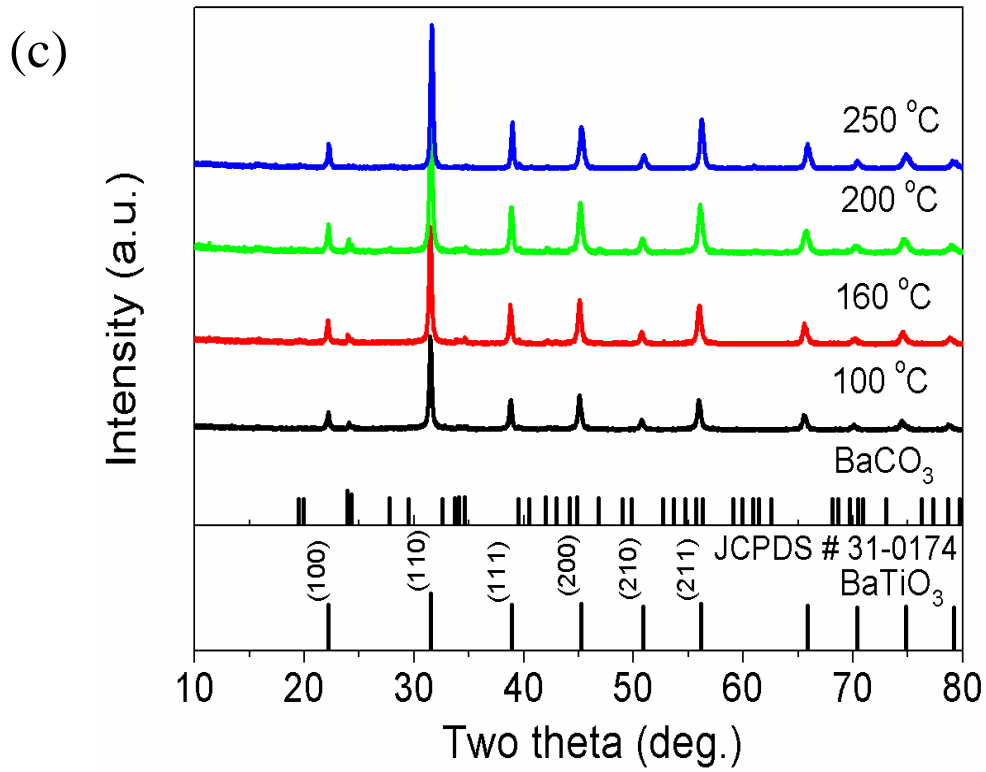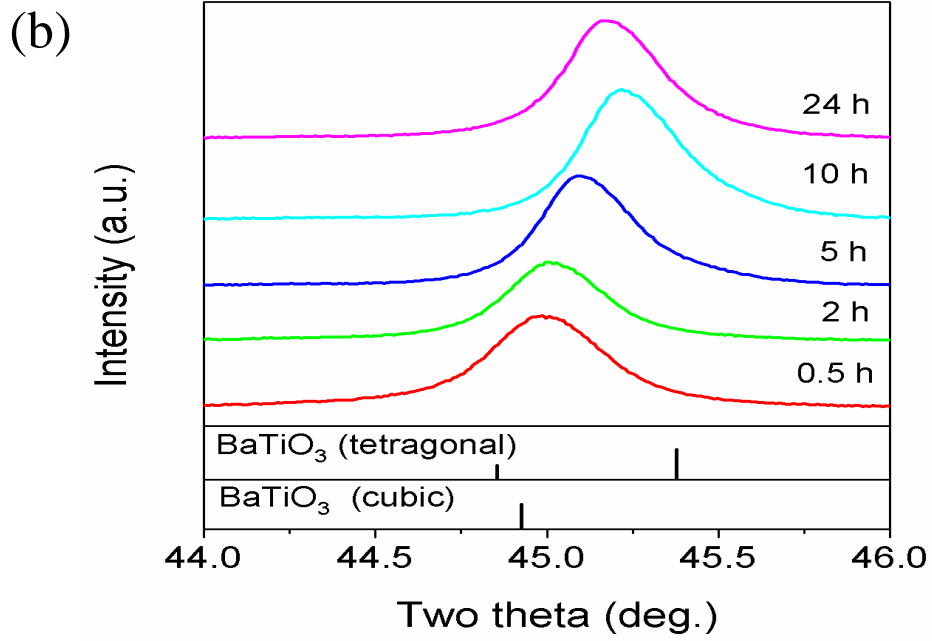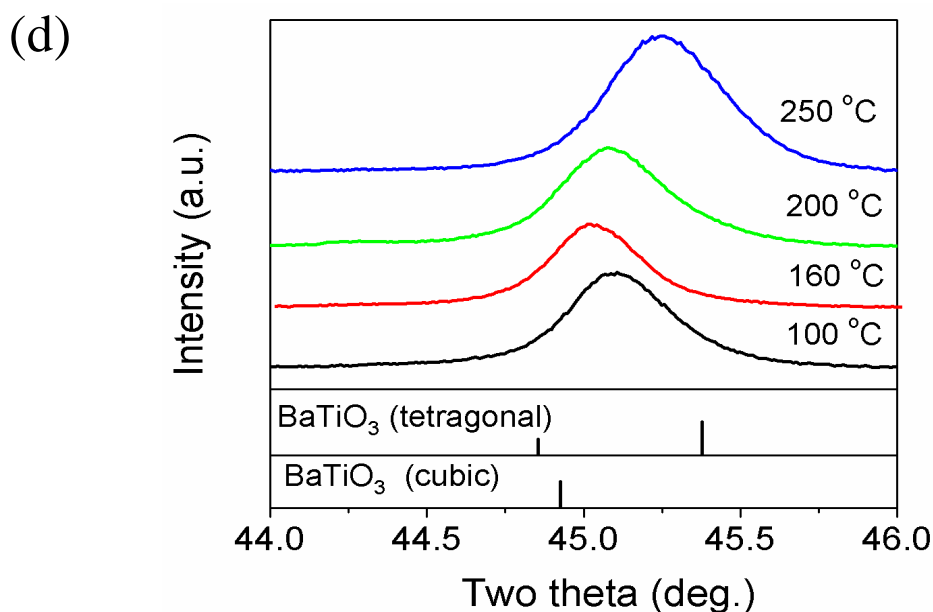
Figure 6-6 XRD patterns of (a) MWCNTs-BT obtained at various synthesis time at 160 ºC, (b) cubic to tetragonal broadening of the 200 peak for MWCNTs-BT obtained at various synthesis time at 160 ºC, (c) MWCNTs-BT obtained at various temperature for 2 h; and (d) cubic to tetragonal 200 broadening of MWCNTs-BT obtained at various temperatures for 2 h. The maximum tetragonal phase was observed for MWCNTs-BT fabricated at 160 ºC for 10 h.

FTIR transmittance spectra for the MWCNTs-BT derived from Methodology Two at various times and temperatures are depicted in Figure 6-7 (a, b). The transmittance peaks around 575 and 420 cm^{-1} are the fingerprint of BT, which occurred due to the stretching and bending of Ti-O-Ti octahedron [380]. The intensity and the area under this peak increased with increasing time and temperature of synthesis. The peak at 1637 cm^{-1} refers to the characteristic peak of carbon skeleton (stretching of C=C) [387] which is present in all of MWCNTs-BT and its intensity does not change. Peaks at 1073 and 3438 cm^{-1} correspond to the functional carboxyl and hydroxyl groups, respectively [388]. The decrease in the intensity of the carboxyl and hydroxyl peaks with the synthesis time and temperature might be due to the replacing of functional groups with BT crystallites. The peak at 1448 cm^{-1} is the signature of the carboxylate (COO^{-}) group due to symmetric and asymmetric stretching. The intensity of the band decreases with the increase in the synthesis time due to the decomposition of CO$_2$ associated with the thermal degradation of carbonate impurities [389]. The peak around 864 cm^{-1} is the fingerprint of the carbonate phase [18]. The intensity of the carbonate peak is reduce for MWCNTs-BT with increasing synthesis time from 0.5 min to 24 h at 160 ºC and as a function of increasing temperature (100 ºC to 250 ºC) for 2 h synthesis. FTIR results corroborate previous XRD

observations (Figure 6-6) but a small peak corresponding to carbonate is present in the FTIR spectra for MWCNTs-BT synthesised at 160 ºC for 10 h and 24 h does not correspond to an equivalent peak in the XRD patterns.
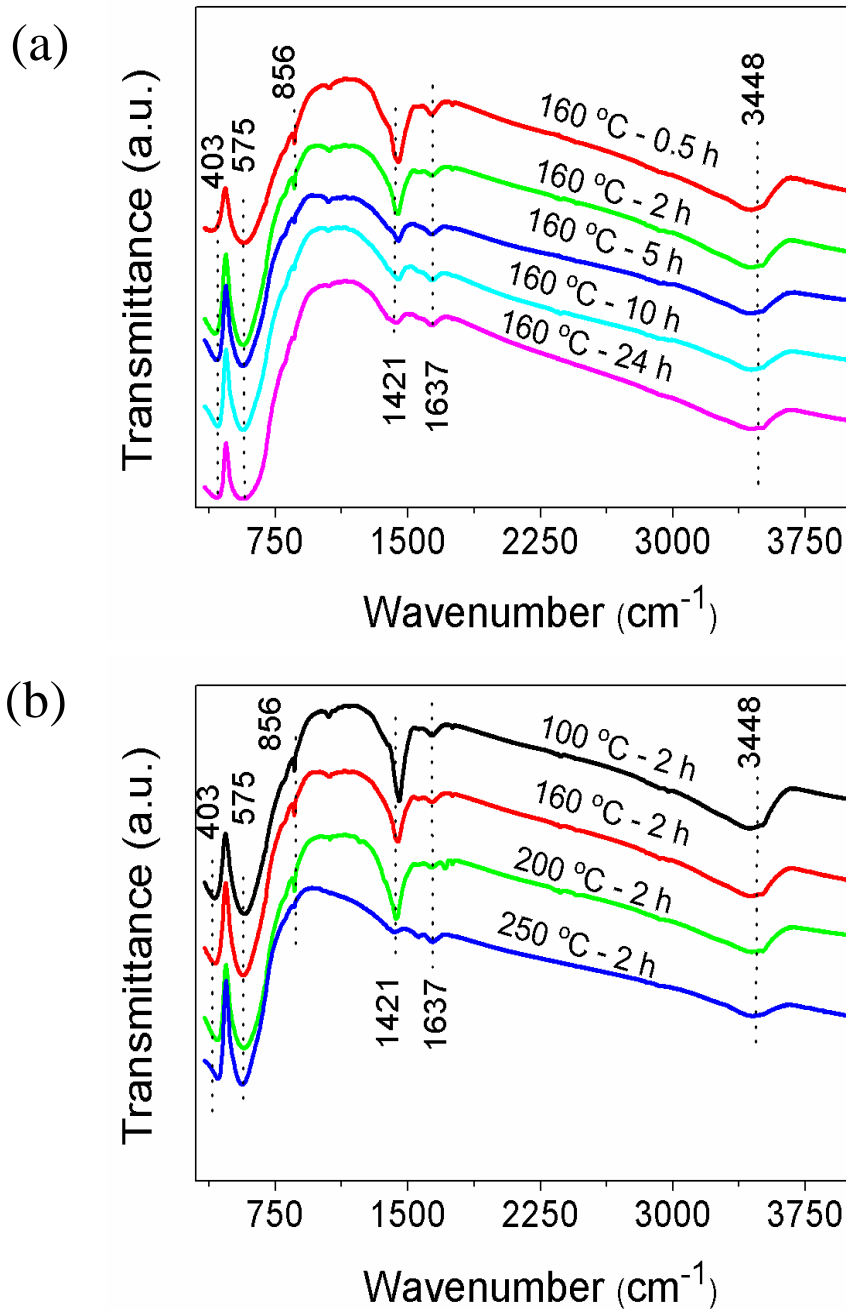
Figure 6-7 FTIR spectra of MWCNTs-BT synthesised (Methodology Two) at (a) 160 ºC for varying times and (b) varying temperature for 2 h. FTIR spectra show the characteristic peaks of BT at 403 and 575 cm^{-1} and for MWCNTs around 1637 cm^{-1}.

Figure 6-8 (a) represents the Raman spectra of BT (prepared by sol gel/hydrothermal method) and MWCNTs-BT synthesised at 160 ºC for different time periods from 30 min to 24 h. Tetragonal BT depicts eight Raman active modes, 3A1g + B1g + 4Eg.[390] BT and MWCNTs-BT peaks at 180, 259 and 517 cm^{-1} are assigned to A1 symmetry transverse component of the optical mode (TO modes). The peak at 304 cm^{-1} is assigned to the B1g mode, indicating the asymmetry within the TiO_6 octahedral [390]. A high frequency longitudinal optical mode (LO) of A1 symmetry is assigned to the peak at 715 cm^{-1}. MWCNTs-BT synthesised at 160 ºC for 10 h exhibits a clear peak at 304 cm^{-1}, assigned to tetragonal BT, whereas MWCNTs-BT synthesised for shorter times do not present well defined tetragonal peak at 304 cm^{-1}. The Raman observations therefore corroborate XRD data (Figure 6-6).

Figure 6-8 (b) shows the Raman spectrum for MWCNTs and MWCNTs-BT in the range from 1200 to 1800 cm^{-1}. MWCNTs exhibit two characteristic peaks on at 1336 and other at 1575 cm^{-1}, named as D and G band, respectively. D band is the double resonance band that gives the information about the structural disorder and G band results from the in plane tangential stretching of the C - C bonds in the graphite sheet and gives information about the desired graphitic structure of the tube [359]. MWCNTs-BT show both D and G band fingerprint of MWCNTs, but both characteristic peaks are shifted from their position when compared to pristine MWCNTs. This most likely indicates the presence of BT on the surface of the CNTs which results in a compressive strain and shifts the peak to higher wavenumber. The intensity of these peaks decreased also for composite samples due to presence of $BaTiO_3$ which restricts the phonon interaction with the surface of CNTs [28].

The morphology of MWCNTs-BT was then investigated by SEM, TEM and AFM. SEM (STEM mode) images of MWCNTs-BT synthesis at 160 ºC for 10 h reveal that there is partial coverage of the MWCNTs surface with BT (Figure 6-9 (a-b)). The dark contrast marked by the red circle in the micrograph indicates BT layers on the surface of MWCNTs. The coating thickness was estimated to be ~ 30 nm. The morphology of the MWCNTs-BT was further investigated by AFM (Figure 6-9 (c-d)). The topography and line profile at three different places (marked by crosses in Figure 6-9 (c)) on the MWCNTs-BT was imaged. The line profile (Figure 6-9 (d)) from point 1 corresponds to bare MWCNT having a diameter of 14 nm (determined from the height). The line profile at point 2 and 3 corresponds to the MWCNTs coated with BT, with a diameter of 20 and 75 nm, respectively. It is clear from the STEM and AFM topography micrographs that the MWCNTs are partially covered with BT of varying

thickness up to 2 - 100 nm. The selective coating may be due to localized covalent functoalization of MWCNTs that results in selective covering of MWCNTs with BT.

The tubes were further observed using TEM. Bright field and dark field micrographs of MWCNTs-BT are illustrated in Figure 6-10 (a, b) respectively. The bright field micrograph reveals a surface coating (BT) on the MWCNTs and the accompanying dark field image reveals bright contrast from strongly diffracting regions, confirming that it is crystalline.

Figure 6-11 (a) is a HRTEM micrograph of MWCNTs, which illustrates that they are uniformly covered with BT (40 nm). Inset in Figure 6-11 (a) is a micrograph which illustrates the carbon lattice fringes (0.33 nm), close to the theoretical value (0.34 nm) of MWCNTs [391]. In some cases (Figure 6-11 (b)), micrographs reveal a d spacing of ~0.28 nm which corresponds to (101) BT. The arrows marked in the micrograph indicates the MWCNTs embedded inside the BT clearly showing the expansion of carbon fringes (0.36 nm) after BT covering, indicating they are under stress, and corroborating the observed shift in Raman peak. EDS spectra from the MWCNTs-BT depicts the presence of Ba and Ti element, Figure 6-11 (c). MWCNTs-BT prepared at 250 ºC for 2 h were also investigated by HRTEM and revealed a similar structure / microstructure.
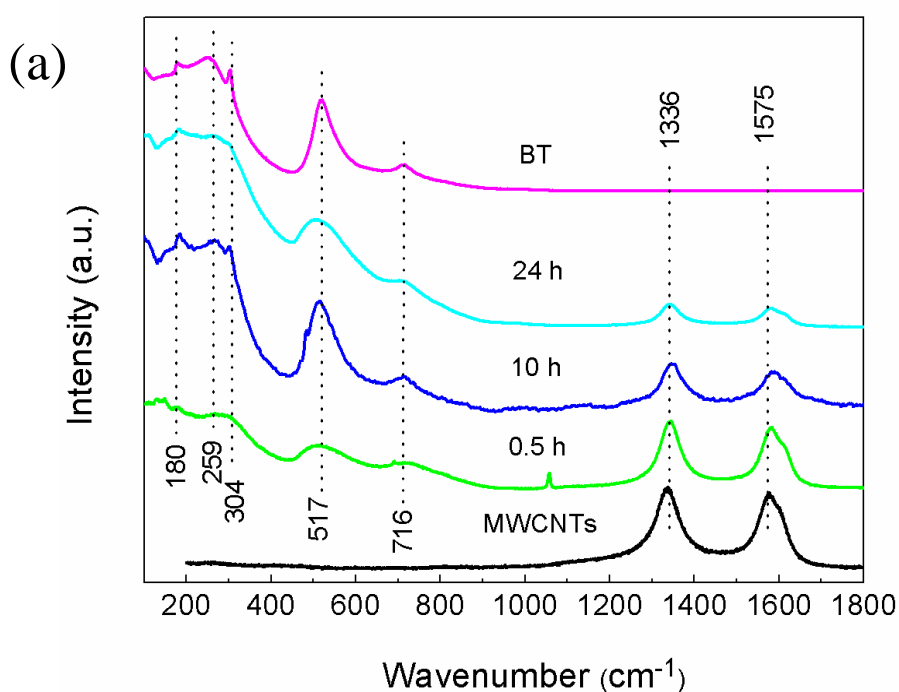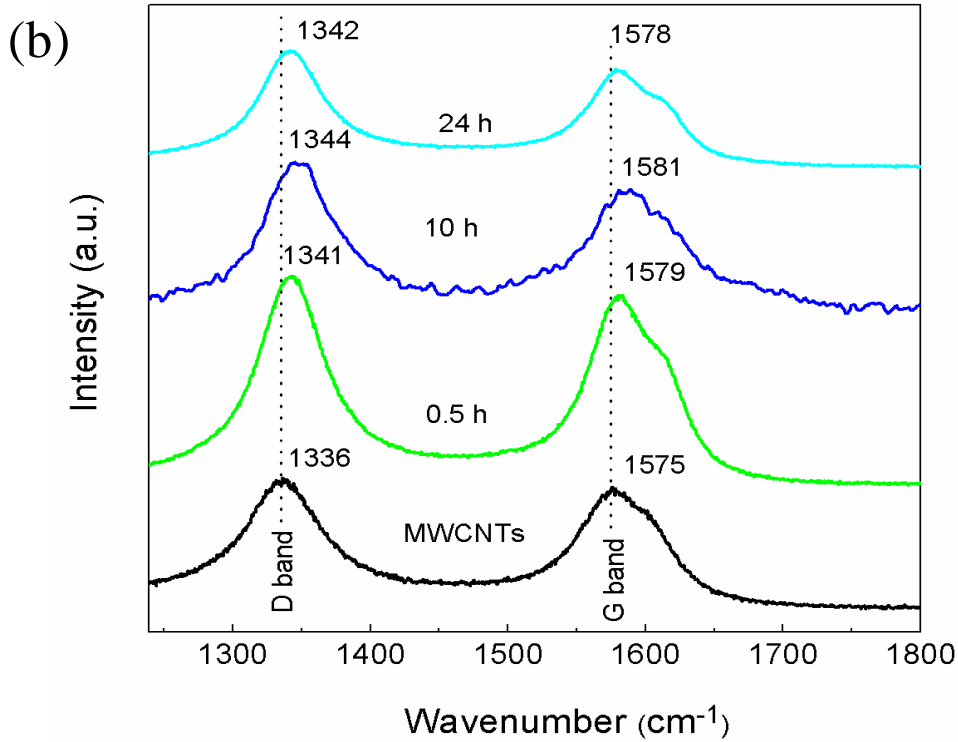
Figure 6-8 Raman Spectra of (a) BT and MWCNTs-BT and (b) MWCNTs and MWCNTs-BT, synthesis at 160 ºC fabricated by the hybrid sol gel / hydrothermal method for different reaction times. MWCNTs-BT synthesised at 160 ºC for 10 h exhibit a tetragonal peak at 304 cm^{-1} and a shift in the characteristic peak of MWCNTs which suggests that they are under compression.
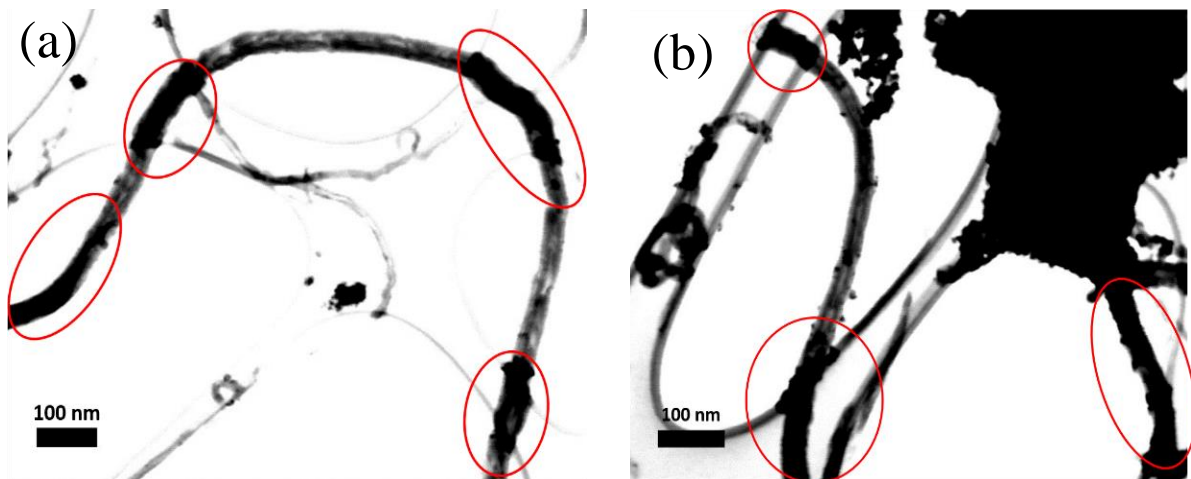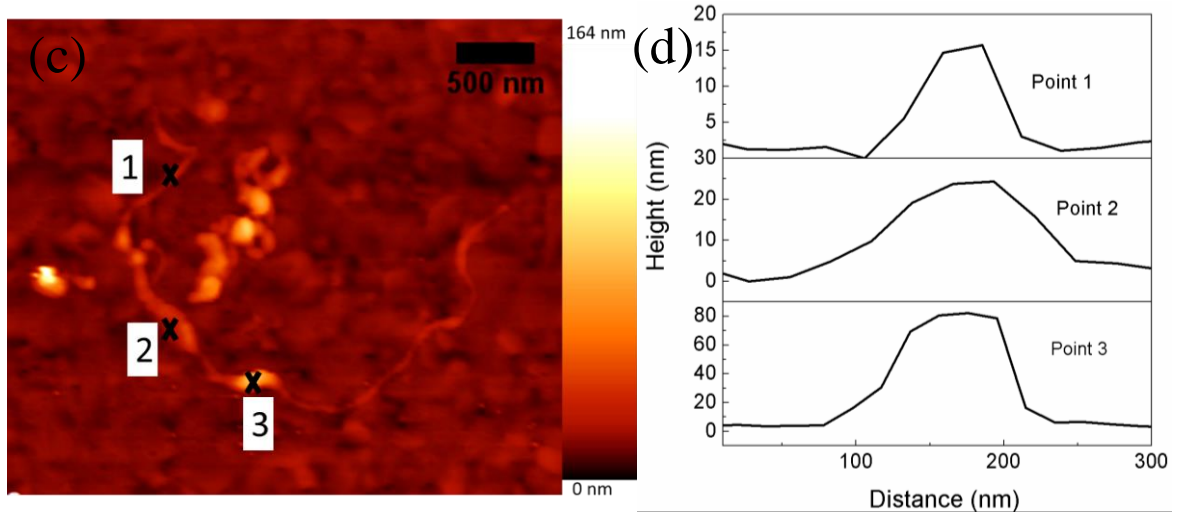
Figure 6-9 (a-b) STEM micrograph of MWCNTs-BT fabricated at 160 ºC. The coated part of the MWCNTs are marked by red circles. (c) AFM topography of MWCNTs-BT and (d) line profile of the topography corresponding to three points marked in the topography image. SEM and AFM results illustrate the selective deposition of BT on the MWCNTs.
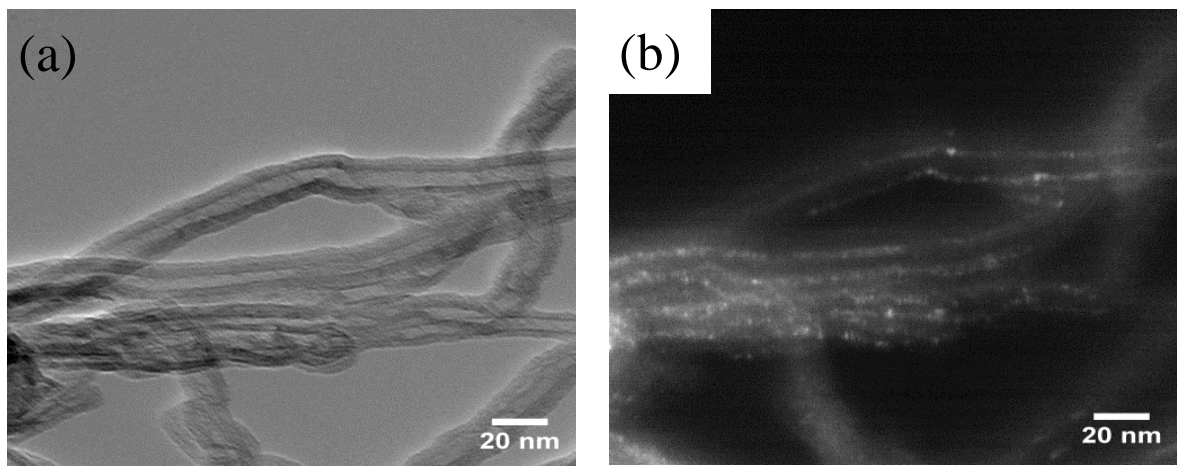
Figure 6-10 (a) Bright and (b) dark field micrographs of MWCNTs-BT fabricated at 160 ºC for 2 h which show partial coverage of MWCNTs with BT.
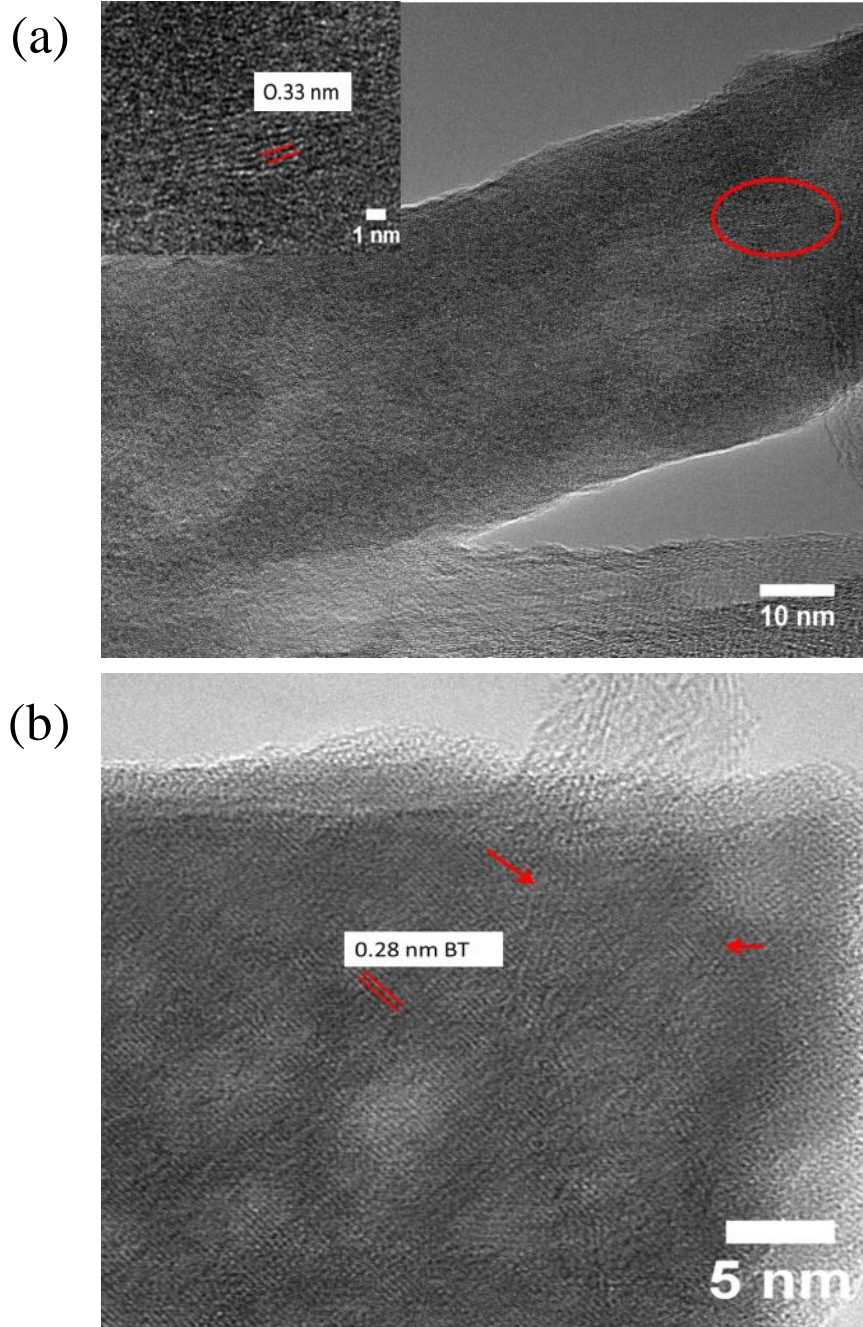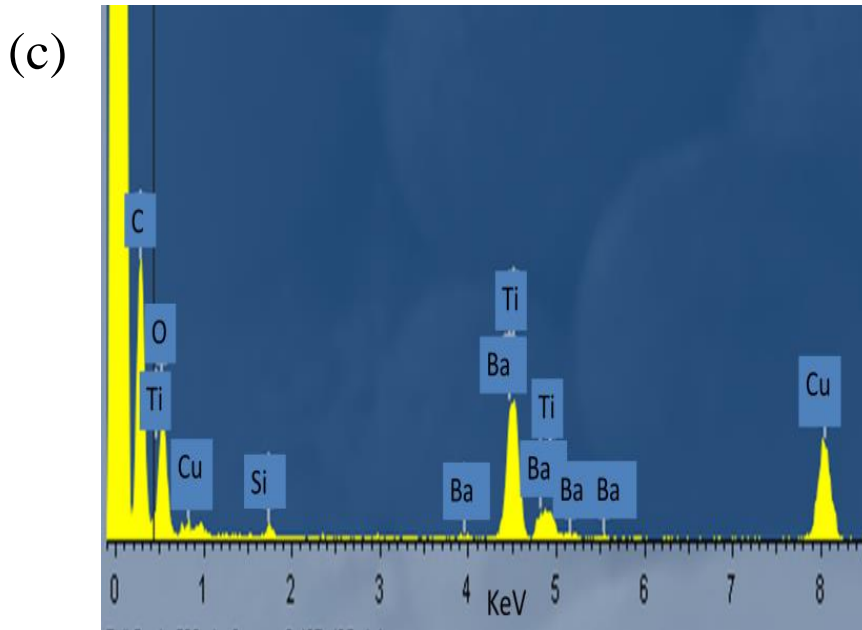
Figure 6-11 (a) MWCNTs coated with BT about 10 - 12 nm,, (b) high magnification of BT covered the MWCNTs and (c) EDS spectra of MWCNTs-BT composite, HRTEM studies clearly indicates the presence of BT on the surface of MWCNTs.

Figure 6-12 is a schematic representation of the possible steps occurred during the formation of BT layers on MWCNTs using the hybrid sol gel/hydrothermal method. The functionalized surface of the MWCNTs reacts with the amorphous BT sol network and the Ba ions become entrapped by the amorphous Ti. On heating, the amorphous Ti network opens and the Ba atoms penetrate inside [363]. Consequently, there is not enough Ba ions residual in the vicinity of the Ti network to react with the carbon skeleton of MWCNTs to form $BaCO_3$. During growth, amorphous sol undergoes a reaction in which movement of the gel surface is the rate controlling step [311] resulting in the formation of crystalline BT on the surface of the MWCNTs. The chemical equation for reaction mechanism for the formation of BT is given below:

$$Ba\,(CH_3)COO + H_2O \rightarrow Ba\,(C_2H_3O_2).H_2O \qquad\qquad (1)$$

$$Ti(OPr^i)_4 + acacH + ethanol \rightarrow Ti(OH)_x\,(OET)_{3-x}\,(acac) + Pr^iOH \quad (2)$$

$$Ba\,(C_2H_3O_2).H_2O + Ti(OH)_x\,(OET)_{3-x}\,(acac) + KOH \rightarrow$$

$$BaTiO_3\,(s) + 2\,(CH_3)_4\,K^+CH_3COO\,(aq) + H_2O\,(l) \qquad\qquad (3)$$

MWCNTs
functionalized
with carboxyl and
hydroxyl groups

- Ba²⁺
- Ti⁴⁺
- O²⁻

Titanium network
where Barium ion
entrapped

BaTiO₃
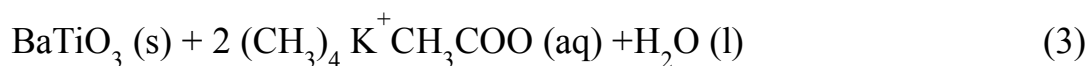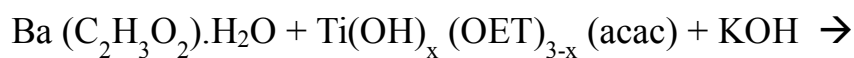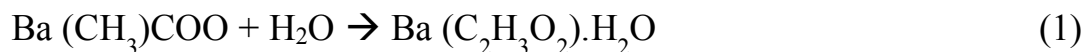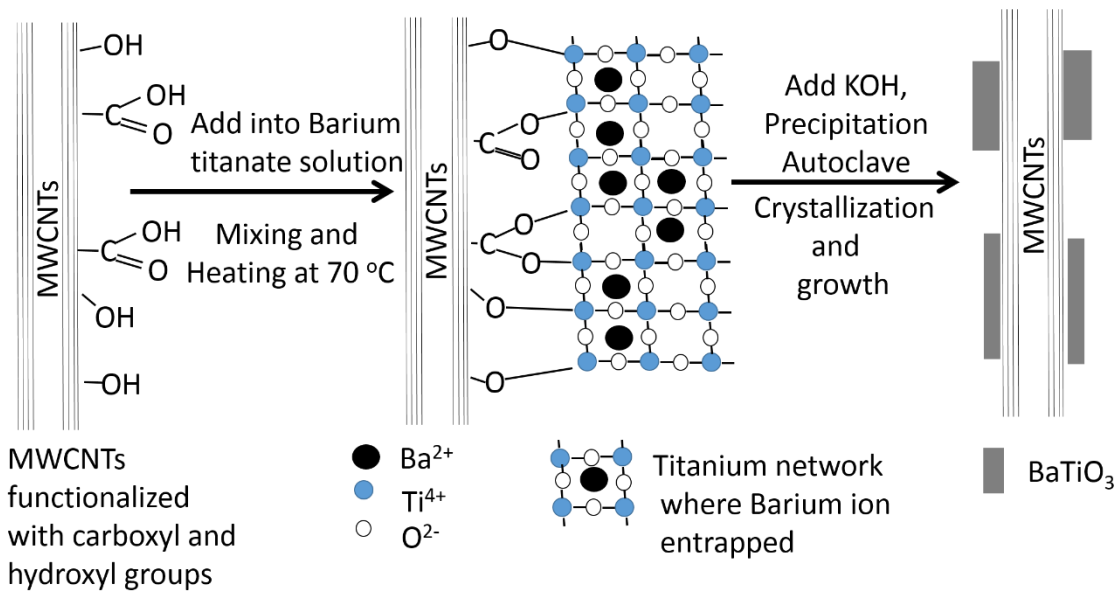
Figure 6-12 Schematic for the formation of MWCNTs-BT from sol gel / hydrothermal method: Ba ions entrapped inside the network of titanium helping reducing the formation of BaCO₃ at the surface of MWCNTs.

Figure 6-13 illustrates the AFM-PFM response of the MWCNTs-BT, acquired in contact mode. The topography micrograph (Figure 6-13 (a)) represents two or more entangled tubes covered with BT. The line profile that corresponds to the topography image reveals that the diameter of the MWCNTs-BT is ~60 - 80 nm whereas, the MWCNTs diameter are ~25 nm. The out of plane response was obtained with the application of peak to peak 10 V ac Figure 6-13 (b)
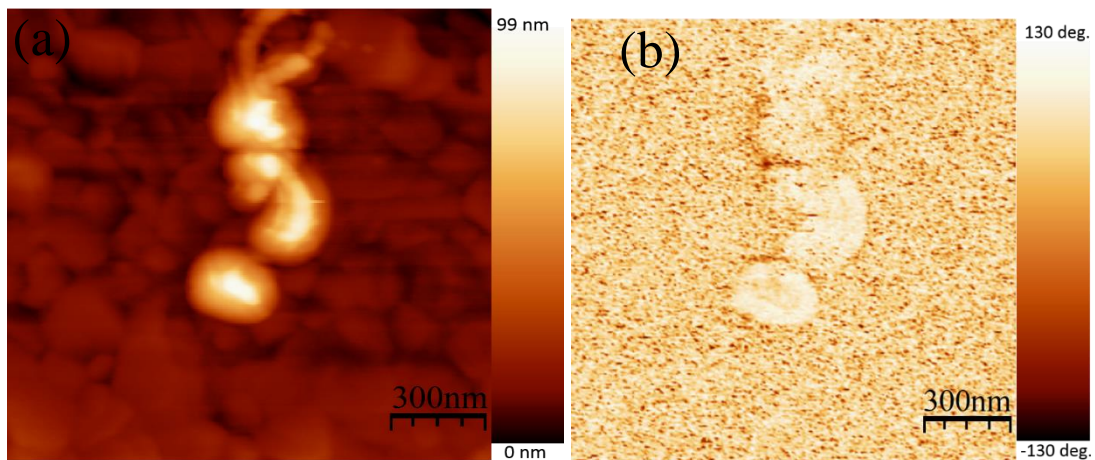
Figure 6-13 (a) Topography and (b) phase response (out of plane) of MWCNTs-BT obtained at 160 ºC by sol gel / hydrothermal method AFM-PFM with the application of 10 V in contact mode.

The electromechanical responses were caried out by sweepingthe AC voltage from 0 to 20 V in contact mode on the selected points. The electromechanical response from MWCNTs-BT is illustrated in Figure 6-14 (a). The amplitude measured as a function of the applied voltage shows a linear increase with the applied voltage, and confirms an linear electromechanical effect (Figure 6-14 (b)). In Figure 6-14 (a), points marked by red, corresponds to where V_{ac} sweeps were performed with a bias up to 20 V. The high bias above 20 V results in the dielectric breakdown. The value of the d_{zz} measured varied at each point, possibly indicating a slight difference in orientation / thickness of BT on the MWCNTs, as previously suggested. [392] The average value of d_{zz} is ~15 pm/V. The hysteresis of MWCNTs-BT demonstrates that the domains of BT on the MWCNTs can be switchable with the application of applied voltage (Figure 6-14 (c)). The amplitude response on the same area is given in Figure 6-14 (d).
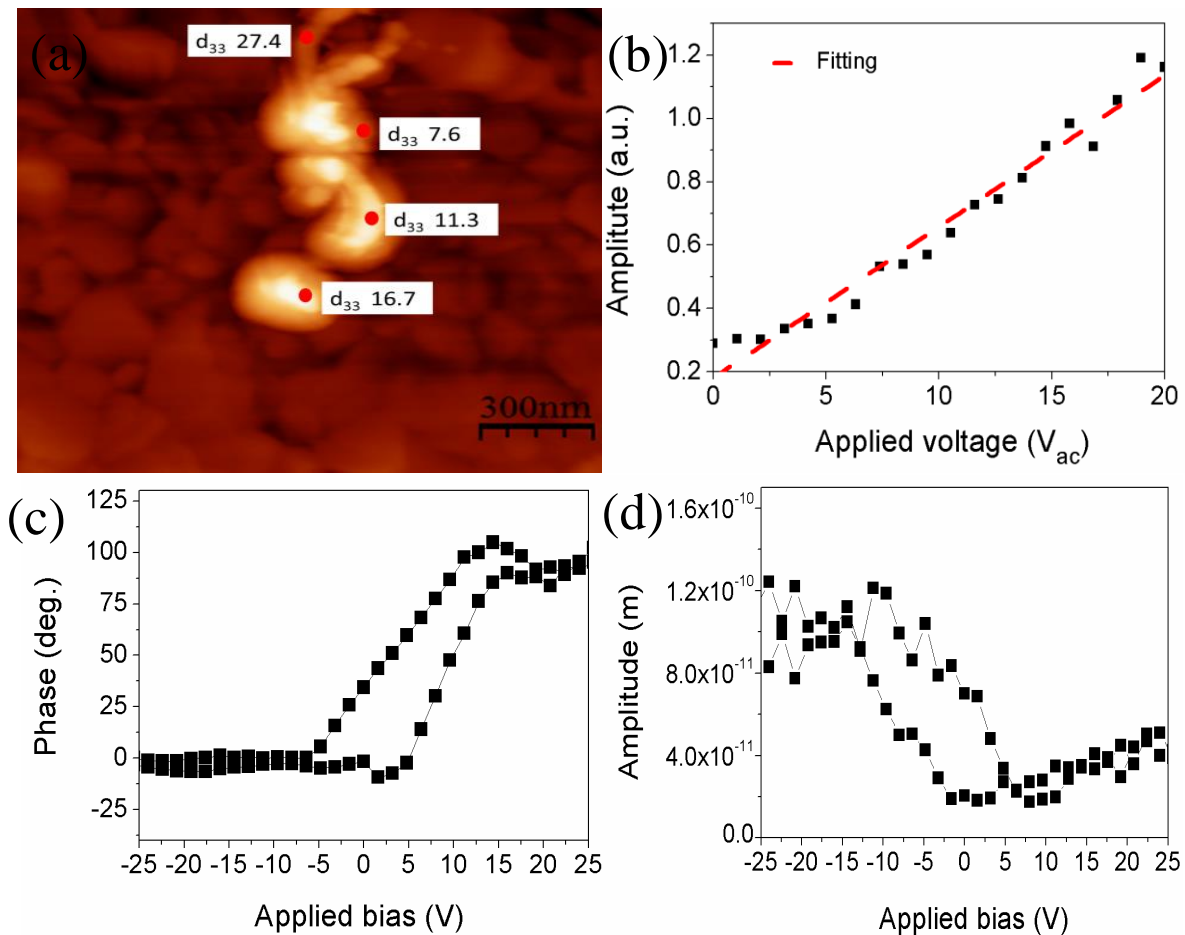
Figure 6-14 (a) Topography micrograph marked with red dots corresponds to the d_{33} measurements; (b) Vac sweeps depicts the linear variation of amplitude as a function of applied voltage; (c) PFM phase hysteresis and (d) amplitude response obtained with the application of ±25 V to MWCNTs-BT obtained by sol gel / hydrothermal method at 160 ºC.

6.3.2 Covering non-covalent functionalized MWCNTs with BT

It was clear from the above results that covalent functionalized MWCNTs can be covered with BT at particular areas, which might be the result of the localized covalent functionalization. In order to have uniform coverage of MWCNTs with BT, MWCNTs were functionalized non-covalently with SDS to promote large area functionalization. So, that conformal covering of MWCNTs with BT can be obtained. The results obtained on the covering of non-covalent functionalized MWCNTs with BT are presented and discussed hereafter.

Figure 6-15 (a) illustrates HRTEM micrographs of the SDS functionalized MWCNTs used in the present studies having diameter ranges from 10 to 30 nm. Figure 6-15 (b) represents the SEM micrographs of SDSMWCNTs-BT synthesised at 250 °C for 12 h from 0.01 M BT solution evidencing SDSMWCNTs-BT tubes with diameter of 50 to 200 nm, alongside with the few BT particles and uncovered MWCNTs. The SEM micrograph of SDSMWCNT-BT obtained from 0.1 M of BT solution is given in Figure 6-15 (c), SDSMWCNTs-BT obtained from 0.1 M of BT mainly consists of BT particles with irregular morphology and a very few tubes. It was clear from the SEM analysis that the initial concentration of BT precursor has a significant effect on the morphology of the final product. This can be explain based on the difference in the concentration of the SDS and BT. When we used a high concentration of BT solution (0.1 M) the nucleation and growth occurs in the conventional way and BT particles are formed. Whereas when BT concentration is around 0.01 M, preferential nucleation occurs at SDS molecules and BT grows from there. Hence, 1 D SDSMWCNTs-BT structures were obtained from the less concentrated BT solution.

(a)
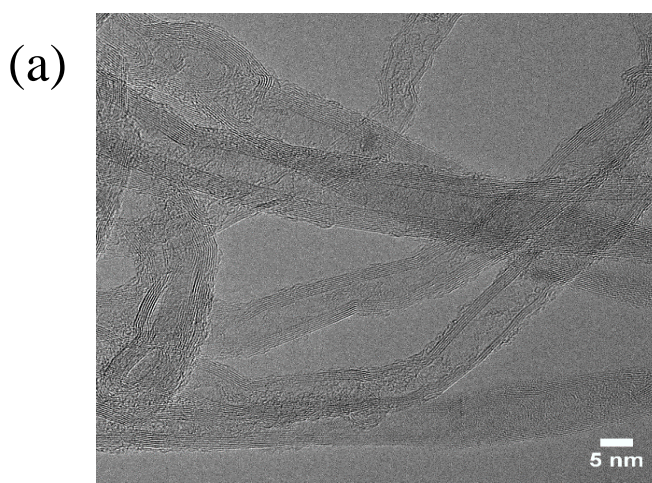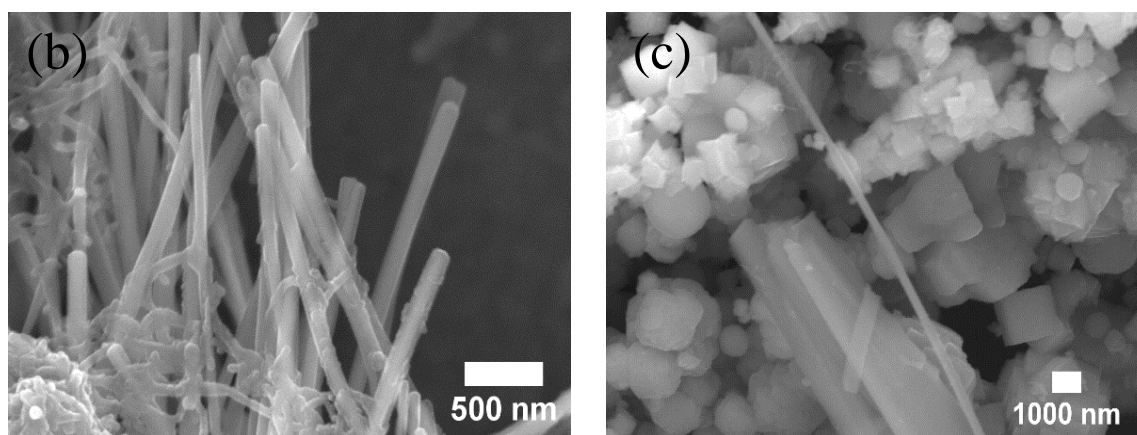
Figure 6-15 (a) HRTEM micrograph of SDS functionalized MWCNTs; SEM micrographs of SDSMWCNTs-BT synthesised from (b) 0.01 M and (c) 0.1 M BT solution. BT tubes were formed when the initial concentraion of the BT solution is 0.01 M.

The 1D SDSMWCNTs-BT structures obtained from 0.01 M solution were further investigated under a HRTEM. The HRTEM micrograph illustrates BT tubes having the diameter of 30, 50 and 70 nm and length up to 2 µm (Figure 6-16 (a)). Further, magnified view of the tubes depicts the presence of MWCNTs, which are embedded beneath the BT layer. The magnified view depicts the d_{002} spacing of 0.2 nm that corresponds to BT crystallographic plane as shown in the inset of Figure 6-16 (b). The diameter of the SDSMWCNTs-BT tubes is around 90 nm with CNTs diameter close to 60 nm, hence the thickness of BT layer on CNTs is around 15 nm (Figure 6-16 (b)). In some SDSMWCNTs-BT tubes, the coverage of BT is so dense that it was difficult to visualize carbon skeleton of MWCNTs. The variation in the diameter of the SDSMWCNTs-BT might be due to the difference in the original diameters of MWCNTs (10 to 60 nm) used in the present studies. The SDSMWCNTs-BT fabricated at 250 ^{o}C for 2 h are illustrated in Figure 6-16 (c-d). MWCNTs (having 10 nm diameter) are uniformly covered with BT having a diameter of ~20 nm. The magnified view of the BT covered SDSMWCNTs depicts the carbon and BT lattices with the spacing of 0.33 nm and 0.23 nm, respectively (Figure 6-16 (c)). HRTEM results clearly proves that the MWCNTs are conformal covered with BT and form 1D structures. HRTEM analysis at the interface between SDSMWCNTs and BT depicts three different sets of lattice spacing as illustrated in Figure 6-17, having the d spacing of 0.35, 0.37 and 0.23 nm. The lattice spacing of 0.35 nm corresponds to CNTs lattice and 0.23 nm to BT (111) plane. However, the lattice spacing of 0.37 nm between CNTs and BT planes corresponds to $BaCO_3$ (111) plane (JCPDS- 05-0378) (illustrated in Figure 6-17 inset on the top right). The elemental mapping of MWCNTs-BT

structures is represented in Figure 6-18. The tubes of SDSMWCNTs-BT with diameter of 115 nm depict the uniform distribution of barium, titanium and oxygen throughout the tube. The elemental mapping confirms the uniform distribution of barium and titanium elements throughout the structure.
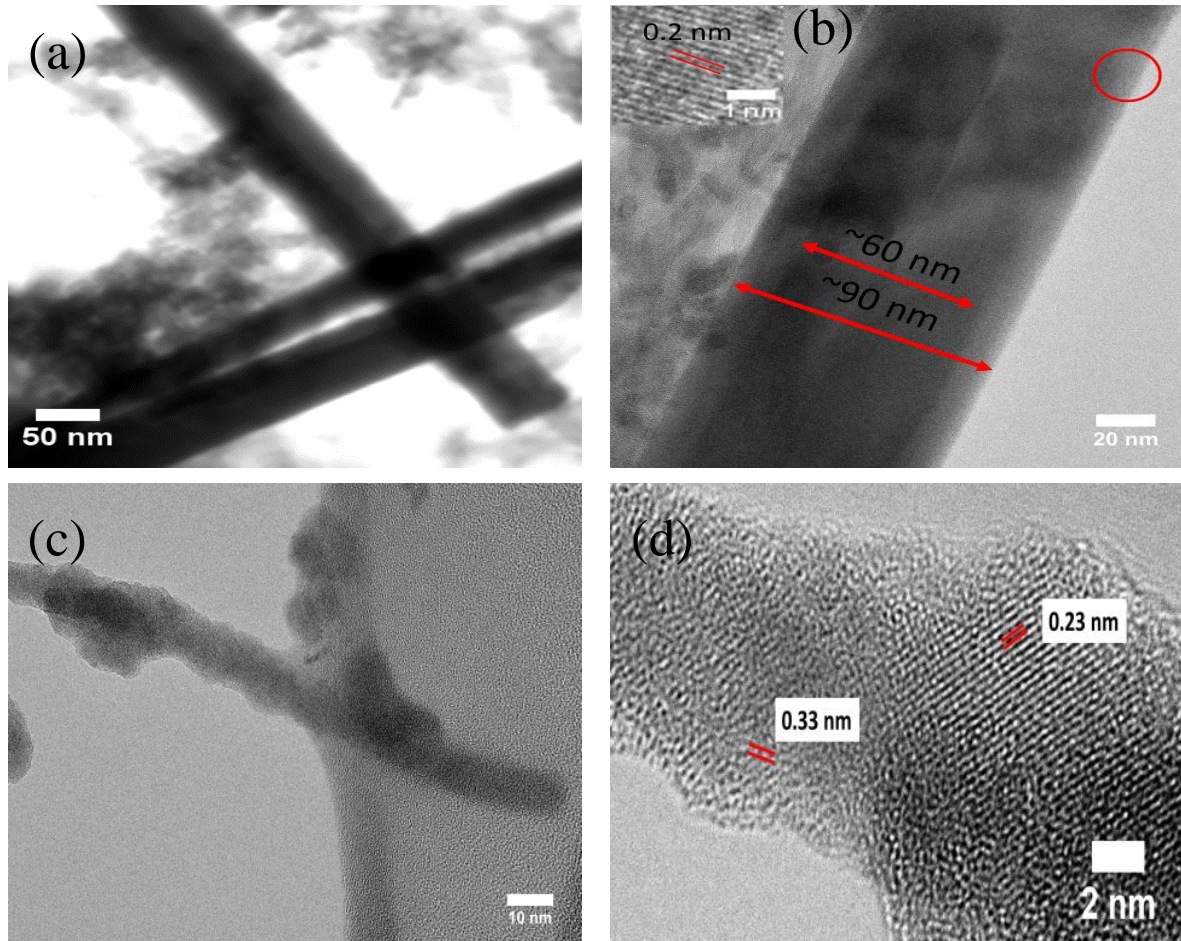
Figure 6-16 HRTEM micrographs of SDSMWCNTs-BT tubes synthesised from 0.01 M solution at 250 °C for 12 h, tubes with diameters of 30, 50 and 70 nm were obtained (a). A magnified view of the tube shows d spacing of 0.2 nm (shown in inset) (b). HRTEM micrograph of SDSMWCNTS-BT obtained at 250 °C for 2 h MWCNTs covered with BT (c) and magnified view depicts the lattice fringes of 0.33 nm and 0.23 nm corresponds to CNTs and BT (d).
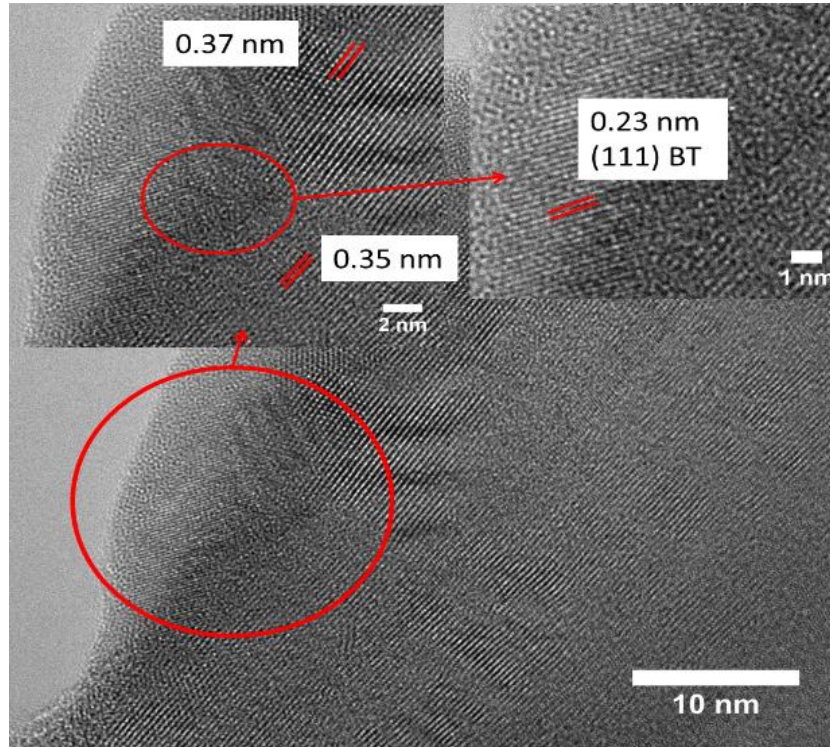
Figure 6-17 HRTEM micrograph of SDSMWCNTS-BT synthesised at 250 ºC – 12 h, depicts the interface between the BT particle and MWCNTs, there are three different d spacings: 0.37, 0.23 and 0.35 nm observed corresponds to BaCO₃, BT and MWCNTs, respectively.
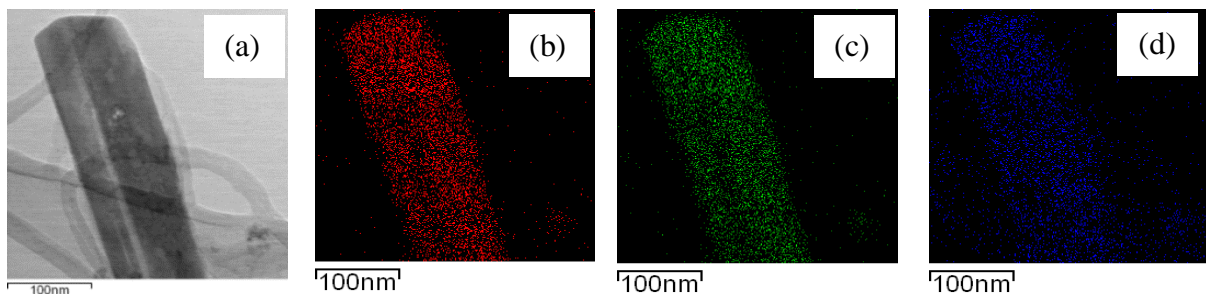
Figure 6-18 Elemental mapping of SDSMWCNTs-BT (a) STEM micrograph; mapping of (b) barium, (c) titanium and (d) oxygen elements. The elemental mapping depicts uniform distribution of element corresponds to BT.

XRD pattern of the SDSMWCNTs-BT at 250 ºC for 2, 12 and 48 h, fabricated from the initial molar concentration of 0.01 M and SDSMWCNTs-BT obtained at 250 ºC - 12 h from 0.1 M concentration of BT precursor is given in Figure 6-19 (a). The diffraction peaks match well with a tetragonal BT cell having space group P4mm indexed to JCPDS no. 05-0626.

Diffraction peaks for Ba(Ti_2O_5) and TiO_2 (secondary phases) were also identified for all the samples. The peaks from the secondary phases are very stable and are not eliminated with the increase of the reaction time. According to literature the Ba(Ti_2O_5) is stable phase and can only be eliminated by heating above 1100 ºC, and in case of hydrothermal processing it is unlikely to eliminate once it has formed. [393] To confirm, if the SDSMWCNTs-BT tubes fabricated at 250 ºC for 2, 12 and 48 h are tetragonal or cubic, the diffraction peak around 2θ~45º were looked for splitting or broadening. An asymmetric broadening (Figure 6-19 (b)) was found and can be attributed to the (200)/(002) reflection of tetragonal structure for above mentioned samples. It is know from the literature the particle size less than 300 nm attribute to the peak broadening in contrary to splitting [320, 394].
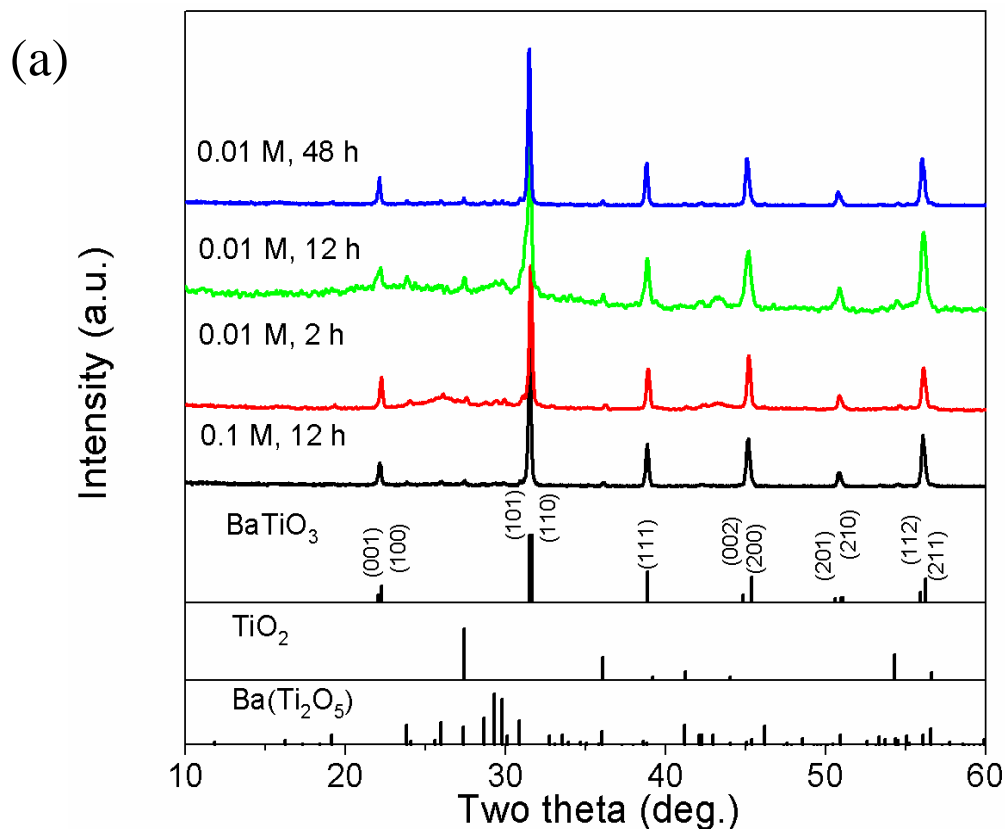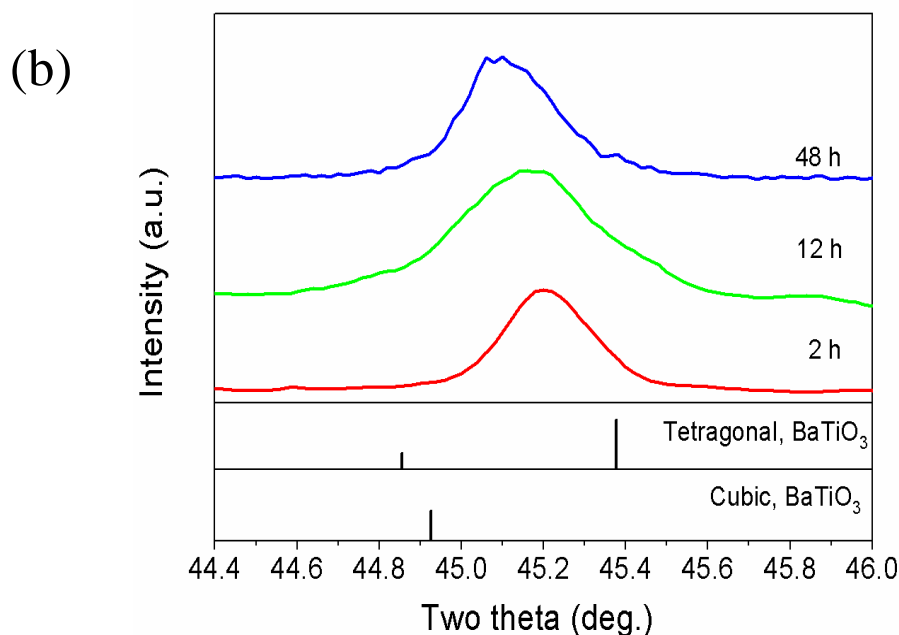
Figure 6-19 XRD pattern of the SDSMWCNTs - BT at 250 ºC for 2, 12 and 48 h, fabricated from the initial molar concentration of 0.01 M and SDSMWCNTs-BT obtained at 250 ºC - 12 h from 0.1 M concentration of BT precursor (a) and the tetragonality of the SDSMWCNTs – BT for the sample fabricated at 250 ºC for 2, 12 and 48 h determined from the broadening of 200 peak (corresponds to cubic) in to 200/002 (corresponds to tetragonal). (b), asymmetric broadening was found for all the samples attribute to tetragonal structure.

FTIR spectrum of MWCNTs, SDSMWCNTs and SDSMWCNTs-BT are represented in Figure 6-20 from wavenumber 4000 to 350 cm^{-1}. Peak at 3446 cm^{-1} corresponds to hydroxyl group [388], and is present for both MWCNTs and SDSMWCNTs. The second group of peaks occur at 2977 and 2924 cm^{-1} and are assigned to the asymmetrical and symmetrical stretching of $-CH_2-$ present in SDSMWCNTs, where pristine MWCNTs depicts only the peak assigned to the symmetrical stretching. The transmittance peaks at 1579 and 1384 cm^{-1} can be attributed to the monodentate carboxylate mode and symmetrical vibrations of $-CH_3$, respectively. All the above mentioned peaks disappeared after the formation of BT on the tubes. The peak at 1629 cm^{-1} is associated with the vibration of the carbon skeleton from the carbon nanotubes; this peak is very clear for pristine MWCNTs and SDSMWCNTs but not so clear for SDSMWCNTS-BT. For SDSMWCNTs two more peaks are present in comparison to MWCNTs; one at 1058 cm^{-1} assigned to the symmetrical stretching vibration of S=O and a second one at 881 cm^{-1} assigned to the asymmetrical stretching vibration of C–O–S [346, 347]. After the formation of BT on MWCNTs, the FTIR spectra reveals a significant decrease in the intensity of the peak at 1058 cm^{-1} and the disappearance of the peak at 881 cm^{-1} what might

be due to the formation of BT by the replacing of the sulphur ions (from SDS). The huge transmittance peak for SDSMWCNTS-BT at 1442 cm^{-1} may corresponds to carboxylate groups [18]. The characteristic peaks for BT that appears around 418 and 563 cm^{-1} are from the stretching and bending of the Ti-O octahedron of BT [380]. Peak around 856 cm^{-1} is from the carbonate phase, indicating the formation of BaCO$_3$. In agreement with HRTEM analysis of SDSMWCNTs-BT reveals the formation of BaCO$_3$ at the interface of MWCNTs. The formation of BaCO$_3$ may results in deficiency of Ba ions in the solution that as a consequence might result in the formation of secondary phases, Ba(Ti$_2$O$_5$) and TiO$_2$, as it was observed.
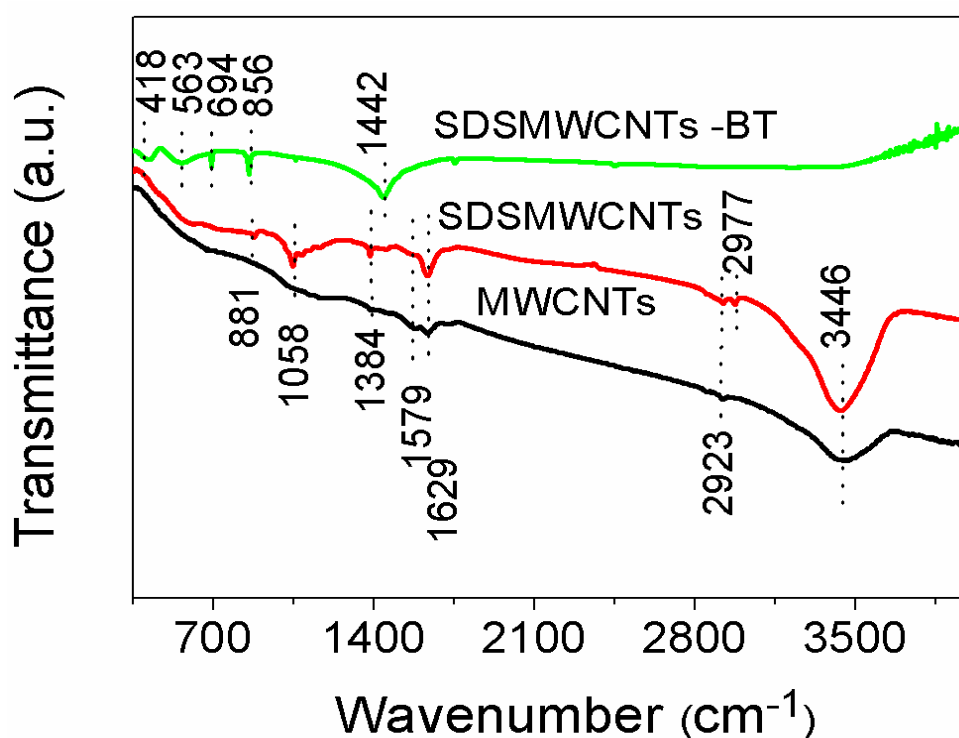
Figure 6-20 FTIR spectra of MWCNTs, SDSMWCNTs and SDSMWCNTs-BT, depicts the SDS functionalized peaks at 1058 and 881 cm^{-1} and characteristic peaks for the formation of BT at 563 and 418 cm^{-1}.

From the above analysis, a schematic is proposed on the formation of 1D SDSMWCNTs-BT (Figure 6-21). MWCNTs functionalized with SDS results in the non-covalent functionalization. Where the hydrophobic part (C-C chain) of the SDS is adsorbed on the MWCNTS by Van Der Waals interactions and the hydrophilic part of the surfactant is oriented toward the aqueous phase [395]. SDS functionalization make CNTs stiffer due to the rigidity of the SDS and align them unidirectionally, this also provide with better dispersion of MWCNTs in solution. [396, 397] It has been experimentally and theoretically verified that

SDS molecules adsorbed on the CNTs based on chirality and electrical properties [398, 399]. Moreover, SDS adsorbed on the surface of MWCNTs in three different type, named as cylindrical adsorption, hemimicellar adsorption and random adsorption (shown in Figure 6-21), This dependents on the concentration of SDS in the media [400] and on the size and chirality of the tubes, as stated above. This could be the reason that not all the MWCNTs are conformal covered with SDS due to different size of the MWCNTs used in the present studies and also the chirality.

FTIR of SDSMWCNTs-BT indicates the intensity of transmittance band from S=O and C-O-S has been extinct and decrease in intensity after the formation of BT. It indicates the S=O was replaced by Ti-O network during the nucleation and/or growth process, this results in the deposition of BT on the surface of MWCNTs. The nucleation and growth of the BT on the surface of MWCNTs might be dependent on the type of adsorption of SDS on the MWCNTs. This might be the reason, why some of the tubes are uniformly covered with BT, few of them partially and others are not at all.

The formation of secondary phase $Ba(Ti_2O_5)$ and TiO_2 occurred due to the deficiency of Ba ions in the solution, which is only possible if the Ba ions from the suspension form BaO or $BaCO_3$. HRTEM results depicts the formation of $BaCO_3$ at the interface of SDSMWCNTs-BT. The possible reason for the formation of $BaCO_3$ phase at the interface is due to aliphatic chains (C-C) of SDS, Which reacts with Ba ions to form $BaCO_3$. Nevertheless, in our previous studies we demonstrated that sol gel hybrid hydrothermal method restrict the formation of $BaCO_3$ for the fabrication of MWCNTs-BT. But it seems same is not true when surfactant with long aliphatic chains present along the periphery of the MWCNTs.

The topography and out of plane PFM amplitude and phase response with the respective line profile presented on the right of the Figure 6-22 (a-c). The line profile from the topography micrograph illustrates the ~ 50 nm height of the SDSMWCNTs-BT. The phase response depicts that most of the component of the polarization are aligned along the same direction of the applied field. The point poling was carried out on the tube and imaged after poling with +30 V (on top) and -30 V (on bottom) dc bias for 0.5 min marked in Figure 6-22 (b). The phase response after poling depicts the domains poled with negative 30 V appears dark in contrast, this depicts orientation of the domains has changed from the rest of the surrounding domains; (Figure 6-22 (b) on right), whereas, when the domains oriented along the same direction of

electric field (poled by +30 V) the domains look more brighter than before due to increase in the density of the domains oriented along the applied field.
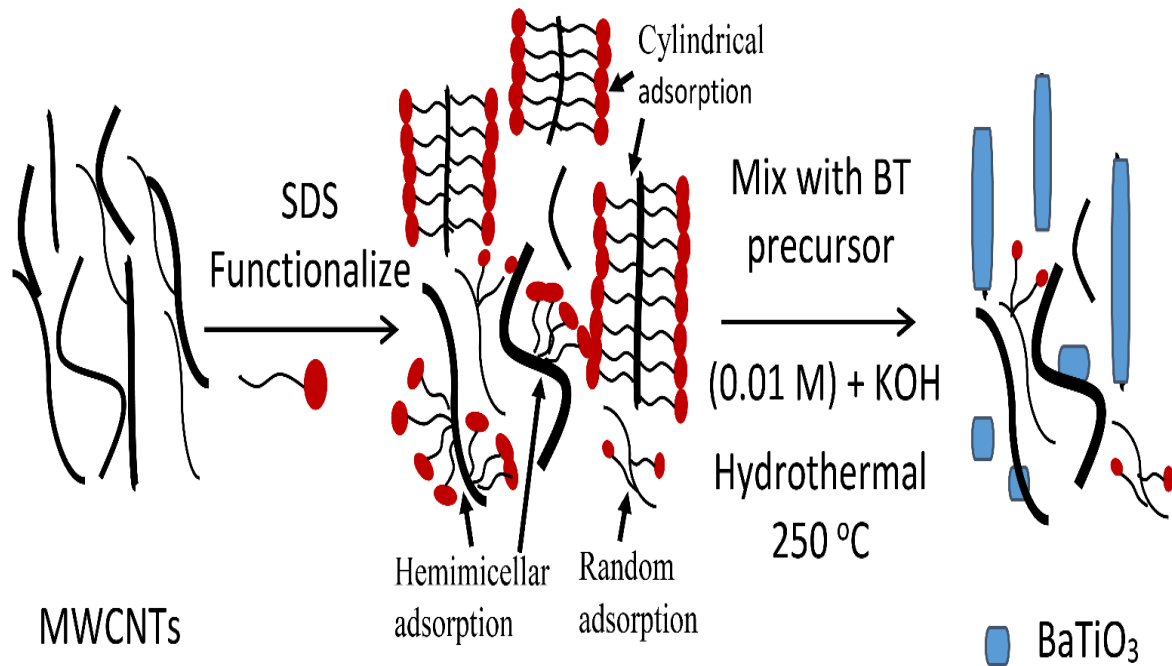
Figure 6-21 Schematic representation of the formation of SDSMWCNTs-BT nanotubes using non-covalent functionalization. SDS adsorbed on the surface of MWCNTs in three different ways named as cylindrical adsorption, random adsorption and hemimicellar adsorption; the functionalized MWCNTs mixed with BT precursor and subjected to hydrothermal condition to obtained SDSMWCNTs-BT. Different type of adsorption results in semi cover or uniform cover of SDSMWCNTs with BT.
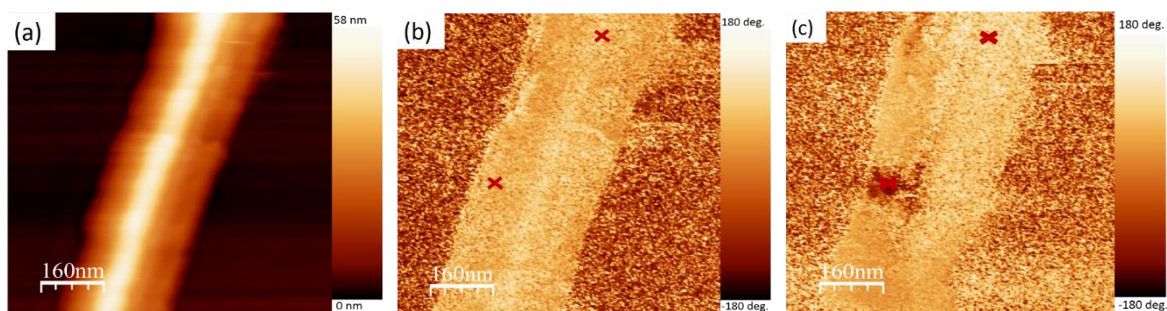
Figure 6-22 AFM-PFM micrograph of SDSMWCNTs-BT tubes: (a) topography, (b) phase response (out of plane) and (c) point poling on the marked point with +30 V on top and -30 V on the bottom the poling response is read with the applied field of 15 V in contact mode. The poling depicts the dipoles can be aligned from positive to negative direction with the application of external field.

The electromechanical responses were carried out with the application of AC voltage in contact mode on the different points on tube. The tip was approach to the point of interest and the electromechanical response was measured as the function of applied voltage. The linear increase of the amplitude with the applied voltage are observed, which is typical response expected from the piezoelectric materials. Where, the slope obtained from amplitude vs V_{ac} plot (illustrate as inset in Figure 6-23) and force is calculated from the force calibration curve. The average value of d_{33} is approximately 2 pm/V which is quite low compare to the bulk (d_{33} = 75 pm/V) [401].
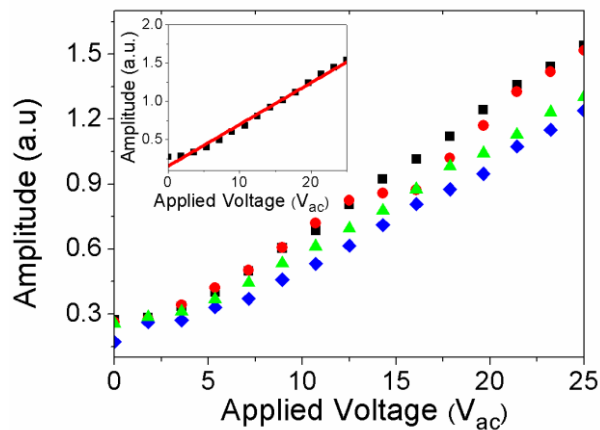
Figure 6-23 Amplitude as a function of applied voltage (V_{ac}) plot for SDSMWCNTs-BT; illustrates the linear change in amplitude with applied voltage and the slope gives the value of effective d_{33}, in this case it is around 2 pm/V.
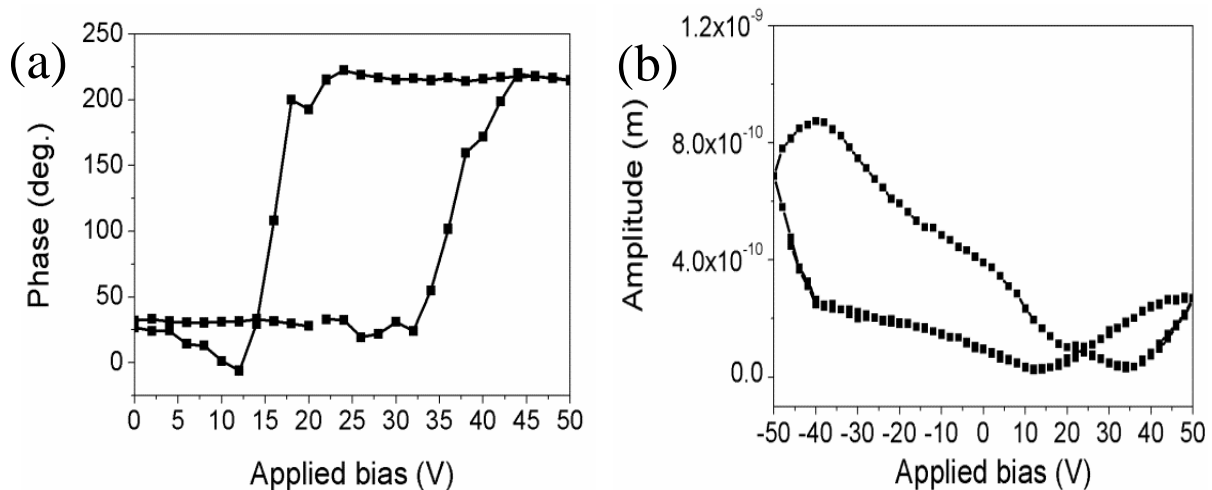
Figure 6-24 (a) Hysteresis loops and (b) amplitude obtained from SDSMWCNTs-BT tube with the application of ±50 V dc bias. The shift in FE loop is due to self-polarization of BT tube, the results clearly depict the ferroelectric behaviour of the tubes.

The low d_{33} was also reported for the $SrBi_2Ta_2O_9$ nano sphere is 2 pm/V [402] and also for cubic crystal of 10 nm of BT is 1.5 pm/V [227]. The reason for low value of d_{33} might be the orientation of the domains in BT, which is explained by caring out systematic measurements on thin films by PFM [392].

Local piezoelectric hysteresis measurements were recorded to demonstrate the ferroelectric behaviour of the tubes. Figure 6-24 (a) and (b) depicts the hysteresis phase loop and amplitude response from the SDSMWCNTs-BT, respectively. The hysteresis phase and amplitude loops were acquired by scanning with dc bias ± 50 V. A square hysteresis phase loop and butterfly amplitude loop were observed, this indicate the tubes are ferroelectric in nature. The self-polarization of the SDSMWCNTs-BT is clearly indicated by the shift of phase hysteresis loop along the positive side of the applied bias. The PFM studies on tubes established that SDSMWCNTs-BT indicates they are ferroelectric in nature.

6.4   Conclusions

The present studies demonstrate an low cost methodology of coating covalent functionalized MWCNTs with BT using a sol-gel hybrid hydrothermal method and succinctly illustrates the ineffectiveness of conventional hydrothermal synthesis due the formation of $BaCO_3$. The MWCNTs-BT are ferroelectric and exhibit an electromechanical response (15 pm/V). However, the covering of MWCNTs is local and non-uniform what might be related to the covalent functionalization of MWCNTs.

Further studies on non-covalent functionalized MWCNTs demonstrated a more conformal covering of SDSMWCNTs with BT using sol gel hybrid hydrothermal method. HRTEM showed that SDSMWCNTs-BT have diameters ranging from 20 to 200 nm. The local PFM response proves that MWCNTs-BT tubes are ferroelectric and piezoelectric with d33 of 2 pm/V.

This strategy can also be extended to the other compounds for materials with high crystallisation temperatures. The formation of nano composites of BT on MWCNTs is a significant step forward in the development of 3D memory cells.

Chapter 7

7   Multiwall carbon nanotubes – Bismuth ferrite oxide (BFO)

Abstract:

This chapter demonstrates the fabrication of MWCNTs- $BiFeO_3$ (BFO) structures. MWCNTs-BFO structures were obtained by two approaches: chemical solution deposition method (sol gel) and physical method (sputtering). In the first approach MWCNTs were used to fabricate 1D structures of MWCNTs-BFO from a sol gel solution of BFO. It was found that MWCNTs provides the critical role in the fabrication of monophasic BFO by curbing the formation of secondary phase (Bi_2O_3). TEM observations clearly illustrate that opening and semi filling of MWCNTs with BFO precursor occurs during the processing of MWCNTs-BFO. Through the annealing process of MWCNTs-BFO to obtained crystalline BFO the MWCNTs were completely oxidized and 1D BFO monophasic nano rod like structures were formed. The BFO nano rod like structures, mimicking the morphology of the MWCNTs, have crystallites with an aspect ratio of 1:3 or above, and diameters in the range of ~20 - 50 nm. BFO nano rod like structures depicted a weak ferromagnetic loop with coercive field of 956 Oe at 5 K.

In the second approach, Vertically Aligned MWCNTs (VA-MWCNTs) as bottom electrodes for microelectronics were used. As a proof of concept BFO films were fabricated by *in-situ* deposition on the surface of VA-MWCNTs by RF magnetron sputtering. *In-situ* deposition temperature of 400 ºC and deposition time up to 2 h was used, BFO films cover the VA-MWCNTs and no damage occurs either in the film or VA-MWCNTs. In spite of the macroscopic lossy polarization behaviour, the ferroelectric nature, domain structure and switching of these conformal BFO films were verified by piezo force microscopy. G type antiferromagnetic ordering with weak ferromagnetic ordering loop was proved for BFO films on VA-MWCNTs, having a coercive field of 700 Oe.

7.1 Introduction

Recently special attention has been paid to materials, designated as multiferroics that possess two or more ferroic properties, as ferroelectricity, ferroelasticity and ferromagnetism. The possibility of combining and controlling two different physical phenomena in a single material is indeed considered the epitome of functionality. Multiferrroics are because of that very promising from the technological pointy of view for modern electronics, as memory elements, sensors, and spintronics. Bismuth ferrite is one of the few single phase multiferroic materials. BFO has a rhombohedral distorted perovskite structure with space group of R3c and displays ferroelectricity below ~ 830 ºC and antiferromagnetism below 370 ºC [163]. BFO has a very large intrinsic polarization (theoretically predicted to be as high as ~100 µC/cm^2) [403] and room – temperature multiferroism. This predicted high switching polarization is indeed higher than the one of the most commercialised ferroelectric materials for memory applications (PZT based compositions). So besides the multiferroic properties and due to the large remanent polarization BFO is a promising material for applications in which polarization switching is required (as memory applications). Indeed BFO is the ferroelectric material of Fujitsu 256 Mb FeRAMs [207]. However, high dielectric losses, leakage current and tendency to fatigue are the main hurdles to overcome for any kind of electronic applications. However, the practical application of BFO is hinder due to high leakage current attributed to the co-existence of Fe^{3+} and Fe^{2+} ions along with oxygen vacancies [404]. In addition the formation of secondary phases Bi_2O_3, Fe_2O_3, $Bi_2Fe_4O_9$, and $Bi_{25}FeO_{39}$ [405] make it difficult to achieve significant superior multiferroic properties.

The synthesis of monophasic BFO is difficult due to the particular kinetics and thermodynamic properties of Bi_2O_3 – Fe_2O_3 system. Using solid state reaction methods is extremely hard to obtained pure BFO. Various modified synthesis approaches has been used to obtained monophasic BFO such as microwave sintering [406], liquid sintering [404], plasma assisted sintering [407] and mechanochemical methods [408] as well as various chemical methods such as co-precipitation [409] and hydrothermal [410]. Some of these methodologies have found some success in achieving pure BFO but no definite reaction mechanism for obtaining pure BFO phase has been identified yet. In order to stabilize the perovskite structure and to lower the conductivity of BFO doping with

different elements has also been reported and revealing promising results [411]. Nevertheless, synthesis a stoichiometric BFO and understanding the reaction process is still a point of open discussion among researchers.

Due to the technological importance of nano structured materials, efforts have been made to fabricate nano structures of BFO [412, 413]. Various chemical methods have been used to fabricate 1D BFO structures, broadly, distinguished as template and template free methods. Details on some of these methodologies have been given in Chapter 2 of this thesis. In template methods, a sacrificial template is usually Anodic Aluminum Oxide (AAO). These templates are filled with BFO solution followed by annealing (500 - 600 ºC) and removing of template carried out by chemical or by thermal etching to obtain 1D BFO structures [414]. However, BFO reacts with AAO template and forms secondary phases, which results in poor properties. 1D BFO structures have also been obtained by template free method using electrospinning, hydrothermal and combustion methods [415-417]. The use of BFO 1D nano structures have been also demonstrated for 3D memory cells by depositing BFO on ZnO nano rods by RF sputtering using LaNiO$_3$ as a buffer layer at 450 ºC; these nano structures depict piezoelectric coefficient (d$_{33}$) of 33 pmV^{-1} and a polarization of 133 µC/cm^{-2} [418]. CNTs with extraordinary electrical and mechanical properties make them a typical choice as a material for future microelectronic devices. The detailed literature review on CNTs for electronics and CNTs-FE composites is presented in Chapter 2. On a short note, CNTs are seen as possible alternative to the expensive indium tin oxide (ITO) substrates used in solar cells [419] or as channel material in FETs [11, 30]. More recently, vertical aligned MWCNTs were also coated with SrTiO$_3$ (STO) by pulse laser deposition, in order to reduce the work function of CNTs so that electron field emission can be controlled for FET applications. Here the main purpose was the coverage of a carpet type layer of CNTs, instead of individual CNTs. However, the authors did not address synthesis and phase formation [30].

There are no studies on the fabrication of MWCNTs -BFO heterostructures or the use of MWCNTs as templates to fabricate BFO nano structures using chemical or physical methods. Therefore, we studied the use of chemical solution method and physical method to fabricate MWCNTs-BFO nano structures by sol gel and RF

sputtering, respectively. A comprehensive study on the phase formation, interface, electrical and magnetic properties is addressed in this chapter.

7.2   Experimental

Approach one: sol gel method to cover covalent functionalized MWCNTs

Prior to the fabrication of MWCNTs-BFO structures a sol gel solution of BFO was prepared. 0.2 M BFO solution was obtained by mixing at room temperature in the stoichiometric proportions (1:1) bismuth(III) nitrate (BiNO$_3$.5H$_2$O, $\geq$ 98 %, Sigma Aldrich) and iron(III) nitrate (Fe(NO$_3$)$_3$.9H$_2$O, $\geq$ 98 %, Sigma Aldrich). Each precursor was dissolved in deionised water (5 ml each) before mixing to get a transparent BFO solution. Later, nitric acid (65 %, Panreac) as a solvent and citric acid ($\geq$ 99.5 %, Merck) as a chelating agent were added to the BFO solution in the molar ratio of 20:5. At this stage the solution was light yellow in colour. This solution was mixed at 70 ºC with vigorous stirring for 2 h before being used for the synthesis of 1D BFO. Covalent functionalized MWCNTs were used in this work (details about the MWCNTs are presented in Chapter 3).

MWCNTs-BFO powders were obtained by uniformly dispersing 10 mg of MWCNTs in 10 ml of BFO solution by ultra-sonication for 2 h (Branson, USA, 40 kHz) resulting in a dense black solution. The solution was refluxed at 100 ºC for 2 h, during this process NO$_2$ was evaporated, and the total volume of solution reduced. The solution was further heat treated in the oven (150 ºC for 2 h) to get dried powders of MWCNTs-BFO. The obtained amorphous powders of MWCNTs-BFO were annealed at various temperatures, from 300 up to 550 ºC and time period of 2 h to obtained crystalline nano structures of MWCNTs-BFO. BFO solution (without CNTs) was also used to obtain BFO powders for comparison purposes. Figure 7-1 illustrates the steps to produce MWCNTs-BFO and BFO powders from sol gel solution.
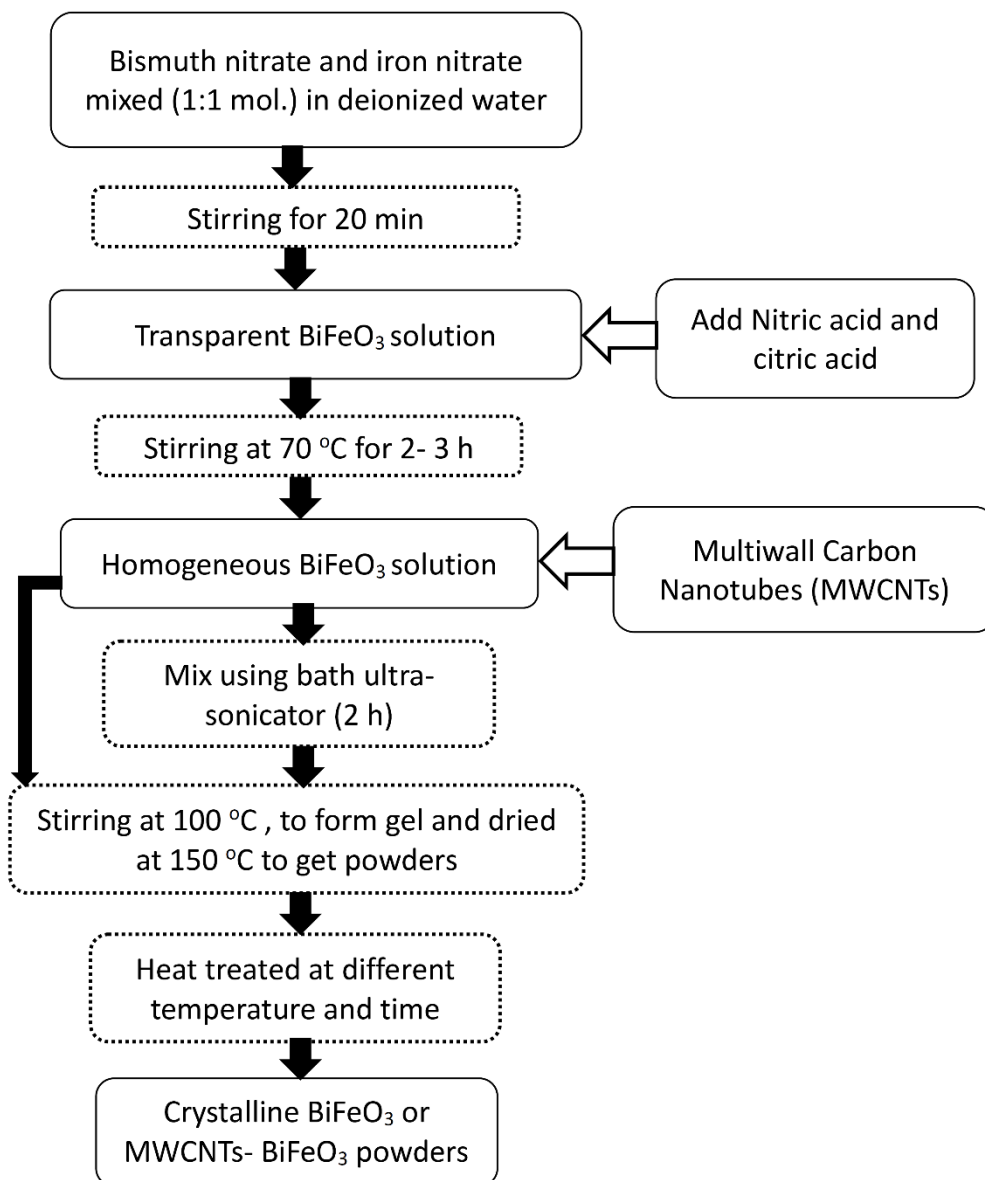
Figure 7-1Flow chart illustrates the steps followed to synthesised MWCNTs-BFO and BFO powders.

Approach two: covering Vertically Aligned (VA)-MWCNTs with BFO by sputtering

Bismuth(III) oxide (Bi_2O_3, Riedel-deHaën, 99.5 %) and iron(III) oxide (Fe_2O_3, Merck 99 %), powders were used as precursors for the synthesis of $BiFeO_3$ targets. The powders were mixed according to the BFO stoichiometry in a ball miller for 24 h using ethanol as media. The mixed powders were dried in an oven at 100 °C for 24 h followed

by a calcination step at 720 °C for 3 h. The BFO calcined powders were then ball milled for 5 h to obtain a finer particle size distribution. Next, these powders were uniaxially pressed in a 2 inch diameter die with an applied pressure of 1-5 MPa and finally heat treated at 800 °C for 4 h to obtain a dense ceramic target for sputtering. Figure 7-2 indicates the steps to fabricate BFO ceramic targets.
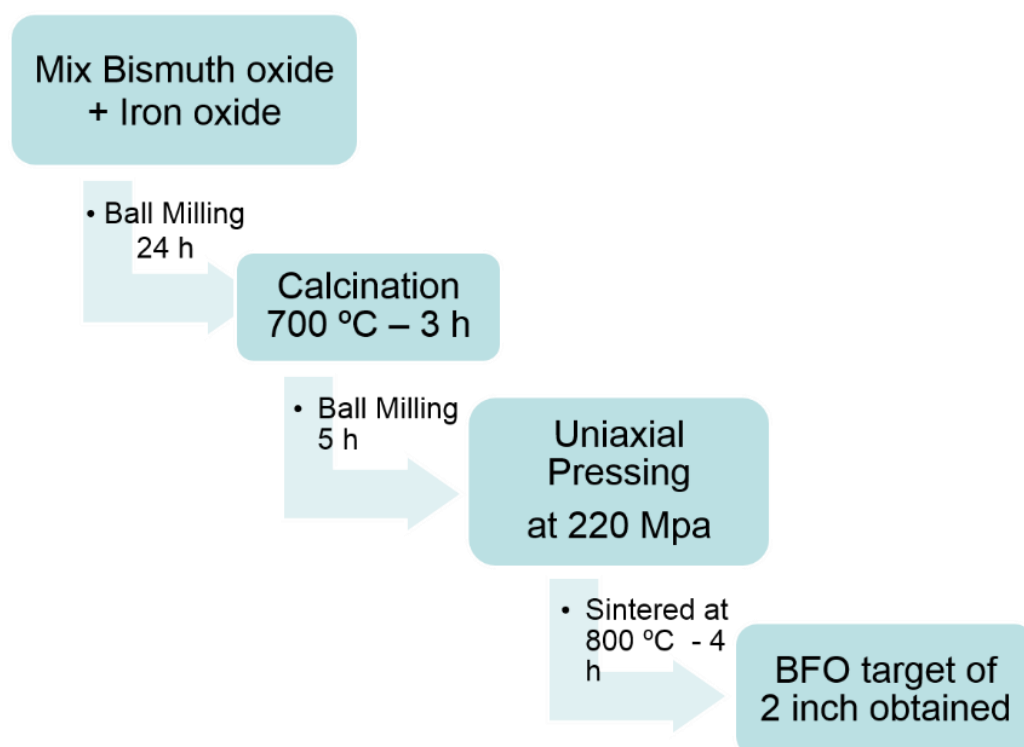
Figure 7-2 Flow chart of the steps to obtained BFO targets.

VA-MWCNTs grown on Si substrates with diameter and length of 5-20 nm and 1-2 mm, respectively, were used as substrates (CVD Materials Corporation, USA) (details are presented in chapter 3 and 4). BFO deposition was carried out in a RF sputtering unit (CRIOLAB - Equipamento Criogénico e de Laboratório Lda) at different temperatures and exposure times in an atmosphere of argon / oxygen with a flow rate of 15 and 5 sccm, respectively, and a working pressure of $7x10^{-4}$ Torr. The deposition was carried out at 60 W and working distance of 100 mm.

MWCNTs-BFO structures were characterized by differential thermal and thermo gravimetric analysis (DTA/TG) using SETARAM Labsys TG-DTA12 system. For the DTA/TG analysis alumina crucibles were used, and the measurements carried out up to 500 ºC with a heating rate of 5 ºC/min. *In-situ* X-Ray diffraction measurements as a function of the temperature were performed using Panalytical X'pert-Pro powder diffractometer. The diffraction patterns were acquired from 10 ° to 60 ° (2θ) with a step length of 0.02º. A platinum substrate was used for *in-situ* studies, which were carried out up to 550 ºC in air with an heating rate of 5 ºC/min. *Ex-situ* XRD (Rigaku, Geigerflex D/Max-C, Cu *Kα*) was used to characterize MWCNTs-BFO and VA-MWCNTs-BFO fabricated at different temperatures. MWCNTs-BFO and VA-MWCNTs-BFO were characterized by Raman in a HR 800, Jobin Yvon spectrometer, using the excitation lines of 532 nm. Scanning electron microscope ((SEM), Hitachi S4100), Transmission electron microscope ((TEM), Hitachi H9000-NA) and High Resolution TEM ((HRTEM), JEOL 2200) were used to study the morphology of the nano structures obtained by sol gel method and sputtering. The power samples of MWCNTs-BFO and VA-MWCNTs-BFO were dispersed in chloroform and transfer to Cu grids for TEM analysis. The dielectric response of VAMWCNTs-BFO were measured using a precision LCR (inductor capacitor resistor) meter (Model HP4284A) connected to a PC via a GPIB card and working in the frequency range from 1 kHz to 1 MHz. P-V loops were measured in a ferroelectric test system (aixACCT, TF ANALYZER 1000 Measurement System). Topography analysis and local piezoelectric response was measured using a MFP-3D Asylum Research Atomic Force Microscope, equipped with Zurich Instruments (HF2LI) external lock-in amplifier and a Tektronix (AGF320) function generator for BFO deposited on VAMWCNTs. Magnetic measurements were carried out on crystalline BFO 1D structures and VAMWCNTs-BFO using vibrating sample magnetometer (Cryogenic VSM). Magnetic hysteresis loops were measured at room temperature as well as 5 K in the field of 10 T for MWCNTs-BFO.

7.3   Results and Discussion

7.3.1   Approach one: MWCNTs-BFO fabricated by sol gel method

DTA/TG analysis of amorphous powders of BFO and MWCNTs-BFO are presented in Figure 7-3. DTA curves depict one endothermic peak followed by three exothermic ones for BFO and MWCNTs-BFO in the temperature range 100 to 350 oC, respectively (Figure 7-3). The endothermic and exothermic peaks in between 100 to 175 oC correspond to the evaporation of water and solvent for both powders. The total weight loss is ~6 % as from the TG analysis (marked as region I) (Figure 7-3). The next two exothermic peaks for BFO and MWCNTs-BFO at 230 ^{o}C and 330 ^{o}C are associated with the decomposition of organics used in the preparation. The weight loss in the range of 175 ^{o}C and 350 ^{o}C is around ~32 % for BFO and MWCNTs-BFO (region II and III). The DTA depicts two exothermic peaks for BFO and three exothermic peaks for MWCNTs-BFO in the region of 350 to 500 ^{o}C, respectively, highlighted and magnified view is illustrated as an inset in Figure 7-3 (a). *In-situ* XRD with temperature was performed on MWCNTs-BFO (Figure 7-3 (b)) and BFO (Figure 7-3 (c)) powders under the same conditions as in DTA/TG, to identify the phase formation. According to the *in-situ* XRD, BFO phase appears at 450 ^{o}C for both powders and the crystallinity of the phase improved further with the temperature (matched with JCPDS 20 - 0169). By comparing the phase formation results obtained from *in-situ* XRD with DTA for MWCNTs-BFO and BFO it is clear that the exothermic peak that starts at 438 ^{o}C and continues up to 450 ^{o}C corresponds to the formation of the BFO phase. TG curve depicts small weight loss less than 1 % for BFO and around 2-3 % for MWCNTs-BFO curve in the range from 425 and 500 ^{o}C, which might be due to the evaporation of some residual solvents; and in the case of MWCNTs-BFO the additional weight loss may correspond to the oxidation of MWCNTs. The oxidation of MWCNTs has been studied for the tubes used in the present studies, according to which MWCNTs start to oxidized at 420 ^{o}C in air (Chapter 4). There are few exothermic peaks before and after the BFO exothermic peak (438 ^{o}C) for BFO and MWCNTs-BFO (Figure 7-3 (a)). These peaks may correspond to the formation of intermediate and/or secondary phases. Unfortunately the XRD peaks corresponding to secondary and intermediate phases were not observed in the *in-situ* XRD investigation.
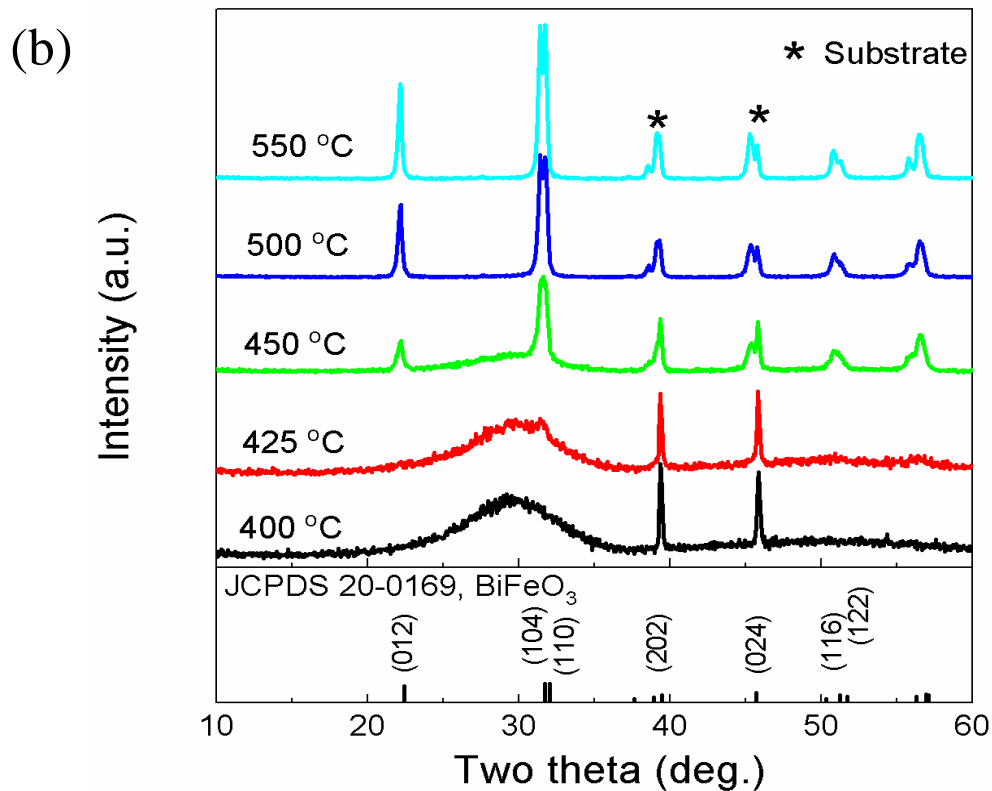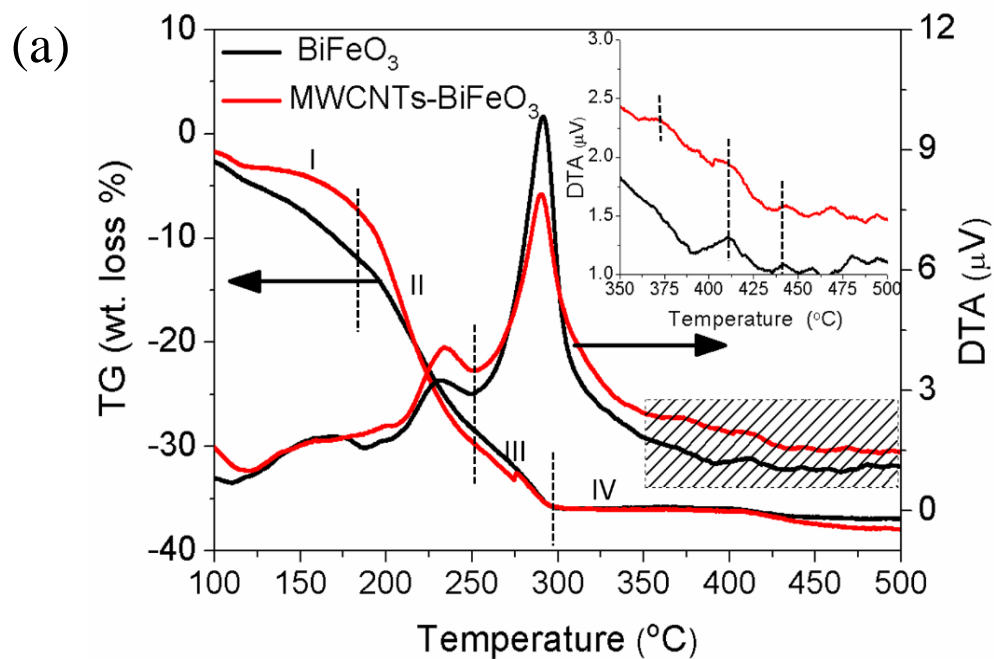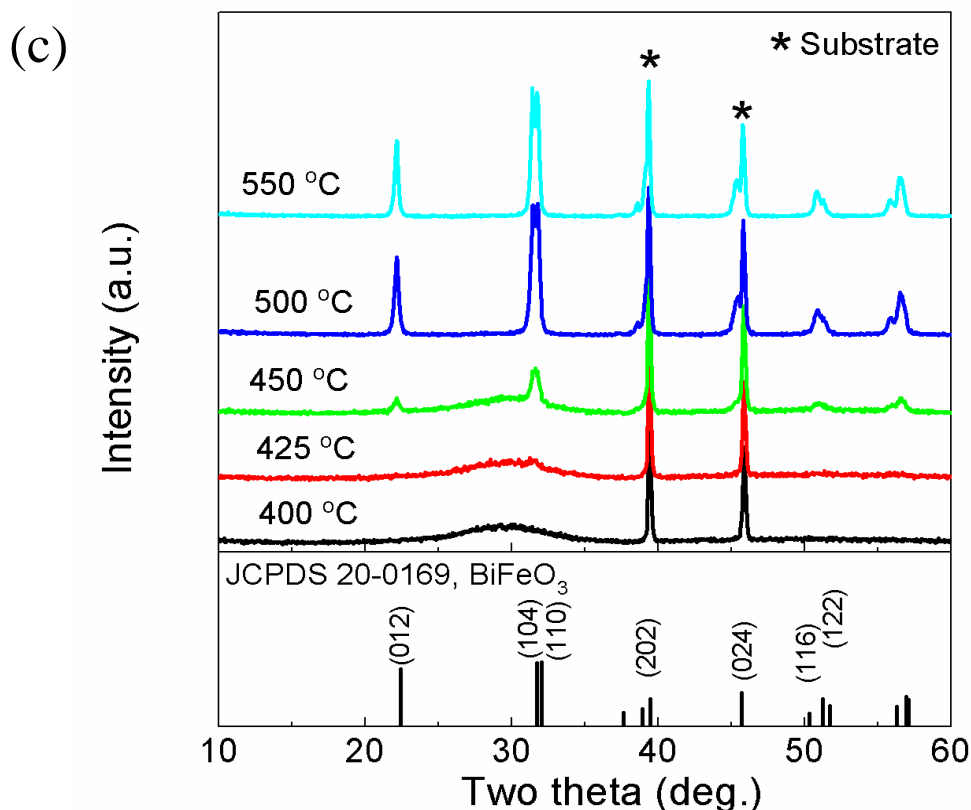
Figure 7-3 (a) DTA/TG analysis of BFO and MWCNTs-BFO powders, (b) in-situ XRD of MWCNTs-BFO and (c) BFO with heating rate of 5 ºC/min. DTA and in-situ XRD results confirms the BFO formation at 450 ºC.

Further, BFO and MWCNTs-BFO were studied by *ex-situ* XRD as a function of annealing temperature and time of 2 h (Figure 7-4). The XRD analysis illustrate that rombohedral BFO with R3c space group was formed at 350 ºC for BFO and MWCNTs-BFO, where diffraction peaks corresponds to the JCPDS 20 - 0169. BFO and MWCNTs-BFO annealed at 350 ºC depicts the presence of intermediate phases Bi_2O_3 and α FeO. However, the amount of Bi_2O_3 is small for MWCNTs-BFO heat treated at 350 ºC for 2 h in comparison with BFO prepared under the same conditions. With the further increase in annealing temperature to 420 ºC almost monophasic BFO was obtained for MWCNTs-BFO. Whereas, for BFO the intensity of the Bi_2O_3 peak has increased with annealing temperature from 350 to 420 ºC. Further increase in annealing temperature (500 ºC) for BFO depicts the formation of additional bismuth rich secondary phase $Bi_{25}FeO_{39}$. The formation of secondary phase with increasing annealing temperature has been reported in different studies, as referred in the introduction.
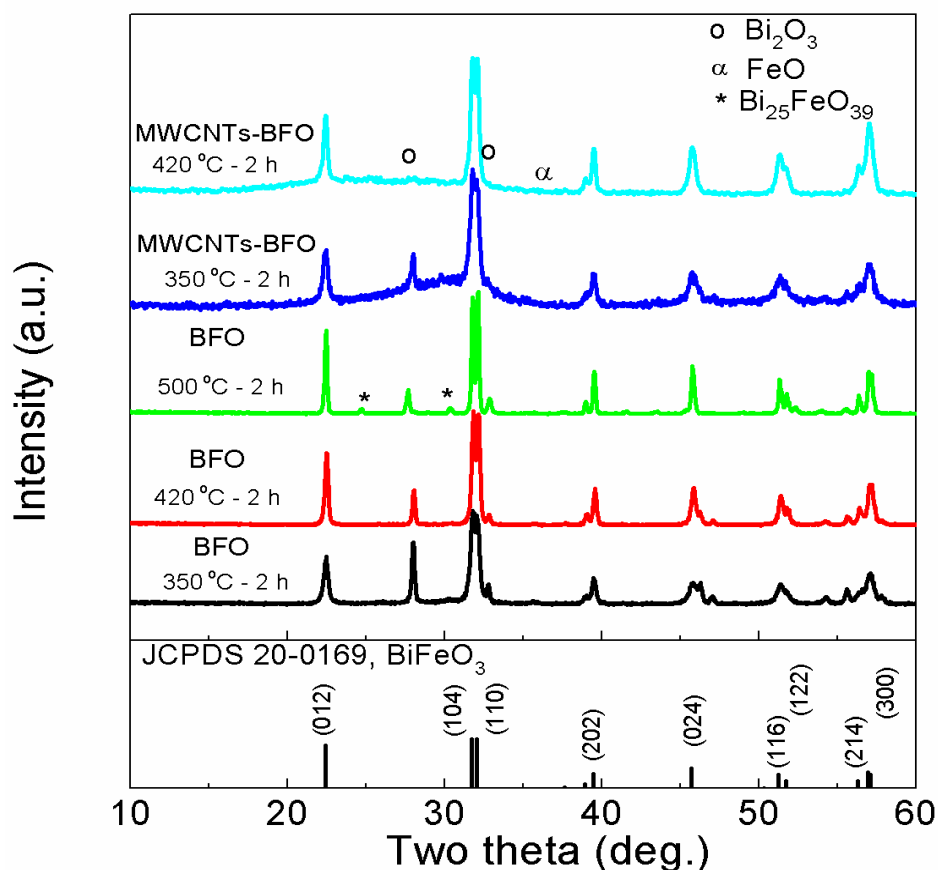
Figure 7-4 Ex-situ XRD pattern for BFO and MWCNTs-BFO powders annealed at 350 and 420 °C for 2 h. Monophasic BFO was obtained for MWCNTs-BFO after annealing at 420 °C for 2 h. BFO annealed at 500 °C depicts the bismuth rich phase $Bi_{25}FeO_{39}$, where-as the BFO and MWCNTs-BFO depicts the Bi_2O_3 and FeO as secondary phase. The presence of MWCNTs reduce the oxygen pressure due to the oxidation of MWCNTs at annealing temperature of 420 °C hence curb the formation of Bi_2O_3 phase.

The *ex-situ* XRD answered some of the questions raised from DTA analysis on the unidentified exothermic peaks. The *ex-situ* XRD confirms that the exothermic peak, between 400 and 425 °C, observed before the BFO formation might correspond to the formation of Bi_2O_3 (intermediate phase), and the same is true for MWCNTs-BFO. It is known from reported studies that a reducing oxygen pressure plays an important role on restricting the formation of Bi_2O_3 during the fabrication of BFO [420]. In the present investigation monophasic BFO phase was obtained for MWCNTs-BFO with the annealing temperature of 420 °C for 2 h. This might be due to the oxidation of CNTs, which create a reducing atmosphere and results in the lack of oxygen for the formation of

Bi_2O_3 phase. On the contrary, MWCNTs-BFO anneal at 350 ºC depicts Bi_2O_3; this annealing temperature is below the oxidation temperature of MWCNTs, resulting in the formation of Bi_2O_3.

DTA of MWCNTs-BFO presents an additional exothermic peak between 350 and 400 ºC, which corresponds to the oxidation of MWCNTs. In our previous work on the thermal stability of MWCNTs, it was observed that MWCNTs start to oxidize at 420 ºC in air. However, the presence of impurities can lower the oxidation temperature of MWCNTs [421], moreover during the refluxing of MWCNTs in the nitric solution, the tubes were severely damaged as observed in the TEM. This might also account for the early oxidation of CNTs. The decrease in oxidation temperature for MWCNTs treated in nitric acid for different time interval has also been reported recently [422]. This result corroborates our observation that the exothermic peak between 350 and 400 ºC corresponds to the oxidation of MWCNTs; therefore no carbon nanotubes remain after the annealing of MWCNTs-BFO at 420 ºC for 2 h.

Raman spectroscopy is an important tool for the characterization of CNTs. The Raman spectra of CNTs usually exhibits three characteristic bands for MWCNTs. The tangential stretching of carbon atoms results in G band (1500 -1600 cm^{-1}), that is a characteristic feature of the graphitic layers. The second and third characteristic bands are from defective graphitic structures, named as D mode (~1330 cm^{-1}) and D´ band (1610 cm^{-1}) [423]. In the present work, the Raman spectra for MWCNTs and MWCNTs-BFO (before annealing) were studied (Figure 7-5). All the characteristic bands of MWCNTs (G, D and D´ band) are marked in the spectra. MWCNTs and MWCNTs-BFO (before annealing) depict all the three characteristic peaks as mentioned above. There is no significant Raman peak shift for MWCNTs after being covered with BFO. However, the intensity of both D and G band is reduced for MWCNTs-BFO in comparison to MWCNTs, due to the less number of photons that interacts with the C-C skeleton of MWCNTs. The MWCNTs-BFO annealed at 420 ºC for 2 h does not depict the characteristic peaks for MWCNTs.
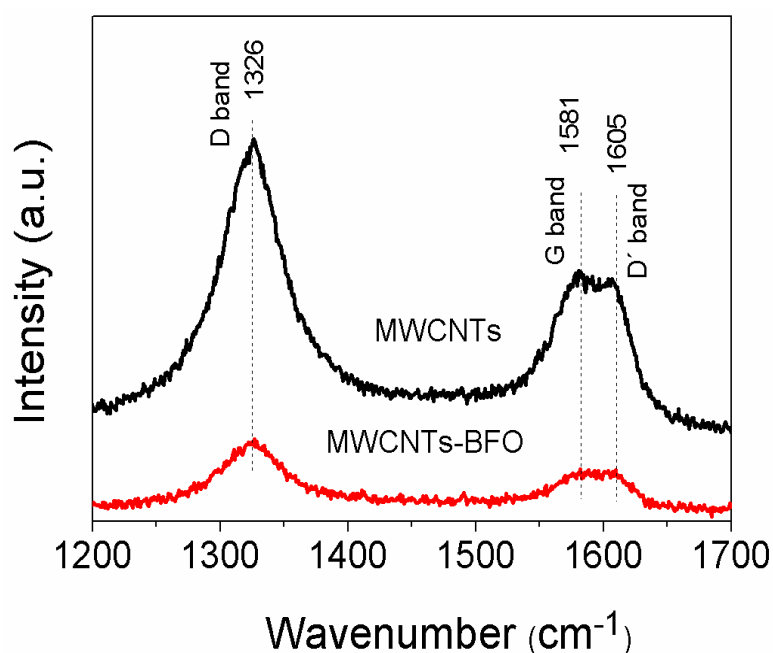
Figure 7-5 Raman spectra for functionalized MWCNTs and MWCNTs-BFO (before annealing). After the deposition of BFO solution on MWCNTs the intensity of the characteristic CNTs peaks were reduced and no peak shift was observed.

MWCNTs-BFO before and after heat treatment were characterized by electron microscopy. $BiFeO_3$ amorphous particles are present on the surface as well as inside the tubes, as depicted in Figure 7-6 (a). Magnified HRTEM micrograph from one of the tubes illustrates the presence of amorphous BFO particles along the walls, as well as inside the tubes, marked by arrows in Figure 7-6 (b). The inset in Figure 7-6 (b) depicts the magnified view of MWCNTs tip; tips were oxidized what might have occurred during the refluxing in nitric suspension at 100 ºC, permitting the partially filling of MWCNTs with BFO solution.

The process of opening and filling of MWCNTs is possible by two approaches; wet chemical and physical methods. In the wet-chemistry approach the cap of CNTs can be removed by refluxing in nitric basic suspensions of the metal oxide and simultaneous filling of metal salts took place what is highly depended on the wetting capabilities. The opening of CNTs with nitric acid was first demonstrated by Tsang *et al* [118] that used this approach to fill in the tubes with various metals from their respective nitrate

precursors. The use of nitric solution results in the removal of the MWCNTs cap due to its weak sp^3 hybridization in comparison to strong sp^2 hybridization of the walls. The second approach, the physical method is a two-step process; in the first step the cap of CNTs is removed by thermal oxidation and in the second one, CNTs without caps are immersed inside the metal solution, resulting in the filling [424]. In both methods the filling of tubes occurred through capillary forces. Ugarta *et al* have demonstrated that liquids with lower surface tension (< 190 mN/m) are effective for filling and wetting the nanotubes, being nitrates salts among them [120].

In the present work, the oxidation of CNTs cap and partial filling of MWCNTs occurred due to refluxing of nitric acid followed by the filling and wetting of MWCNTs, in a single step. 1D structures formed after annealing at 420 ºC are illustrated in Figure 7-6 (c,d). SEM micrograph depicts the 1D structure of MWCNTs-BFO having a diameter in the range of 10 – 100 nm but the morphology of the tubes is not uniform. TEM studies confirm the formation of 1D BFO structure and crystalline BFO attached together to form 1D morphology. The tip of the 1D MWCNTs-BFO structure is irregular and widen; this is due to the presence of excess amount of precursor at the open end of the tubes, resulting in the formation of irregular "mouth". From SEM and TEM micrographs it looks like that the 1D structure is formed due to attachments of nano size crystals. These crystals were further analysed under HRTEM.
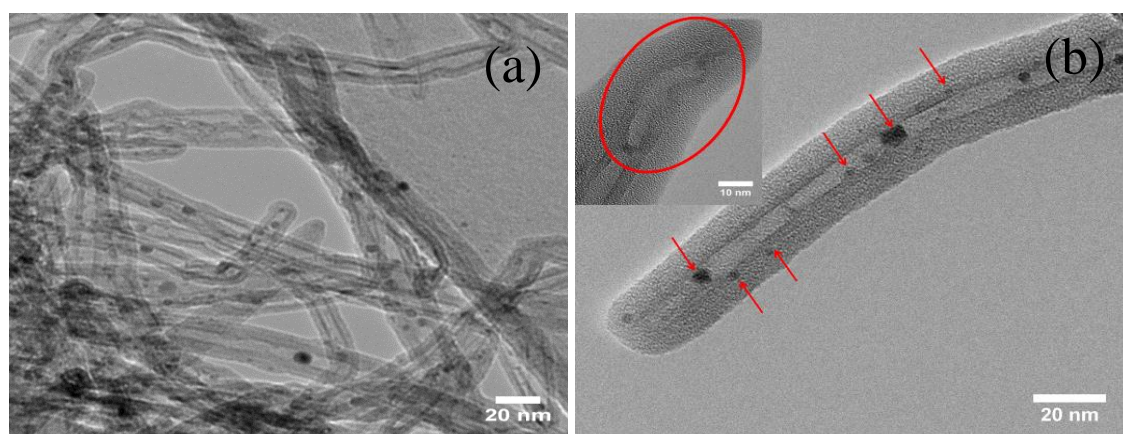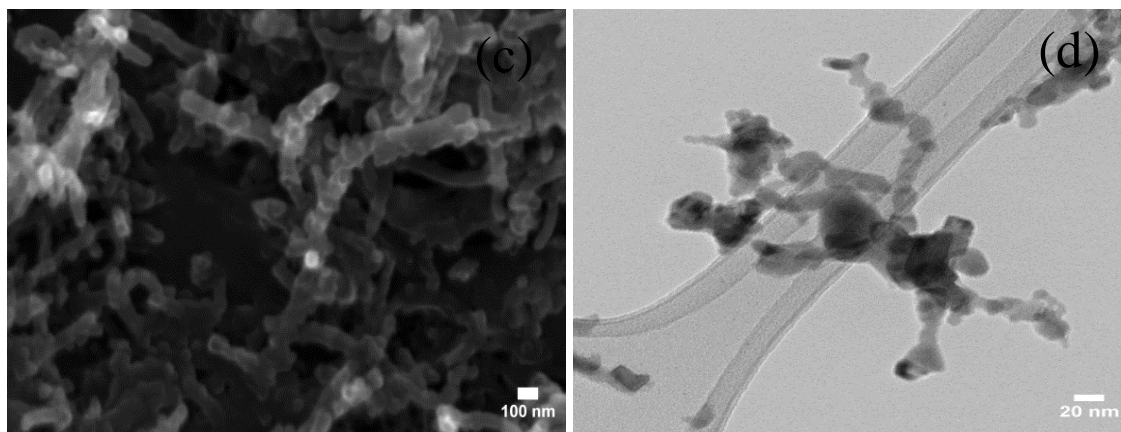
Figure 7-6 TEM micrographs of MWCNTs-BFO before annealing: (a) MWCNTs coated with BFO solution, (b) a detail of a MWCNT coated with BiFeO₃ solution showing amorphous particles deposited on the walls and inside the tubes; inset illustrates the magnified view of MWCNT where the CNTs lattice along the cap has been oxidized. MWCNTs-BFO after annealing at 420 ºC for 2 h: (c) SEM micrograph illustrate the nano structure of BFO and (d) TEM micrograph represents the BFO nano structures with non-uniform thickness all along the structures.

HRTEM micrographs of 1D MWCNTs-BFO annealed at 420 ºC depict the presence of various crystalline 1D particles with aspect ratio of 1:3 and above. The interplanar spacing is around 0.28 nm (presented in inset of Figure 7-7 (a)), which corresponds to (012) crystalline plane of BFO. Figure 7-7 (b) depicts the magnified view from one of the crystalline particles; the particle imitates the morphology of CNTs. The CNTs lattices were not observed during the HRTEM investigation of MWCNTs-BFO. This corroborates the findings of Raman and supports our discussion on the role of MWCNTs oxidation on the formation of monophasic BFO. From the morphology of crystalline BFO it can be concluded that MWCNTs acted as a template for the fabrication of 1D BFO. Chemical composition of MWCNTs-BFO investigated by energy dispersive X-Ray spectroscopy (EDS) spectra (inset in Figure 7-7 (b)) confirms the presence of bismuth and iron elements in the composite; the additional peaks such as Cu are from the TEM grid.
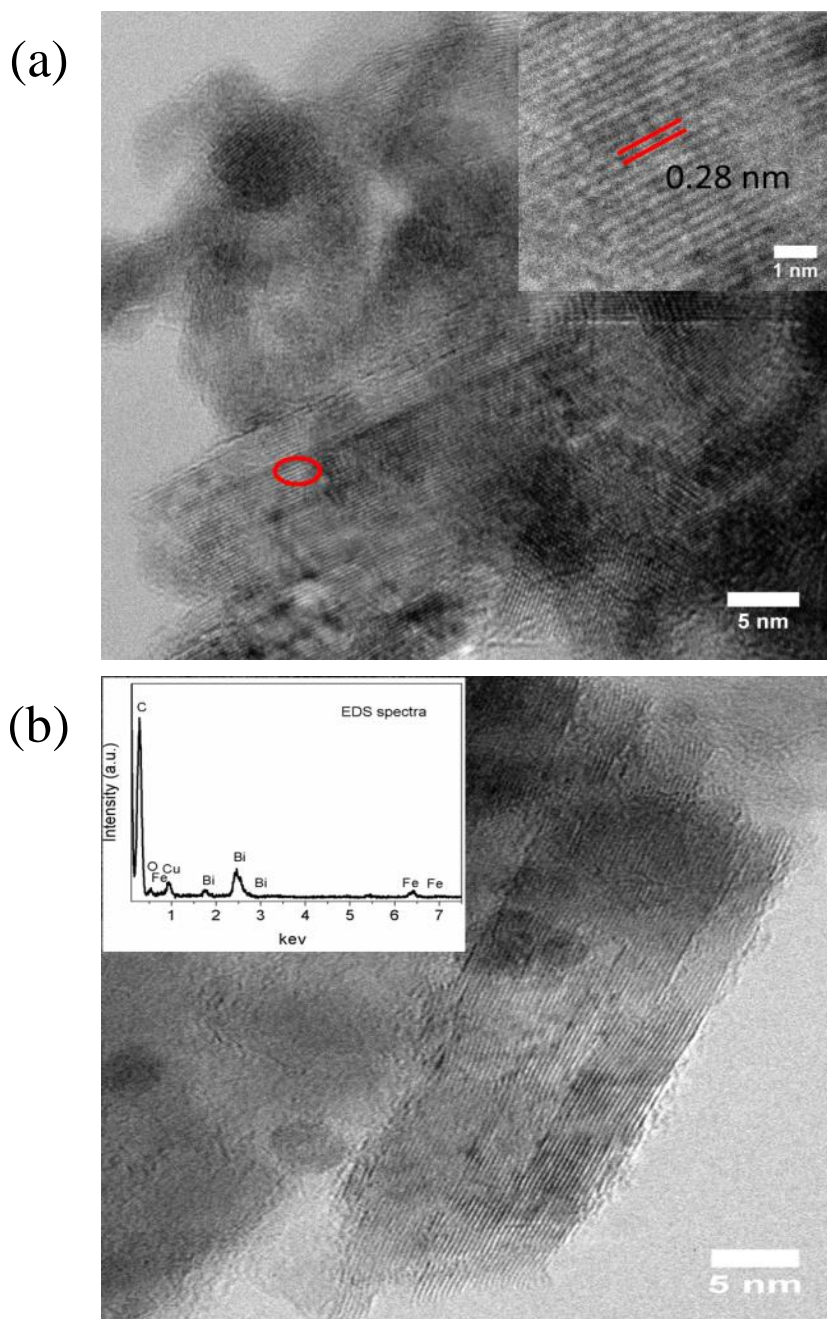
Figure 7-7 HRTEM micrograph of MWCNTs-BFO annealed at 420 °C for 2 h (a) depicts crystalline particles with aspect ratio of 1:3 and above; the inset illustrates the lattice spacing of this crystalline particle as 0.28 nm (b) magnified view from the BFO nano structure depicts 1D crystallites and inset illustrate EDS spectra confirm the presence of bismuth and iron elements. MWCNTs were completely oxidized as no MWCNTs found under HRTEM and the crystallites of BFO clearly illustrates the morphology of nano rods, formed due to the template of the MWCNTs.

Figure 7-8 gives the relationship between magnetization and magnetic field for MWCNTs-BFO at 300 K and 5 K. MWCNTs-BFO at room temperature with magnetization at 10 K Oe field is nearly 0.9 emu/g and $2H_c$ of 514 Oe, as illustrated in inset of Figure 7-8. The unsaturated hysteresis loop from MWCNTs-BFO with weak ferromagnetic behaviour is similar to one reported for BFO wires [425], different from the bulk BFO. The average diameter of the BFO wires is around 30 nm, which is lower than the wavelength (62 nm) of the in commensurate spiral spin structure. The BFO particles with size less than 62 nm possess weak ferromagnetic properties due to size confinement effect where the antiferromagnetic order is frequently interrupted at the particle surface. These confinements partially destroy the spiral spin structure and results in the weak ferromagnetic ordering.

At low temperature (5 K) the size effect is more significant, from the broadening of the M-H curve and increase in magnetization values from 0.9 emu/g (300 K) to 2.2 emu/g, as well as cohesive field (2Hc) from 514 Oe to 956 Oe, respectively. The increase of magnetization values at low temperature is the result from the cycloid structure which is more an harmonic at lower temperature and its detrimental effect on the magnetic ordering is diminished [426]. Therefore, in the MWCNTs-BFO nanowires, the spin relaxation from the spatially modulated anti ferromagnetic configuration can be quite significant, resulting in weak ferromagnetic behaviours and enhanced M at low temperature.
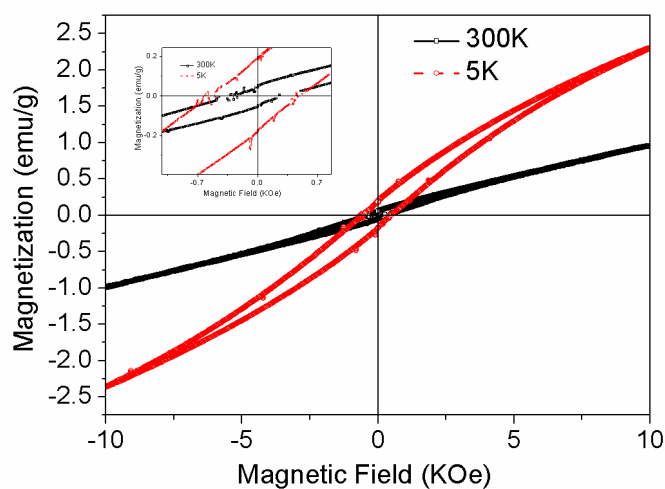
Figure 7-8 Magnetic M-H hysteresis loops of MWCNTs-BFO at 300 and 5 K, where the inset gives a magnified view of the loop near the origin. The MWCNTs-BFO depicts magnetization values of 2.2 emu/g and coercive field (2Hc) of 956 Oe at 5 K.

7.3.2   Approach two: Covering VA-MWCNTs with BFO

XRD patterns of BFO targets and films deposited on VA-MWCNTs synthesised *in-situ* at 400 °C and 600 °C are illustrated in Figure 7-9 (a). The BFO target depicts almost pure BFO rhombohedral phase with minor amounts of secondary phases ($Bi_2Fe_4O_9$, $Bi_{25}FeO_{40}$). The diffraction peaks from the planes (012), (104), (110), (113), (006), (202) and (211) are indexed to the R3c crystal symmetry. At 350 °C the deposited BFO is amorphous as seen by XRD. BFO deposited on VA-MWCNTs at 400 °C for 1 and 2 h is almost monophasic, with trace amounts of Bi_2O_3 (Figure 7-9 (a)). To note that Bi_2O_3 does not have significant effect on the magnetic properties, while increasing the conductivity of the film [427]. Moreover, its amount can be reduced by changing the oxygen partial pressure [420]. As the growth temperature increases from 400 °C to 600 °C, formation of the non-perovskite phase $Bi_2Fe_4O_9$ takes place (Figure 7-9 (a)). Indeed there is a very narrow temperature window in which pure monophasic BFO can be obtained, depending on the processing parameters [428] and purity of the reagents [429]. Secondary phases such as $Bi_2Fe_4O_9$ and $Bi_{25}FeO_{40}$ reduce significantly the electrical response, therefore they should be avoided. In addition, BFO sputtered on VA-MWCNTs at room temperature and later annealed at 500 °C (*ex-situ*) in air and in flowing nitrogen depicts Bi_2O_3 as the major phase with small amounts of BFO and $Bi_2Fe_4O_9$, as observed by XRD (Figure 7-9 (b)). Considering the above, BFO films deposited at 400 °C on VA-MWCNTs were used for further characterization.
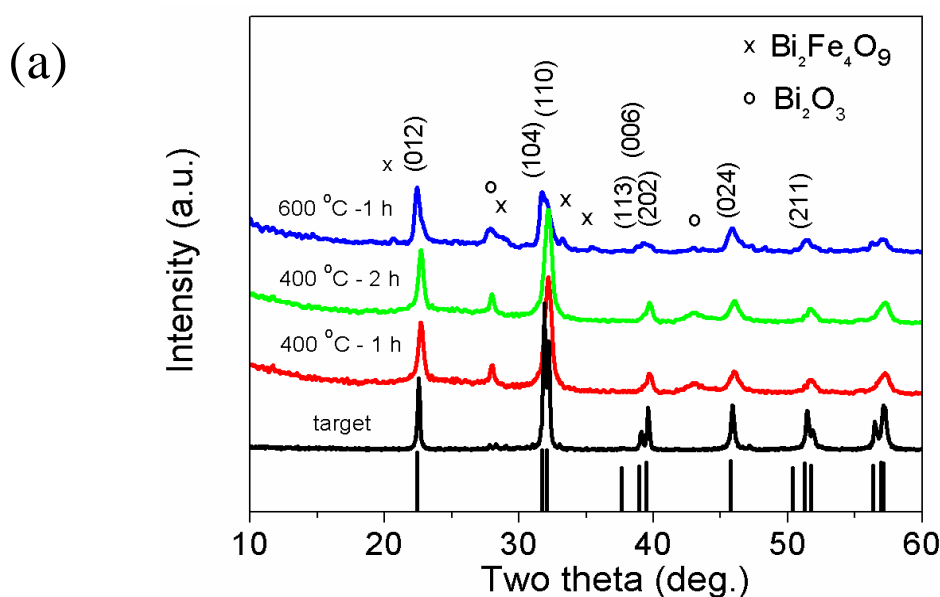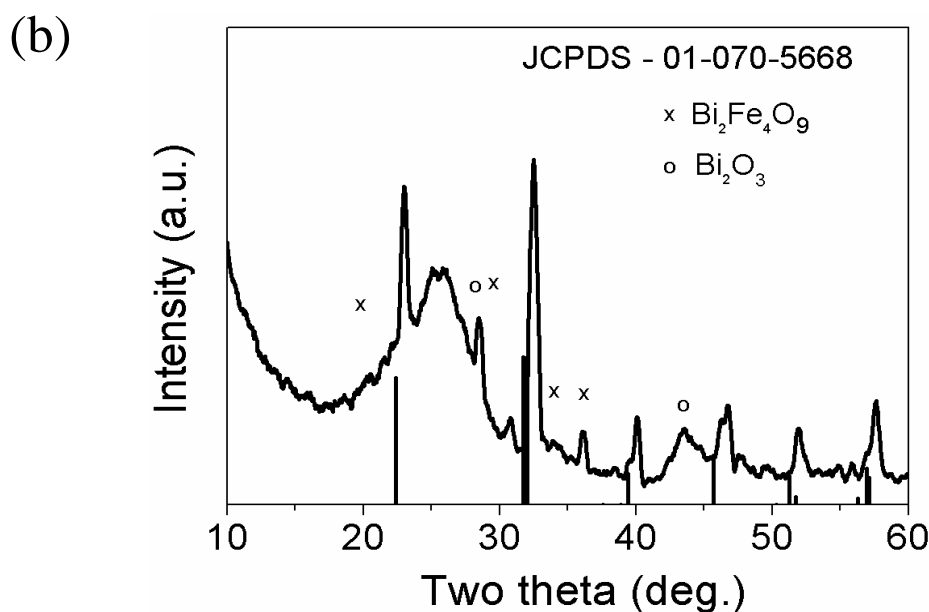
Figure 7-9 XRD pattern of BFO target and BFO films on VA-MWCNTs fabricated in-situ at 400 °C - 1 h, 400 °C - 2 h and 600 °C - 1 h. With the increase in deposition temperature to 600 °C secondary phases are well visible and (b) XRD of BFO deposited on VA-MWCNTs followed by annealing at 500 °C – 2 h in air shows poor crystallization and domination of secondary phases.

The optical micrographs of VA-MWCNTs and BFO on VA-MWCNTs are represented in Figure 7-10 (a,b). The complete covering of VA-MWCNTs by the brownish layer of BFO can be seen. In order to check the microscopic morphology the films fabricated at 400 °C with varying time were investigated by SEM (Figure 7-11). SEM micrographs of BFO on VA-MWCNTs deposited at 400 °C for 1 and 2 h depict uniform coverage on the aligned tubes with rough topography. However, as the deposition time increases (above 2 h) films become porous what may result from the partial or local oxidation of MWCNTs, due to isothermal heating at ~400 °C for prolonged periods of time. Indeed isothermal heating near 400 °C in air results in the oxidation of MWCNTs as reported before (Chapter 4).
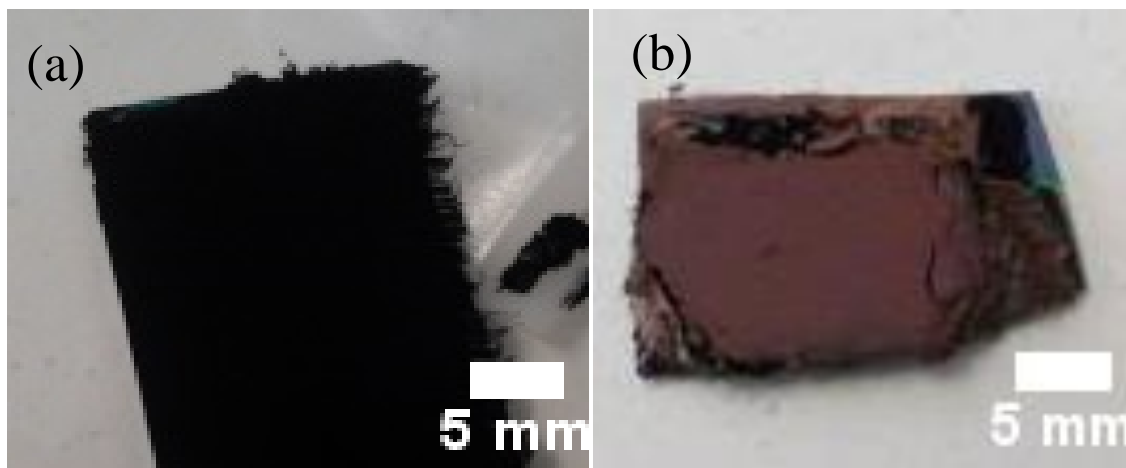
Figure 7-10 Optical images of (a) dense VA-MWCNTs on Si substrate and (b) BFO sputtered on the surface of VA-MWCNTs, deposited at 400 ºC for 2 h. The optical micrographs depict a uniform coverage of VA-MWCNTs with BFO.
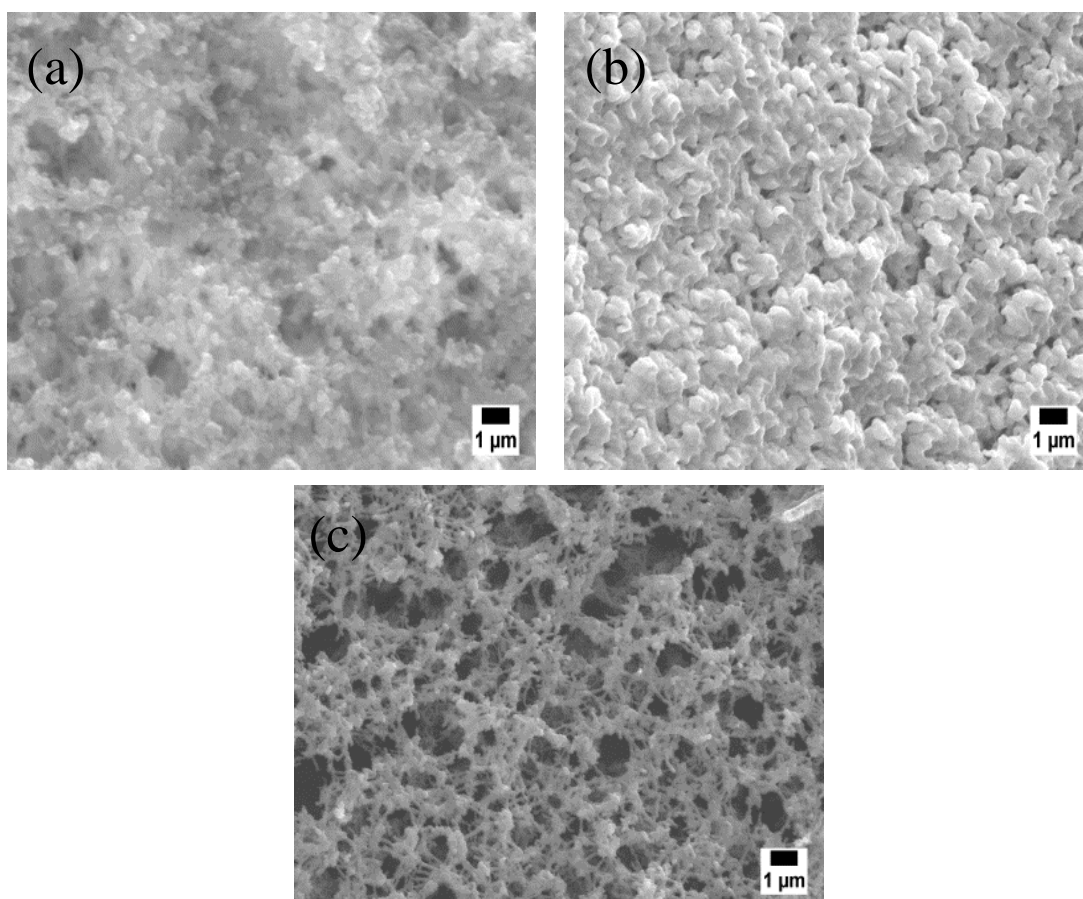
Figure 7-11 Top view SEM micrographs of BFO on VA-MWCNTs deposited at 400 ºC for (a) 1 h (b), 2 h and (c) 4 h. Dense BFO films on VA-MWCNTs are obtained at 400 ºC with a deposition time of 2 h.

VA-MWCNTs (400 °C - 2 h) covered with BFO were removed from the substrate and observed under HRTEM (Figure 7-12). There is a uniform covering of VA-MWCNTs with BFO films with average thickness of 150 nm. Detailed observation of VA-MWCNTs coated with BFO revealed tubes coverage thickness of about 5 - 10 nm in size (Figure 7-12 (a-b)). The inset (marked by a circle in Figure 7-12 (b)) depicts VA-MWCNTs lattices with spacing of 0.34 nm and also intact carbon nanotubes; no visual damage after deposition of BFO can be seen from HRTEM (Figure 7-12 (c) TEM micrograph of as received VA-MWCNTs). BFO crystalline particles with lattice spacing of 0.27 nm from d_{110} plan are also specified in the micrograph.
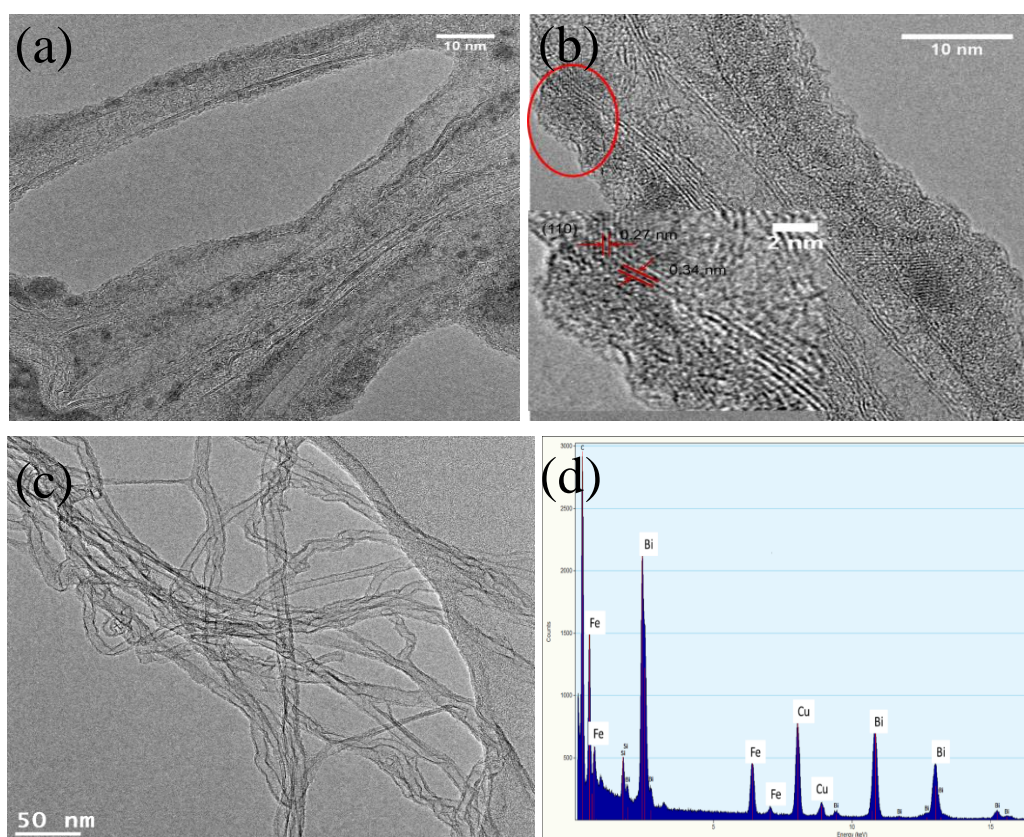
Figure 7-12 HRTEM micrographs of BFO on MWCNTs deposited at 400 °C for 2 h (a). Magnified view of one of the tubes with a 5 nm BFO thick layer (b). A d spacing of 0.34 nm and 0.27 nm was measured for MWCNTs and BFO, respectively (c) HRTEM micrograph of as received VA-MWCNTs, with well-defined carbon walls and covered with some amorphous carbon layer and (d). EDS confirms the presence of Bi and Fe.

EDS analysis on coated VA-MWCNTs identifies Bi, Fe and O elements (Figure 7-12 (d)) and the elemental mapping proves the uniform distribution of Bi, Fe and O

throughout the BFO layer (FFigure 7-13). Under the current experimental settings the best conditions for the fabrication of BFO by *in-situ* RF sputtering on VA-MWCNTs are 400 ºC with deposition time varying between 1 and 2 h for which there is no damage of the morphology of BFO films and MWCNTs.
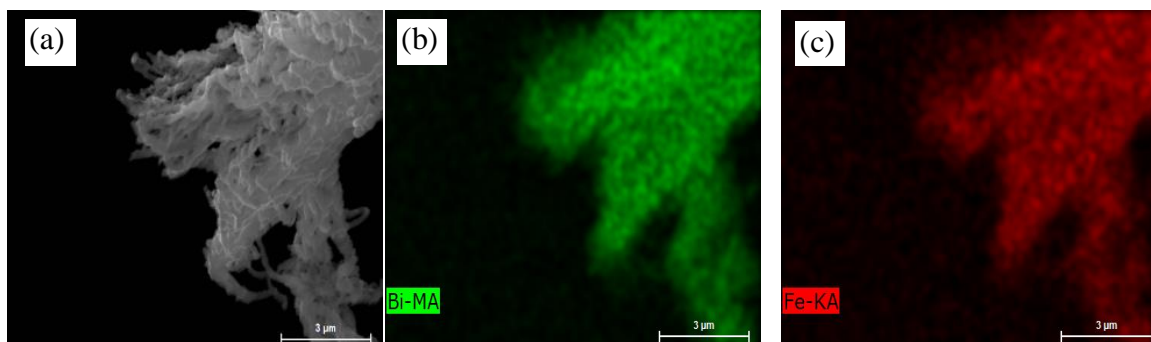
Figure 7-13 SEM elemental maps of MWCNTs coated with BFO at 400 ºC for 2 h (a): bismuth (b) and iron (c) showing a uniform distribution of elements.

BFO films on VA-MWCNTs were further characterized by Raman spectroscopy (Figure 7-14 (a)). VA-MWCNTs used in this work depict two characteristic peaks at 1336 and 1575 cm^{-1} corresponding to D and G band respectively, where the D band is attributed to the breathing vibration of aromatic rings of carbon in the lattice, indicating that the defect level of CNTs and G band corresponds to E2g mode where atoms of the carbon unit cell vibrate tangentially to each other [34]. After the BFO deposition the D and G band of MWCNTs shift to high frequency by ~2 cm^{-1} and the full width half maximum of the peaks also decreases due to less phonons interaction [29]. The shift in Raman peaks gives the information of the stress level of the MWCNTs [430]. In our case, because the observed shift is small it indicates that the stress level developed at the interface is not so strong, as the one observed for example for MWCNTs covered with PZT by pulse laser deposition [28].

The change in the intensity ratio of D and G bands (I_d/I_g) is 1.0 and 1.2 for the MWCNTs and BFO coated VA-MWCNTs in this study, respectively. The increase in the intensity ratio after BFO deposition, may state that the BFO layer constrain the vibration motion of carbon lattice and results in the increase of D band intensity; other possible reason for this shift can be related with the loss of structure, the conversion of significant

number of sp^2 hybridized carbon to sp^3 carbon hybridization during deposition of BFO [431]. From the Raman results one can also conclude that MWCNTs do not deteriorate significantly during the *in-situ* growth of BFO films at 400 ºC corroborating the previous observations.

The group theory predicts 13 Raman active modes $4A_1 + 9E$ for rhombohedral lattice type with R3c space group, as is the case of BFO. Fukumura *et al.* [432] found all the 13 Raman active mode for BFO cubic single crystals [111] at 4 K (A_1 147, 176, 227, 490 cm^{-1} and E 265, 279, 351, 375, 437, 473, 525, 77, 136 cm^{-1}). In the present studies of BFO films on VA-MWCNTs, very weak Raman modes were observed at 121, 245, 458 and 612 cm^{-1}, where 121, 245 and 458 cm^{-1} peaks are from A_1 mode, 245 and 612 cm^{-1} are from E mode (Figure 7-14 (b)). The Raman modes observed for BFO on VA-MWCNTs shift towards lower frequency when compared with the Raman mode observed for bulk BFO [433]. As well known in thin films soft modes are very sensitive to strain and nano structuring and generally it results in the shifting of Raman peaks; the shift upwards in the frequency results from compressive stresses while tensile stresses cause downwards shifts [434]. Therefore, the shift of Raman peaks to lower frequency, as here observed, indicates that BFO films on MWCNTs are in tensile state.
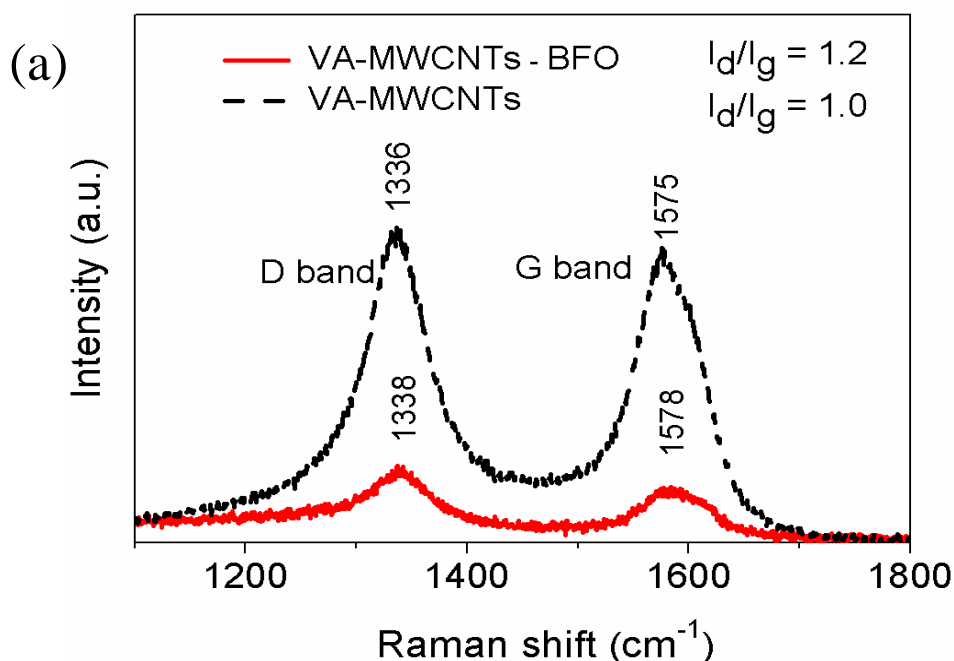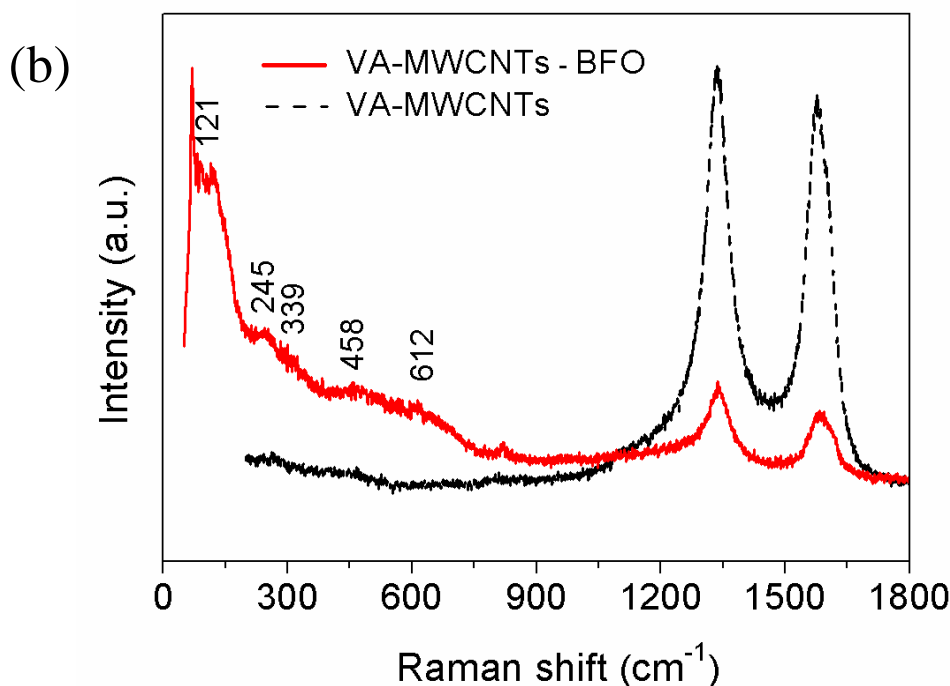
Figure 7-14 Raman spectra of VA-MWCNTs and BFO on VA-MWCNTs (a); comparison of characteristic peaks of MWCNTs and BFO (b). The shift in Raman peaks states that the CNTs and BFO on top of CNTs are under stress.

The capacitance, losses and P-V loops were measured on BFO - MWCNTs composites and are depicted in Figure 7-15 (a, b). BFO-MWCNTs composites show capacitance of 9 pF and dielectric losses ~0.02 at 1 MHz, for an applied voltage of 0.1 V. Lossy P-V loops were observed with polarization values around 1.5 - 2 $\mu C/cm^2$ at 50 and 100 Hz, respectively. Indeed two main limitations of BFO (bulk, films and nanostructures in general) are the high dielectric losses and low resistivity. It is now well recognised that the lossy polarization behaviour of BFO is mainly intrinsic and extrinsic, i.e. created by space charge, defects, cationic and anionic vacancies, etc. The existence of oxygen vacancies has been related to the reduction of Fe^{3+} species to Fe^{2+} $[Bi(Fe^{2+}Fe^{3+})]O_{3-d}$ and Bi deficiency ($Bi_{1-x}FeO_{3-d}$) due to the high volatility of Bi [435-438]. In the present case the synthesis of BFO carried out in reduced oxygen pressure might have contributed to the oxygen vacancies [439] and in addition the CNTs and BFO interface and topography might have contributed to conducting BFO. Because lossy hysteresis loops may hinder the ferroelectric behaviour, therefore domain switching and local electrical polarization were studied by PFM.
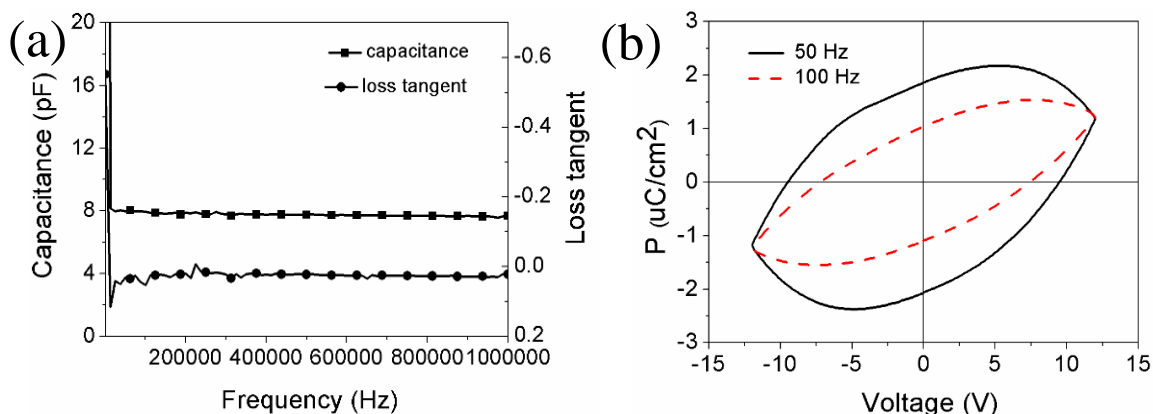
Figure 7-15 Hysterisis loop (a) and dielectric permitivity and looses as a function of frequency (800 Hz to 1 MHz) (b) for BFO films on VA-MWCNTs sputtered at 400 °C for 2 h.

Topography and PFM phase response of BFO films (on top of VA-MWCNTs) were simultaneously acquired with the application of 5 V at 30 kHz between the tip and the ground electrode (MWCNTs) (Figure 7-16 (a, b)). The rms roughness of the BFO on VA-MWCNTs is 25 nm for 2 x 2 μm^2 scan area; this is due to non-uniform surface of VA- MWCNTs. No well-defined grain boundaries can be seen from the topography micrograph for BFO. Nevertheless, the line profile from topography image and piezoresponse depicts most of the response are consisting of mono domains (Figure 7-16 (c)). The piezoresponse image is characterized by strong domain contrast: deep bright and dark areas indicate significant out of plane components of polarization. There is a small fraction of regions with poor contrast likely corresponding to domains with polarization directed parallel to the surface. The piezohistogram acquired from the piezoresponse micrograph depicts the bi-modal distribution of the domains for BFO on VA-MWCNTs (Figure 7-16 (c)). The deconvolution of the piezohistogram into two peaks was done to emphasise the covered area with positive and negative domains. The out of plan phase response centre is 32º for the positive phase and ~- 42º for negative domains (Figure 7-16 (b)). From the fitting peaks and area under them it is clearly suggested that most of the domains are oriented along the applied field. There is a very small area, which is not covered by the two fitting peaks and is representing the number of domains, which do not show out of plane response.
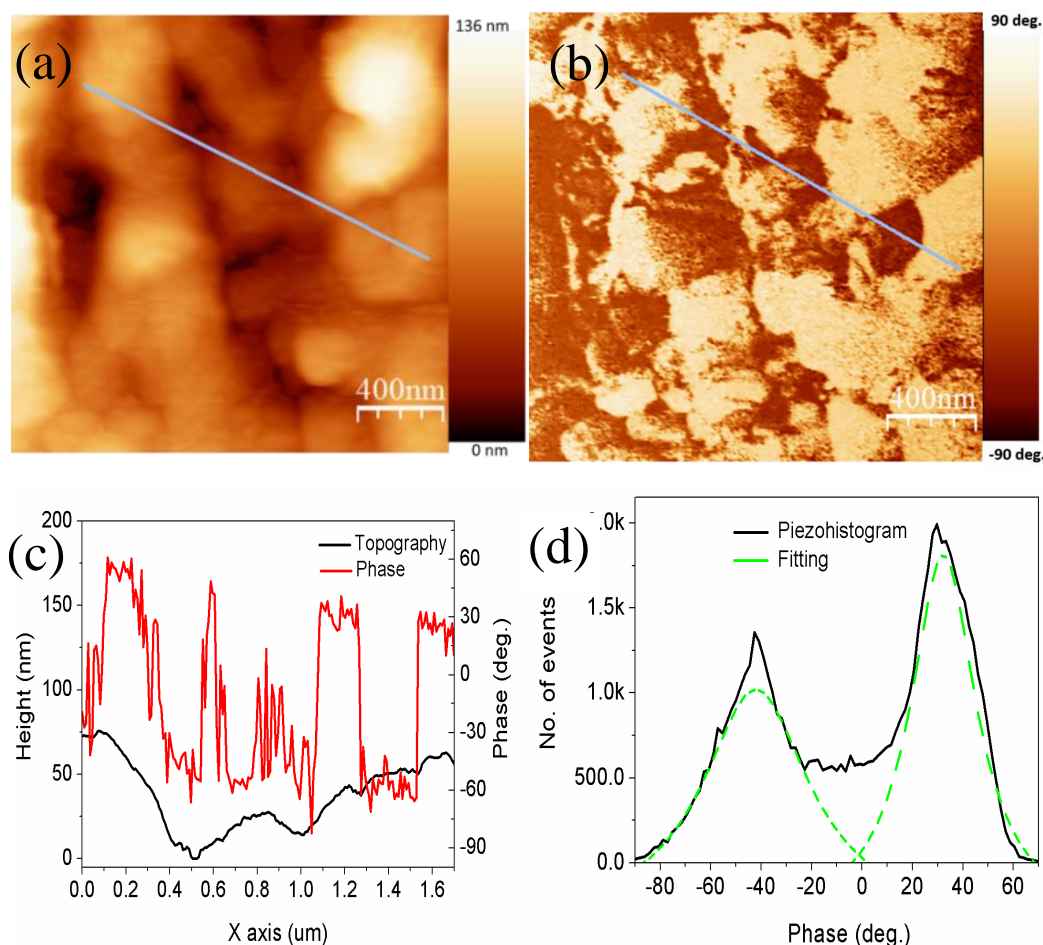
Figure 7-16 Topography (a), out of plane piezoresponse (b) and line profile from topography and piezoresponse (c) from BFO films on VA-MWCNTs. The dark and bright contrast from domains of these BFO films is clearly visible (d) Phase piezohistogram of BFO on VA-MWCNTs.

BFO on VA-MWCNTs was further characterized by point poling to investigate its ferroelectric behaviour. The point poling was performed on two areas, where domains are showing the dark contrast (marked by cross in Figure 7-17 (a)). The marked area on the left of the micrograph was poled by - 30 V and the marked area on the right of the micrograph was poled by + 30 V each for approximately 30 s. After poling both the areas, the piezoresponse was acquired with the application of 5 V depicted in Figure 7-17 (b) (poled area marked by cross). The piezoresponse from the area poled with -30 V, reveals no significant change in the contrast. However, the area poled with +30 V shows a change in the contrast of the area, which confirms the switching of domains with the application of DC bias.

The above poling results indicate that BFO domains can be switched with the application of an electric field. To further strengthen this claim of ferroelectric nature of the BFO on the surface of VA-MWCNTs switching spectroscopy PFM (Switching spectroscopy, SS-PFM) with frequency of 0.2 Hz and period of individual pulses of 0.5 ms, was carried out. Figure 7-18 illustrates ferroelectric hysteresis loop and amplitude loop obtained with the application of ±30 V DC bias. A square PFM loop was obtained with coercive bias of ±10 V. In PFM the measurements are local and come from individual grains or adjacent grains, which reflects more or less single crystal properties. It was proved that BFO films on VA-MWCNTs in spite of the low synthesis temperature and lossy macroscopic polarization response exhibit local ferroelectric behaviour where switching of ferroelectric domains is possible under an applied field.
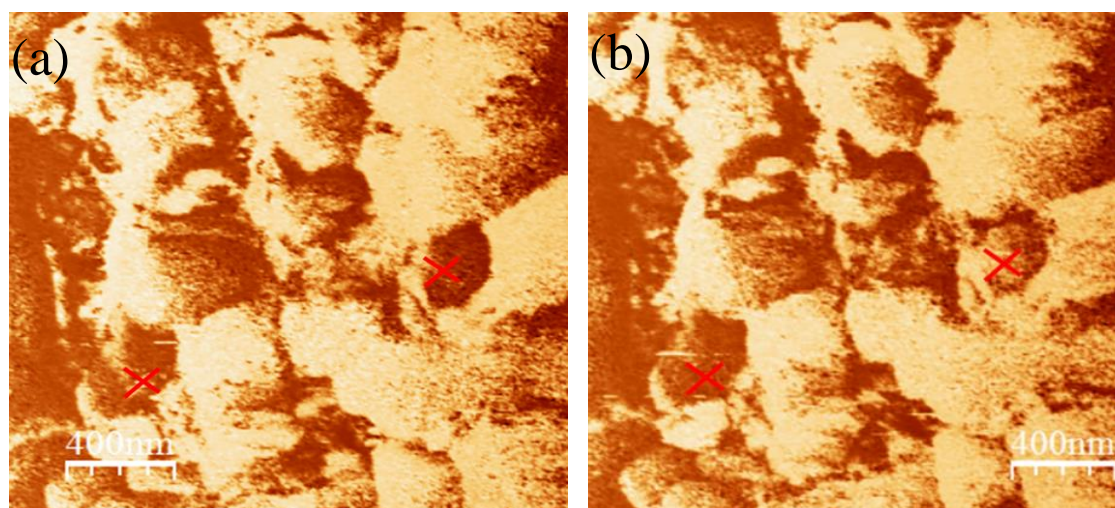
Figure 7-17 Point poling was performed on the area marked by cross, with -30 V on left and +30 V on right: phase response (out of plane) before poling (a) and phase response (out of plane) after point poling for BFO films on VA-MWCNTs (b).
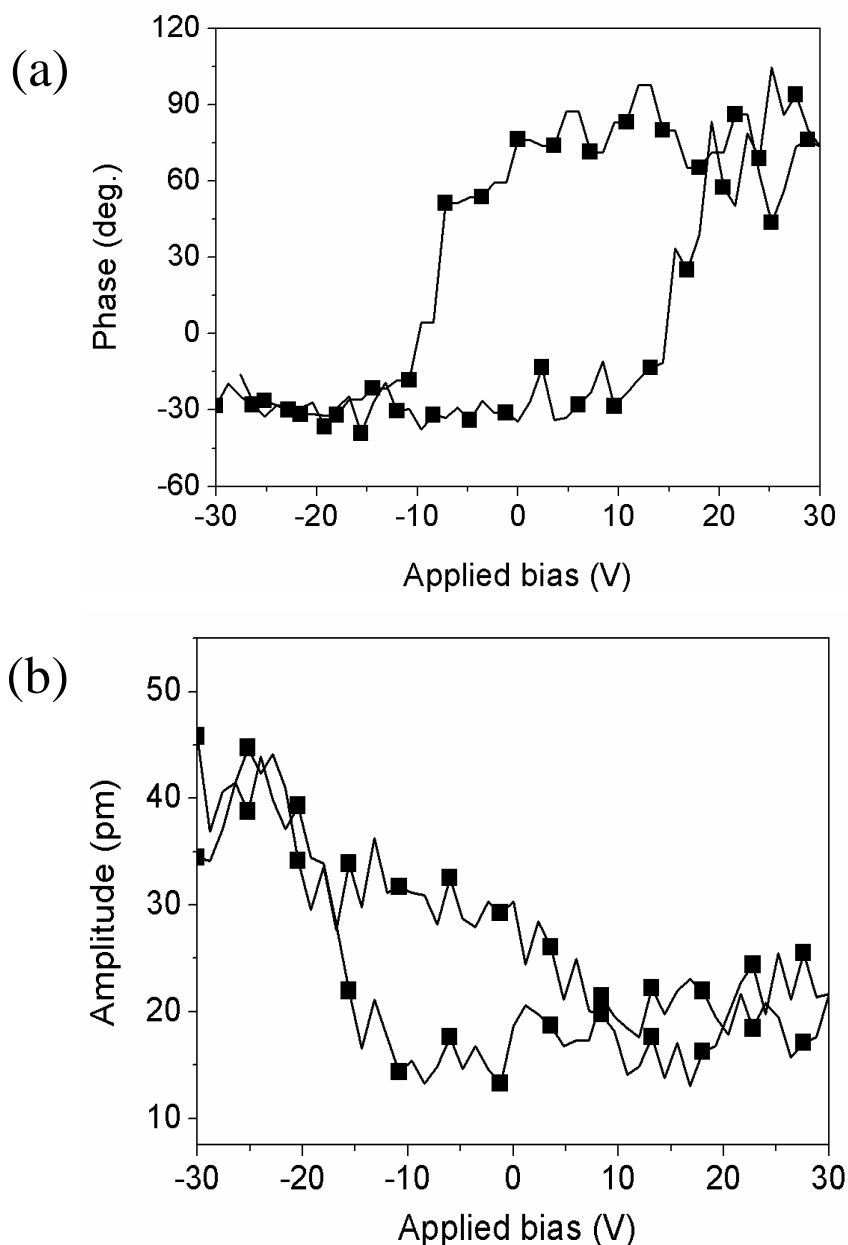
Figure 7-18 Phase hysteresis loop (a) and amplitude loop (b) from BFO films on VA-MWCNTs acquired for 30 V.

In order to confirm the magnetic nature of these BFO films, the magnetization was measured as the function of applied magnetic field (H) of -10000 Oe to 10000 Oe at 300 K and given in Figure 7-19. M-H hysteresis curves of BFO films on VA- MWCNTs at 400 $^{\circ}$C for 2 h depict unsaturated hysteresis loops, indicating the R3c structure with antiferromagnetic nature, similar to the one observed for polycrystalline BFO bulk or single crystals [433]. However, a small coercivity ($2H_c$) of 700 Oe was observed for these

BFO films (represented as inset of Figure 7-19). The weak ferromagnetic behaviour was also observed for nano particles and thin films of BFO as reported before [427, 440]. There are two possible explanations for the weak ferromagnetism in BFO films and nano particles: first, strain effects and oxygen vacancies associated with Fe^{+3} ions in BFO and second, size effects where below 62 nm size the uncompensated spins at the surface of the particle arise [441-443]. Indeed it is clear from the TEM micrographs of BFO films on VA-MWCNTs that the crystalline particles of BFO around the MWCNTs are smaller than 10-20 nm and the small shift in the Raman peak of MWCNTs after BFO deposition also indicates the existence of strains. Therefore, one can assumed that the weak ferromagnetic behaviour of BFO on VA-MWCNTs may be due to the combined effect of strain and size effects. Similar unsaturated weak ferroelectric loops were also reported for BFO nanotubes synthesised by chemical solution methods [414]. The shift in the hysteresis loops shown in inset of Figure 7-19, can be ascribed to the presence of exchange coupling between the ferromagnetic surface and antiferromagnetic cores. The self-orientation of the magnetic domains during the synthesis can also be one of the reasons for the shift in the ferromagnetic loop from the origin.
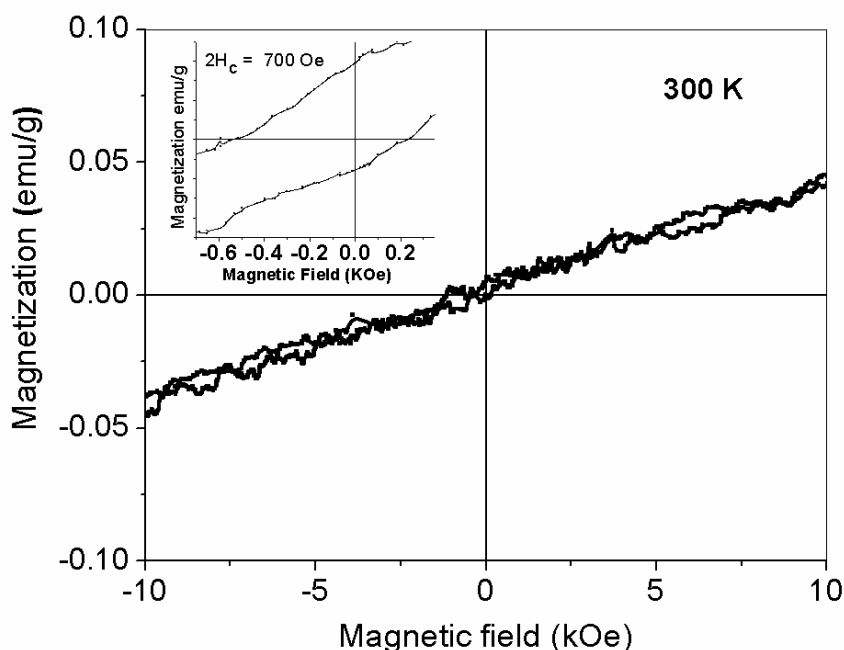
Figure 7-19 Magnetic hysteresis of BFO on VA-MWCNTs at 300 K. BFO on VA-MWCNTs depicts the weak ferromagnetic response with $2H_c = 700$ Oe.

7.4   Conclusions

Form the sol gel method (approach one) the 1D structures of BFO were successfully synthesised with average diameter of 30 nm and aspect ratio of 1:3 and above, at temperatures around 420 ºC. It was learned that reducing atmosphere provided by the oxidation of CNTs plays a crucial role in the formation of pure BFO, namely curbing the formation of the secondary phases. It was also found that the use of nitric acid solvent with metal nitrates is a very interesting way to fill the VA-MWCNTs with functional oxides, in a single step. However, keeping CNTs intact during annealing process is challenging especially for bismuth compounds. The use of VA-MWCNTs work as template and BFO crystalline obtained mimic the morphology of VA-MWCNTs, which is very interesting. The use of VA-MWCNTs to synthesised 1D structures can be useful in the development of materials with enhance magnetic properties.

BFO films on VA-MWCNTs were successfully deposited by RF sputtering (approach two) at 400 ºC without damaging the morphology of both the tubes and films. SEM and HRTEM studies prove the conformal covering of MWCNTs with BFO. These composite structures (BFO on VA-MWCNTs) present a lossy macroscopic hysteretic response with low polarization values of 1-2 pC/cm^2. In spite of that locally at the nanometric scale domains can be reversed from one direction to another under the applied field. It is also clear from the M-H curve that BFO films on VA-MWCNTs are antiferromagnetic without any saturation. The small opening of the magnetization loop near zero indicates the presence of a weak ferromagnetic nature of these BFO films which might be due to size and/strain effects. The results here presented are a proof that BFO films on VA-MWCNTs can find potential applications in photovoltaics, memories and other microelectronic applications.

Chapter 8

8   General conclusions and future work

Conclusions

The present work adds knowledge on the potential use of MWCNTs as bottom electrodes for different microelectronic applications as 3D FERAMs and/or templates to obtain 1D FE nano structures. In this work we demonstrate and proved the concept of the use of low cost, low temperature synthesis of chemical solution deposition (CSD) methods for covering MWCNTs. Due to the close proximity of the oxidation temperature of MWCNTs and the phase formation of FE oxides and due the requirement of an oxidizing atmosphere to get an oxide with proper ferroelectric response, this task is not trivial. Therefore, vital parameters such as thermal oxidation of MWCNTs in different atmospheres, FE oxide phase formation (in the presence of MWCNTs), interface development (FE and MWCNTs) and electrical properties of the prepared MWCNTs – FE nano structure have been experimentally investigated and based on these studies various mechanisms on the formation of MWCNTs - 1D structures were suggested. The current work, in which three different ferroelectric oxides, PZT, BT and BFO were studied, answers to many of the open questions and raises other challenges to be solved in the near future.

The main conclusions of this work can be summarized as:

The thermal stability of MWCNTs depends on size, purity and type of CNTs. Therefore, the thermal properties of the MWCNTs used in this work were investigated by DTA/TG, Raman and TEM. It was found that MWCNTs are stable up to ~400 ºC and start degrading after the initial combustion of amorphous carbon. The oxidation or MWCNTs can be enhanced or delayed by changing the atmosphere conditions and/or heating rate. Oxygen atmosphere accelerates oxidation of MWCNTs that might occur at temperatures as low as 200 ºC and argon atmosphere decelerates the oxidation process shifting the combustion to temperatures as high as 800 ºC. Under a reducing atmosphere with high heating rates MWCNTs are kept intact up to 1300 ºC with negligible damage to CNTs morphology. These results are of the utmost importance for the *in-situ* crystallization of FE with MWCNTs or for the heat treatment of MWCNT-FE structures.

The sol gel method was first investigated for covering the covalent functionalized MWCNTs with FE. A systematic study on the phase formation process by *in-situ* and *ex-situ* XRD, DTA, FTIR and HRTEM was carried out. In these studies PZT was the chosen as the FE oxide. It was found that the perovksite PZT phase forms at 575 ºC for MWCNT-PZT whereas for PZT (without MWCNTs) traces of pyrochlore are still identifiable at 650 ºC. The decrease of temperature is accompanied by a decrease in activation energy for perovskite phase from 68±15 kJ/mol (for PZT) to 27±2 kJ/mol (for MWCNTs-PZT). for holding time of 1 h monophasic perovskite phase in MWCNTs-PZT can be obtained at 500 ºC. HRTEM studies confirm *in-situ* and *ex-situ* XRD and DTA/TG results on the early formation of perovskite PZT phase in presence of MWCNTs. We proposed that MWCNTs act as seeds to reduce the nucleation barrier of perovksite phase formation by providing low energy nucleation sites; in addition the exothermic local oxidation of MWCNTs that might occur in some parts of the tubes result in the increase in the local temperature that might promote the phase formation process. The piezoelectric nature of MWCNT/PZT synthesised at 500 ºC/1 h assessed by PFM proved the concept.

For the case of the synthesis of MWCNTs with BT hydrothermal method was the selected one. In this case the challenge of compatibility with MWCNTs is even higher than in the previous case due to the fact that BT requires a considerably high synthesis temperature than PZT; and in addition, depending on the synthesis methodology, carbonates are formed that are very difficult to eliminate, usually demanding even higher post annealing temperatures (> 1000 ºC) what jeopardises totally the combination with CNTs. Two different hydrothermal strategies were used to cover MWCNTs with BT. In the first strategy the conventional method to synthesize BT at hydrothermal conditions was used, where titanium dioxide particles on MWCNTs act as template site to react with barium precursor to form BT on MWCNTs. By using this strategy we found that BT particles did not adhere to the CNTs walls during the synthesis process. This process also resulted in the formation of reasonable amounts of $BaCO_3$. This lead to the second strategy. We used a sol gel hybrid hydrothermal method to cover MWCNTs with BT. In this case the formation of $BaCO_3$ was significantly reduced, due the limited access of Ba ions (already entrapped between Ti amorphous networks) to the C skeleton. 100 nm structures of MWCNTs – BT structures were fabricated, but unfortunately the coverage of the tubes was not totally complete. The selective (or semi) covering with BT of the

MWCNTs was suggested to be due to the covalent functionalization, which results in the formation of carboxylic and hydroxyl groups on the defect sites of CNTs. Therefore this functionalization is very local and not uniform through-out the tubes. Local electrical measurements by PFM proved the ferroelectric nature of the MWCNTs-BT structures with an electromechanical behaviour of 15pm/V. From the above studies we proved that use of sol gel hybrid hydrothermal method is a suitable methodology to cover uniformly CNTs at low temperature.

To maximise the coverage of MWCNTs with BT the non-covalent functionalization of MWCNTs was exploited, using in this case SDS. In non-covalent functionalization SDS molecules adsorbed uniformly on the surface of MWCNTs (in contrast to the selective adsorption verified in covalent functionalization) and results in large functionalized area. SDSMWCNTs-BT structures were obtained by sol gel hybrid method. It was found that the initial concentration of the BT precursor has a significant effect on the morphology of the tubes. Conformally covered SDSMWCNTs with BT having diameters in the range from 20 to 200 nm were obtained from a 0.01 M BT solution and at 250 ºC. HRTEM confirms that non covalent functionalization, in this case with SDS, plays a crucial role on the covering of MWCNTs. The local PFM response These MWCNTs-BT tubes are ferroelectric with a d_{33} piezoelectric coefficient of 2 pm/V.

MWCNTs were used as templates to fabricate 1D BFO nano structures. It was observed by TEM that the use of nitric acid based solution of BFO results in the opening and filling of MWCNTs with BFO. However, during the crystallization process of BFO above 350 ºC, the MWCNTs oxidize. The decrease in the oxidation temperature for the MWCNTs was a result of the severe damage caused in the MWCNTs during the processing step. Monophasic BFO was obtained at 420 ºC/2 h for MWCNTs-BFO, whereas BFO (without CNTs) under the same heating conditions depicts the presence of secondary phases (Bi_2O_3). The oxidation of MWCNTs decelerates the formation of secondary phase due to the reducing of oxygen atmosphere. HRTEM of BFO crystallites obtained from MWCNTs-BFO shows BFO nano structures having the aspect ratio of 1:3 or above, and the diameter in the range of ~20-50 nm. Week ferromagnetic loops with coercive field of 956 Oe at 5 K were measured in these BFO nano structures.

In the last part of this work, we exploit the potential of using Vertically Aligned (VA) MWCNTs as a bottom conducting electrode to replace the expensive metal electrodes. A successful coating of BFO on the surface of VA-MWCNTs was demonstrated using RF sputtering. The optimum parameters for getting uniform BFO film on the surface of VA-MWCNTs are 450 ºC for 2 h. HRTEM studies prove the conformal covering of MWCNTs with BFO. The local properties measured by PFM clearly illustrate the nanometric domains of BFO on VA-MWCNTs that can be reversed from one direction to another under the external field. The M-H curves from BFO films on VA-MWCNTs show small opening of the magnetization loop near zero, indicating the presence of a weak ferromagnetic nature of these BFO films, which might be due to size and/strain effects.

From the above conclusions it is clear that MWCNTs can be uniformly covered with FE oxides using low cost chemical solution method (presented in Table 8-1) and the obtained MWCNTs-FE depicts local ferroelectric properties. These results are of particular relevance in 3D ferroelectric nano capacitors in which CNTs are proposed as bottom electrodes or template to fabricate 1D nano ferroelectric structures. These composites can be used for 3D FERAMs devices but also for photovoltaic, capacitors and other microelectronic applications.

Future work

Although the presented work responds to many of the current open questions it raises many others, opening future avenues for further research. Here some of them:

To identify the exact role or MWCNTs in the early oxide phase formation *in-situ* HRTEM studies is required.

After the proof of the concept of MWCNTs-FE by low temperature and cost synthesis a full detail electrical characterization is needed. Issues as reliability, fatigue, endurance are key points for future practical application of these 1D capacitors. Studies on the electrical properties as a function of temperature, electric field and magnetic field are required. Since the ferroelectric performance has a direct relation with domain structure, domain studies should be conducted.

Studies on the functionalization of the surface of the tubes as well as on the optimal conditions to fill MWCNTs with FE will add knowledge and will help to design methods by which solution will only fill the tube without getting adsorbed on the outer walls of MWCNTs. This will allow to construct patterns on and around the tubes adding complexity to the MWCNTs – FE structures.

Table 8-1 Illustrate the summary of present work on the covering of MWCNTs with Ferroelectric oxides.

Type of MWCNTs	Coating Ferroelectric (FE) Materials	Method / Precursors	Remarks on Covering MWCNTs with FE
Acid functionalized MWCNTs	$PbZr_{0.52}Ti_{0.48}O_3$ (PZT)	Sol Gel / Lead acetate, titanium tetra-isopropoxide and zirconium tetra-n-propoxide	Uniform coverage of MWCNTs by PZT
Acid functionalized MWCNTs	$BaTiO_3$ (BT)	Hydrothermal / Barium acetate or Barium nitrate, titanium isopropoxide	No covering, BT nucleate away from the surface of MWCNTs
Acid functionalized MWCNTs	$BaTiO_3$ (BT)	Sol gel Hydrothermal / Barium acetate and titanium isopropoxide	Localized covering of MWCNTs with BT
SDS functionalized MWCNTs	$BaTiO_3$ (BT)	Sol gel Hydrothermal / Barium acetate and titanium isopropoxide	Conformal covering of MWCNTs with BT
Acid functionalized MWCNTs	$BiFeO_3$ (BFO)	Sol gel / Bismuth nitrate and iron nitrate	MWCNTs act as templates to form BFO 1D rods
Vertical Aligned - MWCNTs	$BiFeO_3$ (BFO)	RF sputtering / Bismuth oxide and iron oxide	Conformal forming of BFO thin layer on surface of VA-MWCNTs

References

1. Information on: " http://sciencewatch.com/articles/digital-everything-everywhere".

2. Moore, G.E., *Cramming more components onto integrated circuits*. 1965, Electronics.

3. Information on: " http://www.itrs.net/Links/2011ITRS/2011Chapters/2011MEMS.pdf".

4. Zambrano, R., *Challenges for integration of embedded FeRAMs in the sub-180 nm regime.* Integrated Ferroelectrics, **2003**. 53(1): p. 247-255.

5. J. F. Scott, et al., *Nano-ferroelectric materials and devices.* Ferroelectrics, **2006**. 336(1): p. 237-245.

6. Naumov, I., L. Bellaiche, and H. Fu, *Unusual phase transitions in ferroelectric nanodisks and nanorods.* Nature, **2004**. 432(7018): p. 737-740.

7. Scott, J.F., *Applications of modern ferroelectrics.* Science, **2007**. 315(5814): p. 954-959.

8. Information on: " http://www.bbc.com/news/technology-17785464 ".

9. Auciello, O., *The physics of ferroelectric memories.* Phys. Today, **1998**. 51(7): p. 22.

10. Wouters, D.J., et al., *Integration of $SrBi_2Ta_2O_9$ thin films for high density ferroelectric random access memory.* Journal of Applied Physics, **2006**. 100(5): p. 051603-16.

11. Robertson, J., *Growth of nanotubes for electronics.* Materials Today, **2007**. 10(1-2): p. 36-43.

12. Kreupl, F., *Carbon nanotubes in microelectronic applications.* Carbon Nanotube Devices: properties, modelling, integration and applications, **2008**.

13. Kawasaki, S., et al., *Liquid source misted chemical deposition process of three - dimensional nano-ferroelectrics with substrate heating.* Integrated Ferroelectrics, **2007**. 95(1): p. 180-186.

14. Jang, J.E., et al. *Nanoelectromechanical DRAM for ultra-large-scale integration (ULSI).* in *Electron Devices Meeting, 2005. IEDM Technical Digest. IEEE International*. 2005.

15. Jang, J.E., et al. *Nanotube based vertical nano-devices for high integration density.* in *Emerging Technologies - Nanoelectronics, 2006 IEEE Conference on*. 2006.

16. Jang, J.E., et al. *Nanoscale capacitors based on metal-insulator-carbon nanotube-metal (MICNM) structures.* in *Solid-State Device Research Conference, 2005. ESSDERC 2005. Proceedings of 35th European*. 2005.

17. Jang, J.E., et al., *Nanoscale memory cell based on a nanoelectromechanical switched capacitor.* Nat Nano, **2008**. 3(1): p. 26-30.

18. Huang, Q. and L. Gao, *Manufacture and electrical properties of multiwalled carbon nanotube/BaTiO₃ nanocomposite ceramics.* Journal of Materials Chemistry, **2004**. 14(16): p. 2536-2541.

19. Huang, Q. and L. Gao, *Multiwalled carbon nanotube/BaTiO₃ nanocomposites: Electrical and rectification properties.* Applied Physics Letters, **2005**. 86(12): p. 123104-3.

20. Huang, Q., et al., *Sintering and thermal properties of multiwalled carbon nanotube-BaTiO₃ composites.* Journal of Materials Chemistry, **2005**. 15(20): p. 1995-2001.

21. Kawasaki, S., et al., *Conformal oxide coating of carbon nanotubes.* Applied Physics Letters, **2008**. 92(5): p. 053109.

22. Bakhoum, E.G. and M.H.M. Cheng, *Electrophoretic coating of carbon nanotubes for high energy-density capacitor applications.* Journal of Applied Physics, **2009**. 105(10): p. 104314.

23. Bedekar, V., et al., *Synthesis and microstructural characterization of barium titanate nanoparticles decorated SiCN-MWCNT nanotubes – "nanoNecklace".* Ferroelectrics Letters Section, **2010**. 36(5): p. 133 - 140.

24. Bedekar, V., et al., *Controlled synthesis of BaTiO₃-coated multiwall carbon nanotubes.* Journal of the American Ceramic Society, **2010**. 93(11): p. 3618-3623.

25. Yang, Y., et al., *Coaxial multiferroic nanorod arrays.* Journal of the American Ceramic Society, **2010**. 93(2): p. 362-364.

26. Mohammadi, M.R., et al., *Synthesis and crystallization of lead–zirconium–titanate (PZT) nanotubes at the low temperature using carbon nanotubes (CNTs) as sacrificial templates.* Advanced Powder Technology, **2012**. 23(5): p. 647-654.

27. Mendoza, F., et al., *Conformal coating of ferroelectric oxides on carbon nanotubes.* EPL (Europhysics Letters), **2012**. 97(2): p. 27001.

28. Kumar, A., et al., *Ferroelectric–carbon nanotube memory devices.* Nanotechnology, **2012**. 23(16): p. 165702.

29. Kumar, A., J.F. Scott, and R.S. Katiyar, *Dynamic nanocrystal response and high temperature growth of carbon nanotube-ferroelectric hybrid nanostructures.* Nanoscale, **2014**: p. 1064-1070.

30. Pandey, A., et al., *Very stable electron field emission from strontium titanate coated carbon nanotube matrices with low emission thresholds.* ACS Nano, **2012**. 7(1): p. 117-125.

31. Beltran-Huarac, J., et al., *Synthesis and transport properties of La₀.₆₇ Sr₀.₃₃ MnO₃ conformally-coated on carbon nanotubes.* Carbon, **2013**. 65: p. 252-260.

32. Information on: " http://www.nantero.com/mission.html".

33. Ezhilvalavan, S. and V.D. Samper, *Ferroelectric properties of wet-chemical patterned PbZr₀.₅₂Ti₀.₄₈O₃ films.* Applied Physics Letters, **2005**. 86(7): p. 072901.

34.   Kamalasanan, M.N., N.D. Kumar, and S. Chandra, *Dielectric and ferroelectric properties of BaTiO₃ thin films grown by the sol-gel process.* Journal of Applied Physics, **1993**. 74(9): p. 5679-5686.

35.   Wang, J., et al., *Epitaxial BiFeO₃ thin films on Si.* Applied Physics Letters, **2004**. 85(13): p. 2574-2576.

36.   Thompson, S.E. and S. Parthasarathy, *Moore's law: the future of Si microelectronics.* Materials Today, **2006**. 9(6): p. 20-25.

37.   Information on: " http://www.azonano.com/news.aspx?newsID=29018".

38.   Avouris, P., et al., *Carbon nanotube electronics.* Proceedings of the IEEE, **2003**. 91(11): p. 1772-1784.

39.   Javey, A., et al., *Ballistic carbon nanotube field-effect transistors.* Nature, **2003**. 424(6949): p. 654-657.

40.   Franklin, A.D., et al., *Sub-10 nm Carbon Nanotube Transistor.* Nano Letters, **2012**. 12(2): p. 758-762.

41.   Tans, S.J., A.R. Verschueren, and C. Dekker, *Room-temperature transistor based on a single carbon nanotube.* Nature, **1998**. 393(6680): p. 49-52.

42.   Martel, R., et al., *Single-and multi-wall carbon nanotube field-effect transistors.* Applied Physics Letters, **1998**. 73(17): p. 2447-2449.

43.   Bachtold, A., et al., *Logic circuits with carbon nanotube transistors.* Science, **2001**. 294(5545): p. 1317-1320.

44.   Liu, X., et al., *Carbon nanotube field-effect inverters.* Applied Physics Letters, **2001**. 79(20): p. 3329-3331.

45.   Derycke, V., et al., *Carbon Nanotube Inter- and Intramolecular Logic Gates.* Nano Letters, **2001**. 1(9): p. 453-456.

46.   Chen, Z., et al., *The role of metal−nanotube contact in the performance of carbon nanotube field-effect transistors.* Nano Letters, **2005**. 5(7): p. 1497-1502.

47.   Shahrjerdi, D., et al., *High-performance air-stable n-type carbon nanotube transistors with erbium contacts.* ACS Nano, **2013**. 7(9): p. 8303-8308.

48.   Kocabas, C., et al., *Radio frequency analog electronics based on carbon nanotube transistors.* Proceedings of the National Academy of Sciences, **2008**. 105(5): p. 1405-1409.

49.   Steiner, M., et al., *High-frequency performance of scaled carbon nanotube array field-effect transistors.* Applied Physics Letters, **2012**. 101(5): p. 053123.

50.   Che, Y., et al., *T-Gate aligned nanotube radiof frequency transistors and circuits with superior performance.* ACS Nano, **2013**. 7(5): p. 4343-4350.

51.   Zhang, J., et al., *Air-stable conversion of separated carbon nanotube thin-film transistors from p-type to n-type using atomic layer deposition of high-κ oxide and its application in CMOS logic circuits.* ACS Nano, **2011**. 5(4): p. 3284-3292.

52.   Cao, Q., et al., *Medium-scale carbon nanotube thin-film integrated circuits on flexible plastic substrates.* Nature, **2008**. 454(7203): p. 495-500.

53.   Zhang, J., C. Wang, and C. Zhou, *Rigid/Flexible transparent electronics based on separated carbon nanotube thin-film transistors and their application in display electronics.* ACS Nano, **2012**. 6(8): p. 7412-7419.

54.   Wang, C., et al., *User-interactive electronic skin for instantaneous pressure visualization.* Nat Mater, **2013**. 12(10): p. 899-904.

55.   Shulaker, M.M., et al., *Carbon nanotube computer.* Nature, **2013**. 501(7468): p. 526-530.

56.   Zhang, J., et al., *Separated carbon nanotube macroelectronics for active matrix organic light-emitting diode displays.* Nano Letters, **2011**. 11(11): p. 4852-4858.

57.   Kordás, K., et al., *Chip cooling with integrated carbon nanotube microfin architectures.* Applied Physics Letters, **2007**. 90(12): p. 123105.

58.   Graham, A.P., et al., *How do carbon nanotubes fit into the semiconductor roadmap?* Applied Physics A, **2005**. 80(6): p. 1141-1151.

59.   Horibe, M., et al., *Carbon Nanotube Growth Technologies Using Tantalum Barrier Layer for Future ULSIs with Cu/Low- k Interconnect Processes.* Japanese Journal of Applied Physics, **2005**. 44(7R): p. 5309.

60.   Naeemi, A. and J.D. Meindl, *Monolayer metallic nanotube interconnects: promising candidates for short local interconnects.* Electron Device Letters, IEEE, **2005**. 26(8): p. 544-546.

61.   Kong, J., et al., *Nanotube molecular wires as chemical sensors.* Science, **2000**. 287(5453): p. 622-625.

62.   Qi, P., et al., *Toward large arrays of multiplex functionalized carbon nanotube sensors for highly sensitive and selective molecular detection.* Nano Letters, **2003**. 3(3): p. 347-351.

63.   Information on: " http://hyperioncatalysis.com/automotive2.htm".

64.   Endo, M., M. Strano, and P. Ajayan, *Potential applications of carbon nanotubes.* Carbon Nanotubes, **2008**: p. 13-61.

65.   Radushkevich, L. and V. Lukyanovich, *O strukture ugleroda, obrazujucegosja pri termiceskom razlozenii okisi ugleroda na zeleznom kontakte.* Zurn Fisic Chim, **1952**. 26: p. 88-95.

66.   Monthioux, M. and V.L. Kuznetsov, *Who should be given the credit for the discovery of carbon nanotubes?* Carbon, **2006**. 44(9): p. 1621-1623.

67. Wei, B.Q., R. Vajtai, and P.M. Ajayan, *Reliability and current carrying capacity of carbon nanotubes.* Applied Physics Letters, **2001**. 79(8): p. 1172-1174.

68. Lau, A.K.-T. and D. Hui, *The revolutionary creation of new advanced materials—carbon nanotube composites.* Composites Part B: Engineering, **2002**. 33(4): p. 263-277.

69. Terrones, M., *Science and technology of the twenty-first century: synthesis, properties, and applications of carbon nanotubes.* Annual Review of Materials Research, **2003**. 33(1): p. 419-501.

70. Dai, H., *Carbon nanotubes: opportunities and challenges.* Surface Science, **2002**. 500(1): p. 218-241.

71. Ajayan, P.M. and O.Z. Zhou, *Applications of carbon nanotubes*, in *Carbon Nanotubes*. 2001, Springer. p. 391-425.

72. Saito, R., et al., *Electronic structure of chiral graphene tubules.* Applied Physics Letters, **1992**. 60: p. 2204.

73. Iijima, S., *Helical microtubules of graphitic carbon.* Nature, **1991**. 354(6348): p. 56-58.

74. Bethune, D., et al., *Cobalt-catalysed growth of carbon nanotubes with single-atomic-layer walls.* Nature, **1993**: p. 605 - 607.

75. Iijima, S. and T. Ichihashi, *Single-shell carbon nanotubes of 1-nm diameter.* Nature, **1993**. 363: p. 603 - 605.

76. Sinnott, S.B. and R. Andrews, *Carbon nanotubes: synthesis, properties, and applications.* Critical Reviews in Solid State and Materials Sciences, **2001**. 26(3): p. 145-249.

77. Meyyappan, M., *Carbon nanotubes: science and applications*. 2004: CRC press.

78. Dresselhaus, M.S., *Burn and Interrogate.* Science, **2001**. 292(5517): p. 650-651.

79. Dresselhaus, M.S. and P.C. Eklund, *Phonons in carbon nanotubes.* Advances in Physics, **2000**. 49(6): p. 705-814.

80. Poole, C.P. and F.J. Owens, *Introduction to nanotechnology*. 2003: Cambridge Univ Press.

81. Guo, T., et al., *Self-assembly of tubular fullerenes.* The Journal of Physical Chemistry, **1995**. 99(27): p. 10694-10697.

82. José-Yacamán, M., et al., *Catalytic growth of carbon microtubules with fullerene structure.* Applied Physics Letters, **1993**. 62(2): p. 202-204.

83. Ebbesen, T.W. and P.M. Ajayan, *Large-scale synthesis of carbon nanotubes.* Nature, **1992**. 358: p. 220-222.

84. Ajayan, P.M., T. Ichihashi, and S. Iijima, *Distribution of pentagons and shapes in carbon nano-tubes and nano-particles.* Chem. phys. Lett., **1993**. 202: p. 384-388.

85. Lambert, J., et al., *Improving conditions towards isolating single-shell carbon nanotubes.* Chemical Physics Letters, **1994**. 226(3): p. 364-371.

86. Kiang, C.-H., et al., *Carbon nanotubes with single-layer walls.* Carbon, **1995**. 33(7): p. 903-914.

87. Journet, C., et al., *Large-scale production of single-walled carbon nanotubes by the electric-arc technique.* Nature, **1997**. 388(6644): p. 756-758.

88. Guo, T., et al., *Catalytic growth of single-walled manotubes by laser vaporization.* Chemical Physics Letters, **1995**. 243(1): p. 49-54.

89. Gorbunov, A., et al., *Solid–liquid–solid growth mechanism of single-wall carbon nanotubes.* Carbon, **2002**. 40(1): p. 113-118.

90. Terrones, M., *Science and technology of twenty-first century: synthesis, properties, and applications of carbon nanotubes.* Annual Review of Materials Research, **2003**. 33(1): p. 419-501.

91. Kong, J., et al., *Synthesis of individual single-walled carbon nanotubes on patterned silicon wafers.* Nature, **1998**. 395(6705): p. 878-881.

92. Wei, B., et al., *Microfabrication technology: organized assembly of carbon nanotubes.* Nature, **2002**. 416(6880): p. 495-496.

93. Fryer, T.B.J. and B. Grant, *Structure of fibrous carbon.* Nature, **1971**. 233: p. 329 - 330.

94. Hersam, M.C., *Progress towards monodisperse single-walled carbon nanotubes.* Nature Nanotechnology, **2008**. 3(7): p. 387-394.

95. Yao, Y., et al., *"Cloning" of single-walled carbon nanotubes via open-end growth mechanism.* Nano Letters, **2009**. 9(4): p. 1673-1677.

96. Ghorannevis, Z., et al., *Narrow-chirality distributed single-walled carbon nanotube growth from nonmagnetic catalyst.* Journal of the American Chemical Society, **2010**. 132(28): p. 9570-9572.

97. Hata, K., et al., *Water-assisted highly efficient synthesis of impurity-free single-walled carbon nanotubes.* Science, **2004**. 306(5700): p. 1362-1364.

98. Hong, B.H., et al., *Quasi-continuous growth of ultralong carbon nanotube arrays.* Journal of the American Chemical Society, **2005**. 127(44): p. 15336-15337.

99. Terrones, M., et al., *New direction in nanotube science.* Materials Today, **2004**. 7(10): p. 30-45.

100. Fonseca, A., et al., *Synthesis of single-and multi-wall carbon nanotubes over supported catalysts.* Applied Physics A, **1998**. 67(1): p. 11-22.

101. Kónya, Z., et al., *Large scale production of short functionalized carbon nanotubes.* Chemical Physics Letters, **2002**. 360(5): p. 429-435.

102. Nikolaev, P., et al., *Gas-phase catalytic growth of single-walled carbon nanotubes from carbon monoxide.* Chemical Physics Letters, **1999**. 313(1): p. 91-97.

103. Dupuis, A.-C., *The catalyst in the CCVD of carbon nanotubes—a review.* Progress in Materials Science, **2005**. 50(8): p. 929-961.

104. Stadermann, M., et al., *Mechanism and kinetics of growth termination in controlled chemical vapor deposition growth of multiwall carbon nanotube arrays.* Nano Letters, **2009**. 9(2): p. 738-744.

105. Wei, Y.Y., et al., *Effect of catalyst film thickness on carbon nanotube growth by selective area chemical vapor deposition.* Applied Physics Letters, **2001**. 78(10): p. 1394-1396.

106. Sohn, J.I., et al., *Growth behavior of carbon nanotubes on Fe-deposited (001) Si substrates.* Applied Physics Letters, **2001**. 78(20): p. 3130-3132.

107. Mansoor, M., M. Shahid, and A. Habib, *Optimization of ethanol flow rate for improved catalytic activity of Ni particles to synthesize MWCNTs using a CVD reactor.* Materials Research, **2014**. 17: p. 739-746.

108. Dervishi, E., et al., *Carbon nanotubes: synthesis, properties, and applications.* Particulate Science and Technology, **2009**. 27(2): p. 107-125.

109. Burghard, M., *Electronic and vibrational properties of chemically modified single-wall carbon nanotubes.* Surface science reports, **2005**. 58(1): p. 1-109.

110. Balasubramanian, K. and M. Burghard, *Chemically functionalized carbon nanotubes.* Small, **2005**. 1(2): p. 180-192.

111. Eitan, A., et al., *Surface modification of multiwalled carbon nanotubes: toward the tailoring of the interface in polymer composites.* Chemistry of Materials, **2003**. 15(16): p. 3198-3201.

112. Tasis, D., et al., *Chemistry of carbon nanotubes.* Chemical Reviews, **2006**. 106(3): p. 1105-1136.

113. Kamarás, K., et al., *The effect of nitric acid doping on the optical properties of carbon nanotube films.* physica status solidi (b), **2010**. 247(11-12): p. 2754-2757.

114. Kudin, K.N., H.F. Bettinger, and G.E. Scuseria, *Fluorinated single-wall carbon nanotubes.* Physical Review B, **2001**. 63(4): p. 045413.

115. Dujardin, E., et al., *Capillarity and wetting of carbon nanotubes.* Science, **1994**. 265(5180): p. 1850-1852.

116. Ajayan, P.M. and S. Iijima, *Capillarity-induced filling of carbon nanotubes.* Nature, **1993**. 361(6410): p. 333-334.

117. Kiang, C.-h., *Electron irradiation induced dimensional change in bismuth filled carbon nanotubes.* Carbon, **2000**. 38(11): p. 1699-1701.

118. Tsang, S.C., et al., *A simple chemical method of opening and filling carbon nanotubes.* Nature, **1994**. 372(6502): p. 159-162.

119. Chu, A., et al., *Filling of carbon nanotubes with silver, gold, and gold chloride.* Chemistry of Materials, **1996**. 8(12): p. 2751-2754.

120. Ugarte, D., A. Chatelain, and W. De Heer, *Nanocapillarity and chemistry in carbon nanotubes.* Science, **1996**. 274(5294): p. 1897-1899.

121. Kyotani, T., L.-f. Tsai, and A. Tomita, *Formation of platinum nanorods and nanoparticles in uniform carbonnanotubes prepared by a template carbonization method.* Chem. Commun., **1997**(7): p. 701-702.

122. Korneva, G., et al., *Carbon nanotubes loaded with magnetic particles.* Nano Letters, **2005**. 5(5): p. 879-884.

123. Han, W., et al., *Synthesis of gallium nitride nanorods through a carbon nanotube-confined reaction.* Science, **1997**. 277(5330): p. 1287-1289.

124. Govindaraj, A., et al., *Metal nanowires and intercalated metal layers in single-walled carbon nanotube bundles.* Chemistry of Materials, **2000**. 12(1): p. 202-205.

125. Matsui, K., et al., *Formation of nickel oxide nanoribbons in the cavity of carbon nanotubes.* The Journal of Physical Chemistry B, **2001**. 105(24): p. 5682-5688.

126. Hirsch, A. and O. Vostrowsky, *Functionalization of carbon nanotubes*, in *Functional Molecular Nanostructures*, A.D. Schlüter, Editor. 2005, Springer Berlin / Heidelberg. p. 193-237.

127. Illeková, E. and K. Csomorová, *Kinetics of oxidation in various forms of carbon.* Journal of Thermal Analysis and Calorimetry, **2005**. 80(1): p. 103-108.

128. Musumeci, A., et al., *Thermal decomposition and electron microscopy studies of single-walled carbon nanotubes.* Journal of Thermal Analysis and Calorimetry, **2007**. 88(3): p. 885-891.

129. Santangelo, S., et al., *Evaluation of crystalline perfection degree of multi-walled carbon nanotubes: correlations between thermal kinetic analysis and micro-Raman spectroscopy.* Journal of Raman Spectroscopy, **2010**. 42: p. 593–602.

130. Brukh, R. and S. Mitra, *Kinetics of carbon nanotube oxidation.* Journal of Materials Chemistry, **2007**. 17(7): p. 619-623.

131. Zhou, W., et al., *Structural characterization and diameter-dependent oxidative stability of single wall carbon nanotubes synthesized by the catalytic decomposition of CO.* Chemical Physics Letters, **2001**. 350(1-2): p. 6-14.

132. Wiltshire, J.G., et al., *Comparative studies on acid and thermal based selective purification of HiPCO produced single-walled carbon nanotubes.* Chemical physics letters, **2004**. 386: p. 239-243.

133. Nan, Z., et al., *Thermodynamic properties of carbon nanotubes.* Journal of Chemical & Engineering Data, **2009**. 54(4): p. 1367-1370.

134. López, M., et al., *Structural and thermal stability of narrow and short carbon nanotubes and nanostrips.* Carbon, **2005**. 43(7): p. 1371-1377.

135. Colomer, J.F., et al., *Different purification methods of carbon nanotubes produced by catalytic synthesis.* Synthetic Metals, **1999**. 103(1-3): p. 2482-2483.

136.   Hou, P.X., et al., *Multi-step purification of carbon nanotubes.* Carbon, **2002**. 40(1): p. 81-85.

137.   Osswald, S., M. Havel, and Y. Gogotsi, *Monitoring oxidation of multiwalled carbon nanotubes by Raman spectroscopy.* Journal of Raman Spectroscopy, **2007**. 38(6): p. 728-736.

138.   Zhang, X., et al., *Oxidation resistance of multi-walled carbon nanotubes purified with sulfuric and nitric acids.* Journal of Materials Science, **2007**. 42(19): p. 8377-8380.

139.   Hsieh, Y.-C., et al., *Thermal analysis of multi-walled carbon nanotubes by kissinger's corrected kinetic equation.* Aerosol and Air Quality Research,, **2010**. 10: p. 212–218.

140.   Yang, K., et al., *The effect of chemical treatment on the crystallinity of multi-walled carbon nanotubes.* Journal of Physics and Chemistry of Solids, **2008**. 69(1): p. 222-229.

141.   Ebbesen, T.W., et al., *Purification of nanotubes.* Nature, **1994**. 367(6463): p. 519-519.

142.   Gajewski, S., et al., *Purification of single walled carbon nanotubes by thermal gas phase oxidation.* Diamond and Related Materials, **2003**. 12(3-7): p. 816-820.

143.   Andrews, R., et al., *Purification and structural annealing of multiwalled carbon nanotubes at graphitization temperatures.* Carbon, **2001**. 39(11): p. 1681-1687.

144.   Huang, W., et al., *99.9% purity multi-walled carbon nanotubes by vacuum high-temperature annealing.* Carbon, **2003**. 41(13): p. 2585-2590.

145.   Kim, Y.A., et al., *Annealing effect on disordered multi-wall carbon nanotubes.* Chemical Physics Letters, **2003**. 380(3-4): p. 319-324.

146.   Behler, K., et al., *Effect of thermal treatment on the structure of multi-walled carbon nanotubes.* Journal of Nanoparticle Research, **2006**. 8(5): p. 615-625.

147.   Sarkar, S., P.K. Das, and S. Bysakh, *Effect of heat treatment on morphology and thermal decomposition kinetics of multiwalled carbon nanotubes.* Materials Chemistry and Physics, **2011**. 125(1-2): p. 161-167.

148.   Sandler, J., et al., *Variations in the Raman peak shift as a function of hydrostatic pressure for various carbon nanostructures: A simple geometric effect.* Physical Review B, **2003**. 67(3): p. 035417.

149.   Khabashesku, V.N., et al., *Polymerization of single-wall carbon nanotubes under high pressures and high temperatures.* The Journal of Physical Chemistry B, **2002**. 106(43): p. 11155-11162.

150.   Corrias, M., et al., *High purity multiwalled carbon nanotubes under high pressure and high temperature.* Carbon, **2003**. 41(12): p. 2361-2367.

151.   Zhang, M., et al., *Microstructural changes in carbon nanotubes induced by annealing at high pressure.* Carbon, **1999**. 37(4): p. 657-662.

152.   Zhang, M., et al., *Ribbon-like nanostructures transformed from carbon nanotubes at high temperature and pressure.* Nanostructured Materials, **1998**. 10(7): p. 1145-1152.

153. Wei, B., et al., *The mechanism of phase transformation from carbon nanotube to diamond.* Carbon, **1998**. 36(7–8): p. 997-1001.

154. Information on: " http://www3.imperial.ac.uk/materials/research/functionalmaterials".

155. Vilarinho, P.M., *Functional Materials: Properties, Processing and Applications , Scanning Probe Microscopy: Characterization, Nanofabrication and Device Application of Functional Materials*, P.M. Vilarinho, Y. Rosenwaks, and A. Kingon, Editors. 2005, Springer Netherlands. p. 3-33.

156. Carter, C.B. and M.G. Norton, *Ceramics Materials : Science and Engineering*. 2007: Springer.

157. Jaffe, B., W.R. Cook, and H. Jaffe, *Piezoelectric Ceramics*. 2nd ed. Vol. Academic, New York. 1971. 135-56.

158. Busch, G., *Early history of ferroelectricity.* Ferroelectrics, **1987**. 74(1): p. 267-284.

159. Jacques and P. Curie, *Développement par pression de l'électricité polaire dans des crystaux hémiédriques à faces inclinées.* Compt. Rend. Acad. Sci. URSS, **1880**. 91: p. 294-295, 383-387.

160. Haertling, G.H., *Ferroelectric ceramics: history and technology.* Journal of the American Ceramic Society, **1999**. 82(4): p. 797-818.

161. Ramesh, R. and N.A. Spaldin, *Multiferroics: progress and prospects in thin films.* Nat Mater, **2007**. 6(1): p. 21-29.

162. Chu, Y.-H., et al., *Controlling magnetism with multiferroics.* Materials Today, **2007**. 10(10): p. 16-23.

163. Eerenstein, W., N.D. Mathur, and J.F. Scott, *Multiferroic and magnetoelectric materials.* Nature, **2006**. 442(7104): p. 759-765.

164. Van Aken, B.B., et al., *Observation of ferrotoroidic domains.* Nature, **2007**. 449(7163): p. 702-705.

165. Ederer, C. and N.A. Spaldin, *Towards a microscopic theory of toroidal moments in bulk periodic crystals.* Physical Review B, **2007**. 76(21): p. 214404.

166. Hans, S., *Some symmetry aspects of ferroics and single phase multiferroics.* Journal of Physics: Condensed Matter, **2008**. 20(43): p. 434201.

167. Manfred, F., *Revival of the magnetoelectric effect.* Journal of Physics D: Applied Physics, **2005**. 38(8): p. R123.

168. Hill, N.A., *Why are there so few magnetic ferroelectrics?* The Journal of Physical Chemistry B, **2000**. 104(29): p. 6694-6709.

169. Jiang, H., et al., *Dual-tuning microwave devices using ferroelectric/ferrite layers*. 2002, Corning Applied Technologies Corporation (Woburn, MA): US 6498549.

170. Ma, X., et al., *Thick film magnetic nanocomposite films and method of manufacture thereof*. 2004: US 2005/0074600 A1.

171. Pirich, R., et al., *Multiferroic nanoscale thin film materials, method of its facile syntheses and magnetoelectric coupling at room temperature*. 2010: US 20100288964.

172. Zavaliche, F., et al., *Multiferroic Storage Medium*. 2010, Seagate Technology LLC (Scotts Valley, CA, US): US 20100188773.

173. Zou, Y.K., et al., *Heterostructure of ferromagnetic and ferroelectric and the method to make of*. 2008: US 20080145693.

174. Fu Qiuyun, et al., *Double-layer barium titanate-cobalt ferrite multiferroic composite membrane material preparation method thereof*, S.I.P.O.o.t.P.R.C.E.L.P. (SIPO), Editor. 2009, Huazhong University of Science & Technology: CN 200910273198.

175. Information on: " http://www.extremenxt.com/blog/?page_id=77".

176. Valasek, J., *Piezo-electric and allied phenomena in rochelle salt*. Physical Review, **1921**. 17(4): p. 475-481.

177. Erwin Schrödinger, *Studien üder Kinetik der Dielektrika, dam Schmelzpunkt, Pyro-und Piezoelekrizitä*. November, 1912, Akademie der Wissenschaften in Wien: Aus sen Sitzungsberichten der Kaiserl.

178. Wul, B. and I. Goldman, *Dielectric constants of titanates of metals of the second group*. Compt. rend. Acad. sci. URSS, **1945**. 46: p. 139-42.

179. Von Hippel, A., et al., *High dielectric constant ceramics*. Industrial & Engineering Chemistry, **1946**. 38(11): p. 1097-1109.

180. Gray, R.B., *Transducer and method of making the same*. 1949, ERIE RESISTOR CORP.

181. *http://eur-lex.europa.eu/LexUriServ/LexUriServ.do?uri=OJ:L:2003:037:0019:0023 en: PDF*, Directive 2002/95/EC. (Official Journal of the European Union, Editor. Accessed Mar 22, 2012.

182. Information on: " http://leginfo.ca.gov/cgi-bin/waisgate?WAISdocID=6440788735+0 +0+0&WAISaction=retrieve".

183. Lang, S.B. and H.L.W. Chan, *Frontiers of Ferroelectricity*. 2007.

184. Dragan, D., *Ferroelectric, dielectric and piezoelectric properties of ferroelectric thin films and ceramics*. Reports on Progress in Physics, **1998**. 61(9): p. 1267.

185. Scott, J.F. and C.A. Paz de Araujo, *Ferroelectric Memories*. Science, **1989**. 246(4936): p. 1400-1405.

186. Lines, M.E. and A.M. Glass, *Principles and applications of ferroelectrics and related materials*. 1977: Oxford University Press.

187. Goldschmidt, V., *Crystal structure and chemical constitution*. Transactions of the Faraday Society, **1929**. 25: p. 253-283.

188. Desheng, F. and I. Mitsuru, *Ferroelectricity in silver perovskite oxides*, in *Ferroelectrics - Material Aspects*, M. Lallart, Editor. 2011. p. 413-442.

189. Xu, Y. and X. Yuhuan, *Ferroelectric materials and their applications*. Piezoelectric Resonators and Their Applications. 1991, North-Holland: Elsevier, Amsterdam 1991.

190. Cochran, W., *Crystal stability and the theory of ferroelectricity.* Advances in Physics, **1960**. 9(36): p. 387-423.

191. Blinc, R. and B. Žekš, *Dynamics of order-disorder-type ferroelectrics and anti-ferroelectrics.* Advances in Physics, **1972**. 21(93): p. 693-757.

192. Cross, L.E., *Ferroelectric ceramics: tailoring properties for specific applications*, in *Ferroelectric ceramics*. 1993, Springer. p. 1-85.

193. Burfoot, J.C. and G.W. Taylor, *Polar dielectrics and their applications*. Dielectric devices. 1979: Univ of California Press.

194. De Araujo, C.P., J.F. Scott, and G.W. Taylor, *Ferroelectric thin films: synthesis and basic properties*. Vol. 10. 1996: Taylor & Francis.

195. Fousek, J. and V. Janovec, *The orientation of domain walls in twinned ferroelectric crystals.* Journal of Applied Physics, **1969**. 40(1): p. 135-142.

196. Muralt, P., *Ferroelectric thin films for micro-sensors and actuators: a review.* Journal of Micromechanics and Microengineering, **2000**. 10(2): p. 136.

197. Dudley, A.B., *Ferroelectrics for digital information storage and switching.* Report R-212, MIT, **1952**.

198. Auciello, O., J.F. Scott, and R. Ramesh, *The Physics of Ferroelectric Memories.* Physics Today, **1998**. 51(7): p. 22-27.

199. Information on: " http://en.wikipedia.org/wiki/Ferroelectric_RAM".

200. Sumi, T., et al. *A 256 kb nonvolatile ferroelectric memory at 3 V and 100 ns*. in *Solid-State Circuits Conference, 1994. Digest of Technical Papers. 41st ISSCC., 1994 IEEE International*. 1994. IEEE.

201. Takashima, D., et al., *A 76-mm 2 8-Mb chain ferroelectric memory.* Solid-State Circuits, IEEE Journal of, **2001**. 36(11): p. 1713-1720.

202. Shiratake, S., et al., *A 32-Mb chain FeRAM with segment/stitch array architecture.* Solid-State Circuits, IEEE Journal of, **2003**. 38(11): p. 1911-1919.

203. Hoya, K., et al. *A 64 Mb Chain FeRAM with Quad-BL Architecture and 200MB/s Burst Mode*. in *Solid-State Circuits Conference, 2006. ISSCC 2006. Digest of Technical Papers. IEEE International*. 2006.

204. Shiga, H., et al. *A 1.6 GB/s DDR2 128Mb chain FeRAM with scalable octal bitline and sensing schemes*. in *Solid-State Circuits Conference - Digest of Technical Papers, 2009. ISSCC 2009. IEEE International*. 2009.

205.   Shimojo, Y., et al. *High-density and high-speed 128Mb chain FeRAM™ with SDRAM-compatible DDR2 interface*. in *VLSI Technology, 2009 Symposium on*. 2009. IEEE.

206.   Scott, J.F., et al., *Recent materials characterizations of [2D] and [3D] thin film ferroelectric structures*. Journal of the American Ceramic Society, **2005**. 88(7): p. 1691-1701.

207.   Kondo, V.K.M.V.M., V.S.K. Singh, and V.H. Ishiwara, *New ferroelectric material for embedded FRAM LSIs*. Fujitsu Sci. Tech. J, **2007**. 43(4): p. 502-507.

208.   Bottger, U. and S.R. Summerfelt, *Nanoelectronics and Information Technology: Advanced Electronic Materials and Novel Devices,*, in *Ferroelectric Random Access Memories*, R. Waser, Editor. 2003, Willey-VCH, Weinheim. p. 567-588.

209.   Information on: " http://www.itrs.net/Links/2010ITRS/Home2010.htm".

210.   Takashima, D., *Overview and scaling prospect of ferroelectric memories*. CMOS Processors and Memories, **2010**: p. 36 - 380.

211.   Morrison, F.D., et al., *Ferroelectric nanotubes*. Rev. Adv. Mater. Sci., **2003**. 4: p. 114.

212.   Maxim, F.V., *Bottom up strategies for the morphology control of BaTiO₃ particulates*, in *Department of Materials and Ceramic Engineering*. 2010, University of Aveiro: Aveiro.

213.   Spanier, J.E., et al., *Ferroelectric phase transition in individual single-crystalline BaTiO₃ nanowires*. Nano Letters, **2006**. 6(4): p. 735-739.

214.   Xu, Y., *Ferroelectric materials and their applications* Piezoelectric Resonators and Their Applications. 1991, North-Holland: Elsevier, Amsterdam 1991.

215.   Känzig, W. and M. Peter, *Critical domain size in ferroelectrics*. Physical Review, **1952**. 85(5): p. 940-941.

216.   Morozovska, A.N., E.A. Eliseev, and M.D. Glinchuk, *Size effects and depolarization field influence on the phase diagrams of cylindrical ferroelectric nanoparticles*. Physica B: Physics of Condensed Matter, **2007**. 387(1-2): p. 3558-366.

217.   Arlt, G., *Twinning in ferroelectric and ferroelastic ceramics: stress relief*. Journal of Materials Science, **1990**. 25(6): p. 2655-2666.

218.   Li, S., et al., *Size effects in nanostructured ferroelectrics*. Physics Letters A, **1996**. 212(6): p. 341-346.

219.   Junquera, J. and P. Ghosez, *Critical thickness for ferroelectricity in perovskite ultrathin films*. Nature, **2003**. 422(6931): p. 506-509.

220.   Meyer, B. and D. Vanderbilt, *Ab initio study of BaTiO₃ and PbTiO₃ surfaces in external electric fields*. Physical Review B, **2001**. 63(20): p. 205426.

221.   Ghosez, P. and K.M. Rabe, *Microscopic model of ferroelectricity in stress-free PbTiO₃ ultrathin films*. Applied Physics Letters, **2000**. 76(19): p. 2767-2769.

222. Jiang, B., et al., *Size effects on ferroelectricity of ultrafine particles of PbTiO₃.* Journal of Applied Physics, **2000**. 87(7): p. 3462-3467.

223. Ishikawa, K., et al., *Size effect on the phase transition in PbTiO₃ fine particles.* Jpn. J. Appl. Phys., **1996**. 35: p. 5196.

224. Chu, M.-W., et al., *Impact of misfit dislocations on the polarization instability of epitaxial nanostructured ferroelectric perovskites.* Nat Mater, **2004**. 3(2): p. 87-90.

225. Tybell, T., C.H. Ahn, and J.M. Triscone, *Ferroelectricity in thin perovskite films.* Applied Physics Letters, **1999**. 75(6): p. 856-858.

226. Maruyama, T., et al., *Growth and characterization of 10-nm-thick c-axis oriented epitaxial PbZr₀.₂₅Ti₀.₇₅O₃ thin films on (100)Si substrate.* Applied Physics Letters, **1998**. 73(24): p. 3524-3526.

227. Polking, M.J., et al., *Ferroelectric order in individual nanometre-scale crystals.* Nat Mater, **2012**. 11(8): p. 700-709.

228. Fong, D.D., et al., *Ferroelectricity in ultrathin perovskite films.* Science, **2004**. 304(5677): p. 1650-1653.

229. Ebenezer, D.D. and R. Ramesh, *Analysis of axially polarized piezoelectric cylinders with arbitrary boundary conditions on flat surfaces.* Journal Acoust Soc Am, **2003**. 113: p. 1900-8.

230. Morozovska, A.N., E.A. Eliseev, and M.D. Glinchuk, *Ferroelectricity enhancement in confined nanorods: Direct variational method.* Physical Review B, **2006**. 73(21): p. 214106.

231. Morozovska, A.N., M.D. Glinchuk, and E.A. Eliseev, *Ferroelectricity enhancement in ferroelectric nanotubes.* Phase Transitions, **2007**. 80(1-2): p. 71-77.

232. Geneste, G., *Finite-size effects in BaTiO₃ nanowires.* Appl. Phys. Lett., **2006**. 88(11): p. 112906.

233. Naumov, I.I. and H. Fu, *Spontaneous polarization in one-dimensional Pb(ZrTi)O₃ nanowires.* Physical Review Letters, **2005**. 95(24): p. 247602.

234. Hong, J. and D. Fang, *Systematic study of the ferroelectric properties of Pb(Zr₀.₅Ti₀.₅)O₃ nanowires.* Journal of Applied Physics, **2008**. 104(6): p. 064118.

235. Hong, J. and D. Fang, *Size-dependent ferroelectric behaviors of BaTiO₃ nanowires.* Applied Physics Letters, **2008**. 92(1): p. 012906

236. Pilania, G., S.P. Alpay, and R. Ramprasad, *Ab initio study of ferroelectricity in BaTiO₃ nanowires.* Physical Review B, **2009**. 80(1): p. 014113.

237. Shimada, T., S. Tomoda, and T. Kitamura, *Ab initio study of ferroelectricity in edged PbTiO₃ nanowires under axial tension.* Physical Review B, **2009**. 79(2): p. 024102.

238. Cai, M.Q., et al., *Nanosize confinement induced enhancement of spontaneous polarization in a ferroelectric nanowire.* Applied Physics Letters, **2009**. 95(23): p. 232901.

239. Ma, W., *Surface tension and Curie temperature in ferroelectric nanowires and nanodots.* Applied Physics A, **2009**. 96(4): p. 915-920.

240. Zheng, Y., C.H. Woo, and B. Wang, *Surface tension and size effect in ferroelectric nanotubes.* Journal of Physics: Condensed Matter, **2008**. 20(13): p. 135216.

241. Zhang, Y., et al., *Molecular dynamics investigations on the size-dependent ferroelectric behavior of BaTiO₃ nanowires.* Nanotechnology, **2009**. 20(40): p. 405703.

242. Nonnenmann, S.S., et al., *Finite curvature-mediated ferroelectricity.* Nano Letters, **2010**. 10(2): p. 542-546.

243. Yun, W.S., et al., *Ferroelectric properties of individual barium titanate nanowires investigated by scanned probe microscopy.* Nano Letters, **2002**. 2(5): p. 447-450.

244. Morrison, F.D. and et al., *High aspect ratio piezoelectric strontium–bismuth–tantalate nanotubes.* Journal of Physics: Condensed Matter, **2003**. 15(33): p. L527.

245. Luo, Y., et al., *Ferroelectric lead zirconate titanate and barium titanate nanotubes.* Integrated Ferroelectrics: An International Journal, **2003**. 59: p. 1513-1520.

246. Zhang, X., *Synthesis and piezoresponse of highly ordered Pb(Zr₀.₅₃Ti₀.₄₇)O₃ nanowire arrays.* Appl. Phys. Lett., **2004**. 85(18): p. 4190.

247. Yadlovker, D. and S. Berger, *Uniform orientation and size of ferroelectric domains.* Physical Review B, **2005**. 71(18): p. 184112.

248. Wang, Z., *One-dimensional ferroelectric monodomain formation in single crystalline BaTiO₃ nanowire.* Appl. Phys. Lett., **2006**. 89(26): p. 263119.

249. Schilling, A., et al., *Morphological control of polar orientation in single-crystal ferroelectric nanowires.* Nano Letters, **2007**. 7(12): p. 3787-3791.

250. Schilling, A., et al., *Scaling of domain periodicity with thickness measured in BaTiO₃ single crystal lamellae and comparison with other ferroics.* Physical Review B, **2006**. 74(2): p. 024115.

251. Schilling, A., *Ferroelectric domain periodicities in nanocolumns of single crystal barium titanate.* Appl. Phys. Lett., **2006**. 89(21): p. 212902.

252. Saeterli, R., et al., *Polarization control in ferroelectric PbTiO₃ nanorods.* Journal of Applied Physics, **2010**. 108(12): p. 124320-6.

253. Ginzburg, V.L., et al., *On the problem of superdiamagnetism.* Solid State Communications, **1984**. 50(4): p. 339-343.

254. Fu, H. and L. Bellaiche, *Ferroelectricity in barium titanate quantum dots and wires.* Physical Review Letters, **2003**. 91(25): p. 257601.

255. Naumov, I. and H. Fu, *Vortex-to-Polarization Phase Transformation Path in Ferroelectric Pb(ZrTi)O₃ Nanoparticles.* Physical Review Letters, **2007**. 98(7): p. 077603.

256. Gorbatsevich, A. and Y.V. Kopaev, *Toroidal order in crystals.* Ferroelectrics, **1994**. 161(1): p. 321-334.

257. Scott, J.F., *Ferroelectrics: Novel geometric ordering of ferroelectricity.* Nat Mater, **2005**. 4(1): p. 13-14.

258. Kim, K. and S. Lee, *Integration of lead zirconium titanate thin films for high density ferroelectric random access memory.* Journal of Applied Physics, **2006**. 100(5): p. 051604-11.

259. Ganpule, C.S., et al., *Scaling of ferroelectric properties in thin films.* Applied Physics Letters, **1999**. 75(3): p. 409-411.

260. Funakubo, H., et al., *Trial for making three dimensional PZT capacitor for high density ferrorlectric random access memory.* Integrated Ferroelectrics, **2006**. 81(1): p. 219-226.

261. Goux, L., et al., *Composition control and ferroelectric properties of sidewalls in integrated three-dimensional SrBi₂Ta₂O₉ based ferroelectric capacitors.* Journal of Applied Physics, **2005**. 98(5): p. 054507-7.

262. Goux, L., et al., *Scaling potential of pin-type 3-D SBT ferroelectric capacitors integrated in 0.18μm CMOS technology.* Microelectronic Engineering, **2006**. 83(10): p. 2027-2031.

263. Goux, L., et al., *A highly reliable 3-D integrated SBT ferroelectric capacitor enabling FeRAM scaling.* Electron Devices, IEEE Transactions on, **2005**. 52(4): p. 447-453.

264. Menou, N., et al., *Sidewalls contribution in integrated three-dimensional Sr₀.₈Bi₂.₂Ta₂O₉-based ferroelectric capacitors.* Applied Physics Letters, **2005**. 87(7): p. 073502-3.

265. Goux, L., et al., *Scaling potential of pin-type 3-D SBT ferroelectric capacitors integrated in 0.18 μm CMOS technology.* Microelectronic engineering, **2006**. 83(10): p. 2027-2031.

266. Huang, Q. and L. Gao, *Immobilization of rutile TiO₂ on multiwalled carbon nanotubes.* Journal of Materials Chemistry, **2003**. 13(7): p. 1517-1519.

267. Ruangchalermwong, C. and S. Muensit, *Effect of carbon nanotubes incorporation on characteristics of sol-gel derived PZT film* J.Nat.Sci. Special Issue on Nanotechnology, **2008**. 7(1): p. 1.

268. Xia, Y., et al., *One-dimensional nanostructures: synthesis, characterization, and applications.* Advanced Materials, **2003**. 15(5): p. 353-389.

269. Gruverman, A. and A. Kholkin, *Nanoscale ferroelectrics: processing, characterization and future trends.* Rep Prog Phys, **2006**. 69: p. 2443.

270. Han, H., et al., *Nanostructured ferroelectrics: fabrication and structure–property relations.* Advanced Materials, **2011**. 23(40): p. 4599-4613.

271. Alexe, M., C. Harnagea, and D. Hesse, *Non-conventional micro- and nanopatterning techniques for electroceramics.* Journal of Electroceramics, **2004**. 12(1-2): p. 69-88.

272. Nagarajan, V., A. Stanishevsky, and R. Ramesh, *Ferroelectric nanostructures via a modified focused ion beam technique.* Nanotechnology, **2006**. 17(1): p. 338.

273. Nagarajan, V., et al., *Dynamics of ferroelastic domains in ferroelectric thin films.* Nat Mater, **2003**. 2(1): p. 43-47.

274. Schilling, A., et al., *Domains in ferroelectric nanodots.* Nano Letters, **2009**. 9(9): p. 3359-3364.

275. Alexe, M., et al., *Patterning and switching of nanosize ferroelectric memory cells.* Applied Physics Letters, **1999**. 75(12): p. 1793-1795.

276. Alexe, M., et al., *Polarization imprint and size effects in mesoscopic ferroelectric structures.* Applied Physics Letters, **2001**. 79(2): p. 242-244.

277. Alexe, M., et al., *100-nm lateral size ferroelectric memory cells fabricated by electron-beam direct writing.* Applied Physics A, **2000**. 70(3): p. 247-251.

278. Bühlmann, S., et al., *Size effect in mesoscopic epitaxial ferroelectric structures: Increase of piezoelectric response with decreasing feature size.* Applied Physics Letters, **2002**. 80(17): p. 3195-3197.

279. Lee, K. and S. Baik, *Ferroeleastic domain structure and switching in epitaxial ferroelectric thin films.* Annual Review of Materials Research, **2006**. 36(1): p. 81-116.

280. Vrejoiu, I., et al., *Ferroelectric nanostructures.* Journal of Vacuum Science & Technology B, **2009**. 27(1): p. 498-503.

281. Seifert, A., et al., *Microstructural instability in single-crystal thin films.* Journal of Materials Research, **1996**. 11(06): p. 1470-1482.

282. Alexe, M. and D. Hesse, *Self-assembled nanoscale ferroelectrics.* Journal of Materials Science, **2006**. 41(1): p. 1-11.

283. Szafraniak, I., et al., *Epitaxial lead zirconate titanate nanocrystals obtained by a self-patterning method.* Integrated Ferroelectrics, **2004**. 61(1): p. 231-238.

284. Szafraniak, I., et al., *Self-assembled ferroelectric nanostructures.* Integrated Ferroelectrics, **2004**. 68(1): p. 279-286.

285. Roelofs, A., et al., *Towards the limit of ferroelectric nanosized grains.* Nanotechnology, **2003**. 14(2): p. 250.

286. Szafraniak, I., et al., *Ferroelectric epitaxial nanocrystals obtained by a self-patterning method.* Applied Physics Letters, **2003**. 83(11): p. 2211-2213.

287. Roelofs, A., et al., *Piezoresponse force microscopy of lead titanate nanograins possibly reaching the limit of ferroelectricity.* Applied Physics Letters, **2002**. 81(27): p. 5231-5233.

288. Szafraniak, I. and M. Alexe, *Hydrothermal growth of nanosize ferroelectrics.* Ferroelectrics, **2003**. 291(1): p. 19-26.

289. Chu, M.-W., et al., *Elastic coupling between 90° twin walls and interfacial dislocations in epitaxial ferroelectric perovskites: A quantitative high-resolution transmission electron microscopy study.* Physical Review B, **2005**. 72(17): p. 174112.

290. Fujisawa, H., et al., *Ferroelectricity of the 1.7 nm-high and 38 nm-wide self-assembled $PbTiO_3$ island.* Journal of the European Ceramic Society, **2004**. 24(6): p. 1641-1645.

291. Shimizu, M., et al., *Self-assembled $PbTiO_3$ Nanoislands prepared by MOCVD.* Integrated Ferroelectrics, **2004**. 62(1): p. 109-113.

292. Nonomura, H., et al., *Self-assembled $PbTiO_3$ nano-islands prepared on $SrTiO_3$ by metalorganic chemical vapor deposition.* Japanese Journal of Applied Physics, **2003**. 42: p. 5918.

293. Alexe, M., et al., *Ferroelectric nanotubes fabricated using nanowires as positive templates.* Applied Physics Letters, **2006**. 89(17): p. -.

294. Young, R.J., *Micro-machining using a focused ion beam.* Vacuum, **1993**. 44(3): p. 353-356.

295. Giannuzzi, L.A. and F.A. Stevie, *Introduction to focused ion beams: instrumentation, theory, techniques and practice.* 2005: Springer.

296. Craighead, H.G. and L.M. Schiavone, *Metal deposition by electron beam exposure of an organometallic film.* Applied Physics Letters, **1986**. 48(25): p. 1748-1750.

297. Pauleau, Y., *Chemical physics of thin film deposition processes for micro-and nano-technologies.* Vol. 55. 2002: Springer.

298. Wessels, B.W., *Metal-organic chemical vapor deposition of ferroelectric oxide thin-films for electronic and optical applications.* Annual Review of Materials Science, **1995**. 25: p. 525-546.

299. Yoshimura, M. and K. Byrappa, *Hydrothermal processing of materials: past, present and future.* Journal of Materials Science, **2008**. 43(7): p. 2085-2103.

300. Schneller, T., et al., *Chemical solution deposition of functional oxide thin films.* 2013: Springer.

301. Eason, R., *Pulsed laser deposition of thin films: applications-led growth of functional materials.* 2007: John Wiley & Sons.

302. Nalwa, H.S., *Handbook of Nanostructured Materials and Nanotechnology, Five-Volume Set.* Vol. 3. 1999: Academic Press.

303. Brinker, C.J. and G.W. Scherer, *Sol-gel science: the physics and chemistry of sol-gel processing.* 1990: Access Online via Elsevier.

304. Klein, L.C., *Sol-gel optics: processing and applications.* 1994: Springer.

305. Livage, J., *Sol-gel chemistry and molecular sieve synthesis*. Studies in surface science and catalysis, **1994**. 85: p. 1-42.

306. Livage, J., *Sol-Gel chemistry and molecular sieve synthesis*, in *Studies in surface science and catalysis*, M.S.H.G.K. J.C. Jansen and J. Weitkamp, Editors. 1994, Elsevier. p. 1-42.

307. Information on: " http://www.centexbel.be/solgel-treatment".

308. Demazeau, G., *Solvothermal processes: a route to the stabilization of new materials*. J. Mater. Chem., **1999**. 9(1): p. 15-18.

309. Walton, R.I., *Subcritical solvothermal synthesis of condensed inorganic materials*. Chemical Society Reviews, **2002**. 31(4): p. 230-238.

310. Eckert, J.O., et al., *Kinetics and Mechanisms of Hydrothermal Synthesis of Barium Titanate*. Journal of the American Ceramic Society, **1996**. 79(11): p. 2929-2939.

311. Kerchner Jeffrey, A., et al., *Nucleation and formation mechanisms of hydrothermally derived barium titanate*, in *Synthesis and Characterization of Advanced Materials*. 1997, American Chemical Society. p. 106-119.

312. Modeshia, D.R. and R.I. Walton, *Solvothermal synthesis of perovskites and pyrochlores: crystallisation of functional oxides under mild conditions*. Chemical Society Reviews, **2010**. 39(11): p. 4303-4325.

313. Sun, X.M., et al., *A CTAB-assisted hydrothermal orientation growth of ZnO nanorods*. Materials Chemistry and Physics, **2003**. 78(1): p. 99-104.

314. Bae, C., et al., *Template-directed synthesis of oxide nanotubes: fabrication, characterization, and applications*. Chemistry of Materials, **2008**. 20(3): p. 756-767.

315. Li, D. and Y. Xia, *Electrospinning of nanofibers: reinventing the wheel?* Advanced Materials, **2004**. 16(14): p. 1151-1170.

316. Zhan, S., et al., *Co-electrospun BaTiO$_3$ hollow fibers combined with sol-gel method*. Journal of Dispersion Science and Technology, **2008**. 29(9): p. 1345-1348.

317. Mensur Alkoy, E., C. Dagdeviren, and M. Papila, *Processing conditions and aging effect on the morphology of PZT electrospun nanofibers, and dielectric properties of the resulting 3–3 PZT/polymer composite*. Journal of the American Ceramic Society, **2009**. 92(11): p. 2566-2570.

318. Rørvik, P.M., T. Grande, and M.-A. Einarsrud, *One-dimensional nanostructures of ferroelectric perovskites*. Advanced Materials, **2011**. 23(35): p. 4007-4034.

319. Pacholski, C., A. Kornowski, and H. Weller, *Self-assembly of ZnO: from nanodots to nanorods*. Angewandte Chemie International Edition, **2002**. 41(7): p. 1188-1191.

320. Yang, J., et al., *Ultrathin BaTiO$_3$ nanowires with high aspect ratio: A simple one-step hydrothermal synthesis and their strong microwave absorption*. ACS Applied Materials & Interfaces, **2013**. 5(15): p. 7146-7151.

321. Kanyó, T., et al., *Quantitative characterization of hydrophilic−hydrophobic properties of MWNTs surfaces.* Langmuir, **2004**. 20(5): p. 1656-1661.

322. Young, T., *An essay on the cohesion of fluids.* Philosophical Transactions of the Royal Society of London, **1805**. 95: p. 65-87.

323. Yuan, Y. and T.R. Lee, *Contact angle and wetting properties*, in *Surface Science Techniques*. 2013, Springer. p. 3-34.

324. Warren, B.E., *X-ray Diffraction*. 1969: Courier Dover Publications.

325. Information on: " http://universe-review.ca/F13-atom04.htm".

326. Griffiths, P.R. and J.A. De Haseth, *Fourier transform infrared spectrometry*. Vol. 171. 2007: John Wiley & Sons.

327. Gans, P., *Vibrating molecules. An introduction to the interpretation of infrared and Raman spectra*. 1971, Chapman and Hall.

328. Information on: " http://chemwiki.ucdavis.edu/Organic_Chemistry/Organic_Chemistry _With_a_Biological_Emphasis/Chapter__4%3A_Structure_Determination_I/Section_4. 2%3A__Infrared_spectroscopy".

329. *http://en.wikipedia.org/wiki/Raman_spectroscopy*.

330. *http://www.horiba.com/us/en/scientific/products/raman-spectroscopy/tutorial-faqs/ raman-tutorial/the-theory-of-raman-spectroscopy/*.

331. Jorio, A., et al., *Determination of nanotubes properties by Raman spectroscopy.* Philosophical Transactions of the Royal Society of London. Series A: Mathematical, Physical and Engineering Sciences, **2004**. 362(1824): p. 2311-2336.

332. Williams, D.B. and C.B. Carter, *Transmission electron microscopy: a textbook for materials science.* Micron, **1997**. 28(1): p. 75-75.

333. Information on: " http://www.jeol.co.jp/en/science/sem.html".

334. Goldstein, J., et al., *Scanning electron microscopy and X-ray microanalysis*. 2003: Springer.

335. Binnig, G., C.F. Quate, and C. Gerber, *Atomic force microscope.* Physical Review Letters, **1986**. 56(9): p. 930.

336. García, R. and R. Perez, *Dynamic atomic force microscopy methods.* Surface science reports, **2002**. 47(6): p. 197-301.

337. Information on: " http://ip.physics.leidenuniv.nl/index.php/theses".

338. Information on: " http://www.emrl.de/r_m_2.html".

339. Foner, S., *Versatile and sensitive vibrating-sample magnetometer.* Review of Scientific Instruments, **2004**. 30(7): p. 548-557.

340.   Kissinger, H.E., *Reaction kinetics in differential thermal analysis.* Analytical Chemistry, **1957**. 29(11): p. 1702-1706.

341.   Coats, A.W. and J.P. Redfern, *Kinetic parameters from thermogravimetric data.* Nature, **1964**. 201(4914): p. 68-69.

342.   Kim, Y.A., et al., *Thermal stability and structural changes of double-walled carbon nanotubes by heat treatment.* Chemical Physics Letters, **2004**. 398(1-3): p. 87-92.

343.   Vuković, G.D., et al., *Removal of cadmium from aqueous solutions by oxidized and ethylenediamine-functionalized multi-walled carbon nanotubes.* Chemical Engineering Journal, **2010**. 157(1): p. 238-248.

344.   Vuković, G., et al., *Synthesis, characterization and cytotoxicity of surface amino-functionalized water-dispersible multi-walled carbon nanotubes.* Applied Surface Science, **2009**. 255(18): p. 8067-8075.

345.   Gao, Z., et al., *Investigation of factors affecting adsorption of transition metals on oxidized carbon nanotubes.* Journal of Hazardous Materials, **2009**. 167(1–3): p. 357-365.

346.   Zhao, L. and L. Gao, *Coating multi-walled carbon nanotubes with zinc sulfide.* Journal of Materials Chemistry, **2004**. 14(6): p. 1001-1004.

347.   Shan, Y. and L. Gao, *In situ coating carbon nanotubes with wurtzite ZnS nanocrystals.* Journal of the American Ceramic Society, **2006**. 89(2): p. 759-762.

348.   Hooker, M.W., *Properties of PZT-based piezoelectric ceramics between-150 and 250 °C.* 1998: Citeseer.

349.   Villegas, M., et al., *Influence of the calcining temperature on the sintering and properties of PZT ceramics.* Journal of Materials Science, **1993**. 28(13): p. 3482-3488.

350.   Chandratreya, S.S., R.M. Fulrath, and J.A. Pask, *Reaction mechanisms in the formation of PZT solid solutions.* Journal of the American Ceramic Society, **1981**. 64(7): p. 422-425.

351.   Hiremath, B.V., A.I. Kingon, and J.V. Biggers, *Reaction sequence in the formation of lead zirconate-lead titanate solid solution: Role of raw materials.* Journal of the American Ceramic Society, **1983**. 66(11): p. 790-793.

352.   Piticescu, R.M., et al., *Hydrothermal synthesis of ultradisperse PZT powders for polar ceramics.* Journal of the European Ceramic Society, **2004**. 24(6): p. 931-935.

353.   Lencka, M.M., A. Anderko, and R.E. Riman, *Hydrothermal precipitation of lead zirconate titanate solid solutions: thermodynamic modeling and experimental synthesis.* Journal of the American Ceramic Society, **1995**. 78(10): p. 2609-2618.

354.   Surowiak, Z., M.F. Kupriyanov, and D. Czekaj, *Properties of nanocrystalline ferroelectric PZT ceramics.* Journal of the European Ceramic Society, **2001**. 21(10–11): p. 1377-1381.

355.   Linardos, S., Q. Zhang, and J.R. Alcock, *Preparation of sub-micron PZT particles with the sol–gel technique.* Journal of the European Ceramic Society, **2006**. 26(1–2): p. 117-123.

356.   Wu, A., et al., *Seeding studies in PZT thin films.* Materials Research Bulletin, **1998**. 33(1): p. 59-68.

357.   Scott, J.F., *[3D] nano-scale ferroelectric devices for memory applications.* Ferroelectrics, **2005**. 314(1): p. 207-222.

358.   Wu, A., et al., *Lead zirconate titanate prepared from different zirconium and titanium precursors by sol-gel.* Journal of the American Ceramic Society, **1998**. 81(10): p. 2640-2644.

359.   Mahajan, A., et al., *Studies on the thermal decomposition of multiwall carbon nanotubes under different atmospheres.* Materials Letters, **2013**. 90(0): p. 165-168.

360.   Lashgari, K. and G. Westin, *Preparation of PZT film and powder by sol-gel technique using Ti- and Zr-alkoxides and a novel Pb-precursor; Pb(NO$_3$)$_2$ 1.5EO$_3$.* Journal of Sol-Gel Science and Technology, **1998**. 13(1/3): p. 865-868.

361.   Yang, W.-D., *PZT/PLZT ceramics prepared by hydrolysis and condensation of acetate precursors.* Ceramics International, **2001**. 27(4): p. 373-384.

362.   Zak, A.K. and W.H.A. Majid, *Effect of solvent on structure and optical properties of PZT nanoparticles prepared by sol–gel method, in infrared region.* Ceramics International, **2011**. 37(3): p. 753-758.

363.   MacLaren, I. and C.B. Ponton, *A TEM and HREM study of particle formation during barium titanate synthesis in aqueous solution.* Journal of the European Ceramic Society, **2000**. 20(9): p. 1267-1275.

364.   Liu, Y., K. Tai, and S.J. Dillon, *Growth kinetics and morphological evolution of ZnO precipitated from solution.* Chemistry of Materials, **2013**. 25(15): p. 2927-2933.

365.   Kwock, C. and S. Desu, *Ceramic Transactions: Ferrelectric Films*. Vol. 25. 1992, OH: ACS,Westerville.

366.   Peng, C. and S. Desu, *Ferroelectric Thin Films II*. Vol. 243. 1992, Pittsburgh, Pa.: Mater. Res. Soc. Symp. Proc. .

367.   Tani, T., Z. Xu, and D.A. Payne. *Preferred orientations for sol-gel derived PLZT thin layers*. in *MRS Proceedings*. 1993. Cambridge Univ Press.

368.   Kwok, C.K. and S.B. Desu, *Low temperature perovskite formation of lead zirconate titanate thin films by a seeding process.* Journal of materials research, **1993**. 8(02): p. 339-344.

369.   Suzuki, H., et al., *Low-temperature processing of Pb(Zr$_{0.53}$Ti$_{0.47}$)O$_3$ Thin film from stable precursor sol.* Journal of the European Ceramic Society, **1999**. 19(6–7): p. 1397-1401.

370. Jianming, Z., et al., *Influence of lead titanate seed layer on orientation behaviour and ferroelectric characteristics of sol-gel derived PZT thin films.* Journal of Physics: Condensed Matter, **1999**. 11(4): p. 1139.

371. Fu, Z., A. Wu, and P.M. Vilarinho, *Effect of seed layer thickness on texture and electrical properties of sol−gel derived ($Ba_{0.8}Sr_{0.2}$)TiO_3 thin films.* Chemistry of Materials, **2006**. 18(14): p. 3343-3350.

372. Wu, A., et al., *Early stages of crystallization of sol−gel-derived lead zirconate titanate thin films.* Chemistry of Materials, **2003**. 15(5): p. 1147-1155.

373. Bretos, I., et al., *Activated solutions enabling low-temperature processing of functional ferroelectric oxides for flexible electronics.* Advanced Materials, **2014**. 26: p. 1405-1409.

374. Priya, S. and S. Nahm, *Lead-free piezoelectrics.* 2011: Springer.

375. Takeuchi, T., et al., *Preparation of fine-grained $BaTiO_3$ ceramics by spark plasma sintering.* Journal of Materials Research, **2002**. 17(03): p. 575-581.

376. Uchino, K., E. Sadanaga, and T. Hirose, *Dependence of the crystal structure on particle size in barium titanate.* Journal of the American Ceramic Society, **1989**. 72(8): p. 1555-1558.

377. Harizanov, O.A., *Formation and crystallization of an acetate-acetylacetonate derived sol–gel $BaTiO_3$.* Materials Letters, **1998**. 34(3–6): p. 345-350.

378. Hu, M.Z.C., et al., *Homogeneous (co)precipitation of inorganic salts for synthesis of monodispersed barium titanate particles.* Journal of Materials Science, **2000**. 35(12): p. 2927-2936.

379. Suchanek, W.L. and R.E. Riman, *Hydrothermal synthesis of advanced ceramic powders.* Advances in Science and Technology, **2006**. 45: p. 184-193.

380. Chien, A.T., et al., *Electrical characterization of $BaTiO_3$ heteroepitaxial thin films by hydrothermal synthesis.* Journal of Materials Research, **1999**. 14(08): p. 3330-3339.

381. Chen, C., et al., *Hydrothermal synthesis of $BaTiO_3$: Crystal phase and the Ba^{2+} ions leaching behavior in aqueous medium.* Materials Chemistry and Physics, **2008**. 110(1): p. 186-191.

382. Maxim, F., et al., *Kinetic study of the static hydrothermal synthesis of $BaTiO_3$ using titanate nanotubes precursors.* Crystal Growth & Design, **2011**. 11(8): p. 3358-3365.

383. Cho, S.-B., M. Oledzka, and R.E. Riman, *Hydrothermal synthesis of acicular lead zirconate titanate (PZT).* Journal of Crystal Growth, **2001**. 226(2–3): p. 313-326.

384. Mahajan, A., et al., *Microscopy studies of carbon nanotubes/ferroelectric composites for microelectronics.* Microscopy and Microanalysis, **2012**. 18(SupplementS5): p. 107-108.

385. Riman, R.E., W.L. Suchanek, and M.M. Lencka. *Hydrothermal crystallization of ceramics.* in *Annales de Chimie Science des Materiaux.* 2002. Elsevier.

386. Li, W., et al., *Structure and electrical properties of BaTiO₃ prepared by sol-gel process.* Journal of Alloys and Compounds, **2009**. 482(1-2): p. 137-140.

387. Shaffer, M.S.P., X. Fan, and A.H. Windle, *Dispersion and packing of carbon nanotubes.* Carbon, **1998**. 36(11): p. 1603-1612.

388. Li, Y.-H., et al., *Self-organized Ribbons of Aligned Carbon Nanotubes.* Chemistry of Materials, **2002**. 14(2): p. 483-485.

389. Doeuff, S., et al., *Hydrolysis of titanium alkoxides: Modification of the molecular precursor by acetic acid.* Journal of Non-Crystalline Solids, **1987**. 89(1–2): p. 206-216.

390. Asiaie, R., et al., *Characterization of submicron particles of tetragonal BaTiO₃.* Chemistry of Materials, **1996**. 8(1): p. 226-234.

391. Donaldson, K., et al., *Carbon Nanotubes: A Review of Their Properties in Relation to Pulmonary Toxicology and Workplace Safety.* Toxicological Sciences, **2006**. 92(1): p. 5-22.

392. Taylor, D.V. and D. Damjanovic, *Piezoelectric properties of rhombohedral Pb (Zr,Ti)O₃ thin films with (100),(111), and "random" crystallographic orientation.* Applied Physics Letters, **2000**. 76(12): p. 1615-1617.

393. Zhu, N. and A.R. West, *Formation and stability of ferroelectric BaTi₂O₅.* Journal of the American Ceramic Society, **2010**. 93(1): p. 295-300.

394. Buscaglia, V., et al., *Grain size and grain boundary-related effects on the properties of nanocrystalline barium titanate ceramics.* Journal of the European Ceramic Society, **2006**. 26(14): p. 2889-2898.

395. Richard, C., et al., *Supramolecular self-assembly of lipid derivatives on carbon nanotubes.* Science, **2003**. 300(5620): p. 775-778.

396. Yu, J., et al., *Controlling the dispersion of multi-wall carbon nanotubes in aqueous surfactant solution.* Carbon, **2007**. 45(3): p. 618-623.

397. Vigolo, B., et al., *Macroscopic fibers and ribbons of oriented carbon nanotubes.* Science, **2000**. 290(5495): p. 1331-1334.

398. Liu, H., et al., *Large-scale single-chirality separation of single-wall carbon nanotubes by simple gel chromatography.* Nat Commun, **2011**. 2: p. 309.

399. Tummala, N.R. and A. Striolo, *SDS surfactants on carbon nanotubes: aggregate morphology.* ACS Nano, **2009**. 3(3): p. 595-602.

400. Wang, H., *Dispersing carbon nanotubes using surfactants.* Current Opinion in Colloid & Interface Science, **2009**. 14(5): p. 364-371.

401. Jona, F. and G. Shirane, *Ferroelectric crystals*. Vol. 108. 1993: Dover New York.

402. Ma, W. and D. Hesse, *Microstructure and piezoelectric properties of sub-80 nm high polycrystalline SrBi₂Ta₂O₉ nanostructures within well-ordered arrays.* Applied Physics Letters, **2004**. 85(15): p. 3214-3216.

403. Ravindran, P., et al., *Theoretical investigation of magnetoelectric behavior in BiFeO₃.* Physical Review B, **2006**. 74(22): p. 224412.

404. Wang, Y.P., et al., *Room-temperature saturated ferroelectric polarization in BiFeO₃ ceramics synthesized by rapid liquid phase sintering.* Applied Physics Letters, **2004**. 84(10): p. 1731-1733.

405. Selbach, S.M., M.-A. Einarsrud, and T. Grande, *On the thermodynamic stability of BiFeO₃.* Chemistry of Materials, **2008**. 21(1): p. 169-173.

406. Saeid, F. and R. Nazanin, *Microwave-induced solid-state decomposition of the Bi(Fe((CN)₆).5H₂O precursor: A novel route for the rapid and facile synthesis of pure and single-phase BiFeO₃ nanopowder.* Vol. 503. 2010, Kidlington,: Elsevier. 6.

407. Mazumder, R., et al., *Spark plasma sintering of BiFeO₃.* Materials Research Bulletin, **2009**. 44(3): p. 555-559.

408. Freitas, V., et al., *Structural, microstructural and magnetic investigations in high-energy ball milled BiFeO₃ and Bi₀.₉₅Eu₀.₀₅FeO₃ powders.* Journal of Alloys and Compounds, **2008**. 461(1): p. 48-52.

409. Liu, Z., Y. Qi, and C. Lu, *High efficient ultraviolet photocatalytic activity of BiFeO₃ nanoparticles synthesized by a chemical coprecipitation process.* Journal of Materials Science: Materials in Electronics, **2010**. 21(4): p. 380-384.

410. Han, S.H., et al., *Synthesis and characterization of multiferroic BiFeO₃ powders fabricated by hydrothermal method.* Ceramics International, **2010**. 36(4): p. 1365-1372.

411. Karimi, S., et al., *Nd-doped BiFeO₃ ceramics with antipolar order.* Applied Physics Letters, **2009**. 94(11): p. 112903.

412. Wang, J., et al., *Epitaxial BiFeO₃ multiferroic thin film heterostructures.* Science, **2003**. 299(5613): p. 1719-1722.

413. Martin, L.W., et al., *Multiferroics and magnetoelectrics: thin films and nanostructures.* Journal of Physics: Condensed Matter, **2008**. 20(43): p. 434220.

414. Wei, J., D. Xue, and Y. Xu, *Photoabsorption characterization and magnetic property of multiferroic BiFeO₃ nanotubes synthesized by a facile sol–gel template process.* Scripta Materialia, **2008**. 58(1): p. 45-48.

415. Xie, S.H., et al., *Nanocrystalline multiferroic BiFeO₃ ultrafine fibers by sol-gel based electrospinning.* Applied Physics Letters, **2008**. 93(22): p. 222904-3.

416. Liu, B., B. Hu, and Z. Du, *Hydrothermal synthesis and magnetic properties of single-crystalline BiFeO₃ nanowires.* Chemical Communications, **2011**. 47(28).

417. Zhao, Y., et al., *Ultra-thin BiFeO₃ nanowires prepared by a sol–gel combustion method: an investigation of its multiferroic and optical properties.* Journal of Materials Science: Materials in Electronics, **2012**. 23(1): p. 180-184.

418. Chiu, K.-C., T.-H. Yang, and J.-M. Wu, *Prominent electric properties of BiFeO₃ shells sputtered on ZnO-nanorod cores with LaNiO₃ buffer layers.* Nanotechnology, **2013**. 24(22): p. 225602.

419. Cole, M., et al., *Dry-transfer of aligned multiwalled carbon nanotubes for flexible Transparent thin films.* Journal of Nanomaterials, **2012**. 2012: p. 8.

420. Yun, K.Y., et al., *Structural and multiferroic properties of BiFeO₃ thin films at room temperature.* Journal of Applied Physics, **2004**. 96(6): p. 3399-3403.

421. Li, Z., et al., *Metal catalyst residues in carbon nanotubes decrease the thermal stability of carbon nanotube/silicone composites.* Carbon, **2011**. 49(13): p. 4138-4148.

422. Andrade, N., et al., *Temperature effects on the nitric acid oxidation of industrial grade multiwalled carbon nanotubes.* Journal of Nanoparticle Research, **2013**. 15(7): p. 1-11.

423. Dresselhaus, M.S., et al., *Raman spectroscopy of carbon nanotubes.* Physics Reports, **2005**. 409(2): p. 47-99.

424. Ajayan, P.M., et al., *Opening carbon nanotubes with oxygen and implications for filling.* Nature, **1993**. 362(6420): p. 522-525.

425. Gao, F., et al., *Preparation and photoabsorption characterization of BiFeO₃ nanowires.* Applied Physics Letters, **2006**. 89(10): p. 102506-3.

426. Zalesskii, A., et al., *57Fe NMR study of a spatially modulated magnetic structure in BiFeO3.* Journal of Experimental and Theoretical Physics Letters, **2000**. 71(11): p. 465-468.

427. Bea, H., et al., *Influence of parasitic phases on the properties of BiFeO₃ epitaxial thin films.* Applied Physics Letters, **2005**. 87(7): p. 072508-072508-3.

428. Catalan, G. and J.F. Scott, *Physics and applications of bismuth ferrite.* Advanced Materials, **2009**. 21(24): p. 2463-2485.

429. Valant, M., A.-K. Axelsson, and N. Alford, *Peculiarities of a Solid-State Synthesis of Multiferroic Polycrystalline BiFeO₃.* Chemistry of Materials, **2007**. 19(22): p. 5431-5436.

430. Ajayan, P.M., et al., *Single-walled carbon nanotube–polymer composites: strength and weakness.* Advanced Materials, **2000**. 12(10): p. 750-753.

431. Graupner, R., *Raman spectroscopy of covalently functionalized single-wall carbon nanotubes.* Journal of Raman Spectroscopy, **2007**. 38(6): p. 673-683.

432. Fukumura, H., et al., *Raman scattering study of multiferroic BiFeO₃ single crystal.* Journal of Magnetism and Magnetic Materials, **2007**. 310(2): p. e367-e369.

433. Deepti, K., et al., *Raman scattering study of polycrystalline magnetoelectric BiFeO₃.* Journal of Magnetism and Magnetic Materials, **2008**. 320: p. 548–552.

434. Katiyar, R. and Y.I. Yuzyuk, *Stress manipulation in ferroelectric thin films and superlattices.* Vibrational spectroscopy, **2007**. 45(2): p. 108-111.

435. Seidel, J., et al., *Conduction at domain walls in oxide multiferroics.* Nat Mater, **2009**. 8(3): p. 229-234.

436. Singh, S.K., K. Maruyama, and H. Ishiwara, *Reduced leakage current in La and Ni codoped BiFeO₃ thin films.* Applied Physics Letters, **2007**. 91(11): p. 112913.

437. Bretos, I., et al., *Defect-mediated ferroelectric domain depinning of polycrystalline BiFeO₃ multiferroic thin films.* Applied Physics Letters, **2014**. 104(9): p. 092905.

438. Kothari, D., et al., *Reduced leakage in epitaxial BiFeO₃ films following oxygen radio frequency plasma treatment.* Journal of Applied Physics, **2013**. 113(21): p. 214109.

439. Yun, K.Y., M. Noda, and M. Okuyama, *Prominent ferroelectricity of BiFeO₃ thin films prepared by pulsed-laser deposition.* Applied Physics Letters, **2003**. 83(19): p. 3981-3983.

440. Jaiswal, A., et al., *Effect of reduced particle size on the magnetic properties of chemically synthesized BiFeO₃ nanocrystals.* The Journal of Physical Chemistry C, **2010**. 114(5): p. 2108-2115.

441. Liu, B., B. Hu, and Z. Du, *Hydrothermal synthesis and magnetic properties of single-crystalline BiFeO₃ nanowires.* Chemical Communications, **2011**. 47(28): p. 8166-8168.

442. Kubel, F. and H. Schmid, *Structure of a ferroelectric and ferroelastic monodomain crystal of the perovskite BiFeO₃.* Acta Crystallogr., Sect. B: Struct. Sci, **1990**. 46: p. 698 - 702.

443. Park, T.-J., et al., *Size-dependent magnetic properties of single-crystalline multiferroic BiFeO₃ nanoparticles.* Nano Letters, **2007**. 7(3): p. 766-772.

Outputs

Papers and extended abstracts

1. A. Mahajan, A. Kingon, Á. Kukovecz, Z. Konya, and P. M. Vilarinho, "**Studies on the thermal decomposition of multiwall carbon nanotubes under different atmospheres**," Materials Letters, vol. 90, pp. 165-168, 2013.

2. A. Mahajan, R. I. Haque, P. M. Vilarinho, and A. Kingon, "**Microscopy Studies of Carbon Nanotubes/Ferroelectric Composites for Microelectronics**," Microscopy and Microanalysis, vol. 18, pp. 107-108, 2012.

3. Amit Mahajan, Pedro M Costa, Ákos Kukovecz, Paula M. Vilarinho, "**A microscopy study of Multiwall Carbon Nanotubes (MWCNTs)/BaTiO$_3$**", submitted to Microscopy and Microanalysis, accepted, 2014.

4. Amit Mahajan; Brian J. Rodriguez, K. Venkata Saravanam, E. Venkata Ramana; Pedro Costa; Paula M. Vilarinho "**Covering vertical aligned carbon nanotubes with a multiferroic compound**" Carbon, 82, 408 – 416, 2015.

5. Amit Mahajan, Ian Reaney, Pedro Costa, Angus Kingon, Zoltán Kónya; Ákos Kukovecz; Paula M. Vilarinho, "**Unveiling the Role of CNTs on the Phase Formation of Nano Ferroelectrics**" Submitted to Physical Chemistry Chemical Physics (2014).

Manuscripts (under Process)

1. Amit Mahajan; Brian J. Rodriguez, Ian Reaney, Angus Kingon, Ákos Kukovecz, Paula M. Vilarinho "**Nucleation of BT on the surface of MWCNTS at low temperature**" to be submitted to Nanoscale.

2. Amit Mahajan; Brian J. Rodriguez, Angus Kingon, Ákos Kukovecz, Paula M. Vilarinho "**Conformal covering of multiwall carbon nanotubes with BaTiO$_3$ by hydrothermal method** " to be submitted to Journal of Material Chemistry.

3. Amit Mahajan; Angus Kingon, Ákos Kukovecz, Paula M. Vilarinho "**Role of CNTs on fabrication of nanostructure of BiFeO$_3$ oxides**" to be submitted to Crystal Growth and Design or Journal of Applied Materials and interface.

Oral and Poster presentations

1 Invited talk on "Combination of Carbon Nanotubes (CNTs) with Ferroelectrics (FE) for Future Electronics" Paula M. Vilarinho, Amit Mahajan, Akos Kukovecz at

Szeged International Workshop on Advances in Nanoscience (SIWAN), Oct.15 – 18, 2014. Szeged, Hungry.

2   Oral presentation on "Fabrication of $BiFeO_3$ on aligned MWCNTs for microelectronic applications" Amit Mahajan, Paula M. Vilarinho and Brian Rodriguez, MC meeting & Closing Conference COST MPO904 Action, 2014, Jan. 30- Feb. 1, 2014, Genoa, Italy.

3   Oral presentation "$BiFeO_3$ on aligned CNTs for microelectronic applications" Paula M. Vilarinho, Amit Mahajan, K. Venkata Saravanan, Pedro M. Costa, Angus Kingon. 6th International conference on Electroceramics (ICE), 09-13 Nov.2013, João Pessoa, Brazil.

4   Oral presentation "Sol gel Hydrothermal Synthesis of $BaTiO_3$/MWCNTs for Microelectronic Applications" Amit Mahajan, Paula M. Vilarinho, Angus Kingon and Ákos Kukovecz, Joint IEEE-UFFC, EFTF, and PFM Symposium, July 22-25, 2013 at the Prague Convention Center, Prague, Czech Republic.

5   Oral presentation on "Hydrothermal Synthesis of $BaTiO_3$/MWCNTs for Microelectronic Applications" Amit Mahajan, Paula M. Vilarinho, Angus Kingon and Ákos Kukovecz. at Materiais 2013, Mar. 25-28, 2013, Coimbra, Portugal.

6   Poster presentation on "The Kinetics of the Ferroelectric Phase Formation in the Presence of MWCNTs" Paula Maria Vilarinho, Amit Mahajan, Angus Kingon, Akos Kukovecz, Zoltan Konya. at MRS Fall Meeting, Nov. 25-30, 2012, Boston Massachusetts, USA.

7   Oral presentation on "One Dimensional (1D) Composites of MWCNT/BiFeO3" Amit Mahajan, Paula M. Vilarinho, Angus Kingon and Ákos Kukovecz at E-MRS 2012 Fall Meeting, 17 to 21 September 2012, Warsaw, Poland.

8   Oral presentation on "Kinetic Studies on the Thermal Stability of MWCNTs", Amit Mahajan, Rubaiyet Iftekharul Haque, Paula M. Vilarinho, Angus Kingon at International Materials Symposium MATERIAIS 2011, 18 to 20 April 2011, Guimarães, Portugal.

9   Poster presentation on "Synthesis of MWCNTs-PZT Composites for Microelectronics" Amit Mahajan, Rubaiyet Iftekharul Haque, Paula M. Vilarinho, Angus Kingon at European science foundation meeting, Nanocarbons 2011, 6 - 11 September 2011, Acquafredda di Maratea, Italy.

10   Poster presentation on "Microscopy Studies of Carbon Nanotubes/FE Composites for Microelectronics" Amit Mahajan, Rubaiyet Iftekharul Haque, Paula M. Vilarinho, Angus Kingon 2nd Joint Congress of the Portuguese and Spanish Microscopy Societies, 18th to 21st of October 2011, Aveiro, Portugal.

11   Poster presentation on "1D Ferroelectric - carbon nanotubes composites" Paula M. Vilarinho, Amit Mahajan , Rubaiyet Iftekharul Haque, Angus Kingon MRS Fall Meeting, 28th Nov. – 2nd Dec. 2010, Boston, MA, USA.